



HAL
open science

Full-field optical coherence tomography for non-contact cellular-level resolution in vivo human cornea imaging

Viacheslav Mazlin

► **To cite this version:**

Viacheslav Mazlin. Full-field optical coherence tomography for non-contact cellular-level resolution in vivo human cornea imaging. Physics [physics]. Université Paris sciences et lettres, 2019. English. NNT : 2019PSLET024 . tel-02626956

HAL Id: tel-02626956

<https://pastel.hal.science/tel-02626956>

Submitted on 26 May 2020

HAL is a multi-disciplinary open access archive for the deposit and dissemination of scientific research documents, whether they are published or not. The documents may come from teaching and research institutions in France or abroad, or from public or private research centers.

L'archive ouverte pluridisciplinaire **HAL**, est destinée au dépôt et à la diffusion de documents scientifiques de niveau recherche, publiés ou non, émanant des établissements d'enseignement et de recherche français ou étrangers, des laboratoires publics ou privés.



THÈSE DE DOCTORAT
DE L'UNIVERSITÉ PSL

Préparée à l'ESPCI Paris et l'Institut Langevin, France

Tomographie optique cohérente pour l'imagerie in vivo de la corne

Soutenue par

Viacheslav MAZLIN

Le 05 09 2019

École doctorale n°564

Physique en Île-de-France

Spécialité

Physique

Composition du jury :

Prof. Vincent BORDERIE Hôpital des Quinze-Vingts, France	<i>Président</i>
Prof. Wolfgang DREXLER Medical University of Vienna, Austria	<i>Rapporteur</i>
Prof. Goran PETROVSKI University of Oslo, Norway	<i>Rapporteur</i>
Dr. Sarah MREJEN Hôpital des Quinze-Vingts, France	<i>Examineur</i>
Dr. Kristina IRSCH Institut de la Vision, France	<i>Examineur</i>
Prof. A. Claude BOCCARA ESPCI Paris, France	<i>Co-directeur de thèse</i>
Prof. Mathias FINK ESPCI Paris, France	<i>Directeur de thèse</i>

Acknowledgements

In every time of my life journey, I was very fortunate to go hand in hand with so many sincere supporting people. All these people are true heroes for me and I am very happy to have an opportunity to express my immense gratitude to them in the lines of this thesis.

First and foremost, I would like to express my sincere appreciation to the two persons, without whom this thesis would not be possible - Claude and Mathias! I am absolutely sure that I had the best scientific (and life!) mentors one can have! Their trust and believe in me were essential through the thesis and, in particular, when stepping into the uncharted scientific and engineering grounds. I am grateful for the independence they have given me to explore different ideas, while at the same time providing support in every moment, when it was needed. I would like to especially remark their truly encouraging passion and optimism toward research, and foresight, that is never limited by the borders of one scientific field.

Besides my advisors, I would also like to thank the rest of my honorable jury members for their valuable time to review my thesis and participate in the thesis defence. Thanks to Prof. Goran Petrovski and Prof. Wolfgang Drexler for writing the thesis reports with their invaluable professional suggestions and comments. Thanks to Prof. Vincent Borderie and Sarah Mrejen for their insightful comments from the medical doctor point of view.

My gratitude goes to Kristina and Kate, with whom we have worked from the very start. I still remember the moment, when we met for the first time and discussed the *in vivo* FFOCT project! It was challenging, ambitious, full of unknown and had the potential to solve real-life problems - the project that I could only dream to work on!

I want to thank the former and current members of LLTech team: Eugénie, Emilie, Alban, Franck, Charles and Bertrand. With all my knowledge on basic mechanical, optical and software principles of FFOCT I am indebted to each of the above people, who were always open for questions and spent generous time on my personal hands-on teaching, which I will always value.

The project would not have been even close to that enjoyable (and either successful) without different generations of FFOCT group members: Peng, Olivier, Egidijus, Jules, Clement, Thu-mai, Daria, Pedro, Kassandra and Amir. Especially, I want to thank my colleague (and friend!) Peng, with whom we shared many days in the dark optical lab trying experiments, discussing and trying experiments again (!) to bring FFOCT to *in vivo* corneal and retinal imaging. I am looking forward to my *revanche* in badminton!

Of course I cannot not mention our R31 office, where I had a pleasure to try some of the tastiest cakes in my life. Have my greetings, the tremendous Kammel, Joris, Maxim, Jules, Paul, Antoine, Julie and Clement, Florian, Aurelien, Olivier, Peng.

Leo, you definitely won the language challenge over me and I am not for a moment sad about that! Your Russian became really, really good, especially given that you have never visited the country. Will be always happy to host you in SPB, plus we should check China with Peng sometime!

Besides, I am also very happy to thank people, who sparkled so many of my interests.

My greatest appreciation goes to Prof. Jérôme Lesueur, who put so much passion into the PSL-ITI program, in which I was lucky to participate. I am convinced that this kind of education track is the future, because a combination of research and entrepreneurship can do much more for the world than the research alone. It is the PSL-ITI, which taught me to think about problems both locally and globally at the same time (from photons to the device on the market). Also, I am truly grateful to PSL-ITI students-friends who made my stay very comfortable in my first year in France!

I would like to thank Valentina Zhurikhina and Andrey Lipovskii, who were always wholeheartedly caring about the students in the first place. Without their support, I might not have been brave enough to move to Finland and France, would not have discovered so many things, and generally would not have been the same person, who I am now.

My passion to physics (and science in general) was undoubtedly shaped by the 6 years of going along the same corridors, discussing and lunching side by side with the brightest minds (and frequently Nobel Prize winners!) in Saint-Petersburg Academic University, conceived by Zhores Alferov.

I would like to say thank you to my teacher and friend Borevich Albert Zenonovich, who instilled my passion for math and who, by example, showed me that steady efforts from day to day can tackle any problem.

I would not have been able to write this text as well without dedication of my favourite English teachers back in school (although, I am sure they can still find many mistakes!). I remember our classes being the most anticipated, most creative and full of personal interactions of teachers and students.

Much more than thank-you I would like to say to my best friends!

Sasha and Max - you were always sincere and reliable through the hard University times!

Igor, Alessia, Ze, Kerstin - you are THE BEST! Moments together with you in Finland were among the most joyful in my life. I feel great pity that, while working on this thesis, I was barely involved in your day to day adventures, but I cannot wait to catch up our time right away!

Sasha, Vitya, Vlad, Kirill, Mitya - thank you for so many fun moments during our life-long friendships, which I treasure! I am looking forward to our summer, tennis matches and non-stop talks!

Jana, thank you for taking this never-boring Dresden - Saint-Petersburg - Maastricht - unknown Belgium village - Berlin - Paris adventure together!

Always with a smile I remember my childhood friends from Belarus and Saint-Petersburg, with whom our life paths have diverged. I am completely convinced, that it is during our 15+ hours/day soccer matches mixed with non-stop talks about everything (from the best penatly-scoring orientation of the foot to the origin of the Universe), I have learned to dream and

learned, that everything is interesting, if you go deeply enough!

Most importantly, I would like to express my biggest appreciation and gratitude to my family for all of their sacrifices, unconditional love and support!

Abstract (English)

This PhD project aimed to create an optical system for non-contact cellular resolution imaging of the human cornea *in vivo*. To achieve that, the contact *ex vivo* time-domain full-field optical coherence tomography (FFOCT) system was transformed into a non-contact *in vivo* imaging device and was for the first time applied to the human eye. FFOCT acquired images from the entire human cornea, limbus, sclera and tear film, revealing cells and nerves, which could be quantified over a millimetric field-of-view, beyond the capability of confocal microscopy and conventional optical coherence tomography (OCT). Blood flow and tear film dynamics could be directly followed and quantified. Furthermore, FFOCT was combined with a conventional OCT to perform real-time axial eye tracking and defocusing correction. The latter enabled real-time FFOCT imaging and display, which opens a path for future device implementation in clinical research and practice. Bench to bedside transfer of FFOCT is further stimulated by several solutions proposed in the manuscript, aiming to reduce the instrumentational complexity. Finally, a related FFOCT device was applied to imaging *in vivo* human retina, revealing the photoreceptors.

Keywords:

Tomography, Microscopy, Coherence, Cornea diagnostics

Résumé (Français)

Ce projet de thèse vise à créer un système optique pour l'imagerie à haute résolution sans contact de la cornée humaine *in vivo*. Pour y parvenir, le système de tomographie par cohérence optique plein champ travaillant dans le domaine temporel *ex vivo* par contact (FFOCT) a été transformé en un dispositif d'imagerie *in vivo* sans contact et a été appliqué pour la première fois à l'œil humain. La FFOCT a permis d'acquérir des images de la cornée, du limbe, de la sclère et du film lacrymal sur des yeux humains, révélant des cellules et des nerfs, pouvant être quantifiés sur un champ de vision millimétrique, bien au-delà des capacités de la microscopie confocale et de la tomographie par cohérence optique (OCT) conventionnelle. Le flux sanguin et la dynamique du film lacrymal ont pu être suivis directement et quantifiés. De plus, la FFOCT a été combinée à un OCT spectral pour effectuer un suivi des mouvements axiaux de l'œil en temps réel et une correction de la défocalisation. Ce dernier ajout a permis l'imagerie et l'affichage FFOCT en temps réel, ce qui ouvre la voie à la mise en œuvre future de dispositifs dans pour la recherche que pour la pratique clinique. Le transfert de FFOCT du laboratoire à l'hôpital est en outre stimulé par plusieurs solutions qui sont proposées dans le manuscrit, dans le but de réduire la complexité instrumentale. Enfin, un dispositif FFOCT apparenté a été appliqué à l'imagerie rétinienne humaine *in vivo*, révélant des photorécepteurs.

Mots clés:

Tomographie, Microscopie, Cohérence, Cornée Diagnostic

Contents

Introduction	1
I Ocular surface: anatomy, functions, diseases, clinical and emerging diagnostic techniques	5
1 Ocular surface structures, diseases and diagnostics in clinics	7
1.1 Introduction to ocular surface structures	9
1.1.1 Cornea	10
1.1.2 Morphological differences between the central and peripheral zones of the cornea	17
1.1.3 Limbus	18
1.1.4 Sclera	19
1.1.5 Bulbar conjunctiva	19
1.2 Ocular surface disorders and diagnostics in clinics	19
1.2.1 Global scope of ocular surface disorders	19
1.2.2 Dry eye disease	19
1.2.3 Fuch's endothelial dystrophy (FECD)	21
1.2.4 Microbial Keratitis	21
1.2.5 Keratoconus	23
1.2.6 Diabetes	23
1.2.7 Limbal stem cell deficiency	24
1.2.8 Conjunctivitis	24
2 State of the art and emerging methods for ocular surface imaging	27
2.1 Brief history of ocular surface imaging methods	28
2.2 Light-tissue interaction in the cornea	29
2.3 Slit lamp biomicroscopy	30
2.4 Specular microscopy	32
2.5 Confocal microscopy	33
2.5.1 Non-contact confocal microscopy	35
2.5.2 Image stitching into a large FOV	36
2.5.3 3D corneal images	37
2.5.4 Confocal microscopy + OCT	37
2.6 Optical coherence tomography	38
2.6.1 Spectral-domain OCT (SDOCT)	39
2.6.2 Swept-source (SSOCT)	42
2.6.3 Time-domain full-field OCT (FFOCT)	43

II Full-field Optical Coherence Tomography in application to <i>in vivo</i> human eye imaging	51
3 From <i>ex vivo</i> to <i>in vivo</i> full-field OCT	53
3.1 Motivation for FFOCT in ocular surface imaging	54
3.2 From contact <i>ex vivo</i> to non-contact <i>in vivo</i> FFOCT	55
3.2.1 Improving sensitivity in non-contact FFOCT	55
3.2.2 FFOCT image reconstruction	57
3.2.3 Performance characteristics	58
3.2.4 FFOCT motorized aligning	59
3.2.5 Problem of defocus and its correction	59
3.2.6 First test of non-contact FFOCT (<i>ex vivo</i> cornea)	61
3.2.7 First <i>in vivo</i> human corneal imaging with FFOCT	62
4 Towards real-time <i>in vivo</i> FFOCT	67
4.1 Concept of real-time <i>in vivo</i> FFOCT	68
4.2 Instrumentation of common-path FF/SD OCT	69
4.2.1 Design of integrated FF/SD OCT instrument	69
4.2.2 Tracking eye position with common-path FF/SD OCT	69
4.2.3 Real-time optical path length matching of FFOCT interferometer arms	72
4.3 Imaging results of common-path FF/SD OCT	72
4.3.1 Imaging <i>ex vivo</i> cornea, moving by the motorized stage	72
4.3.2 Imaging of <i>in vivo</i> human cornea (central)	74
4.3.3 Imaging of <i>in vivo</i> human cornea (peripheral)	76
4.3.4 Cell and nerve quantification	78
4.3.5 Imaging of <i>in vivo</i> human limbus	79
4.3.6 Intermediate conclusion	79
5 Monitoring dynamic processes in the eye with FFOCT	81
5.1 Dynamic processes in the eye - potential for FFOCT	82
5.2 FFOCT <i>in vivo</i> angiography	84
5.3 FFOCT for tear film imaging	87
6 Remark on extending field of view in FFOCT	89
6.1 Extending field of view in FFOCT	90
7 A glance at retinal imaging with FFOCT	93
7.1 Application of FFOCT to retinal imaging	94
8 Simplifying FFOCT	97
8.1 Back to technology fundamentals: a new solution for simple FFOCT	98
8.2 Phase modulation with natural movements of <i>in vivo</i> eye	98
8.3 Intermediate conclusion	104
Conclusions and perspectives	105
Publications	109

A	Light safety	111
A.1	General remarks	111
A.2	Light safety analysis for the FFOCT device according to the ISO 15004-2:2007 standard	112
A.2.1	Security analysis considerations	112
A.2.2	Light safety analysis	116
B	Résumé substantiel (FR)	125
B.1	Introduction	125
B.2	Chapitre 1: Structures superficielles oculaires, maladies et diagnostics cliniques.	126
B.2.1	Brève introduction aux structures de la surface oculaire	127
B.2.2	Troubles de la surface oculaire et diagnostics cliniques	127
B.2.3	Vision globale des troubles de la surface oculaire	127
B.3	Chapitre 2 : Etat de l'art et méthodes émergentes pour l'imagerie de la surface oculaire	129
B.4	Chapitre 3: Imagerie Tomographique par Cohérence optique plein champ (FFOCT) appliquée à l'oeil humain <i>in vivo</i>	132
B.5	Chapitre 4 : Vers la FFOCT <i>in vivo</i> en temps réel	134
B.6	Chapitre 5 : Suivi des processus dynamiques dans l'oeil par FFOCT	137
B.7	Chapitre 6 : Remarque sur l'extension du champ de vision en FFOCT	138
B.8	Chapitre 7 : Un coup d'œil sur l'imagerie de la rétine avec FFOCT	138
B.9	Chapitre 8 : Simplification de la FFOCT	139
	References	141

List of abbreviations

- **OCT**: Optical Coherence Tomography
- **FFOCT**: Full-field Optical Coherence Tomography
- **IVCM**: In vivo confocal microscopy
- **SDOCT**: Spectral-domain Optical coherence tomography
- **SSOCT**: Swept-source Optical Coherence Tomography
- **FF/SD OCT**: Full-field / Spectral-domain Optical coherence tomography
- **NIR**: Near-Infrared Light
- **BM**: Basement membrane
- **SNP**: Sub-basal nerve plexus
- **BL**: Bowman's layer
- **DM**: Descemet's membrane
- **POV**: Palisades of Vogt
- **NA**: Numerical Aperture
- **SLD**: Superluminescent laser diode
- **LED**: Light-emitting Diode
- **FOV**: Field of view
- **DOF**: Depth of focus
- **SNR**: Signal-to-Noise Ratio
- **MPE**: Maximum permissible exposure
- **FWC**: Full-well capacity
- **PZT**: Piezo-electric stage actuator
- **s.d.**: Standard deviation

Introduction

Recently, the 25th anniversary was celebrated by one of the most successful optical technologies ever implemented in medicine and clinical practice. From its initial inception in 1991 [1], optical coherence tomography (OCT) rapidly became an indispensable imaging modality in ophthalmology. Today OCT is the most commonly used ophthalmic imaging procedure by far with an estimated number of ~ 30 million OCT exams performed worldwide every year [2]. The secret to the OCT success is its technology of backscattering light interferometry, which offered possibility of non-invasive, non-contact imaging of the entire anterior segment and retina. Its ability to image the large sections of the eye with a high axial resolution was absolutely unique without existing analogues in other imaging techniques. Within its relatively short history, OCT has seen a tremendous increase in imaging speed, sensitivity, axial and lateral resolutions. In retinal imaging OCT demonstrated superior images comparing to other methods in every aspect: field of view, axial resolution and lateral resolution (thanks to the use of adaptive optics). In anterior eye, or more precisely, corneal imaging, OCT was unreachable in terms of the field of view and axial resolution. However, there was still the last outpost for OCT to be taken - the high resolution *en face* corneal imaging, which was best achieved with the confocal microscopy. This stayed true until the start of the present thesis project. Within the first year we obtained the first high resolution corneal images in the *en face* view [3]. In the next years we further improved the technology to enable real-time imaging, opening the technique for implementation in clinical research and translation into practice. The above was achieved with a special type of OCT called time-domain full-field OCT (FFOCT). FFOCT was originally developed in our laboratory 20 years ago in 1998 [4]. Comparing to the conventional OCT, FFOCT uses high numerical aperture (NA) optics to gain μm -level lateral resolution and a 2D camera to obtain *en face* images without scanning. FFOCT demonstrated numerous applications with the most successful being the instantaneous biopsy analysis during the ongoing surgery. The current thesis project had (and accomplished) a goal of transforming the *ex vivo* FFOCT into an *in vivo* ophthalmic instrument.

The thesis is divided into two parts:

The first part focuses on the cornea and the current state in its diagnostics.

- Chapter 1 gives the background about the structure and functions of anterior eye tissues (including the entire cornea, limbus, sclera and tear film). The supporting images from the electron microscopy, confocal microscopy, OCT, specular microscopy and slit

lamp biomicroscopy will be useful in the next chapters for comparison with FFOCT results. Within the same chapter we will look at several examples of corneal diseases and understand their current diagnostic strategies in clinics.

- Chapter 2 will show the evolution of the anterior eye diagnostic instruments from the golden standard slit lamp to the emerging research devices. We will compare their performances and will try to understand, what makes one instrument successful in clinics.

The second part covers our work on FFOCT.

- In Chapter 3 we will follow the transformation of FFOCT from the contact *ex vivo* device into a non-contact *in vivo* diagnostic tool. The first FFOCT images from the *in vivo* human cornea will be presented. Solutions to the rising problems of defocus, stray light, and eye movements will also be discussed.
- In Chapter 4 the first FFOCT prototype will be combined and synchronized with the spectral-domain OCT (SDOCT) into a FF/SD OCT device, to perform real-time axial eye tracking and defocusing correction on the fly. This enables consistent real-time FFOCT imaging of the entire cornea, limbus and sclera, opening the technology for use in clinical research and practice. Single shot images extracted from real-videos will be demonstrated. Cells and nerves will be quantified according to the existing protocols for confocal microscopy. Images of palisades of Vogt and vasculature at different depths of the inferior limbus will be presented and quantified.
- Chapter 5 will present the first FFOCT angiography data. Images, extracted from the videos of blood flow in the conjunctiva will be demonstrated. Individual blood cells could be resolved within the thin vessels. The fast imaging speed of 275 frames/s (0.6 billion pixels/s) allowed direct monitoring of blood flow dynamics, enabling creation of high-resolution blood flow velocity maps of limbus for the first time. The same chapter will show that FFOCT can be easily converted to a conventional microscope, enabling direct monitoring of tear film evolution. We show lipid tear images with good contrast and measure the tear film velocity and stabilization time following a blink together with the evaporation time of the liquid micro-droplets on the surface of the eye.
- In Chapter 6 we will present a FFOCT configuration with an expanded field of view (up to 3.1 mm × 3.1 mm), potentially useful for measuring the thicknesses of corneal layers in OCT-like fashion.
- Chapter 7 will give a glance at the work on the first *in vivo* human retinal imaging with a conventional FFOCT, in which I had a pleasure to participate together with my colleague Peng Xiao.
- Chapter 8 will show, how natural axial movements of the eye can be used for phase-modulation and FFOCT image retrieval, opening a path for a simple FFOCT without camera-piezo synchronization.

- Annex provides a rigorous ocular safety analysis of several FFOCT imaging configurations.

The conclusion of the manuscript sums up all the achievements of the thesis work and tries to glimpse into the future perspectives of FFOCT.

Part I

Ocular surface: anatomy, functions,
diseases, clinical and emerging
diagnostic techniques

 Ocular surface structures, diseases and diagnostics in clinics

Table of contents

1.1	Introduction to ocular surface structures	9
1.1.1	Cornea	10
	Epithelium	10
	Tear film	12
	Epithelial basement membrane and sub-basal nerve plexus	12
	Bowman's layer	14
	Stroma	14
	Descemet's membrane	16
	Endothelium	16
1.1.2	Morphological differences between the central and peripheral zones of the cornea	17
1.1.3	Limbus	18
1.1.4	Sclera	19
1.1.5	Bulbar conjunctiva	19
1.2	Ocular surface disorders and diagnostics in clinics	19
1.2.1	Global scope of ocular surface disorders	19
1.2.2	Dry eye disease	19
	Schirmer test	20
	Ocular surface staining with fluorescein	20
	Measurement of tear break-up time (TBUT) with fluorescein	21
	Tearscope	21
1.2.3	Fuch's endothelial dystrophy (FECD)	21
1.2.4	Microbial Keratitis	21

1.2.5	Keratoconus	23
1.2.6	Diabetes	23
1.2.7	Limbal stem cell deficiency	24
1.2.8	Conjunctivitis	24

1.1 Introduction to ocular surface structures

The ocular surface is the front part of the eye acting as a clear “window” into the world (figure 1.1). While there is no unique definition of the ocular surface, this term is frequently attributed to the corneal epithelium, bulbar conjunctiva, limbus and tear film. In this text we will take a broader definition, which encompasses the anterior eye with entire thicknesses of cornea, limbus and sclera, but excludes iris and lens. The ocular surface serves three primary goals: it 1) maintains the optical clarity, 2) serves as a refractive surface for the sharp focusing of light on the retina, and 3) provides protection for the structures of the eye against trauma, microbes and toxins. In order to accomplish these and many other unique functions, each part of the ocular surface has a complex and highly-specialized micromorphology, which includes fibers, cells, aqueous phase with nutrients, nerves and blood vessels. A small malfunction in any part of this sophisticated system may lead to a broad range of disorders. Therefore, a detailed description of the structure and functions of these tissues is essential for understanding the disease nature and for coming up with new medical treatments.



Figure 1.1 – Ocular surface visible through slit-lamp macro view [5]. Cornea, covered by the tear film, is visible as a transparent part of the eye, while the sclera is seen as white due to scattering. In between, the corneo-scleral limbus is located. Slit lamp illumination highlights the curvature of the cornea.

Below, I will describe the anatomy and functions of ocular surface structures at the micrometer scale. This background will prove to be useful in the following chapters, when we analyze the images obtained in the course of this thesis.

1.1.1 Cornea

Cornea is the most outer front part of the eye (figure 1.2). It is a thin (only about 0.5 mm thick) tissue, which is nevertheless rigid thanks to the broad presence of collagen. This rigidity is important, because it allows the cornea to keep its steep curvature in the presence of external and internal mechanical stresses (such as pressure from the eyelids), leading to a consistent precise focusing of light on the retina. Corneal shape together with its high refractive index of 1.376 make cornea the strongest refractive surface of the eye (2/3 of the total refractive ocular power). It is transparent to visible and near-infrared light (> 90% transmission in 550 nm - 1200 nm wavelengths band [6]). Several more of the following corneal properties and terminologies will be important in the next chapters. Laterally cornea measures 10 - 12 mm and is divided (by agreement) into several zones: central (4 mm), paracentral (4 - 8 mm), peripheral (8 - 11 mm) and limbal (11 - 12 mm). The central zone is the thinnest (550 μm) and has the steepest anterior and posterior corneal curvatures (7.8 and 6.5 mm respectively). Towards the periphery the thickness gradually increases to 660 μm , while the curvature flattens to about 11 mm. 90% of the corneal thickness is filled with collagen, making up the stromal layer. This layer is squeezed by the acellular membrane-like layers: Basement's and Bowman's from the top and Descemet's from the bottom. Epithelium, the outermost corneal layer (except the tear film, which is considered to be outside of the cornea), lies upon the Basement membrane and Bowman's layer. Single cell layered endothelium, adjacent to Descemet's membrane, terminates the cornea from the bottom.

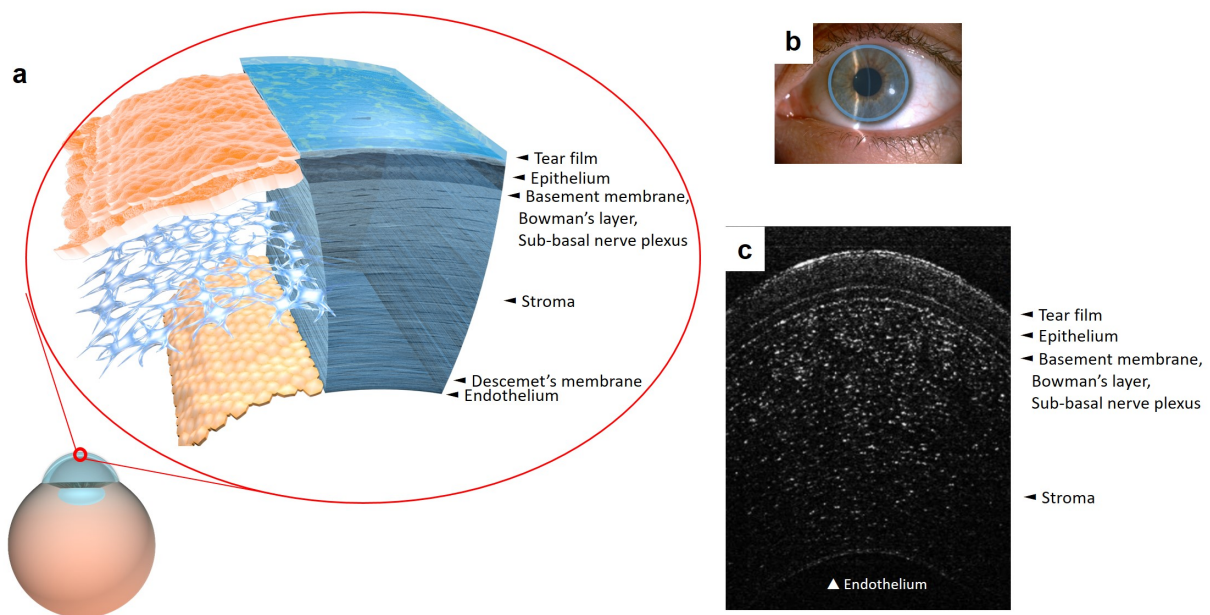


Figure 1.2 – Cornea. (a) Schematic drawing of the eye cross-section with cornea on top. The insert is a 3D drawing of the cornea with *en face* view on cellular mosaics of selected layers. (b) Slit lamp macro image of the human eye. Filled blue circle shows the cornea. (c) Normal human cornea *in vivo*, imaged with a high axial resolution optical coherence tomography (OCT) [7].

Epithelium

Epithelium is the first barrier corneal layer, protecting against mechanical stresses, toxins and microbes. Through the entire epithelial thickness of 50 μm (4 - 7 cell layers), cells keep tight

junctions with their neighbours, thus eliminating possibility of penetration of contaminants into the deeper corneal layers (figure 1.3). The outermost superficial epithelial layer is built of flat polygonal cells about $50\ \mu\text{m}$ in diameter and $5\ \mu\text{m}$ in thickness. When examined with electron or confocal microscopy, this layer shows a highly regular cell mosaic, forming a smooth refractive layer, important for vision. Middle epithelial cells are called intermediate (or wing) cells and have $20\ \mu\text{m}$ diameter and $10\ \mu\text{m}$ thickness. They are followed by the $20\ \mu\text{m}$ thick basal cells, $8 - 10\ \mu\text{m}$ in diameter. Elongated shape helps basal cells to move from the limbus to the central cornea as part of the epithelial renewing process. The whole epithelium is renewed within a week. Another interesting property of epithelial cells is that they need to survive in unique conditions without blood supply (cornea is avascular to keep transparency by avoiding strong light absorption by blood). In order to accomplish that, epithelial cells increase the uptake of oxygen and nutrients from the tear film by increasing the contact surface area using the special structures, protruding from the cell membranes, called microplacae and microvilli. Due to their sub-micrometer size, microplacae and microvilli can be seen only with *ex vivo* electron microscopy. Interestingly, while solving one problem these structures create another one: they form a rough sandpaper-like surface, sufficient to significantly reduce the smoothness, required for proper refraction. To compensate for that, epithelial cells express glycoprotein molecules, which create a hydrophobic surface, which helps in uniform spreading of the tear film to eventually form a smooth refractive surface.

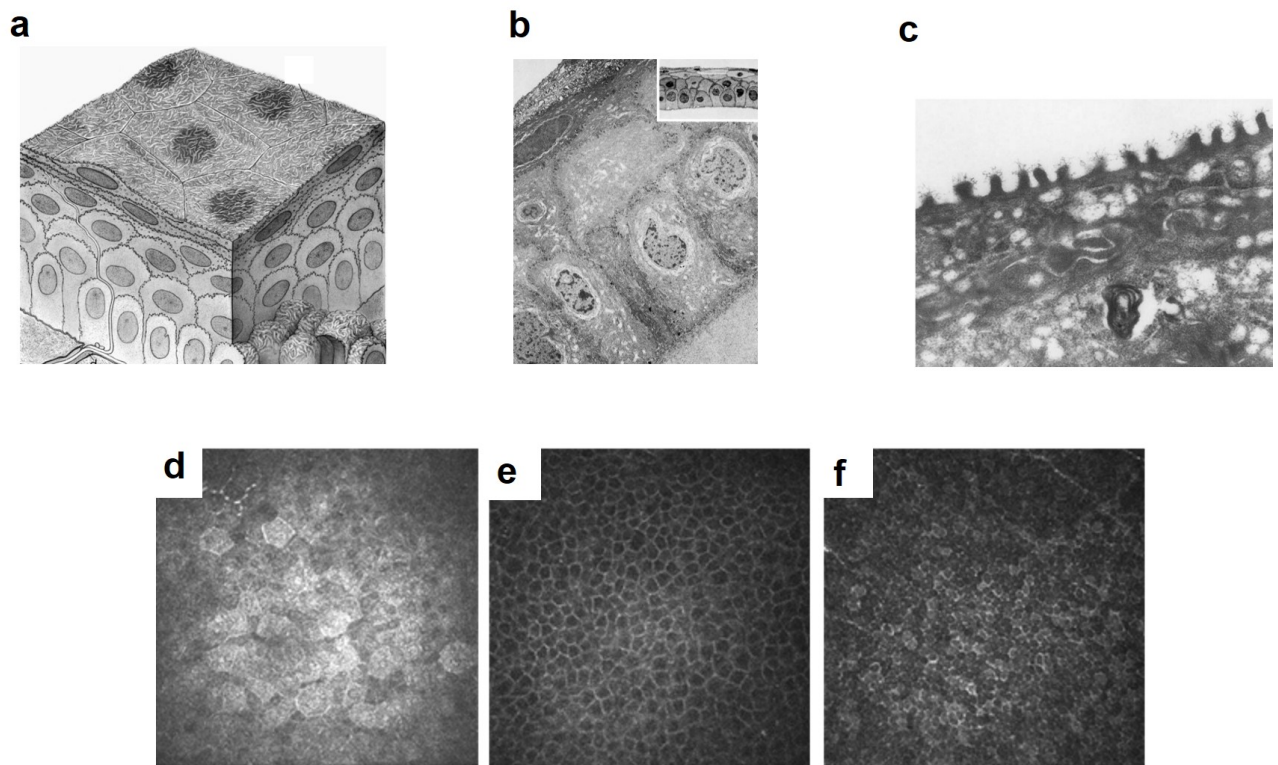


Figure 1.3 – Corneal epithelium. (a) 3D Drawing of the corneal epithelium from [8]. (b) Cross-sectional macro view on epithelium obtained with electron microscopy from [9]. Magnifications: main image - $\times 4,800$, inset - $\times 450$. (c) Close electron microscopy view on surface epithelium from [10]. Microvilli of epithelium extending into the tear film are clearly visible. Magnification $\times 51587$. (d-f) *En face* images of *in vivo* human epithelium (from left to right: superficial, wing and basal cells) seen with the *in vivo* confocal microscopy (IVCM) [11]. Field of view (FOV) = $400\ \mu\text{m}$.

Tear film

The tear film is the first layer of the eye, with which light comes into contact (figure 1.4). Therefore, among all the ocular layers on the way of light air-tear film interface exhibits the largest change in the refractive indexes of the media, which makes this layer the most important for correct focusing of light on the retina. According to the classic model, tear film consists of the three distinct layers, which work together to form a smooth surface. At the bottom the mucus gel overlies the epithelium. This thin ($1\ \mu\text{m}$ thick), but viscous part helps to protect the fragile epithelial surface from the forces of the eyelid movements during blinking. Following the blink, tear film gets evenly distributed over the ocular surface, thanks to the hydrophobic property of epithelium. At the same time, this distribution gets rapidly anchored by the microvilli of epithelium, ensuring the fast stabilization of tear film and clear vision. Most of the tear film volume is comprised by the aqueous layer, $7 - 8\ \mu\text{m}$ thick. On top of the aqueous lies the lipid layer. This $0.1 - 0.2\ \mu\text{m}$ thick layer is composed of oily secretions, which protect the tear film from evaporation. Reflex tearing helps to flush toxins from the ocular surface. Tear film environment also contains immunoglobulin A, lactoferrin, lysozyme components for additional antimicrobial protection. Stabilized tear film surface is very uniform, nevertheless its volume frequently contains the non-uniformities of floating particulate matter about $1 - 50\ \mu\text{m}$ in size. Previous studies attributed them to dust particles, cellular debris (as cornea is updated every week, the old cells should be removed) [12–14] or accumulations of newly secreted lipid from the Meibomian glands [15].

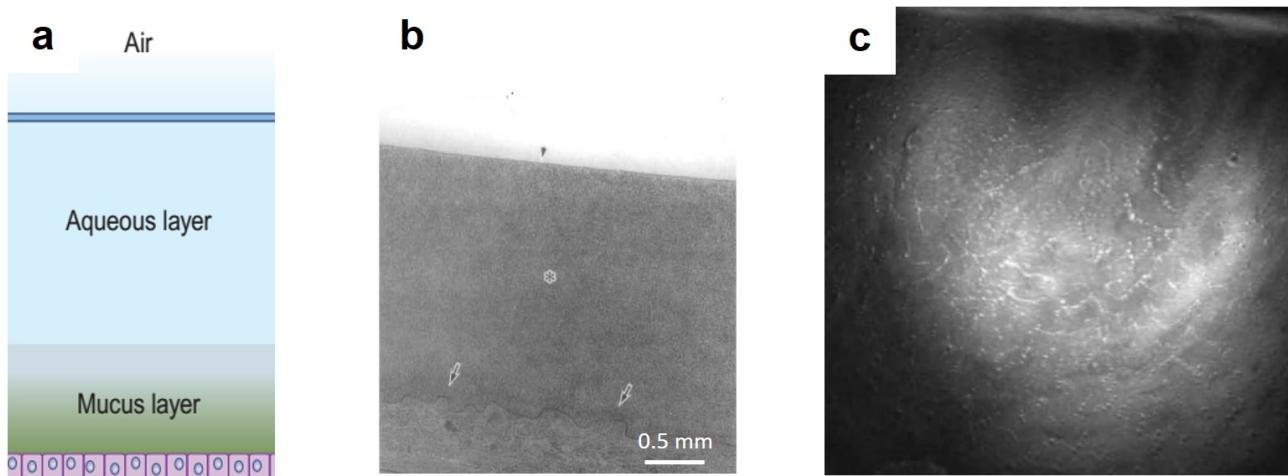


Figure 1.4 – Tear film. (a) Drawing of the tear film cross-sectional structure from [16]. (b) Electron microscopy of the cryofixed rat tear film [17]. Tear film appears as a homogeneous network-like medium. Upper arrow points at the thin dense lipid layer, covering the surface. Lower arrows point at the dense mucous layer, adjacent to the epithelial surface. (c) *In vivo* human tear film imaged *en face* with non-contact prototype of a confocal microscope [18].

Epithelial basement membrane and sub-basal nerve plexus

Right below the epithelium lies the basement membrane (BM) (about $0.5\ \mu\text{m}$ thick) (figure 1.5). It is made of collagen and assists in renewing of the epithelial cells. At approximately the same

depth we can find the sub-basal nerve plexus (SNP), formed by around $1.5 \mu\text{m}$ thick branching nerves [19]. When viewed *en face* in its entirety, SNP forms a spiral or whorl-like pattern. The centre of the spiral, called vortex, is located in human corneas approximately 2 - 3 mm inferior to the corneal apex. As a consequence of this arrangement, the sub-basal nerves are oriented vertically in the superior and inferior parts of the human cornea, and horizontally in left and right lateral parts. This region has the highest density of innervation in the human body about $15 - 27 \text{ mm/mm}^2$ (measured in total length of nerves in the area, divided by the area), 300 - 400 times that of skin epidermis [20]. This explains the strong sensitivity of the cornea to painful stimuli. In fact, only part of the corneal innervation is concentrated here. Thin nerve endings protruding to epithelium also play important roles in the regulation of epithelium renewal and stimulation of tear film production, for example in case of toxins detection. Thicker nerves ($4 - 8 \mu\text{m}$), regulating metabolic interactions, are also found in the anterior and middle stroma.

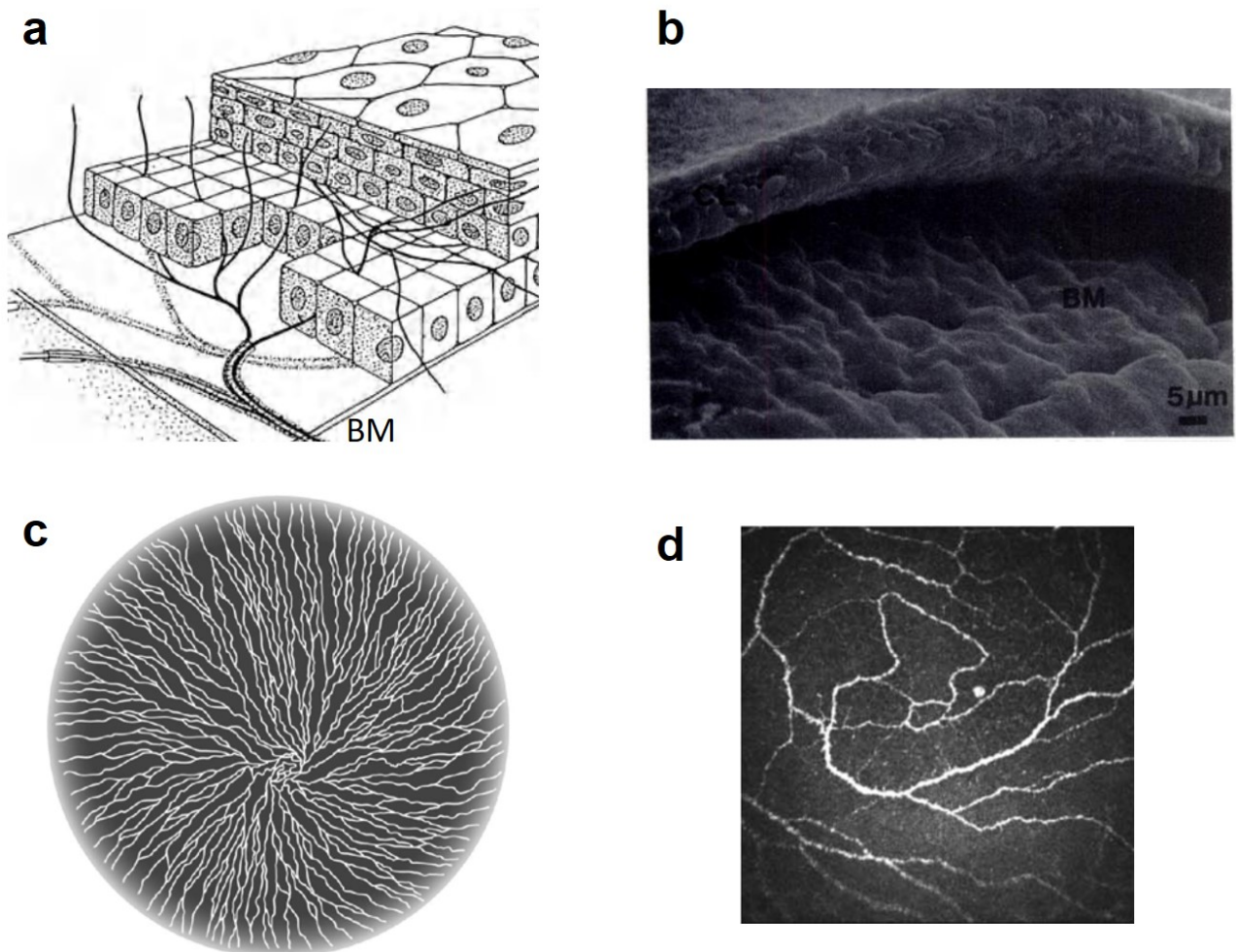


Figure 1.5 – Basement membrane (BM) and sub-basal nerve plexus (SNP). (a) Schematic drawing of the BM and SNP underneath epithelium [18]. (b) Electron microscopy of the BM, exfoliated from the overlying epithelium [21]. (c) Schematic *en face* architecture of the entire human SNP from [22]. (d) *En face* confocal microscopy image ($400 \mu\text{m} \times 400 \mu\text{m}$) from *in vivo* human SNP [22].

Bowman's layer

The Bowman's layer (BL) lies between the epithelial basement membrane and the anterior stroma (figure 1.6). It is an acellular layer, composed of strong, randomly oriented collagen fibers. BL measures 8 - 12 μm in thickness.

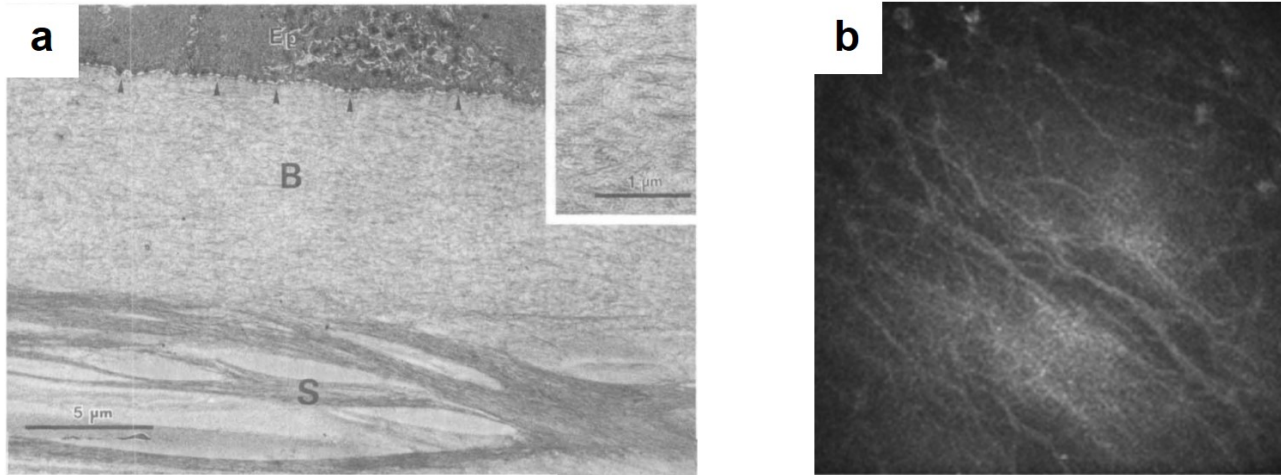


Figure 1.6 – Bowman's layer (BL). (a) Cross-sectional electron microscopy image with low-magnification. Bowman's layer (B) lies between the epithelium (EP), basement membrane (black arrows) and stroma (S) [23]. In the insert, the dense collagen fiber bundles of Bowman's layer are visible. (b) Confocal microscopy image of BL from the *in vivo* human cornea [11]. Dark lines are called the K-structures and are visible, because of the applanating pressure applied to the eye during the contact examination. FOV = 400 μm .

Stroma

Stroma takes the largest part of the corneal thickness (90%), thus it is particularly important for keeping the cornea transparent. Transparency is achieved mainly thanks to the thin sheets (or lamellae) of collagen fibrils (figure 1.7). Each lamellae of fibrils lies on top of each other filling the entire stroma. A lamellae is about 1.5–2.5 μm in thickness, which means that there are about 200–250 lamellae in the normal 0.55 mm thick human cornea. Within each lamellae, the collagen fibrils run in parallel to each other and to the corneal surface. The fibrils are mostly limited to a single lamellae and only occasionally the bundles of fibrils extend from one lamella to another. Orientation of fibrils varies between the neighbouring lamellae. In the anterior stroma the orientation is close to oblique, while in the posterior stroma it is more perpendicular from one layer to the next. The ends of the fibrils are not abundant and so fibrils extend essentially through the entire width of the cornea.

Interestingly, if one considers the simple model, where the light paraxially propagates through the stroma, the cornea should be opaque, due to the large difference between the refractive indexes of the fibrils and ground substance (1.47 and 1.35, respectively) [24]. However, adding into consideration the constructive wave interference of light scattered by the fibrils resolves the problem and leads to the stromal transparency. Not only the arrangement of fibrils plays an important role in the transparency, but also their diameter, kept around 30 nm. This becomes apparent, if we look at sclera. Sclera, like the cornea, is made up of fibrils. However, it is opaque, because the fibrils' diameters can have a much larger range from 30 to 300 nm, which leads to

a stronger light-scattering and visible whiteness of the tissue. As a transparent media, lamellae and collagen of the cornea are not visible with optical imaging methods. The arrangement of parallel rods in a stromal matrix can remind the composition of the civil construction materials, such as fiberglass and metal reinforced concrete. This type of structure gives the cornea its remarkable rigidity and tensile strength.

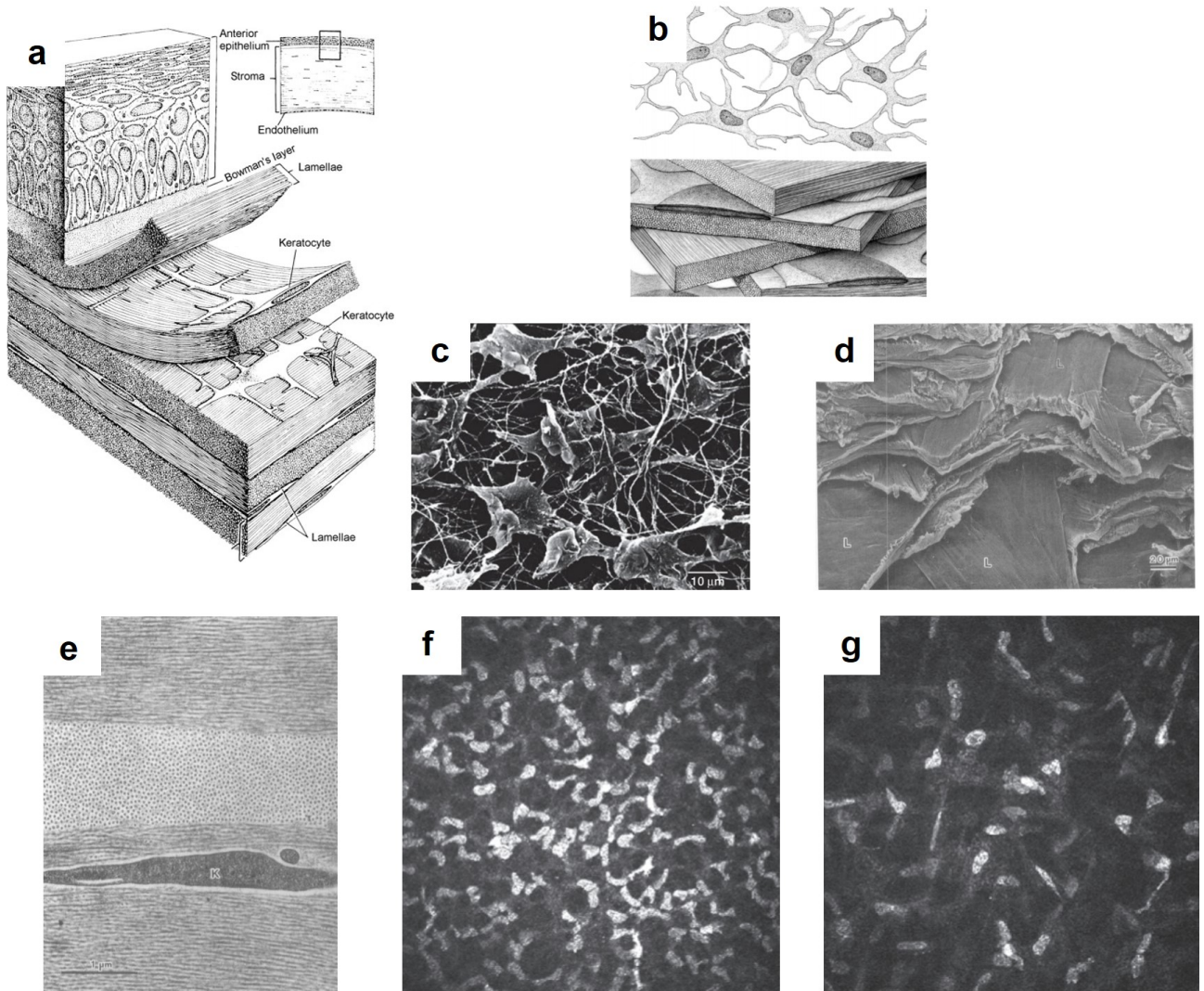


Figure 1.7 – Stroma. (a) Schematic 3D drawing of the stromal lamellae sheets underneath epithelium and Bowman's layer from [8]. (b) Schematic drawing of the stromal compounds. Higher section: keratocyte cells with nuclei. Lower section: lamellae sheets composed of collagen fibrils. Adapted from [8]. (c) Electron microscopy image of keratocyte cells with the surrounding collagen removed. (d) Electron microscopy view on the lamellae sheets (L) [23]. (e) Cross-sectional electron microscopy image of stroma. One can notice a different orientation of collagen fibrils in different adjacent lamellae. Dark central cell is a keratocyte (K) [23], (f,g) *En face* confocal microscopy image of the anterior and posterior stroma, respectively. Bright keratocyte nuclei are more dense in the anterior than posterior stroma. FOV = 400 μm.

During the development or as a consequence of trauma, collagen of the stroma is synthesized by the specialized fibroblast cells, called keratocytes. Stroma contains approximately 2.4 million keratocytes with the higher density anteriorly (1050 cells/mm^2) than posteriorly (770 cells/mm^2). 15 μm diameter keratocyte nuclei are strongly scattering, while the rest of the cell

is more transparent. This transparency is due to the flat cell profile and their even distribution through the cornea. Moreover, as was recently found [25,26], the keratocytes contain special molecules, which can adapt the refractive index of the cell cytoplasm to better match the surrounding and, thus, increase the transparency. Keratocytes are metabolically active and can repair stromal wounds by producing the missing collagen. They can interact with each other through junctions between the cells.

Descemet's membrane

Descemet's membrane (DM) plays a role of basement membrane for the corneal endothelium. It has a thickness of about 10 - 12 μm and contains collagen fibrils arranged in a hexagonal pattern (figure 1.8).

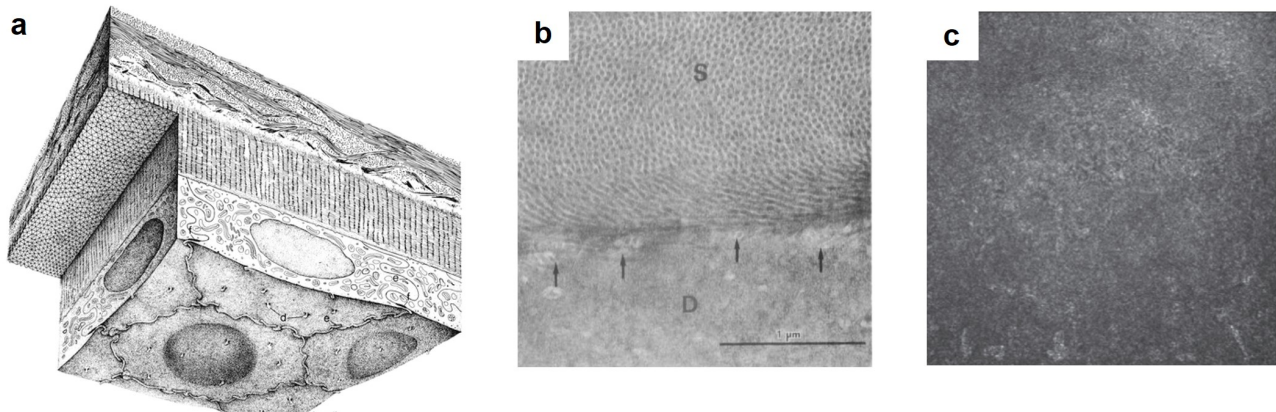


Figure 1.8 – Descemet's membrane (DM). (a) Schematic drawing of the posterior cornea from [8]. Descemet's membrane is the layer in between the stroma and endothelial cell mosaic. (b) Cross-sectional electron microscopy image of descemet's membrane (D) underneath the posterior stromal fibrils (S), adapted from [27]. (c) *En face* confocal microscopy image of DM from *in vivo* human cornea [10]. FOV = 400 μm .

Endothelium

The last corneal layer, consisting of a single layer of flattened hexagonal cells, is called endothelium (figure 1.9). These cells are 5 μm thick and 20 μm wide. The peripheral endothelium has a slightly higher cell density comparing to the central. The cells are not replicating and their concentration gradually decreases with age starting from about 4000 cells/mm^2 at birth. Endothelium functions to pump the fluid out of the stroma and keep it relatively dehydrated (not swollen) to maximize its transparency. In order to respond to this demand, endothelial cells are highly-active metabolically with a large nuclei, numerous mitochondria and Golgi apparatus. To stop bulk aqueous humour from entering the cornea, endothelial cells are tight next to each other in a mosaic pattern. Interestingly, in the absence of vasculature the aqueous humour is the main source of nutrients for the cornea. Therefore, to a limited extent the endothelium needs to let some part of aqueous humour in the cornea. This is achieved by having the semi-permeable gaps between the endothelial cells, allowing nutrients such as glucose, vitamins and amino acids to diffuse into the stroma, while still blocking the large aqueous humour flow.

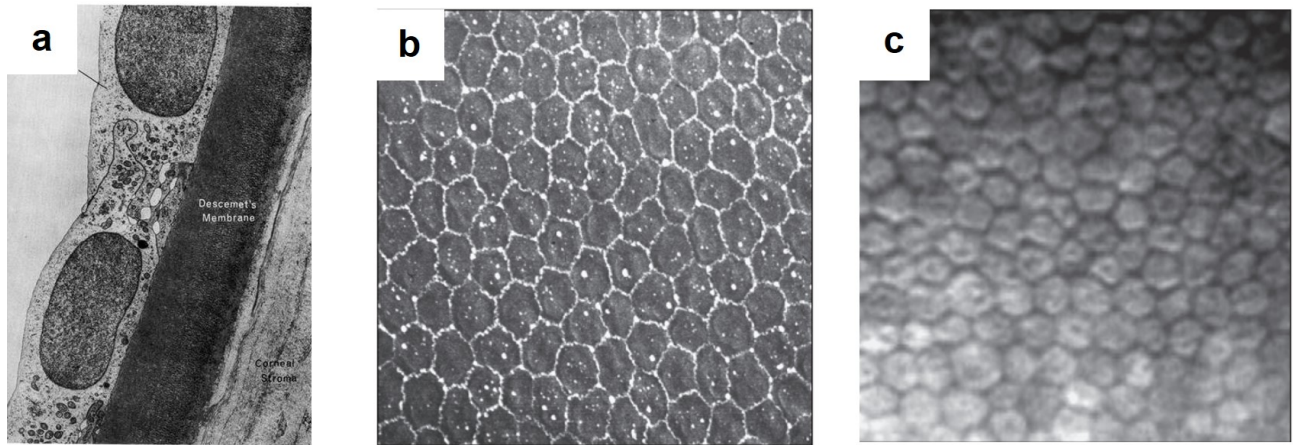


Figure 1.9 – Endothelium. (a) Cross-sectional electron microscopy image of the posterior cornea with endothelium [27]. (b) *En face* view on hexagonal endothelial cell mosaic using scanning electron microscopy from [10]. (c) *En face* specular microscopy image of endothelium from *in vivo* human cornea [10]. FOV about 350 μm .

1.1.2 Morphological differences between the central and peripheral zones of the cornea

Our most important sharp central vision is given by the light, passing through the central cornea. Nevertheless, a significant proportion of light, that we sense, also reaches the retina after passing through the paracentral, peripheral and limbal corneal zones.

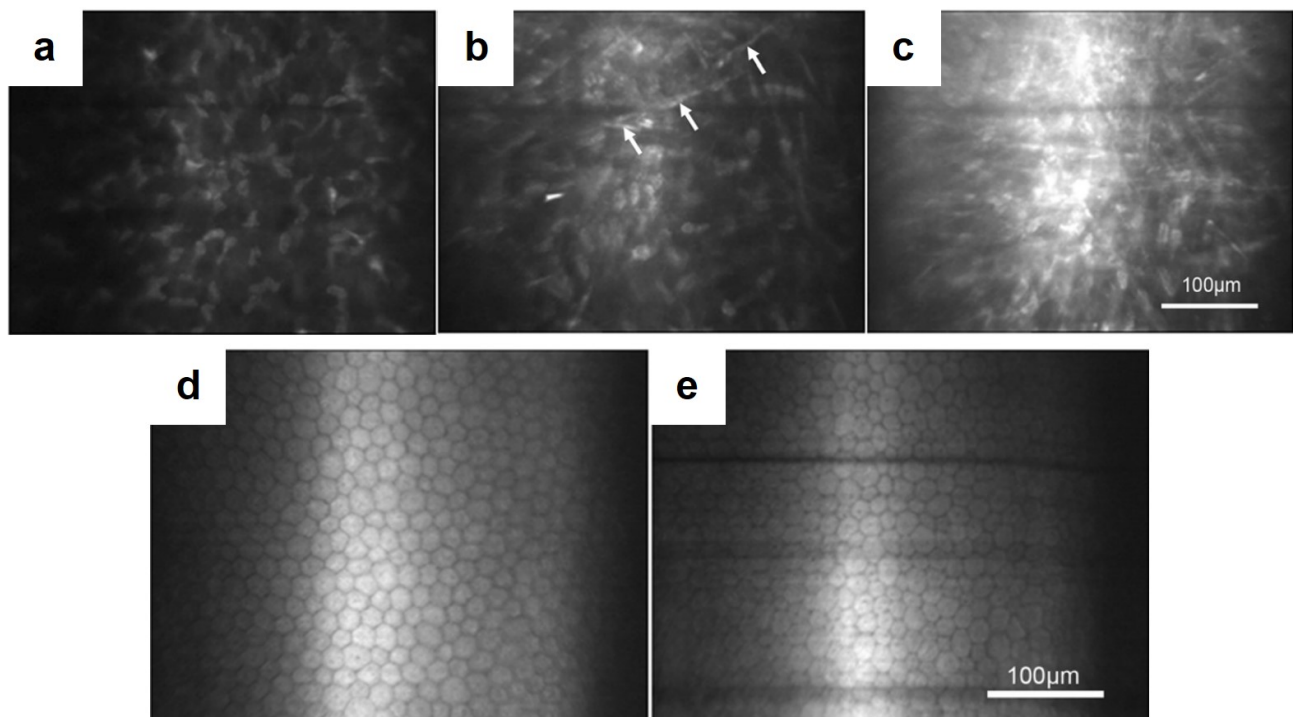


Figure 1.10 – Comparison of the central and peripheral cornea with *in vivo* confocal microscopy [28]. (a-c) Left to right: images from the central to peripheral stroma. On the first image (central cornea) keratocyte cells are easily distinguished, while in the periphery it gets more difficult to resolve them in the presence of the bright scattering background. White arrows show visible elongated fibers. (d,e) Left and right: central and peripheral endothelium, respectively.

As well as the central cornea, these zones can be affected by infectious, immunological diseases, etc. It is important to know the normal structure of the corneal periphery (together with the differences comparing to the central zone), because it allows to distinguish the abnormal conditions, requiring treatment. It is known that the central cornea is optically superior to the peripheral region [28]. Epithelial cell densities in the corneal periphery do not show significant differences comparing to the center. However, this is not true for the stromal keratocytes, which have a significantly denser population in the central cornea. Lamellae of the peripheral cornea are more disorganized (in terms of arrangement or/and size of the fibrils), which leads to an increased scattering from the background and a visible whiteness in the image (figure 1.10). Regarding endothelium, although cells are hexagonal in both regions, the heteromorphism (variability in shape) is greater in the periphery. Moreover, peripheral cell counts give higher numbers [29].

1.1.3 Limbus

Limbus is a 1 - 1.5 mm transitional zone between the corneal periphery and sclera (figure 1.11). This is a specific and unique area, hosting a population of stem cells within the radial stromal ridges, called palisades of Vogt (POV). POV measure about $30\ \mu\text{m}$ in width. Cells generated here on a regular basis replace epithelial cells of the whole cornea. Limbal zone is highly innervated, vascularised, and protected from the potential damage of ultraviolet light by the presence of melanin pigmentation.

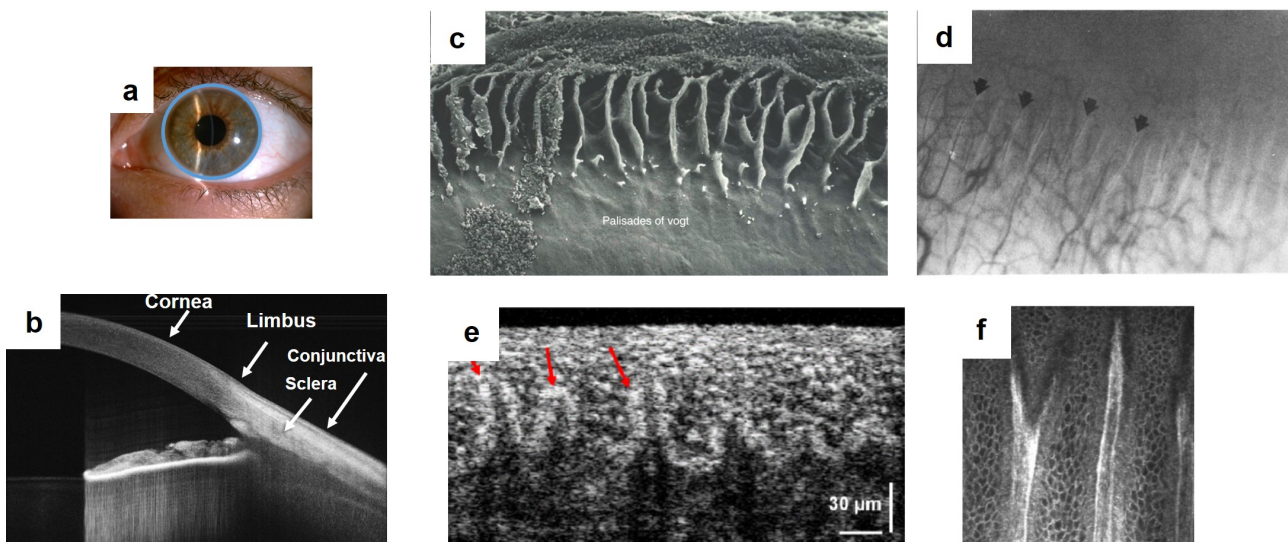


Figure 1.11 – Limbus. (a) Slit lamp macro image of the human eye. Blue circle depicts the location of the limbus. (b) Cross-sectional conventional OCT image of the anterior human eye, showing location of the limbus. Adapted from [30]. (c) Electron microscopy image of the limbal palisades of Vogt (POV), adapted from [31]. Image magnification $\times 77$. Epithelium was partly removed. POV appear to taper down toward the cornea. (d) Limbus with POV (black arrows) and vasculature viewed with a slit lamp, from [32]. (e) Cross-sectional image of the *in vivo* human limbus, obtained using Ultra-high resolution (UHR) OCT with red arrows emphasizing the POV [33]. (f) *En face in vivo* confocal microscopy image of POV from [34]. FOV = $400\ \mu\text{m}$.

1.1.4 Sclera

Sclera is the very peripheral part of the anterior eye, which, like the cornea, consists almost entirely of collagen fibrils. However, contrary to the cornea, these fibrils are more varying in size, shorter and more randomly organized, which explains the visible white opacification of the sclera. Bulk of the sclera is mostly avascular and acellular. Sclera serves as a strong coating for the intraocular structures, protecting against mechanical stresses induced by the eye movements (muscles responsible for eye motion are connected to the sclera tissue) and injuries. It also helps to maintain intraocular pressure.

1.1.5 Bulbar conjunctiva

Bulbar conjunctiva is a thin semi-transparent membrane that covers the surface of the eye from the sclera to the edge of the cornea. At the surface it has 6 layers of epithelium, and beneath, the conjunctival stroma with the collagen fibrils, fibroblast cells and a vascular system. The blood stream supplying the limbus with nutrients comes principally from the anterior ciliary arteries [16]. Conjunctiva serves as a barrier at the surface of the eyeball, which protects against the invasion of chemical, physical and biological agents. Detection of the infection results in the triggering of an inflammatory reaction - blood vessels of the conjunctiva become enlarged and consequently the blood flow increases (hyperaemia).

1.2 Ocular surface disorders and diagnostics in clinics

1.2.1 Global scope of ocular surface disorders

As we have seen from the previous section, the ocular surface is a highly-sophisticated system. A small malfunction in any part of it may lead to a broad range of potentially blinding corneal disorders: degenerative (keratoconus), inherited or infectious (bacterial, viral and fungal keratitis). These and many other conditions frequently lead to a loss of vision (4th leading cause of blindness worldwide [35]), making 1.5 to 2.0 million people unilaterally blind every year. Taking into account that the largest corneal blindness burden falls on the developing countries (more than 90% of the affected population) [36], cost-effective disease prevention through early diagnosis and treatment, and through public health programs is preferable over costly surgical interventions [37]. In this section we will have a look at a few selected examples of the challenging and spread in population diseases. We will see that, while some ocular conditions can be successfully treated at any stage of the disease with a general antimicrobial medication, others require an early, precise and fast diagnosis. On the way, we will explore techniques and devices, used in modern clinical diagnostics.

1.2.2 Dry eye disease

Dry eye is a highly prevalent condition, which affects up to 11% of people 30–60 years of age and 15% of those over 65 years of age. The disease is more common in women than men (2:1) and the prevalence further increases with age. Basically, dry eye leads to a low quality of tear film, which fails to constantly cover the epithelium, leading to a loss of the epithelial cells. This can be due to the fast tear film evaporation, caused by its low osmolarity or, generally, because

of the small tear film production from the meibomian and lacrimal glands. Patients having a dry eye feel dryness, foreign body sensation, see with a decreased contrast, have fluctuation in a quality of vision and photophobia. The most common first line treatment is the daily use of the artificial tears. Medical doctors rely on several techniques to diagnose dry eye.

Schirmer test

In this test, a strip of filter paper is placed on the lower eyelid margin without anaesthesia. After 5 minutes, the strip is removed, and the amount of wetting is measured in millimeters (figure 1.12). Although this test is used frequently, it has been found to lack accuracy and reproducibility: the same person's test results taken at the same time each day for several days can fluctuate widely, and the mean Schirmer test results for normal individuals have been reported to range from 8.1 mm to 33.1 mm. As such, many ophthalmologists avoid using this test.

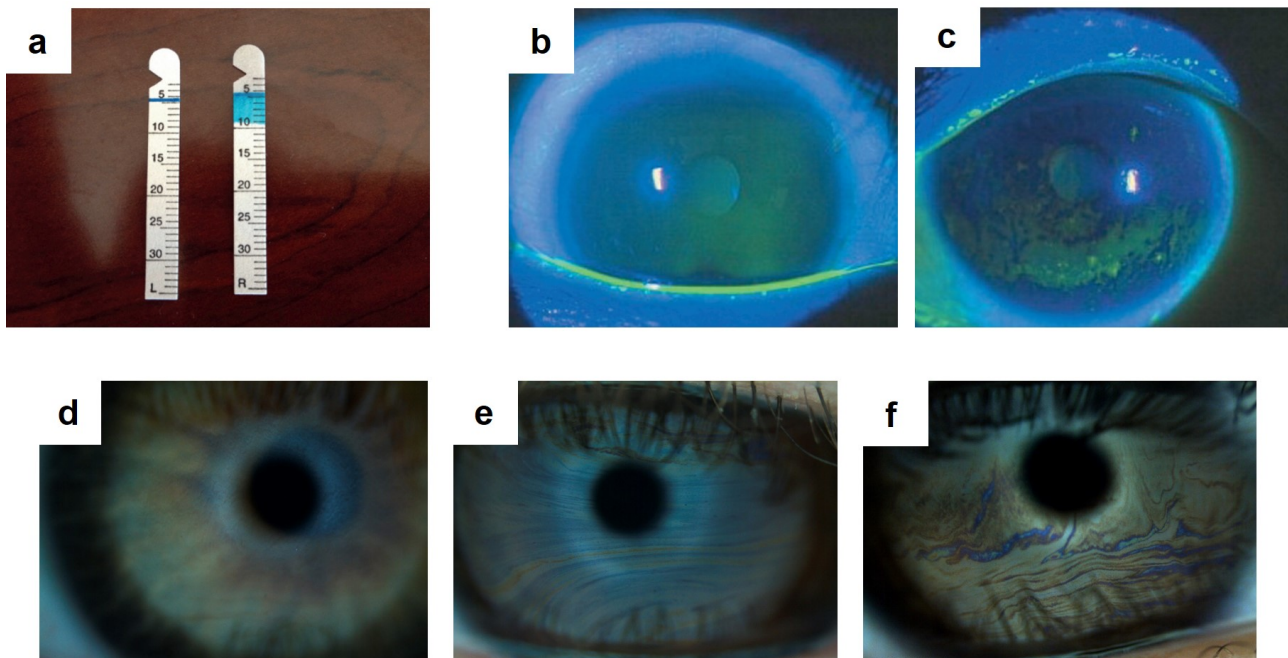


Figure 1.12 – Methods in dry eye diagnosis. (a) Schirmer test strips with millimeter markings. Blue is used to facilitate measurement of tear wetting. Adapted from [16]. (b,c) Slit lamp macro photographs with fluorescein staining of normal subject (left) and dry eye patient with *Sjögren* syndrome (right), from [16]. (d-f) Tear film interference patterns, obtained with a tearscope (adapted from [38]). According to the accepted classification table [39], lipid thickness is normal in a closed meshwork pattern in (a), and is slightly increased in the wave patterns in (e) and (f). It should be noted that the tear film thickness can vary in the normal human eyes, depending on the time after the last blink, preceded duration of the eye closure, etc. Therefore, a precise methodology is required for a successful use of the instrument.

Ocular surface staining with fluorescein

Another way to estimate the tear film quality is to put a fluorescent dye on top of the tear film. Fluorescein cannot penetrate into the uniform corneal epithelium, instead the corneal surface is stained, whenever there is a disruption in the cell-to-cell junctions. Therefore, fluorescein

highlights any part of the ocular surface, where the epithelium was damaged. Visible contrast spots in the inferior human eye can point to a potential dry eye disease (figure 1.12).

Measurement of tear break-up time (TBUT) with fluorescein

With fluorescein one can also evaluate the tear film stability by measuring the time interval between a complete blink and the first appearance of a dry spot. Like the Schirmer test, the TBUT test has been criticized as being unreliable and not reproducible. Many factors may lead to its non-reproducibility, including the volume of the fluorescein administered. Despite this unreliability, it is generally agreed that a TBUT of less than 10 seconds suggests tear film instability, and less than 5 seconds suggests definite dry eye (figure 1.12).

Tearscope

Recently introduced, Tearscope [39] allows to examine tear film by looking at the interference pattern on the surface of the eye, caused by the reflection from the thin lipid layer (figure 1.12). Following the Guillon classification [39], each pattern can be matched to the corresponding lipid thickness. Tearscope just recently entered into the clinical practice, therefore more studies are required to confirm correlation between the lipid layer measurements and the dry eye disease. Nevertheless, already now it is seen as a promising device with a potential for a reliable and quantitative diagnosis.

1.2.3 Fuch's endothelial dystrophy (FECD)

Fuch's is by far the most common corneal dystrophy to require keratoplasty (corneal transplantation). In general, the lifetime risk of FECD is about 0.1 %, however it can rise to 50% with unfavourable genetics [19]. The disease is 2.5 times more likely to develop in women than men. Fuch's dystrophy manifests itself by the presence of the overgrown excrescences (called guttae) of descemet's membrane in the endothelium. That leads to a loss of endothelial cells, and subsequent stromal and epithelial corneal edema. As endothelium stops properly pumping the liquid from the cornea, the latter frequently swells overnight, which leads to blurring of vision during the morning hours. Other symptoms include pain, tearing, and oversensitivity to light. In order to diagnose FECD, instruments that can view endothelial cell mosaic are used, including slit lamp biomicroscope, confocal and specular microscopies (figure 1.13). FECD diagnosis is made following the findings of low counted endothelial cell density and irregular cell shapes (figure 1.13).

1.2.4 Microbial Keratitis

Microbial keratitis is a common, potentially sight-threatening ocular infection caused by the bacteria, viruses, fungi, or parasites. It is a clinical challenge to distinguish microbial keratitis from other noninfectious inflammatory conditions of the cornea resulting from trauma, hypersensitivity, etc. Time constraint makes this challenge even more difficult, as frequently only the correct diagnosis at the very earliest stage of the disease development can lead to a successful recovery without the negative consequences for vision. One example is *Acanthamoeba* keratitis, which affects 1.2 to 3 million people per year [42], mostly contact lens wearers. At the early

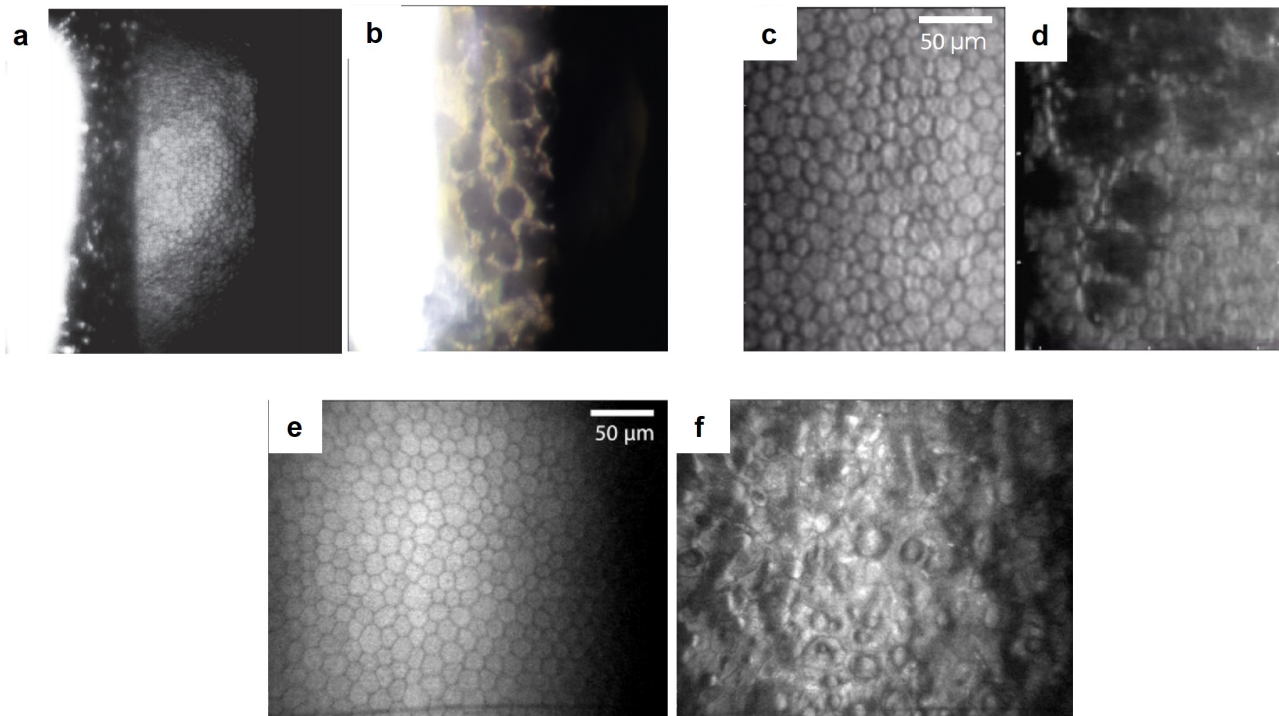


Figure 1.13 – Diagnostic methods of Fuch's endothelial dystrophy. (a,b) With careful aligning, slit lamp biomicroscope can be used to visualize cellular mosaic in normal subjects (a) and Fuch's dystrophy patients (b), adapted from [10]. Magnification: $\times 40$. (c,d) Specular microscopy images of normal (c) and diseased (d) endothelium from [40]. (e,f) *In vivo* confocal microscopy data from normal subject (e) and patient with the disease (f) [41].

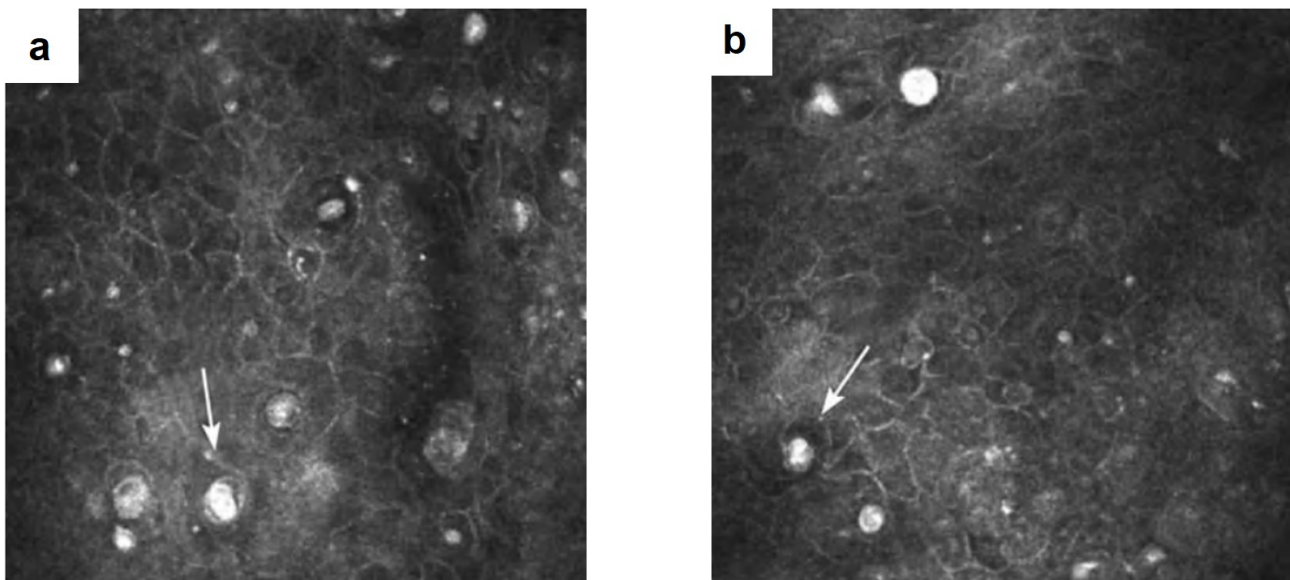


Figure 1.14 – Confocal microscopy in diagnosis of Acanthamoeba keratitis. Characteristic round 20 μm cysts, located in epithelium, are clearly visible.

stages neither the micro-organism, nor its cysts (measuring 11 - 15 μm) can be seen with a routinely used slit lamp biomicroscopy, due to its low resolution. In this case a conventional diagnosis procedure includes collection of scrappings from the ocular surface, followed by the several week growth of biological cultures and, eventually, histology. This is a long process, and even when it is done, the successful detection rate is low. In this situation one could think

about a possibility of prescribing the general broad-spectrum antibiotic for removing the microorganism of the unknown nature. Unfortunately, general anti-microbial agents were found to be unable to eliminate both the trophozoite and cystic forms [43], and targeted medical treatment is needed. A recently adopted in clinics *in vivo* confocal microscope (IVCM) became the first *in vivo* imaging tool to cope with this problem and reliably resolve the cysts [18, 44] (figure 1.14).

1.2.5 Keratoconus

Keratoconus is a disorder characterized by the progressive corneal steepening, resulting in vision blurring, doubling astigmatism and over-sensitivity to light. Other symptoms are central corneal thinning and deformation of the Bowman's layer. Both genetic and environmental processes are likely to be involved in pathogenesis. The signs of keratoconus can be revealed with a clinical Optical coherence tomography (OCT), which provides a high-resolution cross-sectional (side) view of the anterior eye. More precise corneal shape analysis is done with the corneal topographers (keratography) (figure 1.15).

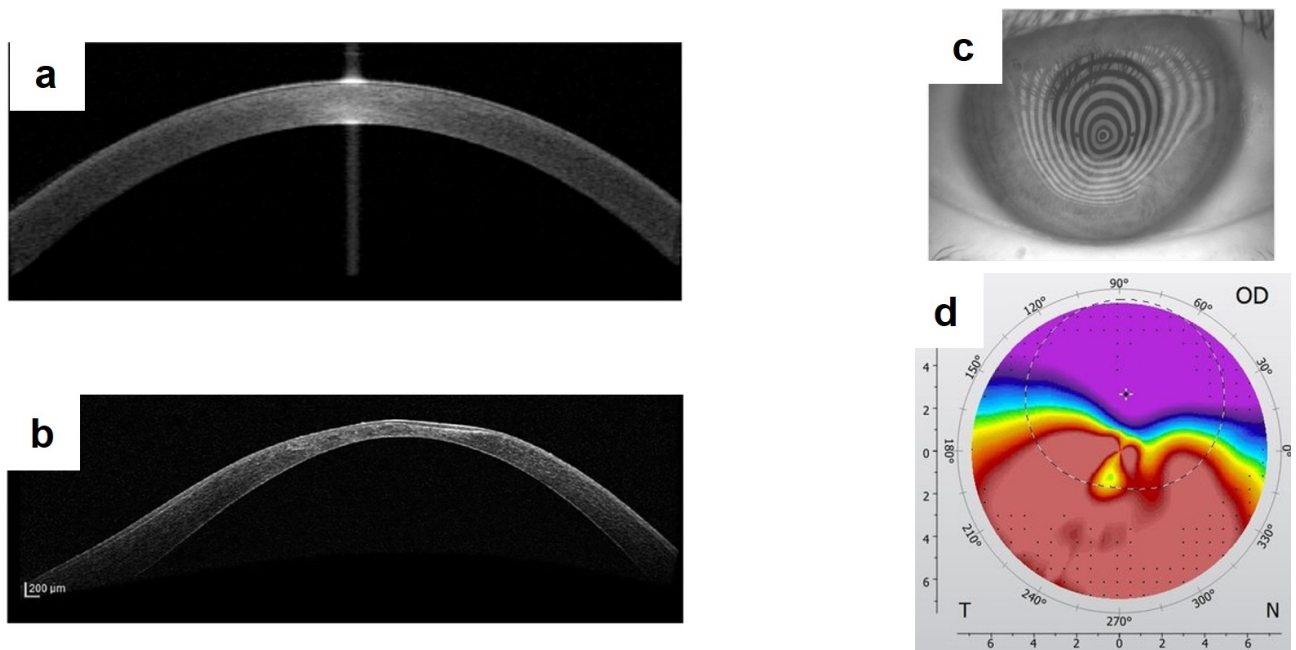


Figure 1.15 – Diagnosis of keratoconus. (a-b) Normal (up) and keratoconic (bottom) eye screened with OCT, adapted from [45, 46]. Central corneal thinning is apparent. (c-d) Keratograph measurements in keratoconic eye from [47].

1.2.6 Diabetes

Diabetes is a disease characterized by a high blood sugar levels over a prolonged period. As of 2017, an estimated 425 million people had diabetes worldwide [48]. In non-emergency cases symptoms include unintended weight loss, blurred vision, headache, fatigue, slow healing of cuts, and itchy skin. One more symptom, associated with diabetes, is a progressive loss of nerves through the entire body. Interestingly, as the cornea is transparent and the most innervated tissue in the human body, it is a perfect candidate for reliably monitoring progress in diabetic

disease. Recent confocal microscopy studies demonstrated the correlation between the severity of diabetes and the sub-basal nerve density in the cornea (figure 1.16) [49].

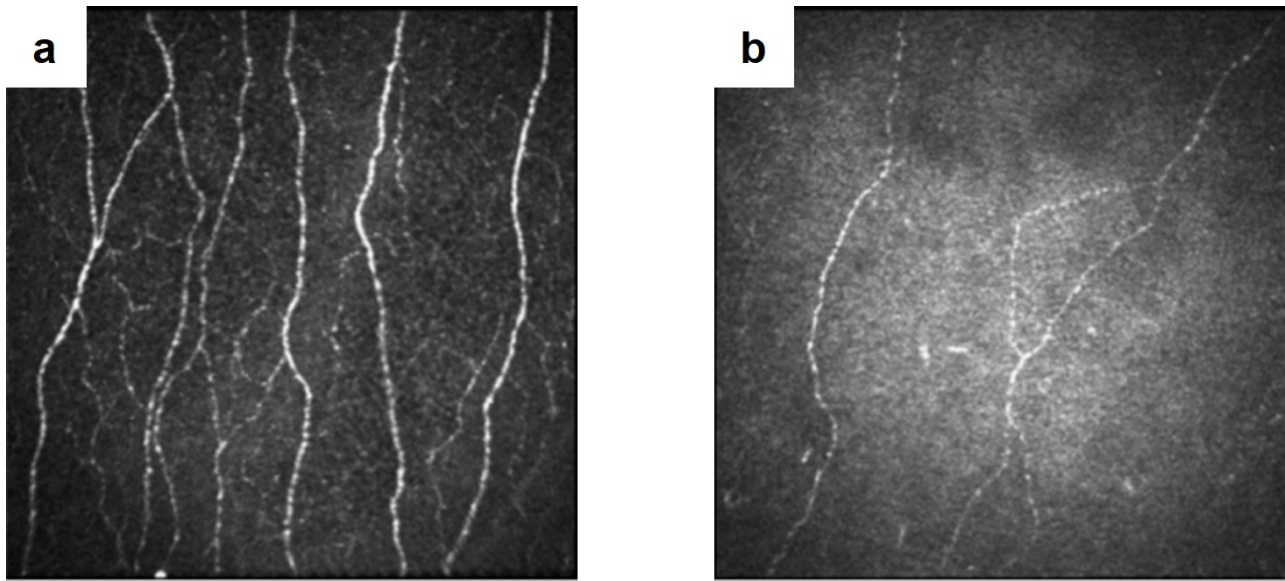


Figure 1.16 – Confocal microscopy recognizes difference in nerve densities in normal and diabetic subjects. (a) Healthy subject. (b) Patient with severe diabetic neuropathy. Adapted from [50].

1.2.7 Limbal stem cell deficiency

Limbal stem cell deficiency (LSCD) is referred to the condition of losing the stem cell population [16]. This can be caused by the damage to the limbus through thermal, chemical burns or even sun ultraviolet (UV) light, from which the limbus is typically protected with the eyelids. Cornea affected with LSCD becomes limited in its ability to repopulate the epithelium, which leads to the clinical symptoms of redness, irritation, photophobia, and decreased vision. On examination, slit lamp and confocal microscopy findings demonstrate the loss of Palisades of Vogt (figure 1.17) [51].

1.2.8 Conjunctivitis

Conjunctivitis is an inflammation of the outer white part of the eye. Beyond the visible redness, the frequent symptoms are the pain, itchiness, swelling. It is a well-spread condition, which contributes to an approximately 1% of the primary eye care visits. Typically, conjunctivitis is not severe and patients recover within one or two weeks. Nevertheless, depending on the conjunctivitis type (allergic, bacterial, viral etc.) the recovery may take longer and even may require months or years of prescribed medication use. Typical screening procedure involves slit lamp exam (figure 1.18), and typical medication are the topical antibiotic drops.

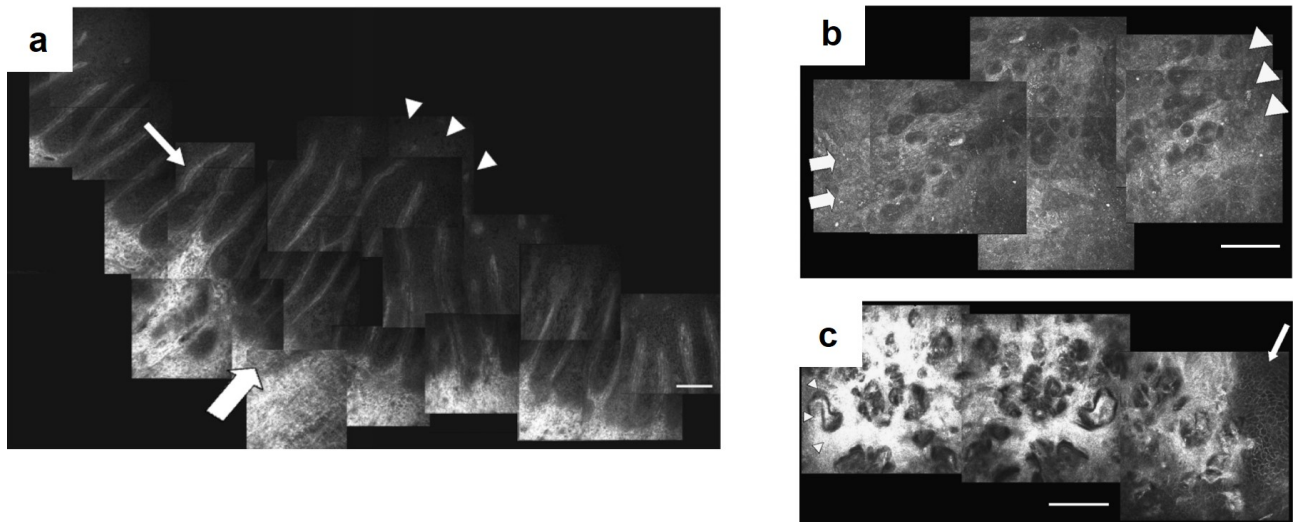


Figure 1.17 – Confocal microscopy based diagnosis of limbal stem cell deficiency (a) Healthy subject with the clear Palisades of Vogt in limbus. (b-c) Superficial (b) and deep epithelium (c) limbal section in patient with LSCD. Palisades of Vogt are lost, limbal epithelial architecture appears irregular. Corneal side is indicated by the arrows, while the conjunctival side by the arrowheads. Bar = 100 μm . Adapted from [51].

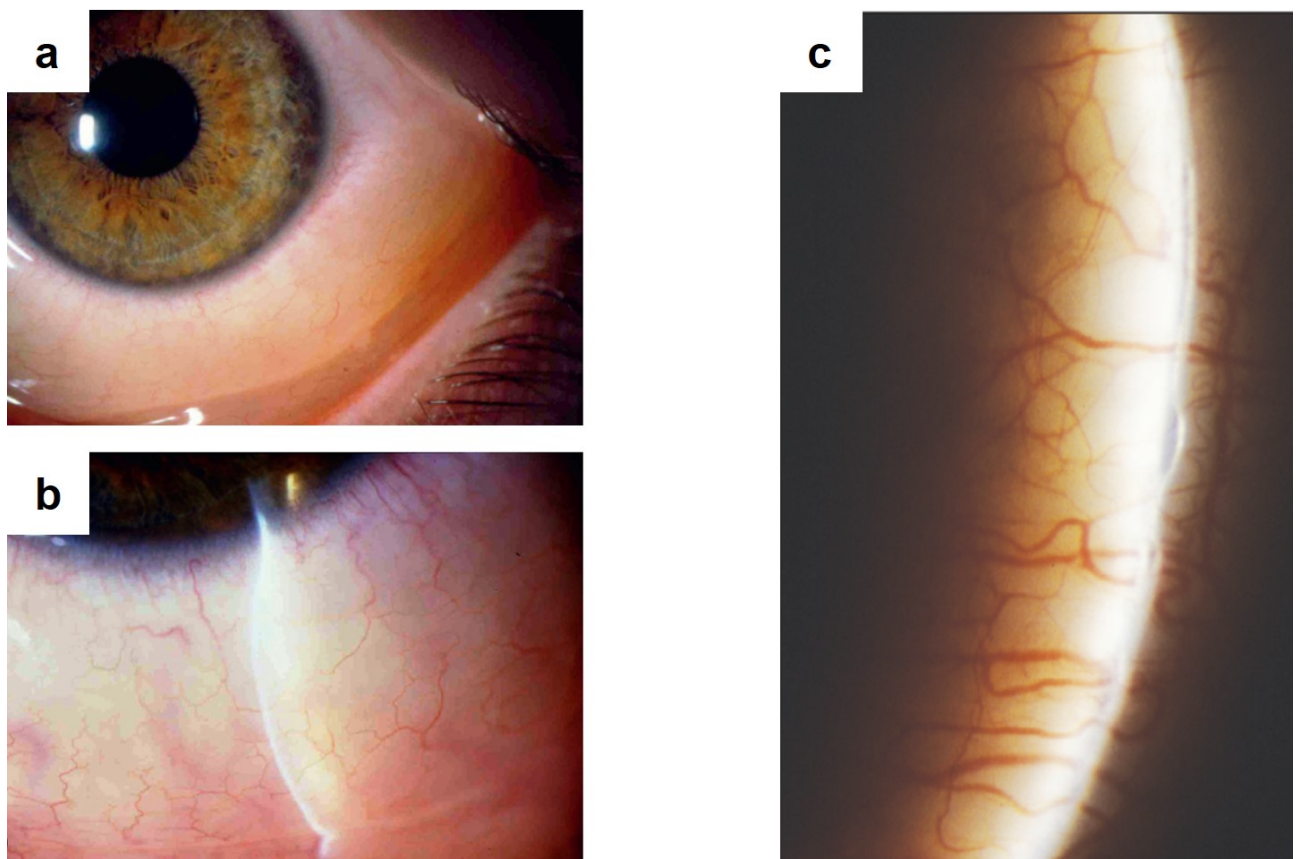


Figure 1.18 – Slit lamp examination of conjunctivitis. (a-b) Images of patient with a swelled conjunctiva, caused by the allergic conjunctivitis from [16]. (c) High-resolution view of vessels with the slit lamp. It is useful for examining the vessel structure and shape (elevations) of the conjunctiva. Adapted from [10].

State of the art and emerging methods for ocular surface imaging

Table of contents

2.1	Brief history of ocular surface imaging methods	28
2.2	Light-tissue interaction in the cornea	29
2.3	Slit lamp biomicroscopy	30
2.4	Specular microscopy	32
2.5	Confocal microscopy	33
2.5.1	Non-contact confocal microscopy	35
2.5.2	Image stitching into a large FOV	36
2.5.3	3D corneal images	37
2.5.4	Confocal microscopy + OCT	37
2.6	Optical coherence tomography	38
2.6.1	Spectral-domain OCT (SDOCT)	39
	Ultrahigh-resolution SDOCT	41
2.6.2	Swept-source (SSOCT)	42
2.6.3	Time-domain full-field OCT (FFOCT)	43
	FFOCT applications	47

2.1 Brief history of ocular surface imaging methods

For more than a century light played an important role in eye disease diagnosis. Initially, this history started from the Fundus photography for imaging the retina. In 1851, Hermann von Helmholtz introduced the Ophthalmoscope. Later, in 1911 Alvar Gullstrand presented the first device, which opened a door to imaging of the entire eye from the retina to the cornea [52]. This device was the slit lamp microscope. After more than 50 years it is still considered to be the most universal and the most commonly used golden standard instrument. Despite its relatively simple design, it was incredibly helpful to ophthalmology specialists, providing a lot of information both about the global and local (up to cellular level) view of the eye. This information was used to understand, diagnose and come up with the strategies to address the majority of ocular conditions. Nevertheless, many diseases were yet to be diagnosed with more precise methods.

In 1974 David Maurice developed the first specular microscope to visualize the endothelium at a high magnification [9]. A good contrast, undisturbed by reflection from other corneal layers, together with a high resolution allowed to quantify cell changes associated with Fuch's endothelial dystrophy and other diseases. Unfortunately, in order to obtain the clear images, the cornea must be transparent (no corneal edema, etc). As another limitation, this instrument did not permit optical sectioning, which made the corneal layers from different depths overlap in one image. Nevertheless, the specular microscope is widely used up to the present day with its advantages being the universality and low-cost. Soon after the creation of the first specular microscope, it was improved by Maurice through applying a confocal approach, patented by Marvin Minsky in 1955. This resulted in the enhanced resolution and contrast, and allowed to obtain the fine optical sectioned images from the endothelium and keratocytes. The next years resulted in a vast improvement in terms of speed and image quality, leading to the *in vivo* confocal microscope (IVCM) - today the state of the art tool (in terms of resolution) for diagnosis through the entire corneal thickness.

The most recent revolution in corneal imaging (and, in fact, the whole eye imaging) happened with the invention of optical coherence tomography (OCT) [1, 53]. Previously described specular and confocal microscopes demonstrated impressive cellular resolution, which was, however, achieved at a cost of shrinking the visible field to just half of a millimeter. The OCT provided an alternative view on the cornea with a large cross-sectional field, covering the whole anterior eye, together with a high axial resolution. That view was widely appreciated by the ophthalmologists as, among many advantages, it provided a reliable way to quantify corneal thickness and iridocorneal angle (according to the name, it is an angle between the cornea and iris). Today OCT is an important part of the routine eye examination, and the technology continues to evolve. One of the recent advancements shows the ability to image cornea with a cell-detail

resolution with an *en face* 1 - 2 mm field of view. Technology behind the images is called *in vivo* time-domain full-field OCT and was developed in a course of this thesis project [3]. It will be explicitly covered in the next chapter, while this chapter will explain the general technical principles underlying the above mentioned devices. We will check their capabilities and limitations related to the ocular surface imaging.

2.2 Light-tissue interaction in the cornea

In order to obtain images of the cornea, instruments should detect the light, which interacted with it. Therefore, before, we move on to the description of the instruments, it is useful to understand, how corneal tissue interacts with the light. As we know from the previous chapter, the cornea consists of multiple layers.

The acellular layers (basement, Descemet's membranes and Bowman's layer) are very thin, constituting less than 4% of the total thickness. They consist of the collagenous tissue like stroma, therefore light scattering from them is minimal. On the other hand, the epithelium is about 50 μm deep (or 10% of the corneal thickness), nevertheless it is still transparent, due to another mechanism - strong homogeneity of the refractive index of all the constituent cells [54].

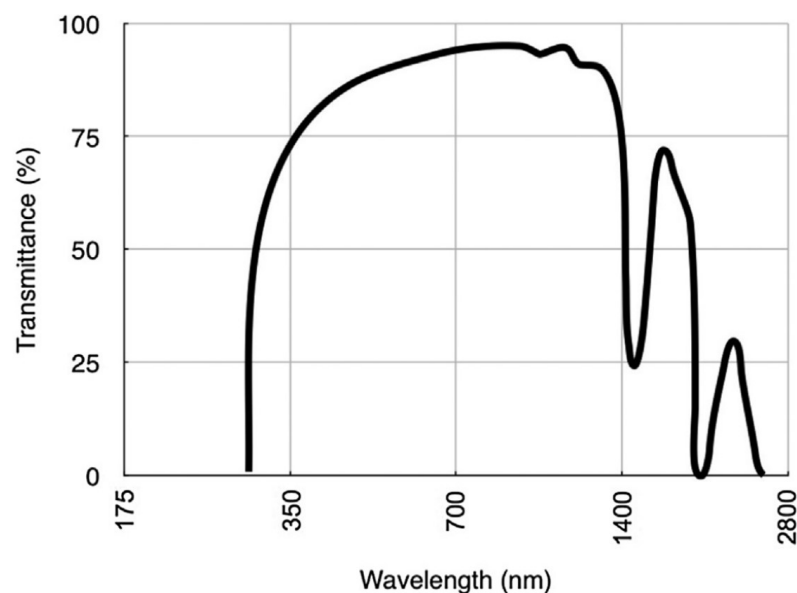


Figure 2.1 – Corneal transmission spectrum [6, 54]

Stroma is the thickest part of the cornea (about 460 μm or 90% of the total thickness). It is not homogeneous, but keeps transparency, because of the special arrangement of the stromal collagen, which permits only the certain distances between the neighbouring fibers and only the certain fiber diameters. The way it works is the following. When the light electromagnetic wave is incident on the stroma, it excites the electrons in the fibrils. Each excited electron oscillates and gives rise to the secondary electromagnetic waves, which propagate in the tissue in all the directions. Waves scattered from one fiber, superpose forming a cylindrical wave, which has the same axis as a collagen fibril. The cylindrical waves radially propagate from each fiber and interfere with each other. The interesting point is (and it was demonstrated theoretically, see [24]) that, under certain conditions of fiber diameters and distances between

the fibers, these secondary cylindrical waves interfere in a way that they cancel out for all the directions except the forward. Exactly this fiber arrangement is found in the live cornea. As a result, what happens, is that almost all the incoming radiation to the cornea is completely scattered, but the scattered waves interfere, transferring all the energy only in the forward direction towards the retina.

In this model we looked only at the stromal fibrils, however stromal body also contains a large number of cells (keratocytes), which constitute 15% of the stromal volume [55]. The cell bodies are thin in the direction of light and are sparsely distributed, nevertheless it is thought to be insufficient to suppress the backscattering. As was found [25,26], the keratocytes contain special molecules, which can adapt the refractive index of the cell cytoplasm to better match the surrounding and, thus, limit the scattering. On the confocal microscopy keratocyte nuclei is bright, while the cell membrane is dim or completely invisible.

While the reflection from inside of the cornea is very weak, the reflection from the interfaces of the cornea with the adjacent tissues is not negligible. Given that the refractive index of the cornea is 1.376, of the tear film - 1.336, of the aqueous humour - 1.336 and of the air - 1.0, it is easy to calculate from the Fresnel equations that the largest reflection is happening at the first air-tear interface (2% of the total light incident on the eye). Next tear-surface epithelium reflection gives just about 0.02%. Endothelium-aqueous humour interface at the inner end of the cornea also gives about 0.02%. While the last two numbers may seem insignificant, they give a lot of backreflected light comparing to the very weakly scattering cornea. This is confirmed in the confocal microscopy, which gives the bright and saturating images from the endothelium and surface epithelium, and relatively dark from the stroma.

To conclude, everything in the corneal structure is built with a focus on the transparency and forward scattering. This leads to an optically clear performance in the broad spectral window (figure 2.1), important for our vision. From the point of corneal microscopy, it means that the backscattered/backreflected signal and contrast between the adjacent tissues is very low, which makes corneal visualization difficult. On another hand, the corneal transparency is positive for microscopy too, because we can image through the entire corneal depth without going into the detail of challenging inverse scattering problems.

2.3 Slit lamp biomicroscopy

The slit lamp is the piece of equipment most frequently used by the ophthalmologist. Essentially it is a traditional microscope, which focuses the incoherent light on the object and collects the backreflected light to produce a magnified image. Nevertheless, there are several important design details, which make slit lamp so popular up to the present day. These details are focused on providing a doctor with all the flexibility to adapt the device on the fly to a particular clinical application.

First of all, the magnification of the instrument can be adjusted in a range from $5\times$ to $50\times$, which corresponds to a numerical aperture (NA) from 0.05 to 0.08. Illumination wavelength can be also chosen between the conventional white-light, blue-light (450 nm) (particularly useful, when eye is stained with a fluorescein) and others by using spectral filters. From the

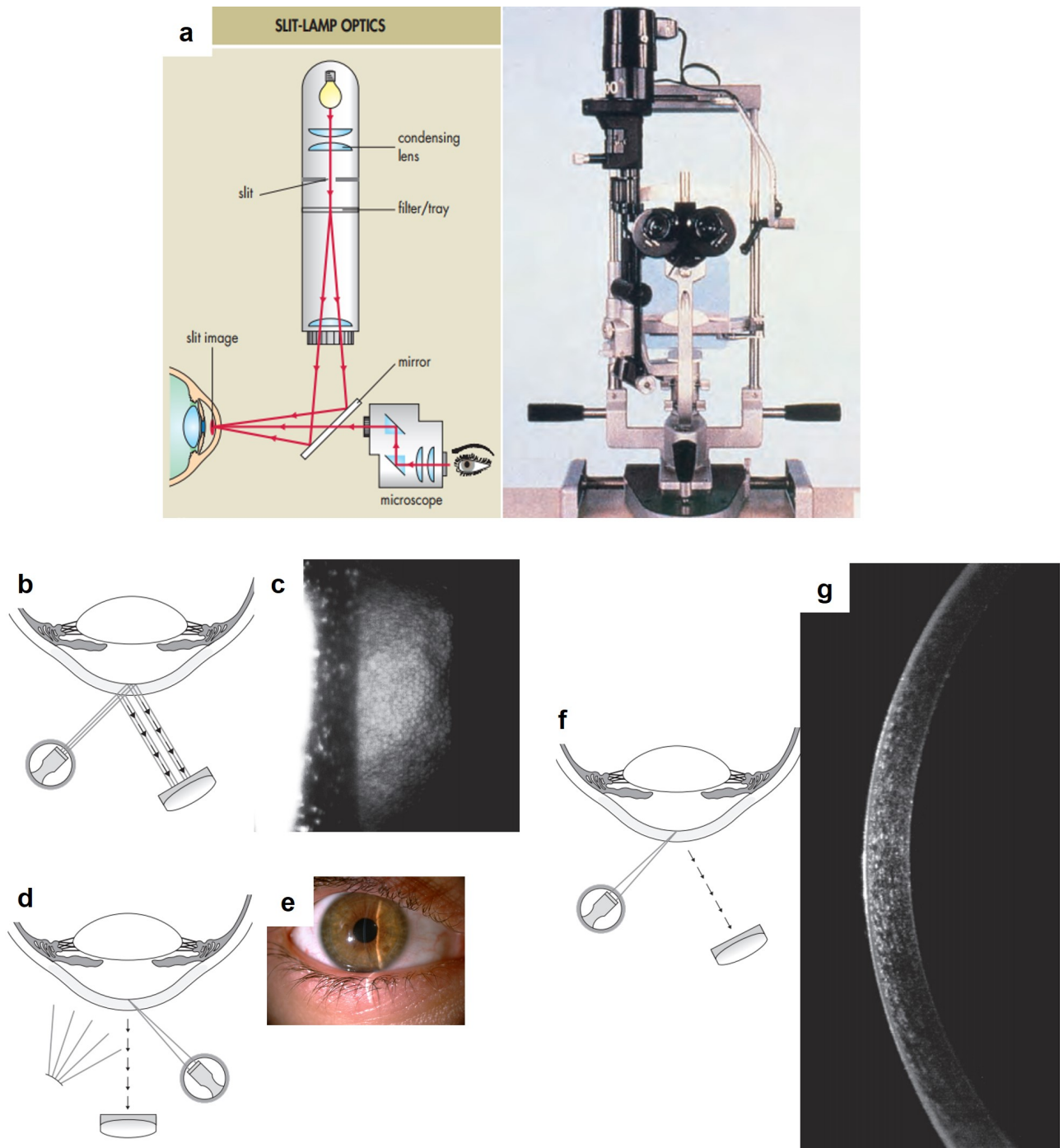


Figure 2.2 – Diagnostics with slit lamp. (a) Schematics of the microscope and an example device photo from [56]. (b-c) Specular reflection configuration: incidence angle of illumination equals the angle of detection, useful for visualization of the endothelial cell mosaic. Illustration from [10]. Image from [57]. (d-e) Combined diffuse and tangential illuminations configuration: slit illumination is coming from the side, highlighting the elevations on the eye, while diffuse illumination enlightens the whole eye. Illustration from [10]. (f-g) optical sectioning configuration with the oblique angle and narrow slit, useful for acquiring OCT-like cross-sectional images. Illustration from [10]. Image from [57].

above parameters we can calculate the diffraction limited resolution achievable with the slit lamp according to the Rayleigh criterion 2.1:

$$\Delta x = \Delta y = \frac{0.61 \cdot \lambda}{NA} = \frac{0.61 \cdot 550nm}{0.08} \approx 4\mu m, \quad (2.1)$$

where λ is the wavelength of light and NA is the numerical aperture. As we can see in (figure 2.2), it is high enough to resolve the 20 μm endothelial cells.

Another essential features of the microscope is the slit aperture, which is focused as an actual object in the image plane, creating a sharp beam of light. The slit illumination arm can be pivoted independently from the detection arm (both are mounted on a single vertical axis) to allow optical sectioning and obtain OCT-like images (figure 2.2). The sectioning thickness can be controlled by changing the width of the slit.

The last important property of the slit lamp is that it permits both the direct viewing of the cornea through the eyepiece and image recording. Viewing through the eyepiece is valuable, because: 1) examiner can directly see the dynamics of the eye without delay, 2) human eye can recognize colors with a high dynamic range of up to about 24-bit depth [58] (however in a logarithmic response instead of linear).

The flexibility to independently adjust the illumination and viewing angles, change the width of the slit, wavelength of illumination and magnification led to a great variety of possible configurations. For any normal and abnormal tissue under investigation, examiner can come up with a suitable configuration, which offers a unique perspective. As several examples: the overall health of the surface cornea, conjunctiva, limbus and sclera is examined using a macro view and a wide diffuse illumination; a narrow slit illumination with angle allows to see the cross-sectional view through the depth of the cornea; making an angle between the illumination and detection allows to capture the specular reflection, useful for examination of the endothelial mosaic.

2.4 Specular microscopy

Endothelial cell layer plays a critical role in the maintenance of the corneal transparency by allowing nutrients to reach the cornea, while blocking the rest of the fluid flow. As we have seen before, this layer can be seen with a slit lamp biomicroscopy, however with a relatively poor resolution. It is still sufficient to resolve some of the endothelial cells, but unsatisfactory to provide a precise and reliable cell counting, critical for many clinical conditions. For example, by assessing the number of the endothelial cells per square millimeter doctor can tell, if the patient has enough healthy endothelial cells to withstand the cataract surgery without the subsequent loss of the corneal transparency. Moreover, obtaining good quality endothelial images with a slit lamp requires a significant experience (especially in the diseased, opacified corneas).

Specular microscope is another type of device, which provides a high resolution view on the endothelial cell mosaic (figure 2.3). In clinics they are easy to use, provide automatic aligning and cell counting features. Strategy used in acquiring the endothelial cell images is somewhat similar to that in slit lamp. Because of the small difference in indexes of refraction between the cornea (1.376) and the aqueous layer (1.336), only 0.02% of the incident light is reflected from endothelium and aqueous interface, which makes it completely hindered by reflections from the air-tear film and tear film-epithelium interfaces. However, by having an angle between the illumination and detection it is possible to spatially separate specular reflection of endothelium

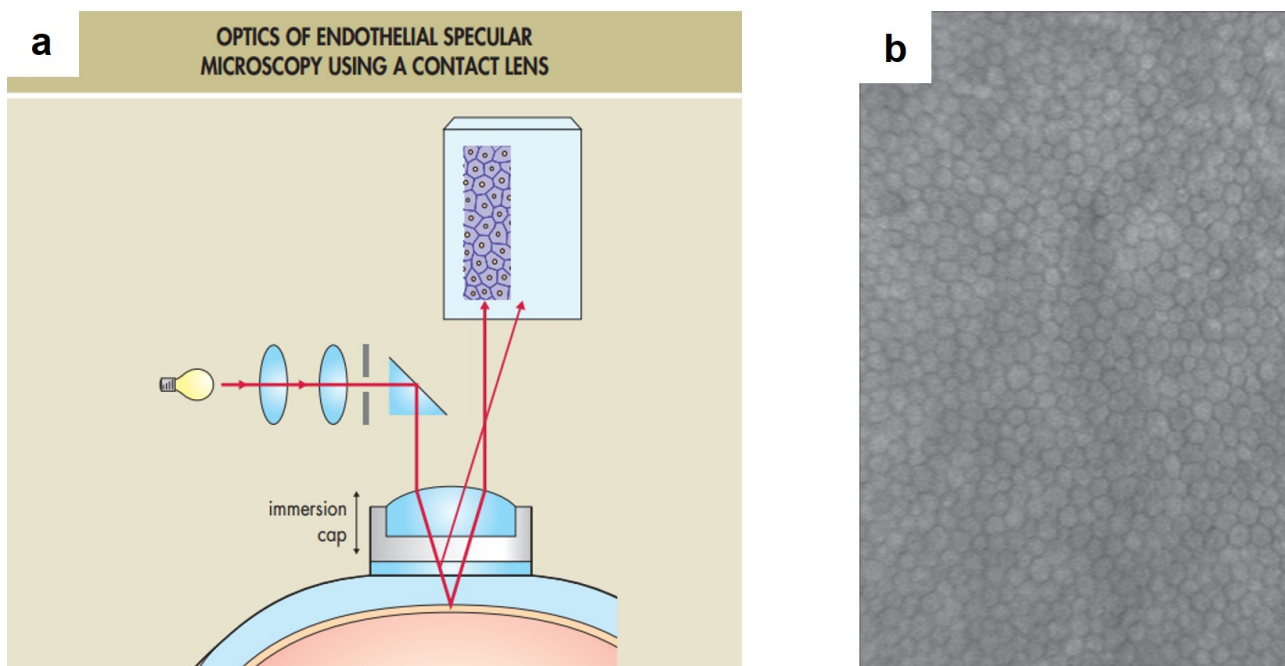


Figure 2.3 – Specular microscopy for endothelial diagnostics. (a) Schematics of the contact configuration from [56]. (b) Endothelial cell mosaic from [10]. FOV $490 \mu\text{m} \times 690 \mu\text{m}$.

from the corneal surface reflection and get a good hexagonal cell contrast [56]. Contrary to the slit lamp, the specular microscope obtains an angle by using a high NA objective, where half of the NA is given to the illumination and half to the detection. Even half of the NA is sufficient to obtain images with a higher resolution comparing to the slit lamp. In a non-contact version of the specular microscope, typical NA is about 0.4. Then, diffracted limited resolution according to the Rayleigh criterion 2.2:

$$\Delta x = \Delta y = \frac{0.61 \cdot \lambda}{NA/2} = \frac{0.61 \cdot 550\text{nm}}{0.2} \approx 1.6\mu\text{m}, \quad (2.2)$$

where $NA/2$ is written, because only the half of the NA is used for detection.

The field of view can be increased by increasing the width of illumination. However, with the wide illumination the unwanted backscattering from the adjacent stromal layers also reaches the camera. In order to avoid this, the modern commercial instruments limit the field of view to about $500 \mu\text{m} \times 700 \mu\text{m}$ [10].

2.5 Confocal microscopy

By carefully adjusting the size of the slit and the angles of illumination/detection, the slit lamp and specular microscopes were able to capture images from the endothelial cells. Endothelium is unique, because it is the last layer before the aqueous humour, which makes it reflect the light in a mirror-like way. Now, if we try to view the other slices within the cornea with the same instruments, we obtain the blurred low-contrast images. The reason is that the conventional microscopy does not fully reject the background out-of-focus light, leading to a mixture of the corneal slices in a final image. Confocal microscopy was introduced with a goal to eliminate much of this out-of-focus light.

Confocal microscope in its basic form is a microscope with the two filtering pinhole apertures (figure 2.4). The first aperture limits the illumination of the tissue to a single point in a focus of the microscope objective. The light reflected from the illuminated tissue spot is collected by an objective lens, passes through another pinhole aperture and gets collected by a detector. The tissue at the focal point is detected, because the backreflected light is focused on a detection aperture, but the light from the tissue sections in the front or behind the focus is blocked by the aperture and does not reach the detector. As a result, out-of-focus signal is suppressed and the in-focus optical section is captured in the image with a high contrast.

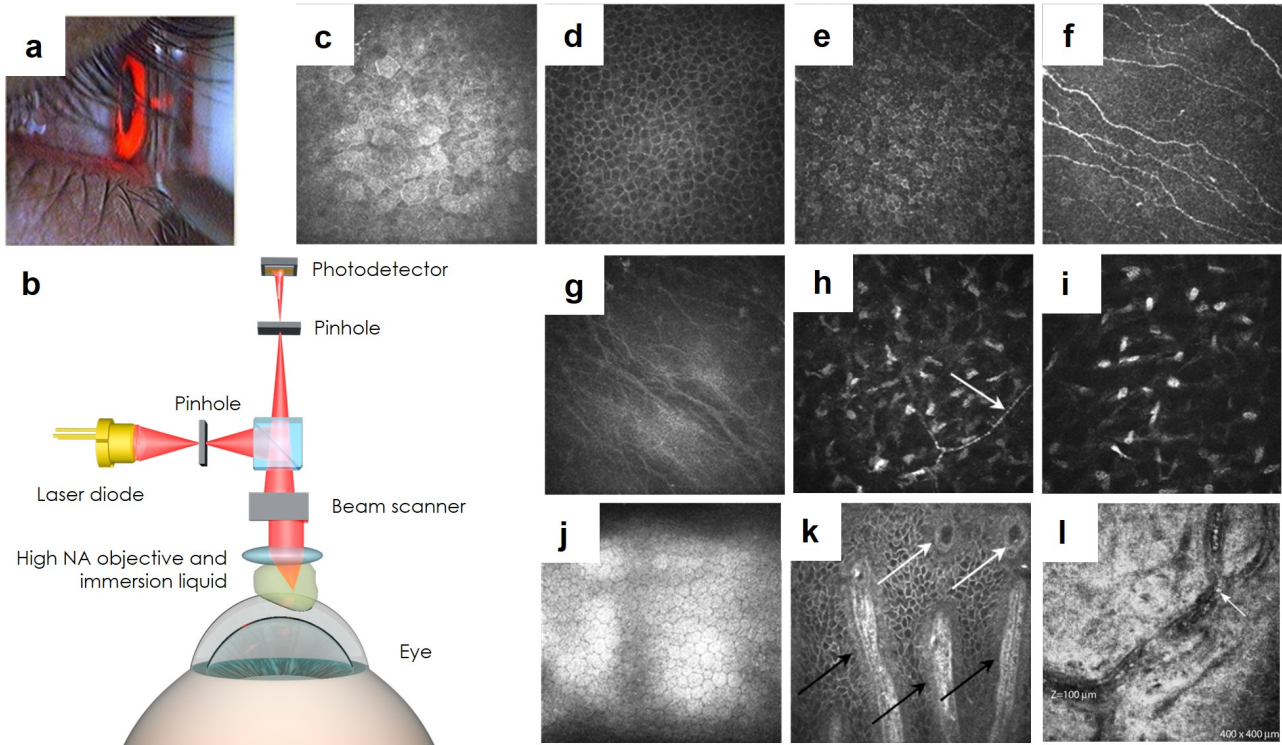


Figure 2.4 – Clinical contact confocal microscopy. (a) Alignment camera view on a patient's eye in contact with the cap of the objective. (b) Schematics of the confocal microscope. (c) Superficial epithelium. (d) Wing cells. (e) Basal cells. (f) Sub-basal plexus nerves. (g) Bowman's layer. Dark lines are called K-structures and are the folds of the layer, appearing due to the applanating pressure from the contact microscope objective. (h) Anterior stroma with an arrow pointing at a stromal nerve. (i) Deep stroma with the elongated keratocyte nuclei. (j) Endothelium. (k) Palisades of Vogt (POV) (black arrows) and focal stromal projections (white arrows) in the limbus. (l) Blood flow in the conjunctiva with a visible erythrocyte (white arrow). Corneal images are adapted from [11, 18]. FOV $400 \mu\text{m} \times 400 \mu\text{m}$.

Use of the pinhole apertures also improves the lateral and axial resolutions through the filtering of the higher orders of the diffraction pattern (Airy disc rings) in the point spread function [59]. We can calculate resolutions of one of the leading confocal imaging instruments available for cornea imaging (HRT III + RCM, Heidelberg engineering, Germany) 2.3,2.4. It uses a 670 nm laser and a 63 \times objective lens with 0.95 NA [10].

$$\Delta x = \Delta y = \frac{0.4 \cdot \lambda}{NA} = \frac{0.4 \cdot 670\text{nm}}{0.95} \approx 0.3\mu\text{m} \quad (2.3)$$

$$\Delta z = \frac{1.41 \cdot \lambda}{NA^2 \cdot n} = \frac{1.41 \cdot 670nm}{0.95^2 \cdot 1.376} \approx 0.8\mu m, \quad (2.4)$$

where Δz is the axial resolution and n is the refractive index of the cornea. The lateral resolution is actually lower than we calculated, limited by the scanning undersampling to about $1 \mu m$ (to gain larger field of view within the same acquisition time). The calculated axial resolution is different from the one typically specified for this system ($7.6 \mu m$ [60]), which may be explained by a slightly opened pinhole aperture (to increase the signal) or by the outdated device specification.

Unfortunately, by shrinking the aperture not only we increased the contrast and resolution, but also reduced the field of view to a size of a diffraction limited spot. Therefore, in order to capture a full-field image, the focal point must be rapidly scanned across the sample and the resulting image reconstructed. Several scanning schemes were proposed with the most advanced being the laser scanning method, where the laser beam is scanned in a raster pattern over the field of view by the means of the horizontally- and vertically-oriented scanning mirrors. The scanning speed sets the limit for the maximal FOV, which is currently about $400 \mu m \times 400 \mu m$.

With the high contrast and signal-to-noise ratio confocal microscopy is able to reveal all the corneal layers, including superficial, wing and basal epithelium with cells, sub-basal nerve plexus with individual nerves, anterior, middle and deep stroma with keratocytes and endothelium cell mosaic (figure 2.4). Moreover, instrument can visualize limbus with Palisades of Vogt and blood vessels with individual erythrocytes. The most significant application of confocal microscopy has been the identification of organisms causing keratitis, particularly *Acanthamoeba*. Its resolution enabled the definitive diagnosis and removed the need for biopsy.

2.5.1 Non-contact confocal microscopy

Microscope objective with a very high NA of 0.95 has a very short working distance (0.17 mm) and requires use of an immersion liquid. Thus, clinical confocal microscope needs a direct physical contact with a patient's eye, preceded by the ocular anaesthesia. This results in a discomfort for the patient, increased risk of corneal damage, risk of infection and exemption of this device from being used in young children and in patient's with the fragile corneas, undergoing a refractive surgery.

As an alternative, a non-contact confocal corneal microscope was also proposed [61]. It used a 0.45 NA non-contact objective (CF Plan EPI SLWD, Nikon) (figure 2.5). While the lateral resolution was unaffected (and still limited by the scanning undersampling), the axial resolution got reduced (theoretically we can estimate it about $\approx 3 \mu m$ or larger, in case the pinhole aperture was slightly opened). Moreover, it was not possible to see the anterior cornea, because the view was hindered by the specular reflection from the surface of the eye.

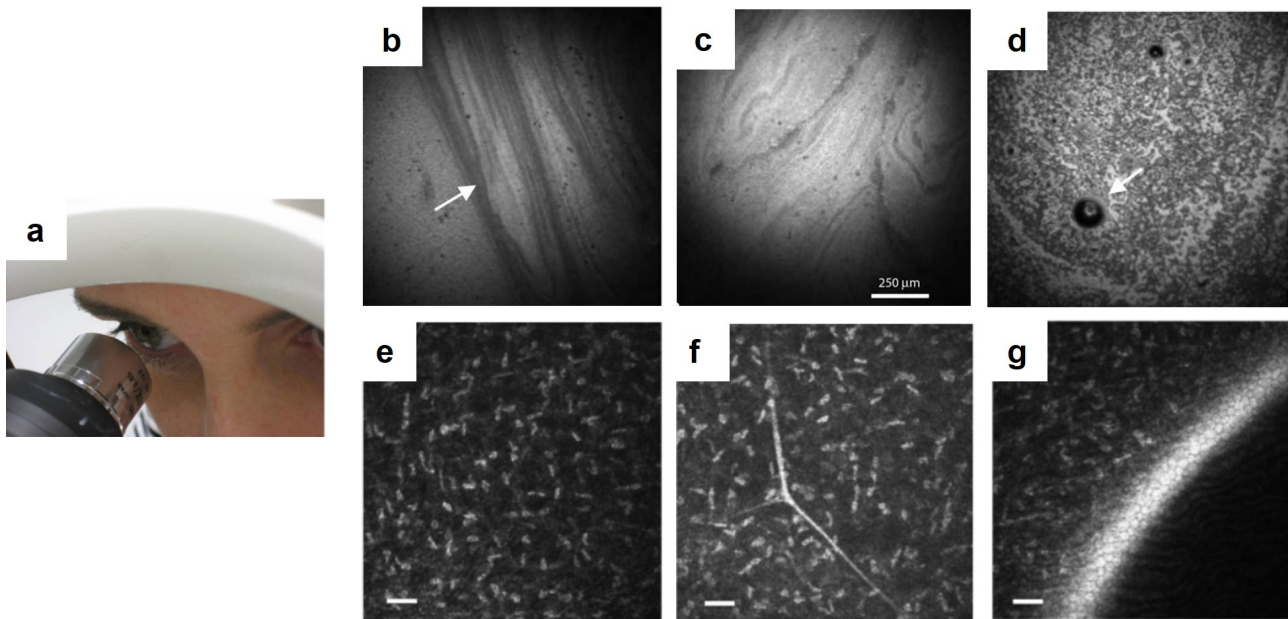


Figure 2.5 – Non-contact confocal microscopy prototype. (a) View on the examined patient. The distance between the objective and the eye is 14 mm. (b-d) Images of the tear film. Lipid film stripes (white arrow in (b)) are visible right after the eye opening. Meibomian granular expressions were found (white arrow in (d)). (e-g) Posterior stroma and endothelium. Larger number of keratocytes are visible in stroma comparing to contact confocal images, which is explained by a thicker optical sectioning. Images are adapted from [61] and [18]. FOV $500 \mu\text{m} \times 500 \mu\text{m}$.

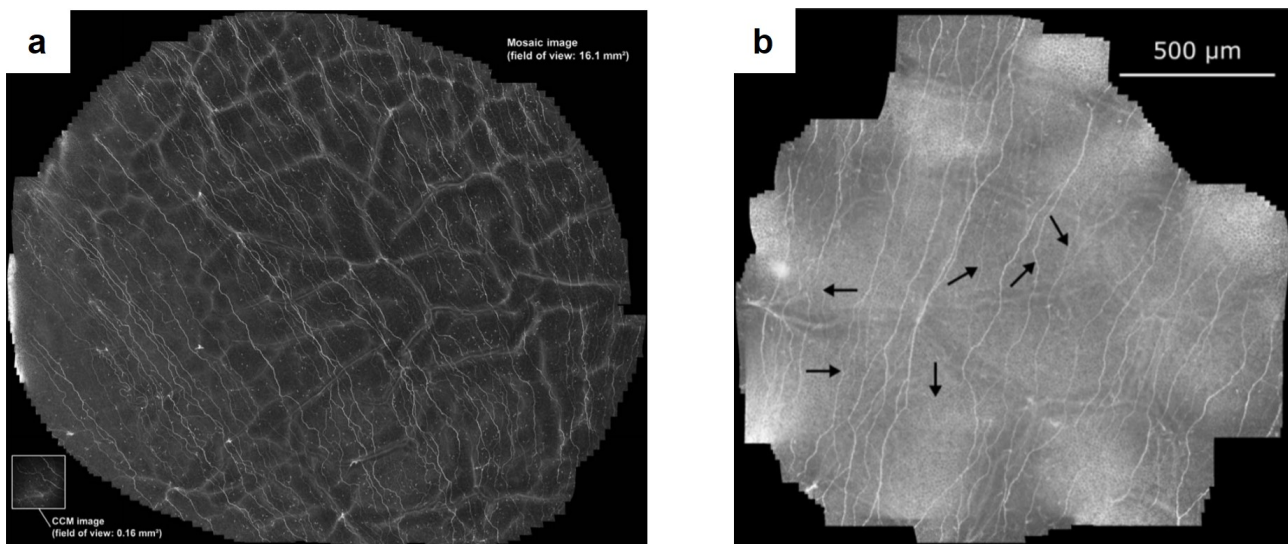


Figure 2.6 – Stitched contact confocal microscopy images of sub-basal nerves. (a) Large field of view (16 mm^2) image of SNP, obtained by stitching 2541 images [62]. K-structures from Bowman's layer were visible due to the applanating pressure, applied on the cornea by the microscope objective. (b) Smaller field of view image with more resolvable nerves from [63].

2.5.2 Image stitching into a large FOV

Small FOV of $400 \mu\text{m} \times 400 \mu\text{m}$ is an important disadvantage, which leads to a long examination time (required to locate a spot of clinical interest). Moreover, nerve and cell countings could be more precise, if a larger field was available. Recent publications proposed to increase the

total image field of view by using the spiral moving eye fixation target and image stitching in post-processing [62, 63]. By stitching together 2541 images the field of view was increased up to 16.1 mm^2 , 100 times comparing to original 0.16 mm^2 (figure 2.6). Although the resulting image was impressive, the technique proved to be difficult in patients. It was not possible to get the images from one out of nine volunteers. Moreover, for successful volunteers many images had to be disregarded due to the eye movements and the procedure had to start again. The long procedures, however could potentially lead to corneal irritation due to the contact nature of the method.

2.5.3 3D corneal images

As we know from the Chapter 2, there is a large clinical interest in the cross-sectional corneal images. Mainly because you can have access to the total thickness of the cornea and the thicknesses of its composing layers. Native confocal microscopy view is *en face* and it does not have the information about the current imaging depth. Recent publication [64], proposed use of a new contact objective cap and the fast motors to acquire volumetric images (figure 2.7). The curved cap, pressing the eye, reduced the lateral movements, while the rapid motor reduced the acquisition time of the volume to 26 seconds. Due to the small range of the motor, the depth of the 3D image was limited to $400 \mu\text{m}$. The FOV of view was reduced to about $300 \mu\text{m}$.

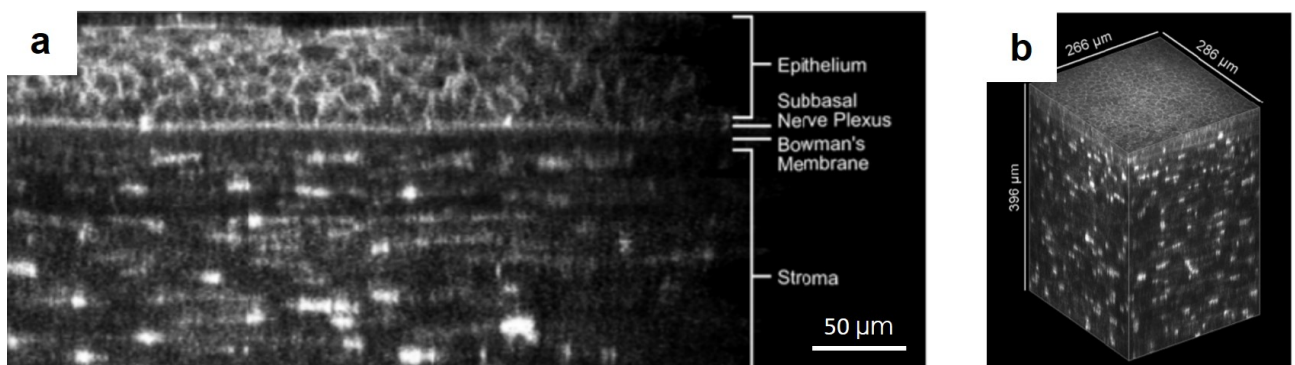


Figure 2.7 – 3D imaging with a contact confocal microscope. (a) Cross-sectional view on the anterior cornea. (b) Total acquired volume. Images are adapted from [64].

2.5.4 Confocal microscopy + OCT

Another way to provide the cross-sectional information is to combine the confocal microscopy with OCT. This was realized in [65].

OCT aided in locating the corneal position, helped in estimating the thicknesses of the corneal layers. Moreover, the field of view in the confocal images was increased to $805 \mu\text{m} \times 805 \mu\text{m}$ (figure 2.8) - a factor of 4 comparing to a clinical confocal microscope. Although the frame rate dropped to 5 frames/second, this bottleneck can be overcome in the future with a faster image acquisition electronics and software.

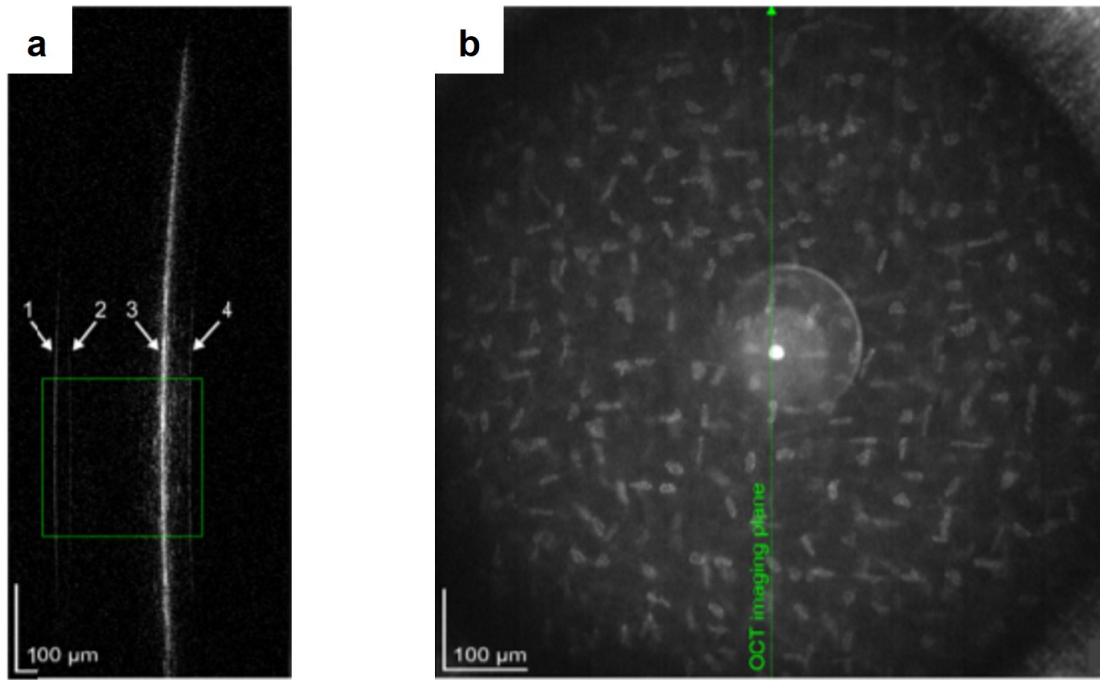


Figure 2.8 – Confocal microscope coupled with OCT. (a) OCT image with the arrows pointing at the reflections from an objective cap (1), at the mirror artifact (2), CCM imaging plane (3) and posterior corneal surface (4). (b) Confocal microscopy image. Images are adapted from [65].

2.6 Optical coherence tomography

Optical coherence tomography (OCT) [66] is a non-invasive imaging modality that demonstrated very successful results in imaging the biological tissues. The power of OCT comes from the ability to "gate" the light reflected back from the sample in terms of the depth, where the light is travelling from. In other words OCT allows non-invasive optical depth-sectioning of the sample. This ability proved particularly useful for imaging the retina of the eye [1], where no alternative sectioning technologies were possible. But even with a new view on the retina, OCT would not have flourished as greatly and as rapidly, if there was no special clinical application, where its cross-sectional view would have been appreciated. Such application existed - a complex disease called neovascular Age-related macular degeneration (nvAMD). It is one of the main causes of blindness in the developed countries, and was not successfully addressed by other technologies. The cross-sectional view was useful because it, for the first time, provided the doctors with an opportunity to look at the retinal elevations caused by nvAMD and monitor its progress. Simultaneously, a new class of drugs, vascular endothelial growth factor (VEGF) inhibitors, were developed to address nvAMD. With OCT and VEGF clinicians were empowered to diagnose, monitor the progress and treat the disease.

When the first anterior-segment optical coherence tomography (AS-OCT) appeared [67], the slit lamp, confocal microscopy and ultrasound have already found their clinical use cases. Nevertheless, like in the case of the retina, OCT high-resolution cross-sectional view was unique and appreciated - the confocal microscopy gave only *en face* image and the penetration depth was small, while resolution of the slit lamp and ultrasound was very low. OCT view was valuable to a large number of clinical applications, in particular those, which required precise measurement of the corneal shape and thickness, iridocorneal angle, etc. [68].

For many years OCT has been recognized as a gold standard diagnostic tool. 25 years of development further improved OCT speed and resolution, on the way opening it to the new clinical applications. In this time frame OCT has undergone several major technological breakthroughs. Initially, it started as an optical coherence domain reflectometry (OCDR) [69, 70], expanded to 2D [1]. On the way, the time-domain (TDOCT) phase-retrieval approach was surpassed by the spectral-domain (SDOCT) scheme [71, 72], bringing improvement in terms of the signal-to-noise ratio [71, 73, 74]. Today the next shift is happening from the SDOCT towards the swept-source OCT (SSOCT) [75], which has a speed advantage. Simultaneously, a number of alternative promising OCT technologies, yet to be used in clinics, are being developed. To name a few examples: Ultrahigh-resolution (in terms of axial resolution) OCT [76], Ultrahigh-resolution (in terms of lateral resolution) OCT [77], rapid scanning OCT, enabling 3D whole anterior eye imaging [78, 79], Line-field OCT [80], Off-axis Swept-source full-field OCT [81], Off-axis time-domain full-field OCT [82] and the conventional time-domain full-field OCT [3, 4, 83], which is the main focus of this thesis.

Below, we will look through the current and emerging technologies, which have been applied to the corneal imaging.

2.6.1 Spectral-domain OCT (SDOCT)

Spectral-domain OCT is a technology, that powers most of the up-to-date clinical OCT devices. It uses a Michelson interferometer, a spatially coherent light sources of low-temporal coherence and a spectrometer to acquire an axial line-section of the sample in a single measurement.

A qualitative explanation, how SDOCT works is the following (figure 2.9). In a classical Michelson interferometer light from the low temporal coherence source (typically, a broadband Superluminescent laser diodes (SLD)) is split by the beam splitter into the two arms: the one with a sample and the second with a mirror. Then, reflected light from the both arms recombines at the beam splitter and gets dispersed by a diffraction grating. Grating spatially separates light into the beams of different wavelengths, and each of them gets detected by the pixels of the line camera array. Suppose that both arms of the interferometer match in terms of the path length (within the coherence length of the light source), then interference happens and we detect the amplitude modulation on top of the original light source spectrum. Interestingly, if we make sample and reference arm lengths different (by more than the coherence length of the light source), interference still happens and we still notice the fringes modulation. The reason is that each of the pixels in the line camera array "sees" only one wavelength, thus it "sees" a coherent light source, which has a coherence length much longer than that of the whole multi-wavelength low-coherent source. In the general case of a continuous backscattering distribution, each depth generates a specific spectral modulation frequency, so, by using a Fourier transform of the spectrum one obtains the reflectivity distribution along the probed depth. The above leads to a great advantage of SDOCT over the time-domain design: with a fixed position of the reference mirror SDOCT can probe different depths of the sample, as the reflection from every depth (within a coherence length of the light, detected by one pixel) creates the interference fringes in the spectrum.

Now in order to discriminate, which interference pattern corresponds to which depth of the sample (or in other words to which separation between the sample and reference arms), we can

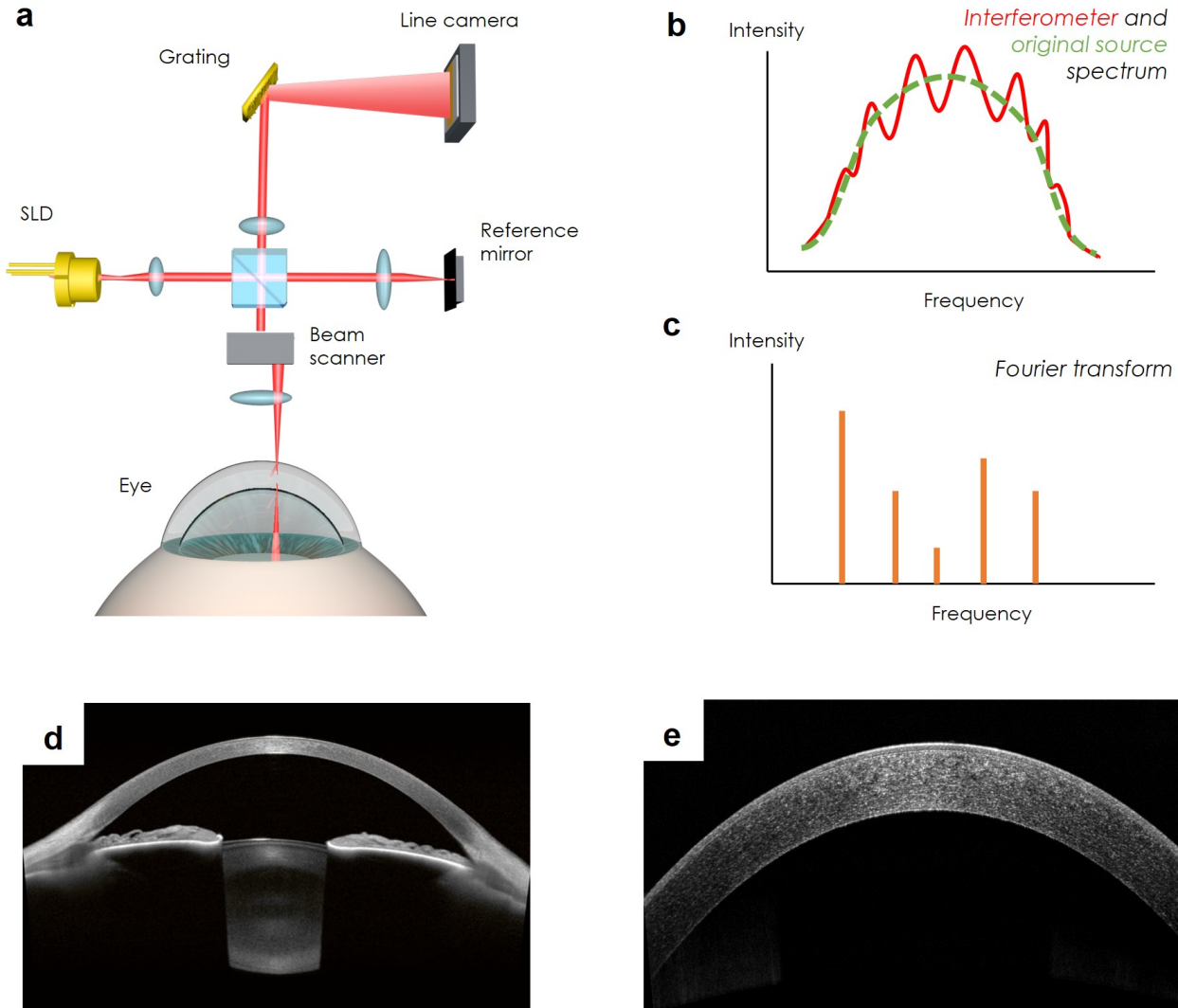


Figure 2.9 – Spectral-domain OCT (SDOCT). (a) Schematics of SDOCT instrumentation. (b) Measured spectrum of interferometer by the line camera (red) and the initial light source spectrum (green). Visible fringe envelope is due to the interference between the reference mirror and sample layers. (c) Fourier transform of red spectrum in (b). Different frequencies correspond to reflections from different depths in the sample. (d) Whole anterior eye imaging with a large DOF SDOCT [84]. (e) High resolution SDOCT view on the cornea [84].

look at the intensity, measured by a single pixel detector 2.5:

$$I \sim |E_r|^2 + |E_s|^2 + 2 \cdot E_r \cdot E_s \cdot \cos(2 \cdot k \cdot \Delta l), \quad (2.5)$$

where E_r and E_s are the electric fields from the reference and sample arms, k - wavenumber, proportional to the inverse wavelength, Δl - length difference between the sample and reference arms. The fringe pattern is determined by the \cos modulation. Suppose Δl is low, then \cos function is slowly modulating with a changing wavelength of light. If, however, the Δl is high, \cos function will be modulating rapidly. Then, the measured spectrum from the sample with multiple reflecting layers, will show the envelope with the several fringe frequencies. By taking a Fourier transform, these frequencies and the corresponding depths of the layers are determined. The amplitude of modulation is proportional to the layer reflectivity. Information about layers positions and reflectivities are enough to create a single 1D depth section of the sample (called

A-line). By scanning the beam in 1D (for example, along x axis) the 2D B-scan image is obtained, while scanning in 2D (along x and y) gives a 3D (C-scan) image. Modern clinical systems use the fast scanning galvanometer mirrors, providing 100 000 A-lines per second.

The axial resolution in SDOCT is inversely proportional to the bandwidth of the light source 2.6. Resolution can be estimated from the known wavelength (840 nm) and spectral bandwidth (50 nm) of the typical clinical OCT systems:

$$\Delta z = \frac{2 \ln 2}{\pi \cdot n} \cdot \frac{\lambda^2}{\Delta \lambda} = \frac{2 \ln 2}{\pi \cdot 1.376} \cdot \frac{(840nm)^2}{50nm} \approx 4\mu m \quad (2.6)$$

Lateral resolution and depth of focus in SDOCT are determined like in conventional microscopy by the NA of the optics. Clinical OCT systems use low-NA, which gives the lateral resolution about 15 μm 2.7 and 1 mm depth of focus (DOF) (as an example configuration) 2.8:

$$\Delta x = \Delta y = \frac{0.61 \cdot \lambda}{NA} = \frac{0.61 \cdot 840nm}{0.035} \approx 15\mu m \quad (2.7)$$

$$DOF = \frac{\pi \cdot \Delta x^2 \cdot n}{\lambda} = \frac{\pi \cdot (15\mu m)^2 \cdot 1.376}{840nm} \approx 1mm \quad (2.8)$$

The axial resolution and lateral resolution (and depth of focus) are completely decoupled. Thus, we can have a large depth of focus with a high axial resolution - ideal case for the cross-sectional images.

The clinical instruments operate in two modes: 1) large DOF with a view on the whole anterior segment, 2) smaller DOF with a higher resolution view on the cornea (figure 2.9).

Ultra-high-resolution SDOCT

A lot of research effort has been put to improve the lateral and axial resolutions of SDOCT. Today many of the laboratory systems demonstrate superior performance comparing to the modern clinical devices.

Improvements in axial resolution are due to the adaptation of more broadband light sources. For example, SDOCT, equipped with a titanium:sapphire laser with 170 nm bandwidth, produces images with 1.2 μm axial resolution in tissue [85]. It is sufficient to measure the thicknesses of the thin Bowman's layer and tear film (figure 2.9). Recently, by using a supercontinuum laser even a sub-micrometer view on the epithelial cells and nerves was achieved [86].

Another research direction is focused on improving the lateral resolution. It is done by simply increasing the NA of the detection optics. The most advanced result was achieved several months ago by implementing a 0.26 NA 10 \times microscope objective [77].

$$\Delta x = \Delta y = \frac{0.61 \cdot \lambda}{NA} = \frac{0.61 \cdot 785nm}{0.26} \approx 1.8\mu m \quad (2.9)$$

Cells and nerves in *in vivo* human cornea were resolved with 1.8 μm lateral resolution 2.9 in a 250 $\mu m \times 250 \mu m$ field (figure 2.9). Similar setup was used to view the limbus with the pronounced palisades and vessel shadows [33]. In both works substantial eye movements artifacts are present in the *en face* images. This is due to the fact that SDOCT acquires primarily the cross-sectional images, and, in order to get an *en face* view, the whole volume of

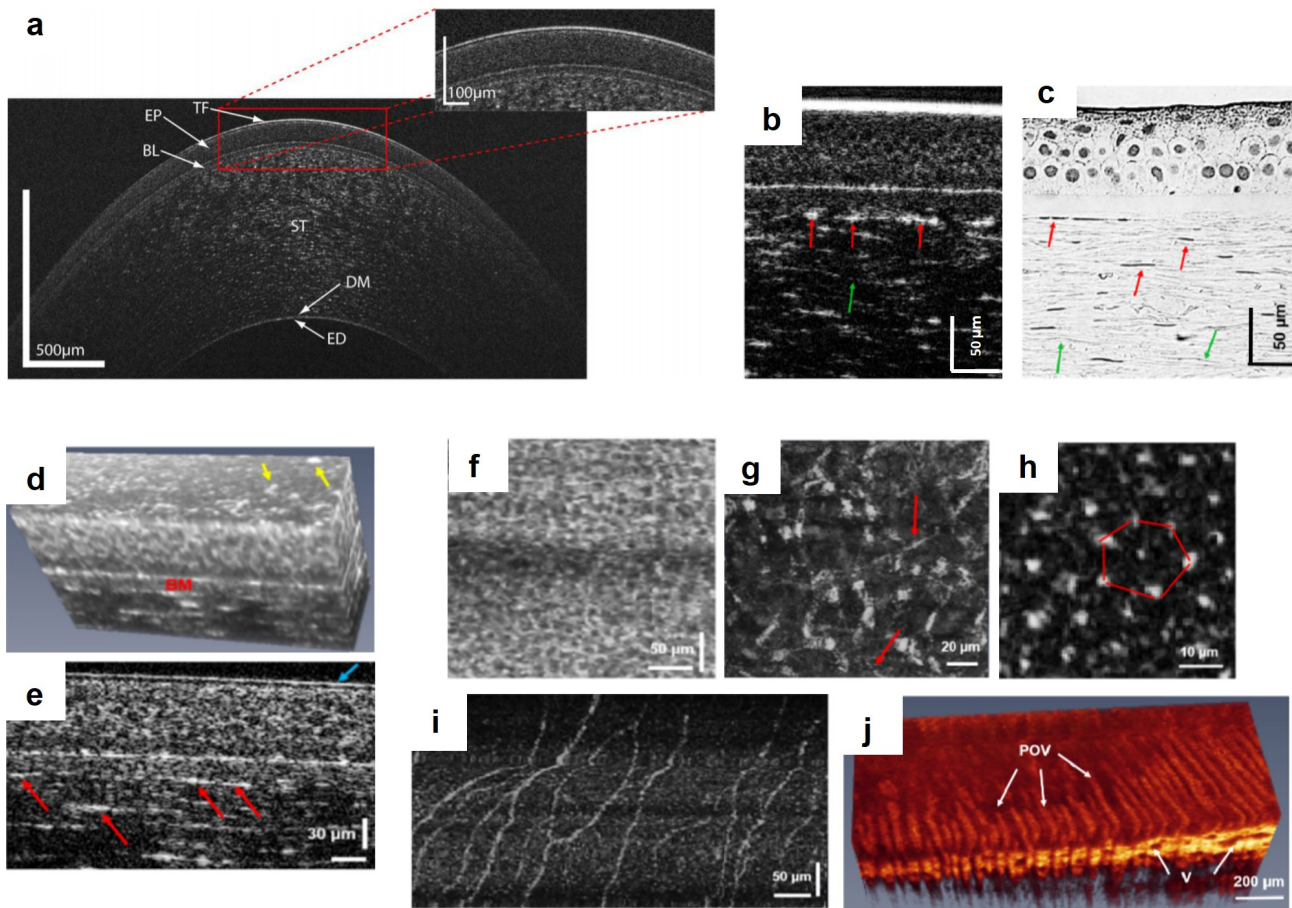


Figure 2.10 – Ultrahigh-resolution SDOCT (UHR-SDOCT) (a) High axial resolution ($1.2 \mu\text{m}$) view on the cornea from [85]. (b,c) Sub-micrometer axial resolution view on anterior cornea from [77] and the corresponding histology. Arrows point at the keratocytes. (d-i) High lateral resolution images of the anterior corneal volume (d), cross-section, extracted from volume (e), epithelial (f), keratocyte (g) and endothelial (h) cells, sub-basal nerves (i). (j) Volumetric image of the palisades of Vogt from the related device [33].

images should be collected. However, it takes time and even the scanning speed of 250 kHz is insufficient to acquire movement-undistorted volume. In the same way SDOCT is limited in a FOV, because the larger FOV volume acquisition takes a longer time, which leads to the visible eye movements artifacts. In the future by using the line-field scanning (line by line instead of point-by-point) the speed can be improved. Nevertheless the method will likely produce smaller FOV and more movement artifacts comparing to full-field OCT, for which *en face* plane is the primary one. In any case, this method is an interesting example, because in addition to an *en face*, it provides the *cross-sectional* view, which has important implications in clinics. The cross-sectional field is limited by the DOF of the microscope objective.

2.6.2 Swept-source (SSOCT)

The next generation of the coming clinical instruments are powered by the Swept-source OCT (SSOCT). Swept-source devices can acquire 3D images of the whole anterior eye with a high signal-to-noise ratio. This is possible thanks to a fast scanning speed (today up to 0.5 million A-lines/second): faster scanning allows to cover larger FOV or/and increase SNR by the pixel

subsampling (pixel is acquired several times and the values are averaged).

The principle of operation is close to that of SDOCT, however there are important differences (figure 2.11). The diffraction grating and line camera in SSOCT are substituted with a single detector. Still, the detector "sees" only one wavelength at a time, because the light source can very rapidly switch (sweep) the wavelength. The intensity is detected for each wavelength, and interferometer spectrum is constructed. The Fourier transform reveals the depths of the reflectors within the sample volume.

Similar to SDOCT the lateral resolution is determined by the NA of the detection optics, while the axial resolution depends on the sweeping range (full bandwidth) of the light source.

In the future we can expect the further increase in the SSOCT scanning speeds. One important limitation of the technology is its price, however with the developed clinical market the cost is likely to drop.

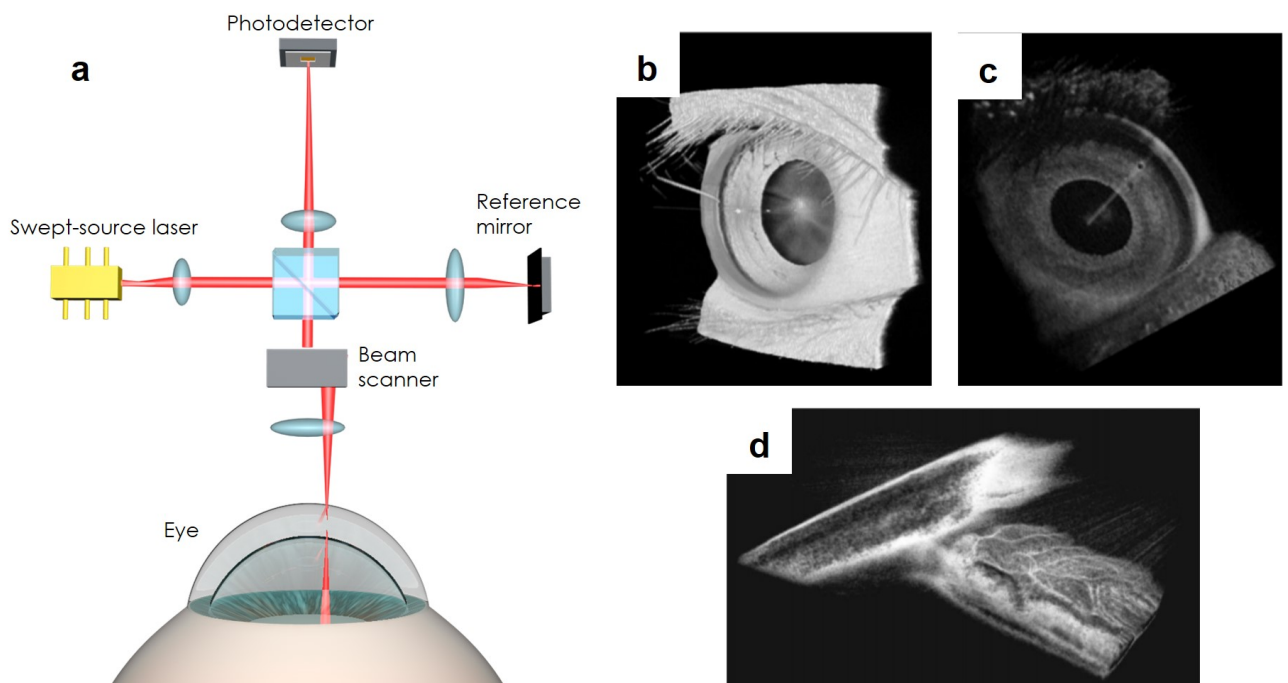


Figure 2.11 – Swept-source OCT (SSOCT). (a) Schematics of instrumentation. (b-c) Whole anterior eye volumetric images from [79, 87]. (d) 3D image of limbus from [87].

2.6.3 Time-domain full-field OCT (FFOCT)

Full-field OCT is an alternative type of OCT, where the primary orientation of the images is *en face*. Because of that, full-field systems are indifferent to the extension of DOF, which is a concern for SDOCT devices. Instead, FFOCT focuses on having a high lateral resolution, which is achieved by using the microscope objectives with a high NA.

In order to understand the origin of FFOCT, it is useful to look at history of OCT in general. Every OCT originates from the very first generation of devices, which used the time domain-approach for amplitude and phase retrieval [1, 69]. These devices used the Michelson interferometer, low-coherence light source, photodetector and were working in the following

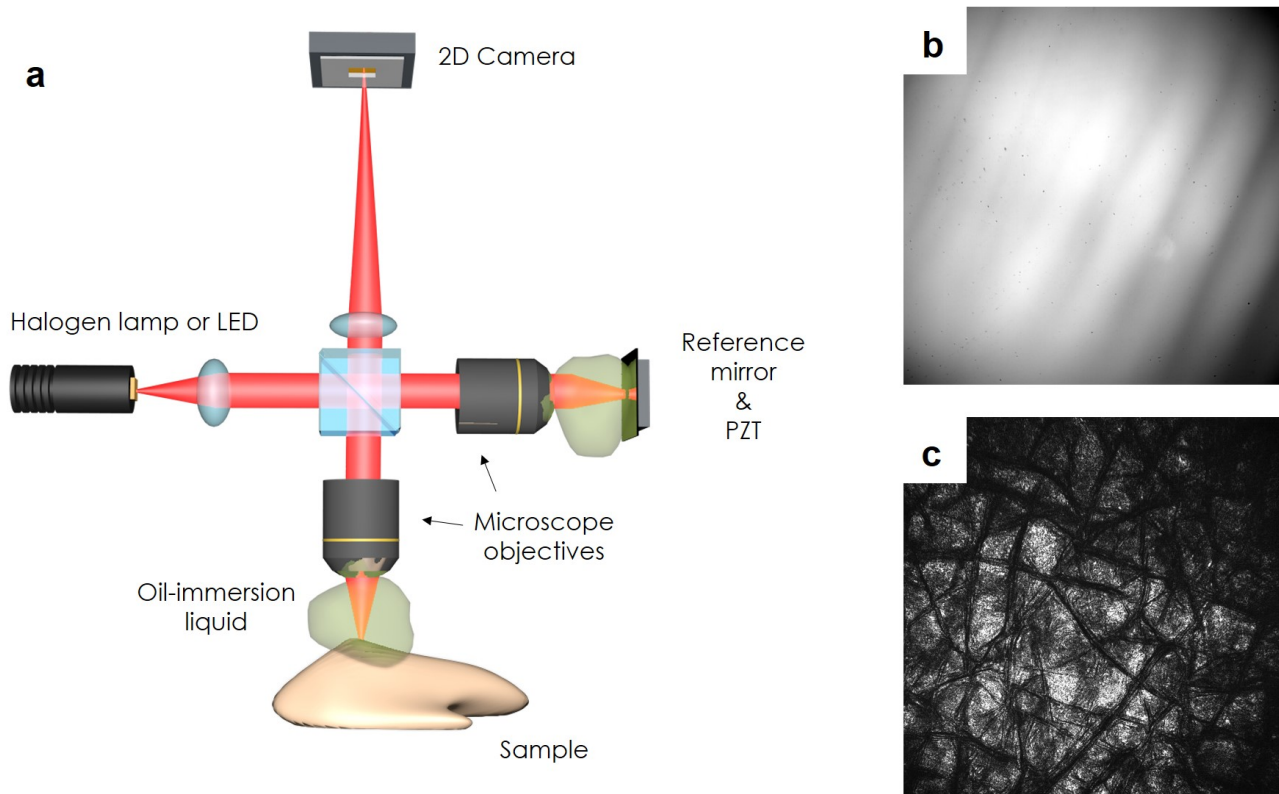


Figure 2.12 – Contact (through immersion liquid) FFOCT. (a) Schematics of instrumentation. (b) Conventional camera image. Typically, amount of incoherent light is so high, that the interference fringes can not be resolved (visible dark lines correspond to the defocused image of the light-emitting diode source chip and not the fringes). (c) Reconstructed FFOCT image from the several conventional camera images (b).

way. Because of the use of light source with low temporal coherence, the interference happens only, if the sample and reference arms are matching with precision below the coherence length. By moving the reference mirror and finding the reference positions, in which the interference fringing happened on the detector, one could reconstruct the A-line profile of the tissue in depth. By scanning the beam in a line or in a plane, the 2D and 3D images could be reconstructed.

As we can see, even a simple 2D reconstruction required the synchronized lateral beam scanning together with the scanning of the reference mirror, which made device complex and speed-limited. Nevertheless, at that time it was the most advanced OCT technology, and several commercial instrument were made based on it. Research in several groups was conducted with a goal of increasing the imaging speed to enable better imaging of *in vivo* moving tissues. The developed SDOCT removed the need for the reference scanning, enabling faster imaging speeds. Its success in ocular imaging determined the main direction for the future technological development in OCT and in the supporting industry (lasers, detectors, fiber optics, etc.).

Another approach to increase the time-domain OCT speed was developed in our laboratory in 1998 [4], and was called full-field OCT (figure 2.12). The idea was to parallelize the acquisition of all the points in *en face* plane by using a 2D camera instead of a point detector. In this way a full-field 2D image of the sample slice could be retrieved without the lateral scanning by performing the simple algebraic operations on the several camera images (capturing the different interference phases). To be more precise, the most common algorithm for 2D full-field slice retrieval uses the 4 camera images. Interference intensities on one camera pixel (x, y)

captured in 4 shots can be written as:

$$I_1(x, y) = \frac{I_0}{4} \cdot \left\{ R_{inc} + R_{coh-sample} + R_{ref} + 2 \cdot \sqrt{R_{coh-sample} \cdot R_{ref}} \cdot \cos[\varphi(x, y) + \psi_1] \right\}, \quad (2.10)$$

$$I_2(x, y) = \frac{I_0}{4} \cdot \left\{ R_{inc} + R_{coh-sample} + R_{ref} + 2 \cdot \sqrt{R_{coh-sample} \cdot R_{ref}} \cdot \cos[\varphi(x, y) + \psi_2] \right\}, \quad (2.11)$$

$$I_3(x, y) = \frac{I_0}{4} \cdot \left\{ R_{inc} + R_{coh-sample} + R_{ref} + 2 \cdot \sqrt{R_{coh-sample} \cdot R_{ref}} \cdot \cos[\varphi(x, y) + \psi_3] \right\}, \quad (2.12)$$

$$I_4(x, y) = \frac{I_0}{4} \cdot \left\{ R_{inc} + R_{coh-sample} + R_{ref} + 2 \cdot \sqrt{R_{coh-sample} \cdot R_{ref}} \cdot \cos[\varphi(x, y) + \psi_4] \right\}, \quad (2.13)$$

where:

- φ is the phase difference between the sample signal and the reference signal;
- ψ is the phase shift induced by the shift of the reference mirror with a piezo element (PZT);
- I_0 is the intensity of the incident light on the sample and reference mirror;
- R_{ref} is the reflectivity of the reference, which is rather uniform;
- $R_{coh-sample}(x, y)$ is the reflectivity of the sample structures within the coherence volume (volume, which distance from the beam splitter matches the distance between the beam splitter and the reference mirror up to the coherence length);
- R_{inc} denotes the contribution of the non-coherent non-interfering stray light on the camera (for example, coming from the beam splitter or planes of the sample outside of the coherence volume).
- \cos term expresses fringes (modulating with a phase $\varphi(x, y) + \psi$), caused by the interference between the sample and reference arms.

By shifting position of the reference mirror using the piezo element, one can set the precise phases ψ between the 4 images. Selecting the $\psi_1, \psi_2, \psi_3, \psi_4$ to be $0, \pi/2, 3\pi/2, \pi$, we see that:

$$I_1(x, y) - I_3(x, y) = \frac{I_0}{2} \sqrt{R_{coh-sample}(x, y) \cdot R_{ref}(x, y)} \cos[\phi(x, y)] \quad (2.14)$$

$$I_2(x, y) - I_4(x, y) = \frac{I_0}{2} \sqrt{R_{coh-sample}(x, y) \cdot R_{ref}(x, y)} \sin[\phi(x, y)] \quad (2.15)$$

Thus,

$$[I_1(x, y) - I_3(x, y)]^2 + [I_2(x, y) - I_4(x, y)]^2 = const \cdot R_{coh-sample}(x, y) \quad (2.16)$$

As the R_{ref} and I_0 are homogeneous, the result is proportional to the $R_{coh-sample}(x, y)$ that is the amplitude of the backscattering light intensity from one slice in the sample. This leads to a conclusion that an entire full-field image of a tissue slice $R_{coh-sample}(x, y)$, can be obtained using just the 4 camera images. FFOCT removed the need for the lateral beam scanning and only the reference mirror scanning was needed for phase retrieval. $R_{coh-sample}(x, y)$ image is

intuitive: the brighter the spot in the image, the more reflective is the tissue in this spot. One more point to note, that distinguishes FFOCT from other imaging techniques: it uses a camera to capture the intensity of light, however the retrieved function $R_{coh-sample}(x, y)$ is proportional to the amplitude. Therefore, we have an additional opportunity to compute the phase map, which is important in some applications.

- **Lateral resolution** in FFOCT is determined (according to Rayleigh criterion) by the NA of the optics used 2.17. To increase the resolution and reduce the aberration effects, FFOCT inserts the microscope objectives in the sample and reference arms, forming a Linnik configuration of interferometer. The typical NA values range from 0.3 to 0.9, while typical wavelengths are visible or NIR, leading to a resolution ranging from about 1 μm to 0.5 μm .

$$\Delta x = \Delta y = \frac{0.61 \cdot \lambda}{NA} \quad (2.17)$$

- **Depth of focus** is also determined by the NA, like in a SDOCT. In *ex vivo* sample imaging through the immersion liquid, DOF does not play an important role, because the axial sectioning is much finer than the DOF. However, in the next chapters we will see that it is very important, when imaging is happening in a non-contact way through the air. For the gaussian beam:

$$DOF = \frac{\pi \cdot \Delta x^2 \cdot n}{\lambda} = \frac{1.2 \cdot \lambda \cdot n}{NA^2} \quad (2.18)$$

- **Axial resolution**, like in SDOCT, is inversely dependent on the bandwidth of the light source. This is intuitive, because the broader the light source spectrum, the lower its temporal coherence and the thinner is the sample slice that interferes with the reference mirror. Typically, FFOCT uses the broadband halogen lamp or light-emitting diode (LED) sources. In fact both exhibit not only the temporal incoherence, but also the spatial incoherence. This is intentional: it is a way to avoid a potential speckle noise originating from the interference of light beams approaching the adjacent pixels on the camera.

$$\Delta z = \frac{2 \ln 2}{\pi \cdot n} \cdot \frac{\lambda^2}{\Delta \lambda} \quad (2.19)$$

- **Field of view** can vary depending on the chosen combination of the microscope objective and tube lens. The maximal achievable FOV is limited to the one specified in the objective specification, for which the field is still flat and aberrations do not disturb the image. Typically, it is close to the field number divided by the magnification. One more thing to consider is the number of pixels on a camera. According to the Nyquist theorem, the optimal performance in terms of resolution happens, when the image size on the 2 pixels equals to the resolution of the optical system.

- **Imaging depth** of FFOCT is largely determined by the sample. The larger the absorption and scattering of light in the sample (however, not like the scattering in corneal stroma), the smaller number of ballistic photons will reach the detector and the shorter is the penetration depth. Imaging depth of FFOCT is close to that of SDOCT and larger than that of the confocal microscope. Recently, the new methods based on Dark-field FFOCT [88] and Smart-FFOCT [89] have shown further improved imaging depth by filtering the multi-diffusion photons with either physical or numerical ways.
- **Sensitivity** is defined as the smallest signal that can be detected with FFOCT (for which signal-to-noise ration (SNR) = 1) and can be written as [90]:

$$R_{\min} \sim \left(\frac{\xi_{sat} + \chi^2}{N\xi_{sat}^2} \right) \cdot \frac{(R_{ref} + R_{inc})^2}{R_{ref}}, \quad (2.20)$$

where:

- R_{min} is the minimum detectable reflectivity at $SNR = 1$;
- R_{ref} is the reflectivity of the reference mirror;
- R_{inc} is the reflectivity, corresponding to the contribution of incoherent light;
- ξ is the full well capacity (FWC) of the camera;
- χ is the electrical noise of the camera;
- N is the number of interferometric images;

We will explore this formula in more detail in the next chapter, when FFOCT will be adapted for *in vivo* operation.

FFOCT applications

Before the beginning of this thesis, FFOCT was limited to *ex vivo* applications. Its high lateral resolution and high sensitivity to the sub-cellular motion were found to be useful for detecting cancer cells in human breast, prostate, brain, liver and bladder tissues [90]. The company emerged, creating a possibility of instantaneous biopsy analysis during an on-going surgery, avoiding the long histology waiting times [91].

In application to ocular surface tissues, FFOCT was used to image the *ex vivo* cornea and determine its suitability for a potential transplantation [92]. The instrument had $800 \mu\text{m} \times 800 \mu\text{m}$ FOV, $1 \mu\text{m}$ lateral and $1 \mu\text{m}$ axial resolutions. It revealed the superficial, wing and basal epithelial cells, basement membrane and Bowman's layer, stroma and endothelium.

Interestingly, there was one attempt of imaging anterior eye of *in vivo* rat [95]. System was able to penetrate further than 1 mm in depth through the cornea and anterior lens. Lateral and axial resolution were again about $1 \mu\text{m}$ and FOV - $300 \mu\text{m}$. It was possible to notice several anterior eye layers, including the epithelium, stroma, endothelium, outer and inner crystalline lens capsule, however the resolution and signal quality were insufficient to resolve the small

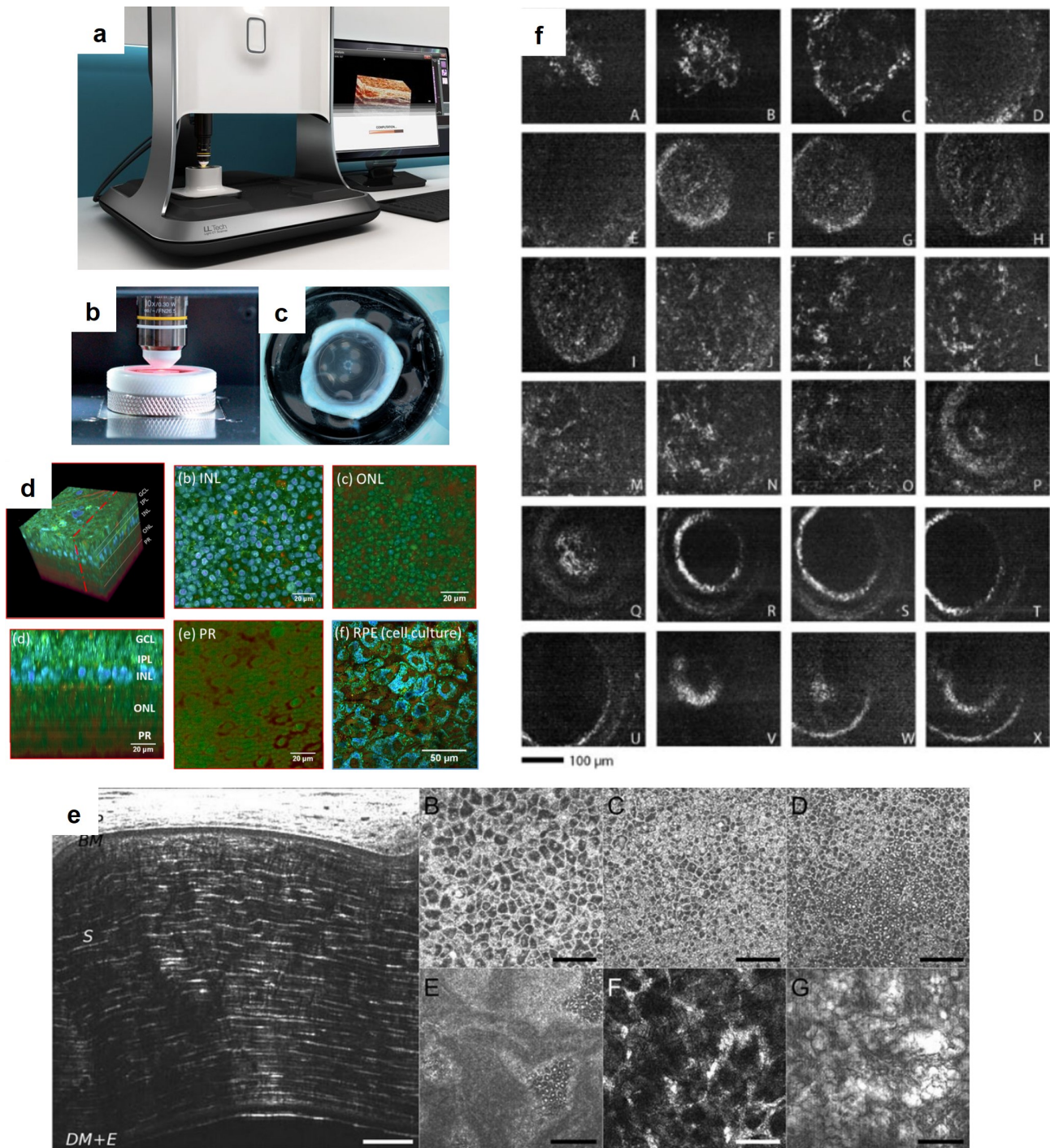


Figure 2.13 – Contact (through immersion liquid) FFOCT imaging of tissues. (a) Rendering of a commercial system for *ex vivo* histology. (b,c) Close view on the sample holder and the sample. (d) Image of *ex vivo* retina from [93]. FOV = 120 μm. Coloring corresponds to different velocities of intracellular movements. Contrast agents of fluorescence were not required. For a simple explanation, see [94]. (e) FFOCT images from *ex vivo* human donor cornea from [92]. Bars = 70 mm in A, 100 mm in B. (d) Images from the anterior eye of *in vivo* rat [95].

cells in the rat eye. The immersion liquid was used between the objective and the eye to suppress the bright stray light reflection from the surface of the cornea. In addition the rat was anaesthetised, which completely suppressed the lateral eye movements, while only the small axial movements, attributed to animal respiration, were left. In order to increase the SNR, 10

images were averaged, resulting in a 40 ms acquisition time per-image.

Now, we arrive to the beginning of my thesis journey, which started with a goal of making FFOCT imaging system for *in vivo* human cornea. This goal was ambitious enough to be the only one, but following the initial success, many more things were achieved. Beyond the demonstrated FFOCT imaging of the *in vivo* human cornea (with cell-resolution and without the physical contact) [3], we achieved the limbal and tear film imaging. We created the first FFOCT angiographic maps of blood flow in the anterior eye. Together with Peng Xiao and co-authors we demonstrated the first images of the human retina, captured with *in vivo* FFOCT [83]. Later, the improved FFOCT showed real-time performance, opening it for use in clinical ophthalmology. These and many more things will be discussed in the following chapters of the thesis.

Part II

Full-field Optical Coherence Tomography in application to *in vivo* human eye imaging

From *ex vivo* to *in vivo* full-field OCT

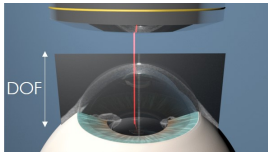
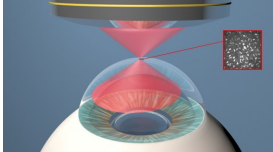
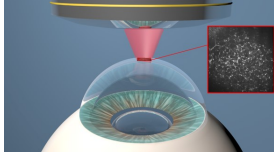
Table of contents

3.1	Motivation for FFOCT in ocular surface imaging	54
3.2	From contact <i>ex vivo</i> to non-contact <i>in vivo</i> FFOCT	55
3.2.1	Improving sensitivity in non-contact FFOCT	55
3.2.2	FFOCT image reconstruction	57
3.2.3	Performance characteristics	58
3.2.4	FFOCT motorized aligning	59
3.2.5	Problem of defocus and its correction	59
3.2.6	First test of non-contact FFOCT (<i>ex vivo</i> cornea)	61
3.2.7	First <i>in vivo</i> human corneal imaging with FFOCT	62

3.1 Motivation for FFOCT in ocular surface imaging

The previous chapters highlighted the importance of high resolution imaging in disease diagnosis. Only two types of instruments, *in vivo* confocal microscopy (IVCM) and some recent modifications of SDOCT, are capable of providing the true cellular resolution through the entire corneal thickness. However, both of them have their drawbacks, which limit the range of clinical conditions, that they can address. *In vivo* FFOCT is a new type of instrument, which in a certain way combines the advantages of SDOCT and IVCM. This becomes apparent by analysing the comparison table 3.1 of these technologies.

Table 3.1 – Comparison of SDOCT, CM and FFOCT

			
	SDOCT SSOCT	CM	FFOCT
View	<i>cross-section</i>	<i>en face</i>	
Depth of focus	$\sim \frac{\lambda}{NA^2}$		
Field of view	inversely connected with NA		
Lateral resolution	$\sim \frac{\lambda}{NA}$		
Axial resolution	$\sim \frac{\lambda^2}{\Delta\lambda}$	$\sim \frac{\lambda}{NA^2}$	$\sim \frac{\lambda^2}{\Delta\lambda}$

SDOCT typically relies on the low-NA objectives for achieving a large DOF and a broad vertical FOV. At the same time low-NA leads to a reduced lateral resolution. Nevertheless, given the fact that SDOCT acquires images in a *cross-sectional* plane, it is very natural that it prioritizes the increase in FOV in this plane over the increase in resolution in the orthogonal plane. Several ultrahigh-resolution SDOCT instruments used the moderate NA (~ 0.3) objectives to acquire the high-resolution 3D images. However, the lateral view was disturbed by the

movements artifacts, because the time required to get an *en face* slice is as long as to get the whole the volume. The potential future increase in the scanning speed will reduce the effect of the artifacts in the field of view (FOV), however the maximal undisturbed FOV will likely be limited. To be more precise, if we were to increase the FOV from the current $250 \mu\text{m} \times 250 \mu\text{m}$ to $1 \text{ mm} \times 1 \text{ mm}$ (area increases by 16 times), we would need to make the lateral scanning 16 times faster - 4 million A-lines/s (and at this speed the lateral scanning artefacts would be still present). Nevertheless, regarding the *cross-sectional* view with isotropic cell resolution - it is undoubtedly of interest.

***In vivo* confocal microscopy (IVCM)**, as an *en face* method does not need a large DOF. Instead it uses a very high-NA (~ 0.95) objective to get the high lateral and axial resolutions. Interestingly, this very high NA is much more forced by the axial resolution, than the lateral one. Suppose, that we are interested to get a $1 \mu\text{m}$ isotropic resolution for IVCM equipped with a 800 nm laser. According to the equations 2.3 and 2.4, $1 \mu\text{m}$ lateral resolution will require a moderate 0.3 NA, while the $1 \mu\text{m}$ axial resolution will need a much higher 0.9 NA. Unfortunately, the so high NA is typically found in the water-immersion objectives, working in contact with a sample. Moreover, even, if a specific non-contact high NA objective is used, the working distance to the sample will be very short, plus the strong specular reflection from the surface will prohibit viewing of the anterior cornea.

FFOCT combines both approaches. Like IVCM it is an *en face* method and does not require large DOF. Also, FFOCT uses moderate NA to get a μm -level lateral resolution. However, contrary to IVCM it does not need a very high-NA objectives to get a high axial resolution, because the axial resolution in FFOCT is decoupled from the NA and depends on the bandwidth of the light source, like in OCT. Therefore, FFOCT can be non-contact using just the moderate NA objectives, have a relatively large field of view and at the same time the lateral and axial resolutions of order of a μm . As a bonus, all the pixels are acquired simultaneously on the camera, removing a possibility for lateral motion artifacts in the images.

3.2 From contact *ex vivo* to non-contact *in vivo* FFOCT

Transformation of the FFOCT device from the contact *ex vivo* to the non-contact *in vivo*, became possible thanks to the very careful selection of every FFOCT component with a strong focus on sensitivity and with respect to the ocular safety norms. Figure (B.10) lightlights the changes between the *ex vivo* and *in vivo* devices. Below, we will implement these and other changes step by step.

3.2.1 Improving sensitivity in non-contact FFOCT

We started with a configuration (a) in figure (B.10). In order to take advantages of FFOCT design over IVCM, we substituted the contact water-immersion objectives with the non-contact ones, having a similar moderate 0.3 NA. Another criteria for the objective selection was the long working distance (18 mm), which removed the risk of accidental contact with an eye.

Unfortunately, without the immersion liquid and, due to the lack of a confocal gating in FFOCT, the bright specular reflection from the surface of the eye was reaching the camera,

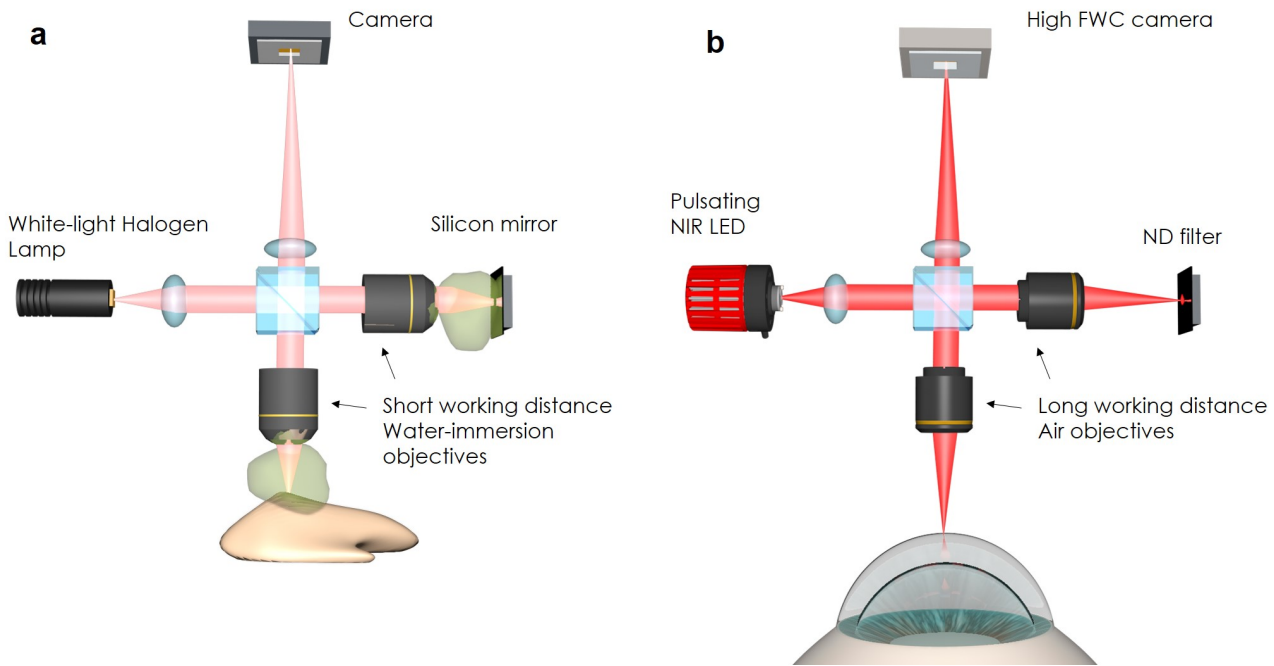


Figure 3.1 – Transformation of FFOCT from *ex vivo* to *in vivo* (a) *Ex vivo* device. (b) *In vivo* device.

greatly reducing the proportion of the useful detected light and fading the signal. In order to get the images we needed to increase the sensitivity. FFOCT sensitivity equation 2.20 from the previous chapter, tells that one way to achieve this is by increasing a full-well capacity (FWC) of the camera ξ . Thus, we substituted the 200Ke^- FWC camera (Photon focus, Germany) by the CMOS camera (model Q-2A750-CXP, Adimec, Netherlands) with the FWC of 2Me^- - maximal available on the market.

Further increase in sensitivity can be achieved by using a reference mirror with a reflectivity similar to the total reflectivity of incoherent light in the optical system $R_{ref} = R_{inc}$ (one can come to this equation by simply taking the derivative of 2.20 with respect to R_{ref}). Most of the incoherent light originates from the specular reflection from the corneal surface, which we previously calculated to contribute about 2% reflectivity. Therefore, we substituted the silicon reference mirror (30% reflectivity) by the glass (4% reflectivity). In order to eliminate the ghost reflections from the back surface of the glass plate, we used not a usual glass, but an absorptive neutral density (ND) filter.

All of the above methods (increase in the FWC, the reduced reference reflectivity) were reducing the saturation of the camera, however saturation is the central factor to sensitivity. To increase the amount of light on the camera, we increased the light exposure by using a powerful 850 nm light-emitting diode (LED) (model M850LP1, Thorlabs, USA) with a small chip area, able to concentrate the light on a millimeter FOV. However, the light power should always be below the level set by the up-to-date ocular safety standards: ANSI Z80.36-2016 authorized in North America and ISO 15004-2:2007 in Europe. The complete and detailed analysis of the light safety can be found in the Appendix A, while here I will limit my writing to a brief safety standards overview and the results. One can notice, that ISO and ANSI standards differ in the limits that they set for exposure at 850 nm. While ANSI claims that the strict corneal safety limit of 60 mW/cm^2 (or 100 mW/cm^2 for Group 2 instruments) is not applicable for exposures with wavelengths below 915 nm, and only the anterior eye limit of

$4 W/cm^2$ (or $20 W/cm^2$ for Group 2 instruments) should be considered. ISO, on the contrary, claims that both limits should be applicable. Our camera is saturated at the corneal irradiance of about $2.6 W/cm^2$. According to ANSI this exposure is below the Group 1 limits and the constant exposure is allowed. However, ISO does not allow the constant exposure and only the pulsed is considered to be safe. In order to satisfy both eye safety standards we made the exposure pulsed with the pulse duration of 34 ms and pause between them of 1000 ms, reducing the average exposure below the maximum permissible level. A detailed analysis of pulsed light safety in addition to the average light safety is provided in the Appendix A.

$$E_{\text{corneal exposure}} = \sum_{380}^{1200} E_{\lambda} \times \Delta\lambda = 2.6 W/cm^2 < 4 W/cm^2 = MPE(ANSI)$$

$$E_{\text{average corneal exposure}} = \left\langle \sum_{770}^{2500} E_{\lambda} \times \Delta\lambda \right\rangle = 86 mW/cm^2 < 100 mW/cm^2 = MPE(ISO),$$

where MPE is maximum permissible exposure of the standard.

Pulsating the LED with the current state of technology is easy (LEDs can produce pulses as short as tens of nanoseconds). Using Labview we made a synchronization between the LED pulsation and the camera exposure, and displayed the images in real-time at 9 frames/s rate. The above was applicable to the corneal safety, but the retinal safety limits also should be considered. However, the retinal safety limits are easily satisfied, because the focused light incident on the cornea becomes rapidly divergent on the retina, due to the moderate NA. The NIR 850 nm wavelength of exposure was selected, because this is one of the most commonly used wavelengths in clinics. NIR is comfortably viewed by subjects, due to the low sensitivity of the retina to NIR light, and poses no danger associated with photochemical damage.

$$E_{\text{retinal exposure}} = \sum_{380}^{1400} E_{\lambda} \times R(\lambda) \times \Delta\lambda = 49 mW/cm^2 < 700 mW/cm^2 = MPE(ISO, ANSI)$$

To conclude, we substituted the contact objectives by the non-contact ones, regained back (to some extent) the sensitivity by changing the camera and reference mirror, were able to saturate the camera by using the powerful LED, while still staying within the eye safety limits thanks to the pulsed exposure.

3.2.2 FFOCT image reconstruction

Another point that was not discussed before is the acquisition speed, which is very important for imaging of moving *in vivo* tissues. Speed is of a particular importance to FFOCT, because not one, but several images with different phases need to be acquired before the movements will destroy the phase correlation. Luckily, our high-FWC camera permits fast image acquisition. By improving the processing in the Labview interface, we achieved the speed of 550 frames/s at 1.7 ms single frame exposure time, synchronized with piezo-element (PZT) modulation in the reference arm. Previously, we have shown that a single FFOCT image can be reconstructed from the 4 conventional camera images. Now, dealing with a problem of eye movements, we considered the total acquisition time of $4 \times 1.7 \approx 7$ ms to be too long to suppress the motion

influence on the image retrieval. Therefore, we switched to the fastest FFOCT retrieval scheme, which requires just 2 images (or 3.4 ms):

$$I_1(x, y) = \frac{I_0}{4} \cdot \left\{ R_{inc} + R_{coh-sample} + R_{ref} + 2 \cdot \sqrt{R_{coh-sample} \cdot R_{ref}} \cdot \cos[\varphi(x, y) + \psi_1] \right\}, \quad (3.1)$$

$$I_2(x, y) = \frac{I_0}{4} \cdot \left\{ R_{inc} + R_{coh-sample} + R_{ref} + 2 \cdot \sqrt{R_{coh-sample} \cdot R_{ref}} \cdot \cos[\varphi(x, y) + \psi_2] \right\}, \quad (3.2)$$

By shifting position of the reference mirror using the piezo element (PZT), we set the phases ψ_1 and ψ_2 equal to 0 and π . Then:

$$I_1(x, y) - I_2(x, y) = \frac{I_0}{2} \sqrt{R_{coh-sample}(x, y) \cdot R_{ref}(x, y)} \cos[\phi(x, y)] \quad (3.3)$$

And,

$$[I_1(x, y) - I_2(x, y)]^2 = const \cdot R_{coh-sample}(x, y) \cdot \cos^2[\phi(x, y)] \quad (3.4)$$

Here we used that I_0 and R_{ref} are homogeneous. By comparing the above equation 3.4 with the one from the 4 phase scheme 2.16, it is apparent that an additional *cos* term exists in the 2-phase scheme. This term denotes the fringe artifacts that are present in the images - main drawback of the fast 2-phase scheme (figure 3.2). As will see later, sometimes these artifacts can be partly suppressed in post-processing.

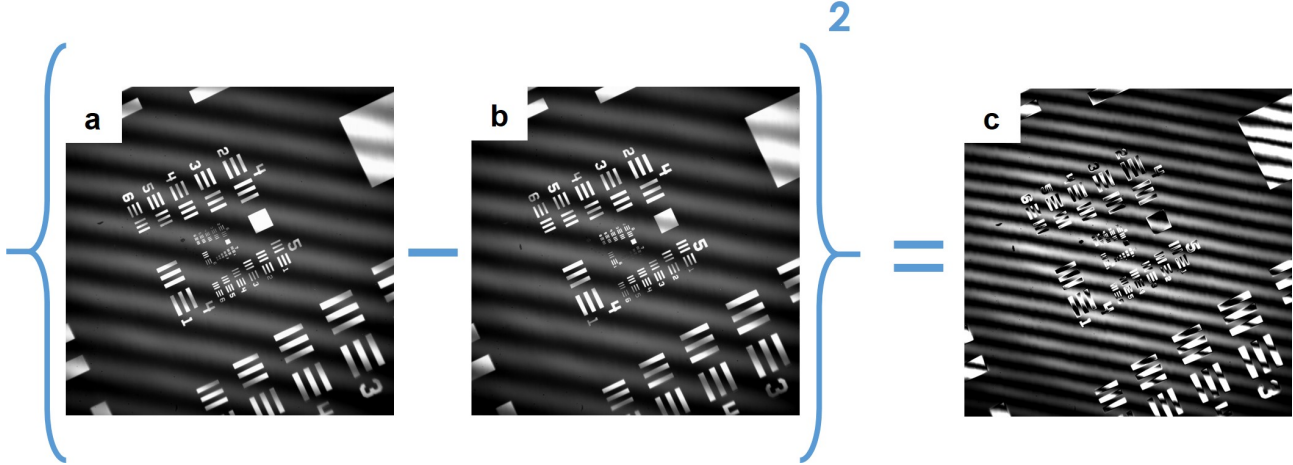


Figure 3.2 – Retrieval of FFOCT image in a 2-phase scheme. (a) Conventional camera image of resolution target. Interference fringes with phase $\psi_1 = 0$ are clearly seen. (b) Conventional camera image of resolution target. Interference fringes are shifted due to the phase shift $\psi_2 = \pi$. (c) Resulting FFOCT image. Fringe modulation is not suppressed.

3.2.3 Performance characteristics

According to Rayleigh criterion, lateral resolution with 0.3 NA objectives is:

$$\Delta x = \Delta y = \frac{0.61 \cdot \lambda}{NA} = \frac{0.61 \cdot 850nm}{0.3} \approx 1.7\mu m \quad (3.5)$$

The lateral resolution of $1.7 \mu\text{m}$ was experimentally confirmed by measuring the visible diameters (FWHM) of the 80 nm gold nanoparticles.

From the full-width-half maximum (FWHM) bandwidth of the light source (30 nm) we can estimate the axial resolution:

$$\Delta z = \frac{2 \ln 2}{\pi \cdot n} \cdot \frac{\lambda^2}{\Delta \lambda} = \frac{2 \ln 2}{\pi \cdot 1.376} \cdot \frac{(850\text{nm})^2}{30\text{nm}} \approx 7.7\mu\text{m} \quad (3.6)$$

FOV was selected to be $1.26 \text{ mm} \times 1.26 \text{ mm}$, because this is the maximal field size, which provides pixel sampling according to Nyquist criterion without a decrease in resolution.

In order to increase the SNR, several images from the same layer were recorded, registered with ImageJ [96, 97] to remove misalignment, resulting from the lateral eye movements, and averaged. This process performed on 10 images allowed to increase the SNR to 74 dB, compared to the 60 dB SNR for a single image. Experimentally, the SNR was estimated as the ratio of the average squared signal A and the noise variance σ^2 in the image: $SNR(\text{dB}) = 10 \cdot \log_{10} [\langle A^2 \rangle / \sigma^2]$. Whereas the camera in FFOCT measures intensity, the FFOCT processing (image subtraction and square) results in images of amplitude. When calculating SNR for amplitude measures, they must be squared, which leads to the SNR being proportional to the number of accumulations N . Therefore, averaging of $N = 10$ images is expected to yield the SNR increase in dB of $10 \cdot \log_{10} N = 10 \text{ dB}$, a value close to the experimentally determined increase of 14 dB. The images shown below typically represent the result after 10 frames averaging.

3.2.4 FFOCT motorized aligning

Our eyes (and the head generally) are constantly moving. To enable possibility to follow roughly the changing position of the cornea, FFOCT is horizontally mounted on the two orthogonal motorized translation stages moving in X and Z directions (figure 3.3). Stages are controlled using a joystick. Translation along the Z axis nearer and farther from the eye allows to focus at different layers of the cornea, while translation along the X axis helps to find an optimal imaging position near the corneal apex.

3.2.5 Problem of defocus and its correction

Unfortunately, the overexposure to stray light is not the only problem that appeared, when we switched from the water-immersion to the air objective. Another obstacle is the mismatch between the position of the objective focus (where light is concentrated in the sample) and the position of the coherence plane (plane inside the sample, which coherently matches with the reference mirror). This effect is called defocus and results in a rapid loss of the signal with the increasing imaging depth (figure 3.4). Two factors are causing the mismatch: 1) the spreading of the focal point into the sample due to Snell's law, originating from the large illumination angle and difference between the refractive indexes of the cornea (1.376) and air (1.0), 2) the shift of the coherence plane in the opposite direction closer to the objectives, also caused by the refractive index difference. To be more precise, in the cornea focus is spread by:

$$z_f = z_0 \cdot n, \quad (3.7)$$

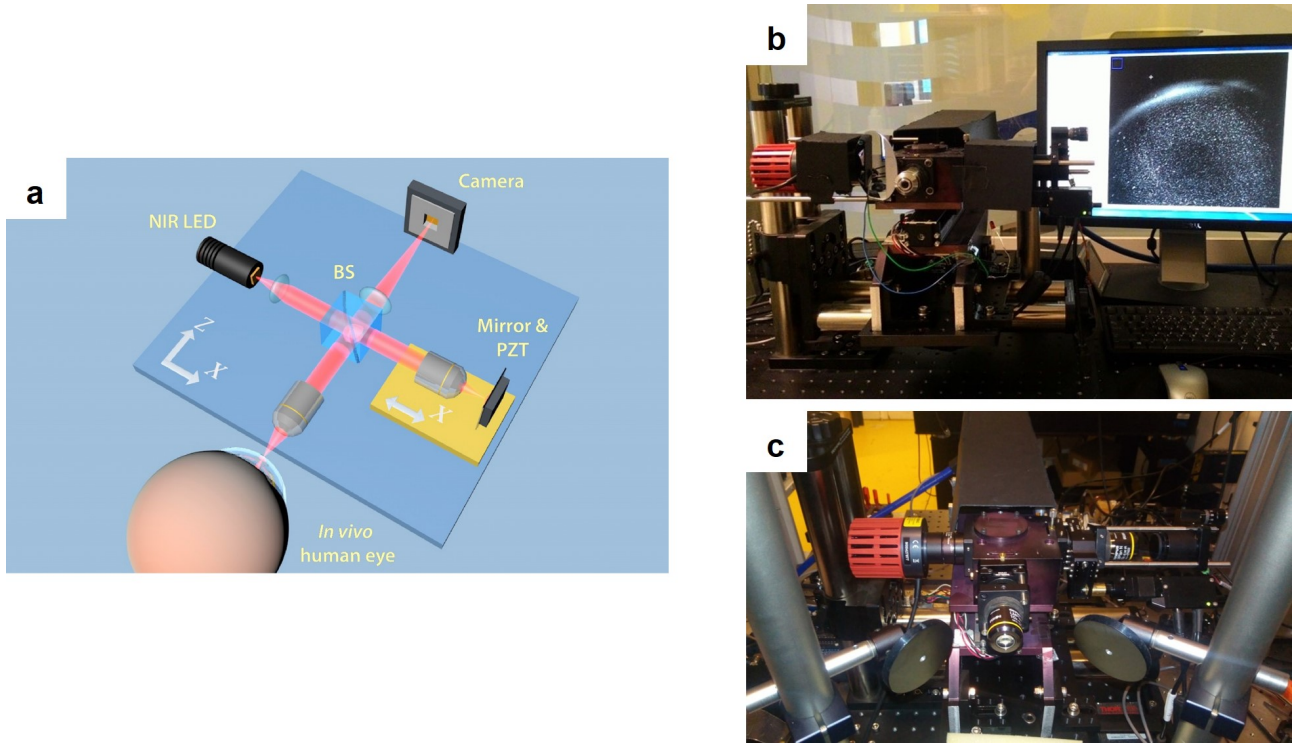


Figure 3.3 – First prototype of a non-contact *in vivo* FFOCT. (a) Schematic illustration of the FFOCT setup. Illumination: NIR LED; BS: beam splitter; PZT: piezoelectric stage actuator. (b,c) Photos of the instrument (underlying translational stages are removed).

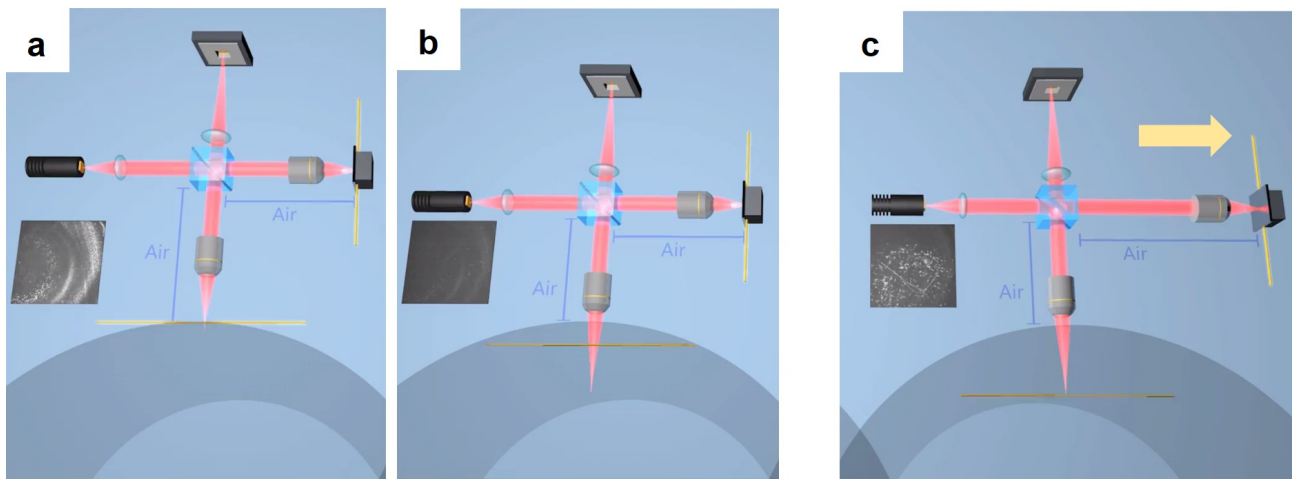


Figure 3.4 – Problem of defocus in FFOCT. (a) Case, when the objective focuses on the surface of the sample. In this case point of focus (red tip) matches with coherence plane (yellow line). (b) Defocus and signal loss, happens with the increasing depth. Snell's law changes the angle of illumination, leading to a deeper focusing. At the same time, the coherence plane goes up, because air in the sample arm is gradually replaced by the cornea with a higher refractive index. (c) By extending the reference arm, the coherence plane can be spread inside the sample to match with a new position of the focus. Signal is recovered.

where z_f is the new position of the focus, z_0 - position of the focus, if there was no cornea, n - corneal refractive index.

While the coherence plane is shifted back:

$$z_{coh} = \frac{z_0}{n}, \quad (3.8)$$

where z_{coh} is the new position of the focus, z_0 - position of the coherence plane, if there was no cornea (in this case it matches with position of the focus), n - corneal refractive index.

Difference between the two locations:

$$z_f - z_{coh} = z_0 \cdot \left(\frac{n^2 - 1}{n} \right) \quad (3.9)$$

Our laboratory has developed a method to compensate for the defocus and to restore the signal by extending the reference arm [98]. More precisely, using 3.9 one can calculate the distance, by which the reference arm should be extended in order to match the coherence plane with a new focus position to allow imaging at a given depth in the cornea (figure 3.4). For example, to image the endothelial cell layer, located $540 \mu\text{m}$ inside a subject's cornea, the reference arm is extended by approximately $350 \mu\text{m}$, and the entire device is moved to have the endothelial layer in the focus. The mentioned approach is easy to implement for imaging static samples, however imaging living eyes, which are constantly moving in a rapid way, due to involuntary movements, requires a real-time, precise and fast reference arm adjustment, which is very challenging. To facilitate the acquisition of the images, the following paradigm was applied. Before starting the image acquisition, we select the corneal layer of interest and extend the reference arm to compensate for the separation between the coherence plane and the focus associated with this layer. Then we start image acquisition (piezo modulation and camera) and view in real time the captured *en face* images. Initially, as the layer of interest is out of the focus, only noise is visible in the images. However, by moving the entire microscope with a motorized translation stage along the Z axis, and keeping the cornea approximately in the objective focus, there is a chance that at some moment microscope will the focus on the selected corneal layer. When it happens, the coherence plane matches with focus plane and the optical path of the sample arm matches with the optical path of the reference arm. As a result a tomography image of the layer appears on display and is manually saved.

From the above follows, that at this stage, we can not perform the real-time imaging. However, in the next chapter a new combined FF/SD OCT will be introduced, which can track the axial position of the eye and acquire images in real-time.

3.2.6 First test of non-contact FFOCT (*ex vivo* cornea)

At first, we tested the device on an *ex vivo* monkey cornea (figure 3.5). FFOCT could penetrate through the entire cornea, revealing the superficial, wing/basal epithelium, Bowman's layer, anterior, middle and posterior stroma, Descemet's membrane and the last endothelial corneal layer. Each image was obtained by averaging about 8 images, leading to $1.7 \text{ ms} \times 8 = 13.6 \text{ ms}$ per image.

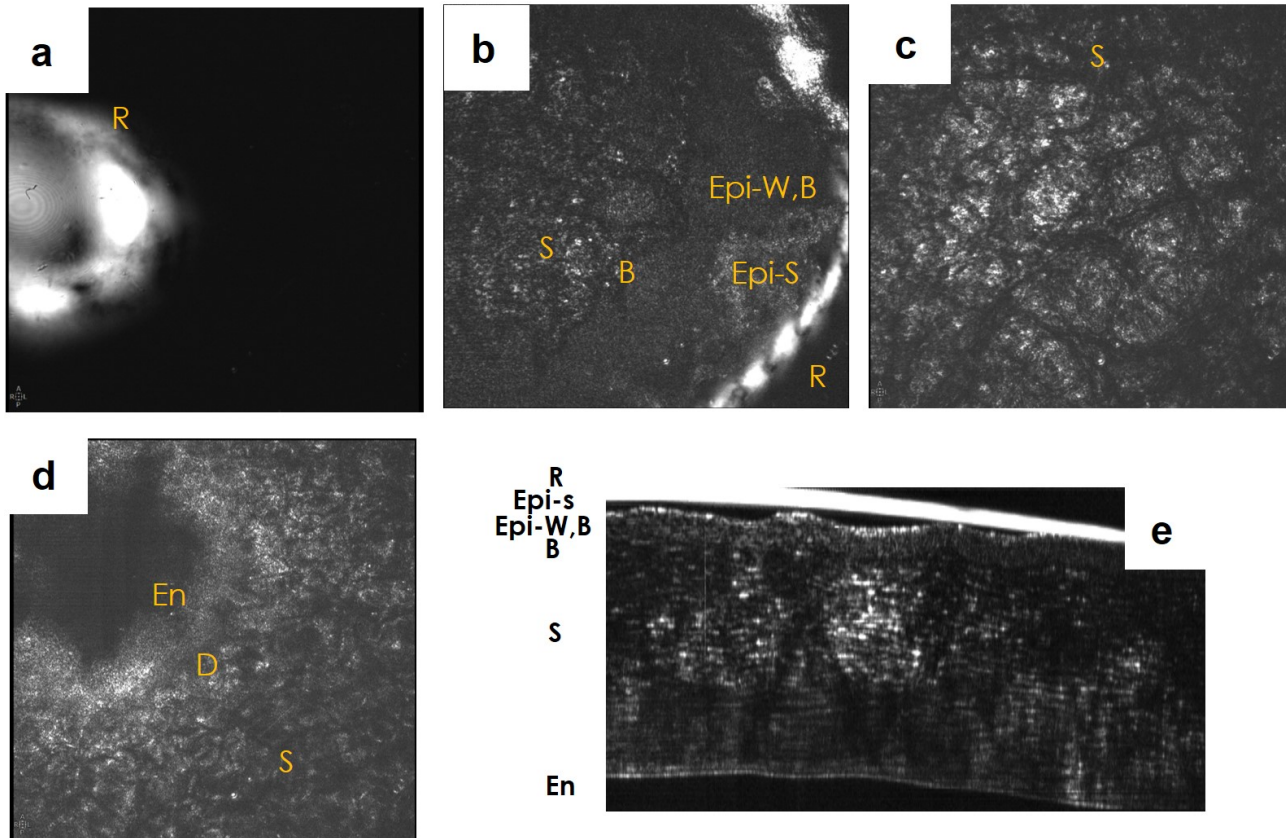


Figure 3.5 – First *ex vivo* images captured with a non-contact FFOCT (a-d) *En face* FFOCT images from the monkey cornea. R - reflection from the air-cornea interface. Epi-S - superficial epithelium, Epi-W,B - wing/basal epithelium. B - thin dark band, corresponding to the Bowman's layer. S - stroma, D - thin dark band, corresponding to the Descemet's membrane, En - endothelium. (e) The cross-sectional slice, reconstructed from the FFOCT images. The corneal and epithelial thicknesses could be easily measured. FOV = 1.26 mm. FFOCT images were averaged about 8 times.

3.2.7 First *in vivo* human corneal imaging with FFOCT

The study was carried out on a 27-year-old male subject with a healthy cornea, which was confirmed by an eye examination preceding the experiment. Informed consent was obtained from the subject and the experimental procedures adhered to the tenets of the Declaration of Helsinki. During the experiment, the subject rested his chin and temples on a custom-built headrest, while looking at a fixation target within the device. The FFOCT examination was non-contact and did not involve introduction of any medication.

For comparison purposes, corneal images from the same subject were also obtained with a contact IVCN (HRT II with Rostock cornea module; Heidelberg Engineering, GmbH), equipped with a 0.9 NA microscope objective. Device provided $300\ \mu\text{m} \times 300\ \mu\text{m}$ field-of-view images. Prior to examination, one drop of a topical anaesthetic, oxybuprocaine and one drop of a gel tear substitute, carbomer 0.3% (Gel-larmes, carbomer-974 P; Théa, Switzerland), with a refraction index similar to that of the cornea, were instilled in the eye.

Figure 3.6 shows *in vivo* images of the anterior part of the human cornea, obtained with FFOCT and IVCN.

The SNP with hyper-reflective branching nerves was visible with FFOCT. Nerve thickness

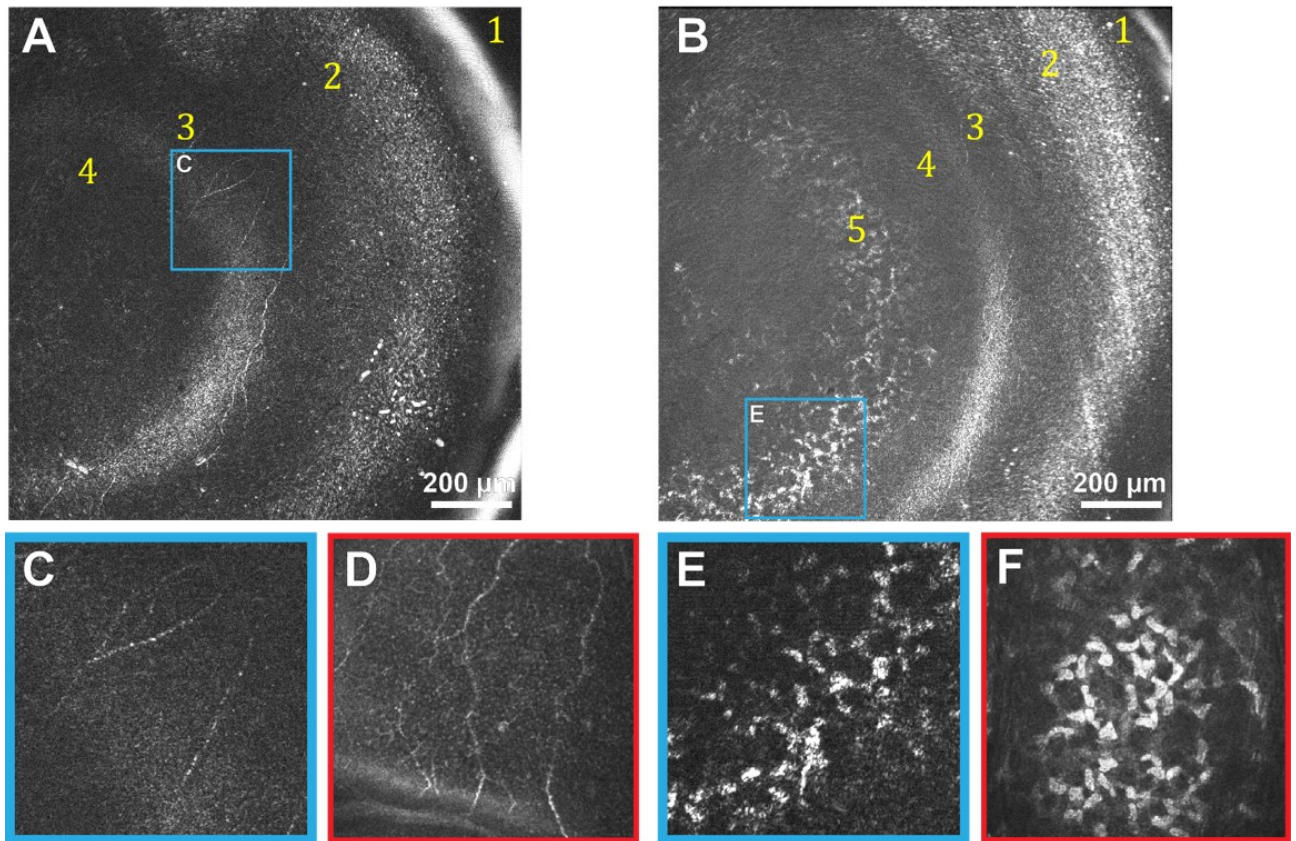


Figure 3.6 – *In vivo* anterior human cornea images, obtained with FFOCT and IVCM [3]. Due to the curvature of the human eye and relatively large field-of-view of FFOCT, imaging planes often cut through several layers, giving an annular shape to them. (A,B): FFOCT images of anterior cornea at different depths. 1 – strong reflection on air-tear film interface, 2 – epithelium, 3 – SNP with nerves clearly seen, 4 – Bowman’s layer, 5 – anterior stroma. Bright band between SNP and Bowman’s layer corresponds to their interface. (C,E): zoomed areas ($300\ \mu\text{m} \times 300\ \mu\text{m}$) of images A and B, corresponding to SNP and stromal keratocyte nuclei. (D,F): confocal microscopy images ($300\ \mu\text{m} \times 300\ \mu\text{m}$) of SNP and anterior stroma. FFOCT images were averaged up to 10 times.

was $3 - 8\ \mu\text{m}$, in agreement with the IVCM data. The length of the visible part of the longest individual nerve was $700\ \mu\text{m}$. The epithelium was visible, however resolving individual cells and distinguishing between superficial, wing, and basal epithelial layers was not possible due to obscuring of the sub-surface signal by a strong surface reflection. Bowman’s layer was seen as a dark layer separating anterior stroma and SNP. The interface of SNP and Bowman’s layer was hyperreflective. In the anterior stroma, the dense population of egg-shaped hyperreflective keratocyte nuclei of approximately $15\ \mu\text{m}$ in diameter was visible. IVCM showed the same structures.

Figure 3.7 depicts mid and posterior stroma of the *in vivo* human cornea. A stromal nerve node connecting four nerves was visible. Thickness of the node was measured to be $80\ \mu\text{m}$, while thicknesses of individual stromal nerves were around $10\ \mu\text{m}$, in agreement with IVCM. Populations of keratocytes were seen in both mid and posterior stroma.

Figure B.13 shows images of posterior stroma and endothelial corneal layers *in vivo*, obtained

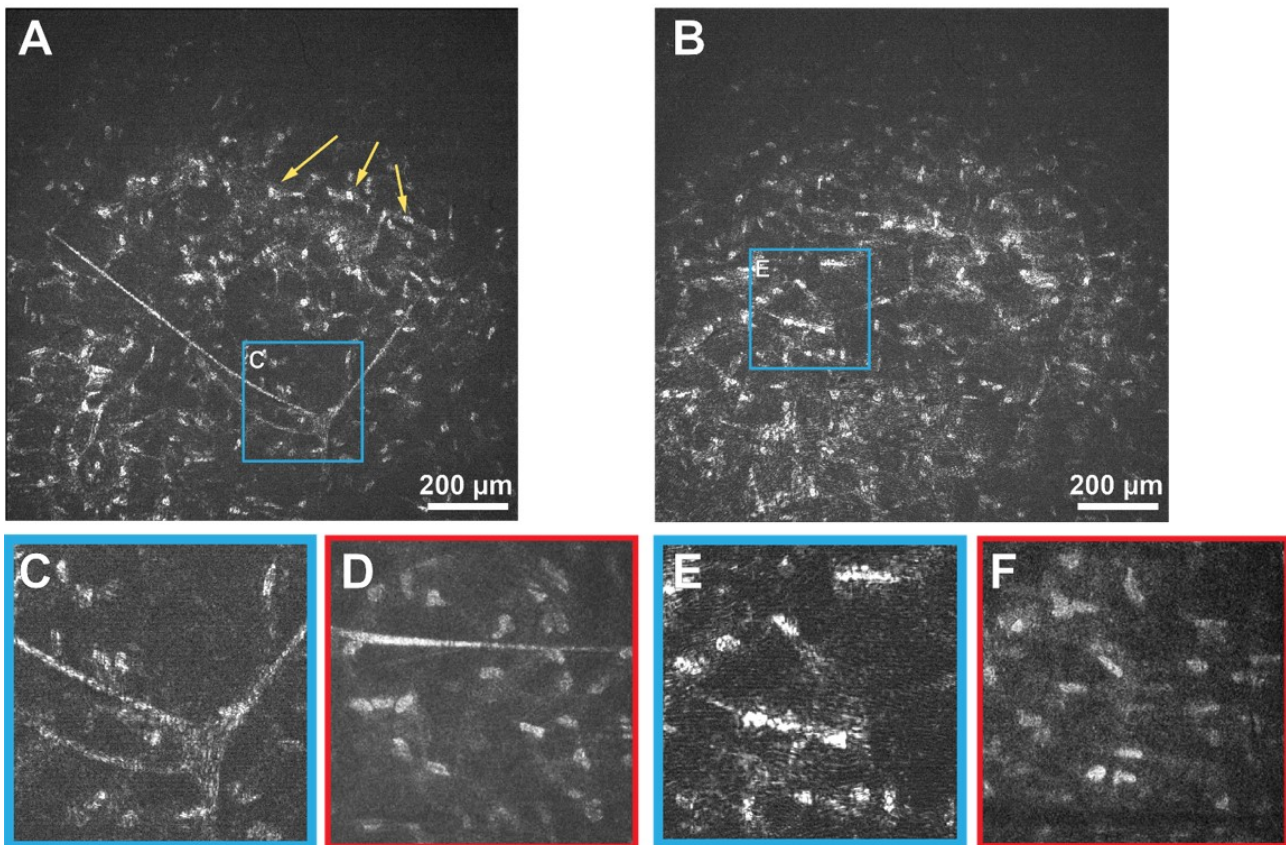


Figure 3.7 – *In vivo* human corneal images of mid and posterior stroma, obtained with FFOCT and IVCM [3]. (A,B) FFOCT images from mid and posterior stromal layers, respectively. Yellow arrows point at a large network of stromal keratocytes. (C,E) zoomed areas ($300\ \mu\text{m} \times 300\ \mu\text{m}$) of A and B, corresponding to the branching stromal nerve and dense population of stromal keratocyte nuclei, with their surrounding cytoplasm. (D,F) confocal microscopy images ($300\ \mu\text{m} \times 300\ \mu\text{m}$) of stromal nerve and keratocyte network. FFOCT images were averaged up to 10 times.

with FFOCT and IVCM. Figure A reveals the keratocytes and, rarely, fiber-like structures, which correspond to nerves or elongated keratocyte cell cytoplasm. Details of the Descemet's membrane could not be seen, neither with FFOCT nor with IVCM, due to its low reflectivity in healthy corneas. The endothelium was seen as a hyper-reflective layer. Zoomed images B and C contain endothelial cells, however viewing was obscured by the interference fringe artifacts. As we have shown before, fringes originate from the 2-phase shifting scheme and are present in all the images. However, in the endothelium and tear film they are the most prominent, visible as concentric rings, due to the mirror-like reflection from these layers. To be more precise, ring fringe shape is the result of mixing a plane wave from the reference arm with the spherical waves from the curved cornea. In the Fourier domain, fringes are visible as a ring. Such rings can be closed or unclosed, depending, if the corneal apex falls within or out of the image. Filtering is done by masking the ring (or ring parts), associated with the fringes. As a result, the hexagonal regular mosaic of endothelial cells, approximately $20\ \mu\text{m}$ in diameter, gets revealed. Additionally, endothelial nuclei $4 - 7\ \mu\text{m}$ in diameter were seen. These findings were in agreement with IVCM.

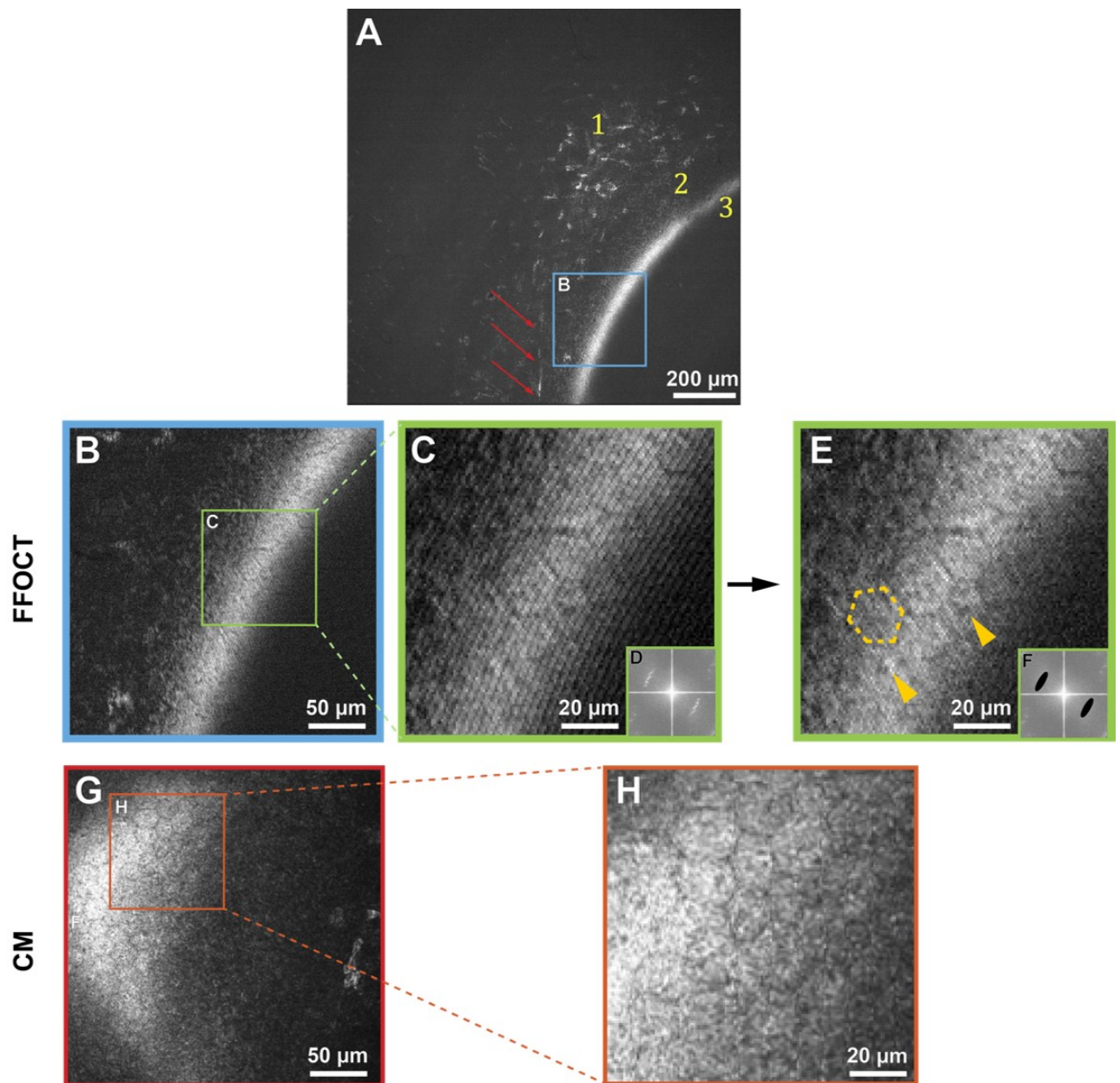


Figure 3.8 – *In vivo* human corneal images of posterior stroma and endothelium, obtained with FFOCT and IVCM [3]. Due to the curvature of the human eye and relatively large field-of-view of FFOCT, the imaging plane cut through several layers, giving an annular shape to the appearing layers. (A) FFOCT image of the posterior cornea. 1 – posterior stromal keratocytes, 2 – Descemet’s membrane; 3 – endothelium. A nerve is shown by the red arrows. (B) zoomed area ($300\ \mu\text{m} \times 300\ \mu\text{m}$) of image A, corresponding to the posterior corneal surface. (G) IVCM image ($300\ \mu\text{m} \times 300\ \mu\text{m}$), depicting posterior corneal surface. (C,H) zoomed endothelial areas of B and G. (E) image C after fringe filtering in the Fourier domain. (D,F) Fourier transforms of images C and E. Dashed yellow outline traces a hexagonal endothelial cell contour, and yellow arrows indicate centered endothelial cell nuclei. FFOCT images were averaged up to 10 times.

As an intermediate conclusion, the first full-field optical coherence tomography instrument capable of *in vivo* imaging of the human cornea was introduced. Particular properties of the FFOCT technique allowed to achieve high lateral and axial resolutions ($1.7\ \mu\text{m}$ and $7.7\ \mu\text{m}$ respectively), comparable to the best *in vivo* corneal imaging devices, while at the same

time operating with a larger field-of-view of 1.26 mm x 1.26 mm and in non-contact way. Unfortunately, due to the problem of defocus, images could be only occasionally acquired. In the next chapter I will introduce a new common-path FF/SD OCT device, which achieves FFOCT imaging in real-time.

Towards real-time *in vivo* FFOCT

Table of contents

4.1	Concept of real-time <i>in vivo</i> FFOCT	68
4.2	Instrumentation of common-path FF/SD OCT	69
4.2.1	Design of integrated FF/SD OCT instrument	69
4.2.2	Tracking eye position with common-path FF/SD OCT	69
4.2.3	Real-time optical path length matching of FFOCT interferometer arms	72
4.3	Imaging results of common-path FF/SD OCT	72
4.3.1	Imaging <i>ex vivo</i> cornea, moving by the motorized stage	72
4.3.2	Imaging of <i>in vivo</i> human cornea (central)	74
4.3.3	Imaging of <i>in vivo</i> human cornea (peripheral)	76
4.3.4	Cell and nerve quantification	78
4.3.5	Imaging of <i>in vivo</i> human limbus	79
4.3.6	Intermediate conclusion	79

4.1 Concept of real-time *in vivo* FFOCT

Every instrument that aspires to become clinical must demonstrate reliable, consistent and reproducible performance. The first *in vivo* FFOCT design was able to capture promising images, however only, when the optical path lengths of the two interferometer arms were perfectly matched, which occurred only, when the cornea happened to land in the perfect position. Indeed, given that the *in vivo* cornea is constantly moving, even during the so-called steady fixation, such matching only occurs at rare random moments, prohibiting consistent real-time imaging of corneal layers, necessary for clinical use of FFOCT. As we discussed in the previous chapter, the mismatch appears due to the problem of defocus. The deeper we image inside the cornea, the further we need to extend the reference arm, thus matching the coherence plane to the new spread position of the focus. If we could track the axial position of the cornea in real-time and shift the reference according to the detected corneal location, FFOCT could acquire images consistently and in real-time. Unfortunately, FFOCT alone does not detect the position of the cornea.

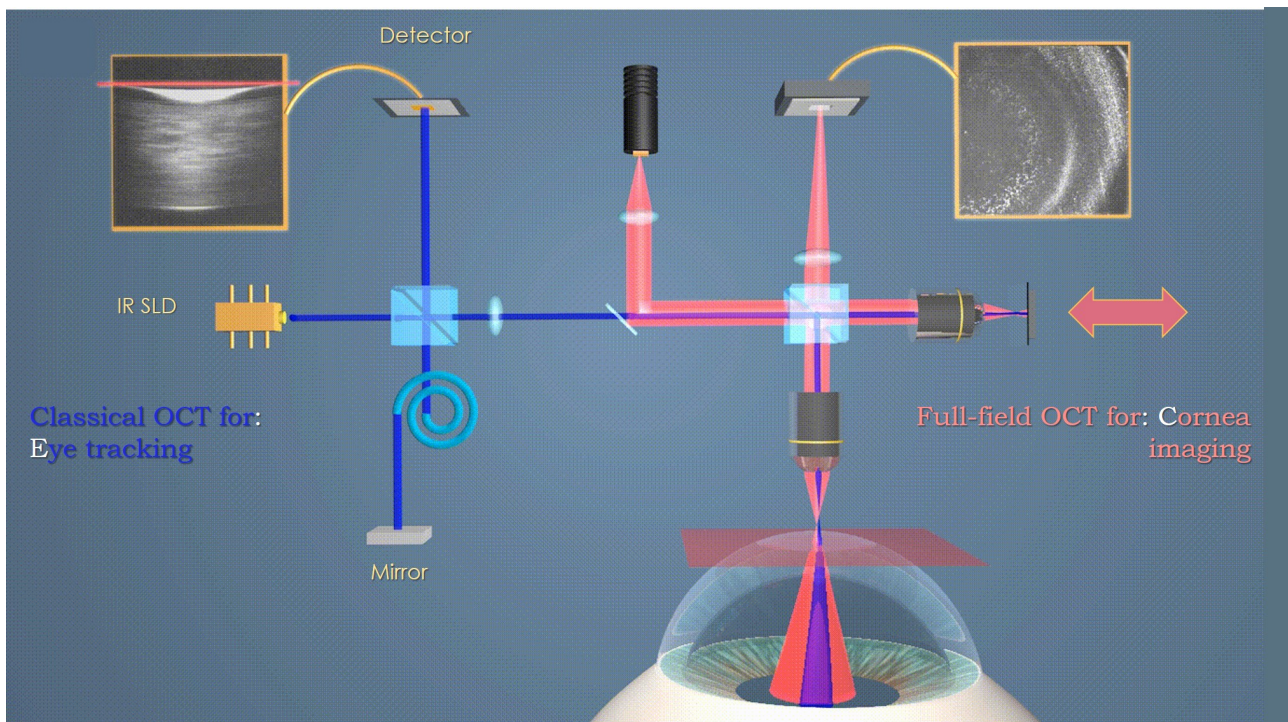


Figure 4.1 – Schematic of common-path FF/SD OCT device for real time imaging. SDOCT interferometer detects the axial corneal location (red line), while FFOCT interferometer adjusts the reference arm length accordingly (red arrow), enabling real-time FFOCT imaging.

This task is, however, possible with the cross-sectional high axial resolution view of SDOCT.

Following this idea, we combined FFOCT with SDOCT creating a common-path FF/SD OCT device (figure 4.1). In real-time SDOCT sends the information about the axial corneal location to the voice coil motor, which rapidly moves the reference arm to match the arms of the FFOCT interferometer, leading to a consistent FFOCT imaging of the moving *in vivo* cornea. In this chapter, I will explain in detail the design of the real-time FF/SD OCT instrument and will show, how we validated its performance by imaging *ex vivo* cornea, mounted on a moving stage. Then, I will demonstrate images, extracted from the real-time videos acquired from *in vivo* human corneas of 3 healthy subjects. Moreover, I will show that the quality of the real-time FFOCT images is sufficient to perform nerve and cell counting in a manner compatible with existing clinical methodologies, opening a door to diagnosis of a broad range of diseases, including, but not limited to, diabetes, acute ischemic stroke, corneal dystrophies, keratitis, etc.

4.2 Instrumentation of common-path FF/SD OCT

Here we will explore in detail, how the common-path FF/SD OCT tracks the eye and matches the FFOCT interferometric arms.

4.2.1 Design of integrated FF/SD OCT instrument

SDOCT is optically integrated through the dichroic mirror into the illumination arm of the FFOCT (figure 4.2). In order to block the SDOCT light from reaching the FFOCT camera, two filters with opposite spectral characteristics (low and high pass at 900 nm cutoff) are positioned at the entrance and exit of the FFOCT device. Glass windows are inserted into the reference arm of SDOCT to dispersion match with FFOCT sample and reference arms. The combined instrument is positioned on the two high-load lateral translation stages, controlled by a driver with a joystick. Beneath, one more stage is used to position the whole device vertically. Custom code written in Labview 2014 and Thorlabs SpectralRadar SDK were used for FFOCT and SDOCT image acquisition and display, peak detection and motor control.

4.2.2 Tracking eye position with common-path FF/SD OCT

SDOCT, coupled to the microscope objective, displays the locations of the corneal surface and other reflecting surfaces in the XZ plane with a high axial resolution of 3.9 μm . In fact, as the peaks in SDOCT image are non-overlapping we can detect them with even higher resolution. The SDOCT device is based on a commercial general-purpose Spectral-Domain OCT (GAN510, Thorlabs, USA). It consists of an interferometer with a galvanometric mirror system (OCTP-900(/M), Thorlabs, USA), which rapidly scans a light beam laterally at 100 kHz to form a 2D cross-sectional image. In order to increase the frame-rate, the lateral extension of the image was limited to 64 pixels. The 2D image is averaged over the lateral dimension and the resulting 1D data is processed with Labview Peak detector VI (National Instruments, USA) to locate the maxima.

Because SDOCT interferometer and FFOCT interferometer share the optical arms, we detect not only the conventional SDOCT peaks corresponding to the reflection from the cornea and from the FFOCT reference mirror, but also the third common-path peak corresponding to the

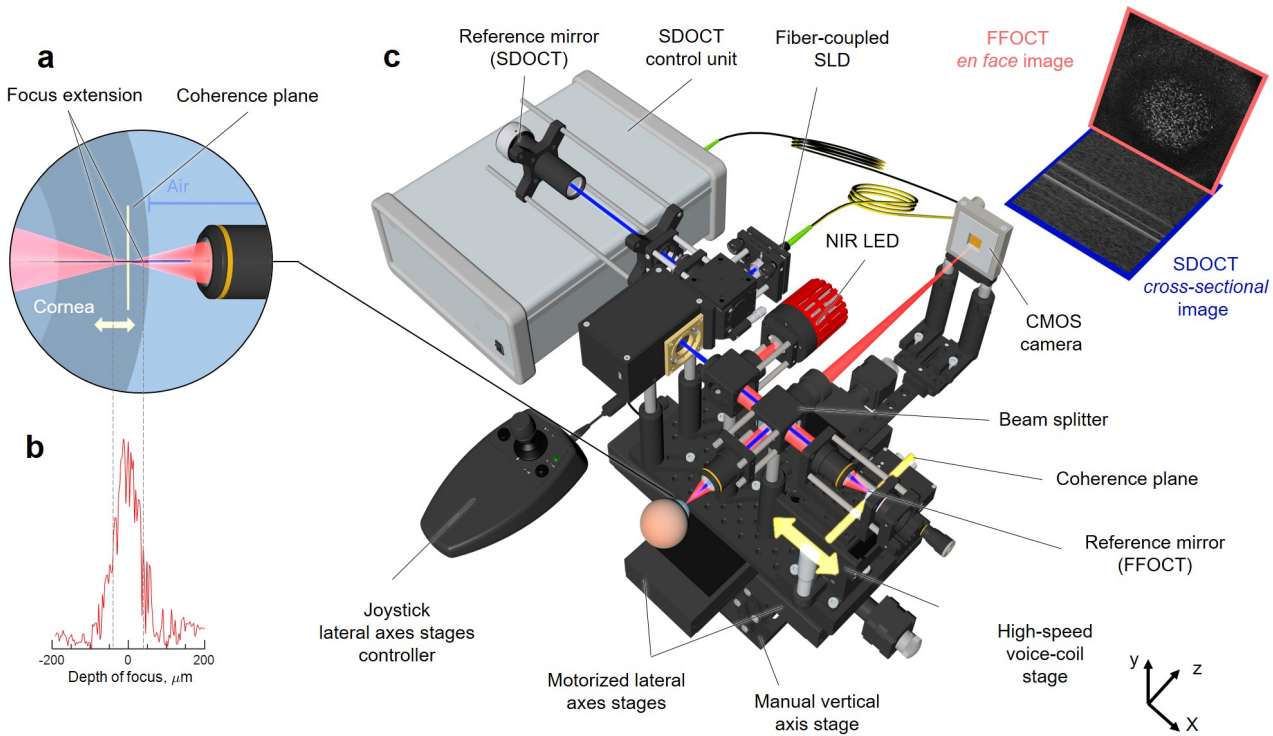


Figure 4.2 – Prototype of common path FF/SD OCT with axial eye tracking and real-time defocus adjustment. (a) Side-view of the FFOCT sample arm with the cornea. Location of the focus changes with changing corneal position, due to refraction at the air-cornea boundary. The location of the coherence plane (depicted in yellow), corresponding to the position of the FFOCT reference arm, also shifts, but in the opposite direction, leading to an optical mismatch between the two and loss of FFOCT signal. (b) Measured depth of focus. (c) The microscope consists of two interferometers: FFOCT, which acquires *en face* images using a 850 nm light-emitting diode illumination (depicted in red), and SDOCT, capturing cross-sectional images with a 930 nm superluminescent diode light (depicted in blue). SDOCT data is used to calculate the current corneal position and the optical mismatch correction required, which is fed into the fast voice coil stage in the FFOCT reference arm. The stage shifts rapidly to place the coherence plane within the changing position of the depth of focus. As a result, the FFOCT interferometer arms match, and *en face* images are acquired consistently and in real-time.

interference inside the FFOCT interferometer (between FFOCT sample and FFOCT reference arms) (figure 4.3). The latter maximum has the advantages that 1) it does not suffer from dispersion, due to the perfect symmetry between the arms of the FFOCT interferometer; 2) it is moving in the same direction on the 2D image as the reference arm, extended for the defocus correction. As a result, since the common-path and reference mirror peaks never overlap, we can simultaneously detect them and calculate (according to formulas in figure 4.4) positions of the cornea, the imaging depth inside the cornea, the optimal reference position for the defocus correction, the actual reference position and the error for validating and improving the feedback loop. By reducing the light entering into the reference arm of SDOCT, we suppress the conventional peak from the cornea to further facilitate acquisition of common-path and conventional reference arm peaks. Maxima were detected over a 1.25 mm lateral range, matching the FFOCT field of view and over a 2.7 mm axial range, determined by the SDOCT spectrometer. Every 8.2 ± 0.5 ms (mean \pm standard deviation (s.d.)) information about the current locations

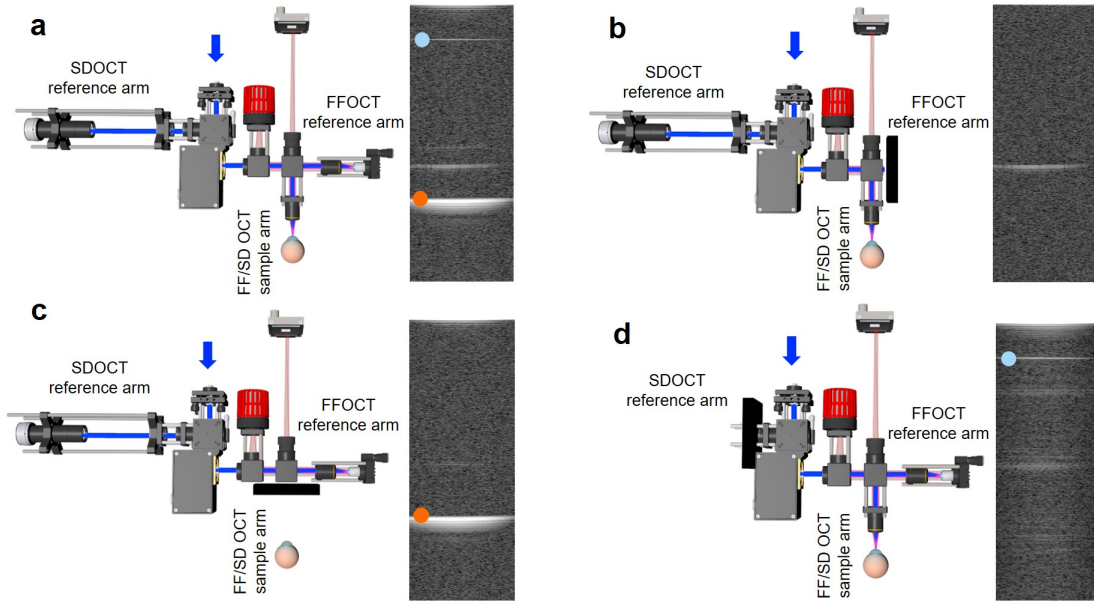


Figure 4.3 – Understanding the peaks in SDOCT images. (a, left) Common-path FF/SD OCT interferometer with light passing through all optical arms. (a, right) SDOCT image with three planes of backscattered/reflected light. (b, left) The same device with blocked FFOCT reference arm. (b, right), SDOCT image with a single reflected peak, corresponding to the surface of the cornea. (c, left) Device with blocked sample arm. (c, right) SDOCT image with reflection from the FFOCT reference mirror (orange). (d, left) Device with blocked SDOCT reference arm. (d, right) SDOCT image shows on top a single sharp reflection, originating from the FFOCT interference and captured by SDOCT (common-path peak) (blue). Its narrowness reflects the perfect dispersion matching in identical FFOCT arms.

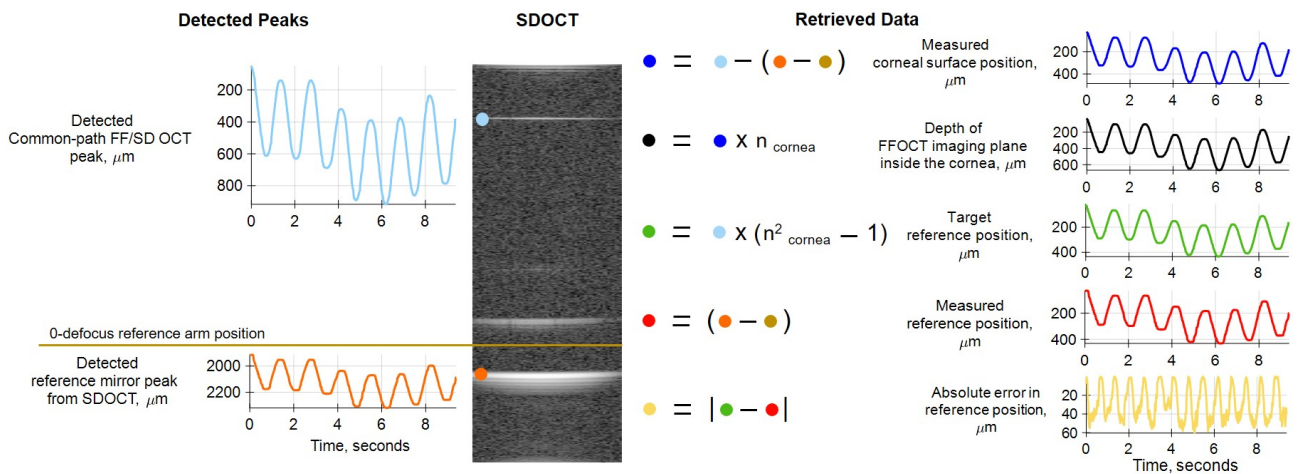


Figure 4.4 – Calculating locations. (left) SDOCT image with common-path and reference mirror peaks being detected in real-time. Both of these maxima move down, when the reference arm is extended for defocusing correction. This facilitates their detection, as we can separate only the common-path peak for the upper area of the SDOCT image and the reference arm peak for the lower part without their overlapping. (right) Using current locations of the two maxima and initial location of the reference mirror, one can calculate corneal surface position in real-time, along with the depth of the FFOCT imaging plane in the cornea, the optimal reference position for the current corneal location, the actual reference position and the error between the two, used for validating and improving the optical arms matching loop.

of the peaks is sent to the FFOCT system, where it is used to correct the optical mismatch between the FFOCT interferometer arms.

4.2.3 Real-time optical path length matching of FFOCT interferometer arms

The amount of the currently required defocus correction shift, computed from the corneal position in SDOCT image, is communicated to a translation stage, responsible for moving the reference arm of FFOCT. SDOCT and the stage are connected to the same personal computer to avoid time delays. The movement of the stage should be precise within the objective's depth of focus (measured ± 35 at FWHM) (figure 4.2) and rapid enough to follow *in vivo* movements of the cornea. The above requirements are satisfied by using a fast voice-coil motor (X-DMQ12P-DE52, Zaber, Canada) with $2.2 \mu\text{m}$ bidirectional accuracy, 1 mm/s velocity and 25 mm/s^2 acceleration. The weak link in the communication is the limited read frequency of the stage encoder, which can accept 20 new positions/s – about 2 times slower compared to the rate of provided positions by SDOCT. FFOCT and SDOCT image acquisitions are controlled using two PCs, which are synchronized with $11 \pm 3 \text{ ms}$ (mean \pm s.d.) precision through the NI-PSP protocol via the local network of the Langevin Institute. This enables simultaneous recording of FFOCT and SDOCT data.

4.3 Imaging results of common-path FF/SD OCT

4.3.1 Imaging *ex vivo* cornea, moving by the motorized stage

We tested and optimized the real-time feedback of the common-path FF/SD OCT instrument by imaging *ex vivo* cornea, mounted on a moving stage. *Ex vivo* macaque cornea was obtained from the partner research institution as recuperated waste tissue from an unrelated experiment. Corneas were dissected from the ocular globes within two hours post-mortem and fixed in 2% paraformaldehyde prior to transfer to the imaging lab. Some edematous swelling occurred, causing enhanced visibility of stromal striae [99], indicative of tissue stress.

At first, the stage was programmed to produce a slow steady movement ($20 \mu\text{m/s}$) to compare the system's performance with the defocus correction enabled and disabled (figure 4.5). With defocusing correction, as the SDOCT detects the cornea coming closer to the objective, and the image plane going deeper into the sample, the voice coil stage extends the reference arm to put it in the optimal position for the current corneal location. As a result, the FFOCT interferometer arms were well matched with $3.7 \pm 0.8 \mu\text{m}$ (mean \pm s.d.) error well within the depth of focus, and FFOCT consistently displayed corneal images from the various depths, while only occasionally the signal vanished, due to phase changes induced by the movement of the sample. Conversely, without defocusing correction, the reference arm position remains fixed and FFOCT images are visible only at a single corneal position within the objective's depth of focus, which corresponds to matched optical path lengths of the arms of the interferometer.

Next, we programmed the stage to move similarly to the physiological movements of the eye (figure 4.5). This was achieved by first measuring the axial movements of the normal human cornea *in vivo* and extracting the underlying frequencies and amplitudes. Two typical

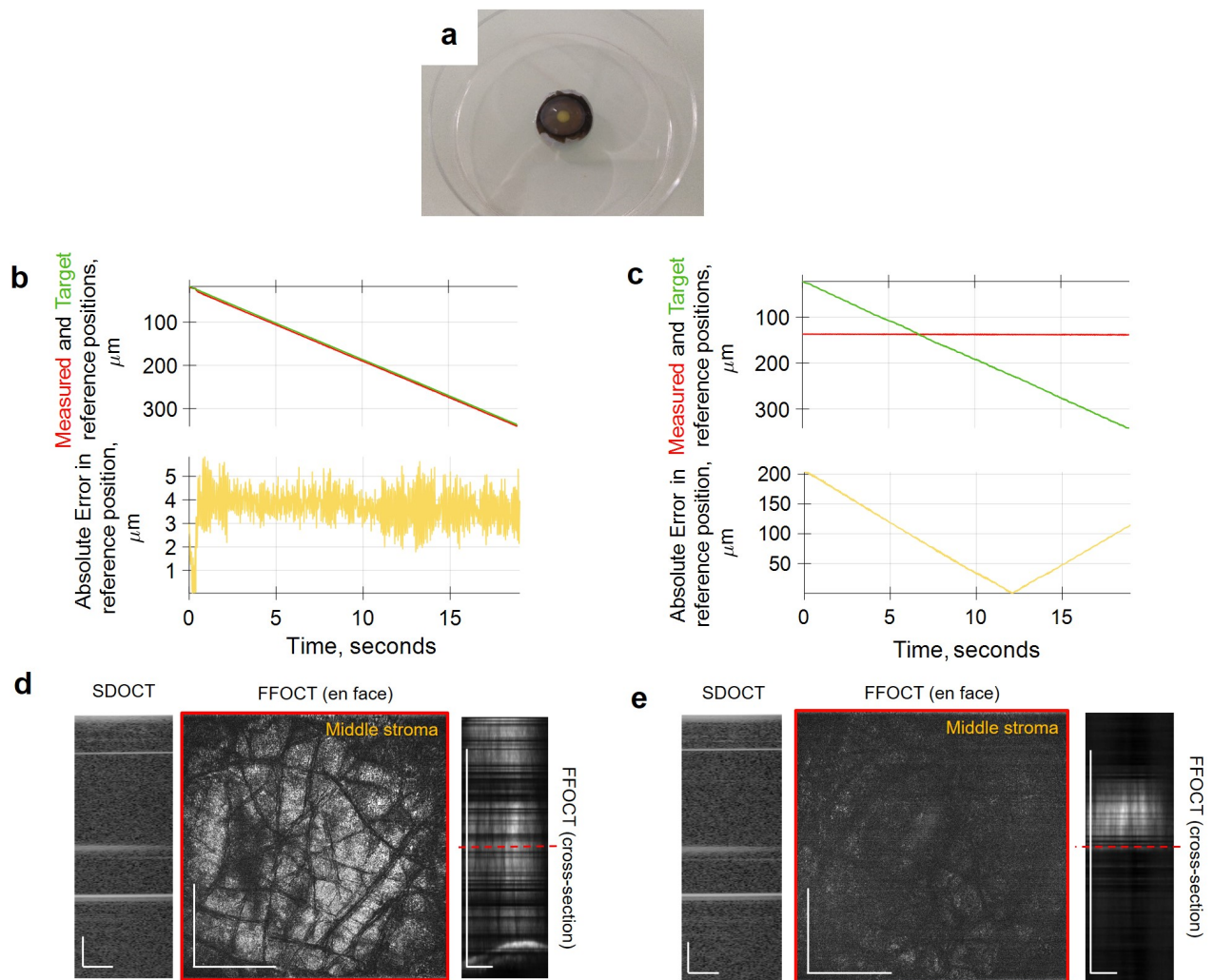


Figure 4.5 – Validating the real-time defocusing correction on steadily moved *ex vivo* cornea, driven by the motorized stage. (a) Photo of *ex vivo* macaque cornea sample (without motor mount). (b) Steadily moving *ex vivo* cornea, defocusing correction is active. Plots with measured reference mirror position (red), required reference location for ideal defocusing correction (green) and error between the two (yellow). (c) Corresponding SDOCT, *en face* FFOCT and cross-sectional FFOCT images. Red line shows location of *en face* FFOCT image. FFOCT images are consistently acquired from various depths, while only occasionally the signal is vanishing due to additional phase introduced to the tomographic signal by the movement of the sample. (d) Plots for steadily moving *ex vivo* cornea, with defocusing correction being off. (e) Without defocusing correction, the reference arm position was fixed and FFOCT images were visible only at a single corneal position within the objective’s depth of focus, where the interferometric arms match. Sample had visible stromal striae, indicative of tissue stress [99]. All scale bars 400 μm .

movements were visible: 1) heartbeat at 1.1 Hz with higher harmonics at 2.2 Hz, 3.3 Hz, etc., and 2) slow breathing at 0.34 Hz, both in agreement with the literature [100]. We used the frequencies with the two highest amplitudes (0.34 Hz with 33 μm amplitude and 1.1 Hz with 13 μm amplitude) as our input for the motorized stage with the sample. In the two cases, defocusing correction demonstrated errors of $1.5 \pm 2.2 \mu\text{m}$ and $5.3 \pm 4.0 \mu\text{m}$ (mean \pm s.d.), respectively, within the depth of focus. Higher frequencies were not important, as the corresponding amplitudes were smaller than the axial resolution as well as the depth of focus of the FFOCT device.

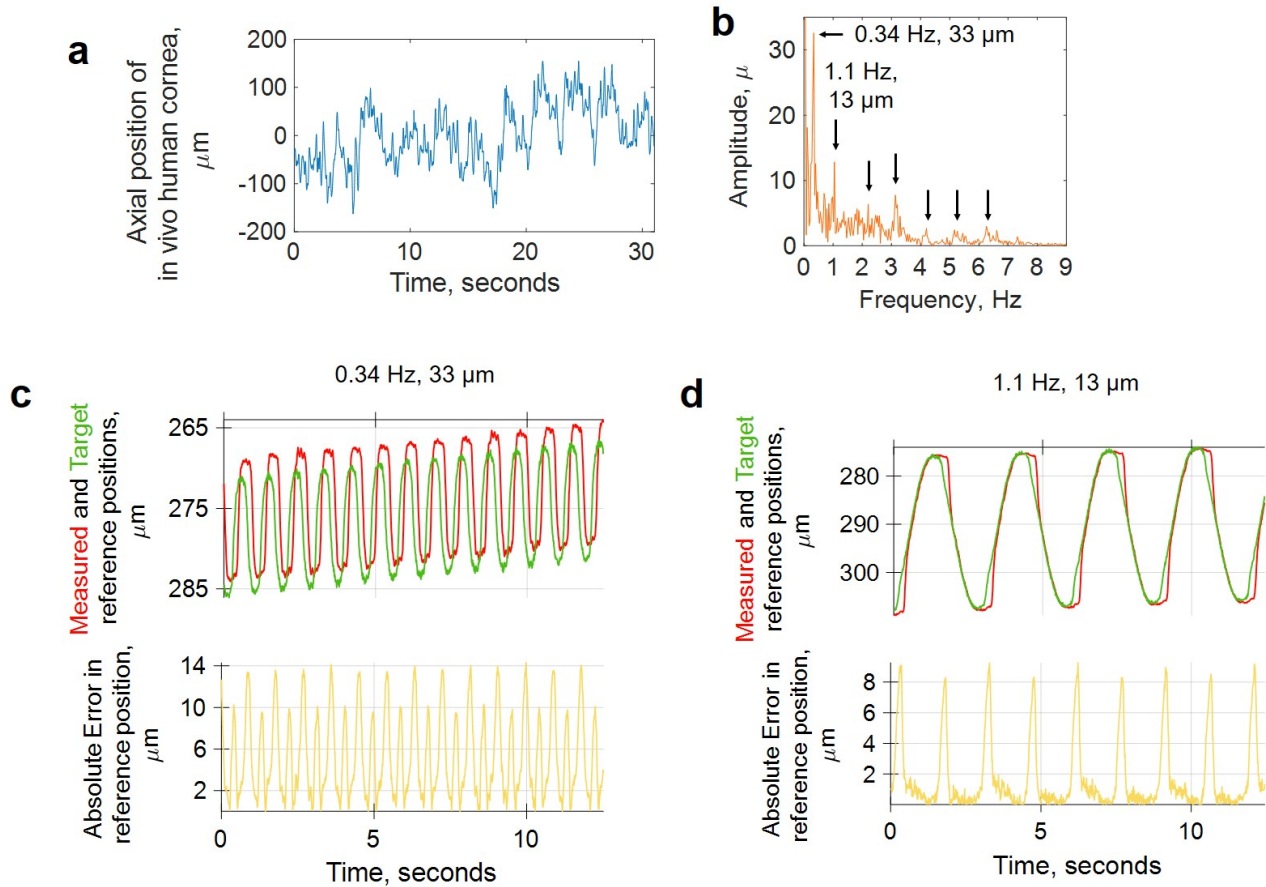


Figure 4.6 – Validating the real-time defocusing correction on physiologically moving *ex vivo* cornea, driven by the motorized stage. (a) Axial position of the *in vivo* human cornea over time, measured with SDOCT. (b) Extracted amplitudes and frequencies of the *in vivo* human corneal axial movements. (c) Test of defocusing correction with *ex vivo* cornea physiologically moving at 0.34 Hz and with 33 μm amplitude. (d) Test of defocusing correction with *ex vivo* cornea physiologically moving at 1.1 Hz and with μm amplitude.

4.3.2 Imaging of *in vivo* human cornea (central)

We applied common-path FF/SD OCT to view the *in vivo* human cornea in real-time. The study was carried out on three healthy subjects (1 female and 2 males, aged 36, 24 and 26 years), which was confirmed by a routine eye examination in the hospital preceding the experiment. Informed consent was obtained from all subjects and the experimental procedures adhered to the tenets of the Declaration of Helsinki. During the experiment, subjects were asked to sit in front of the system and rest their chin and temples on a standard headrest. While one eye was imaged, the second eye was fixating on a target. When imaging non-central parts of the cornea, the subject's head was tilted by the examiner to position the eye's surface plane perpendicular to the direction of the incoming light beam. Examination was non-contact and without introduction of cycloplegic or mydriatic agents, nor topical anaesthetics. Light irradiance on the cornea was 86 mW/cm^2 , below the maximum permissible levels of up-to-date ANSI Z80.36-2016 and ISO 15004-2:2007 ocular safety standards. Focusing the light beam on the cornea results in a widely spread out low-irradiance beam on the retina, leading to an retinal exposure level at 2% of the limit. Illumination was comfortable for viewing, due to the low sensitivity of the retina to NIR and IR light. For more explicit evaluation of light safety

see Appendix A.

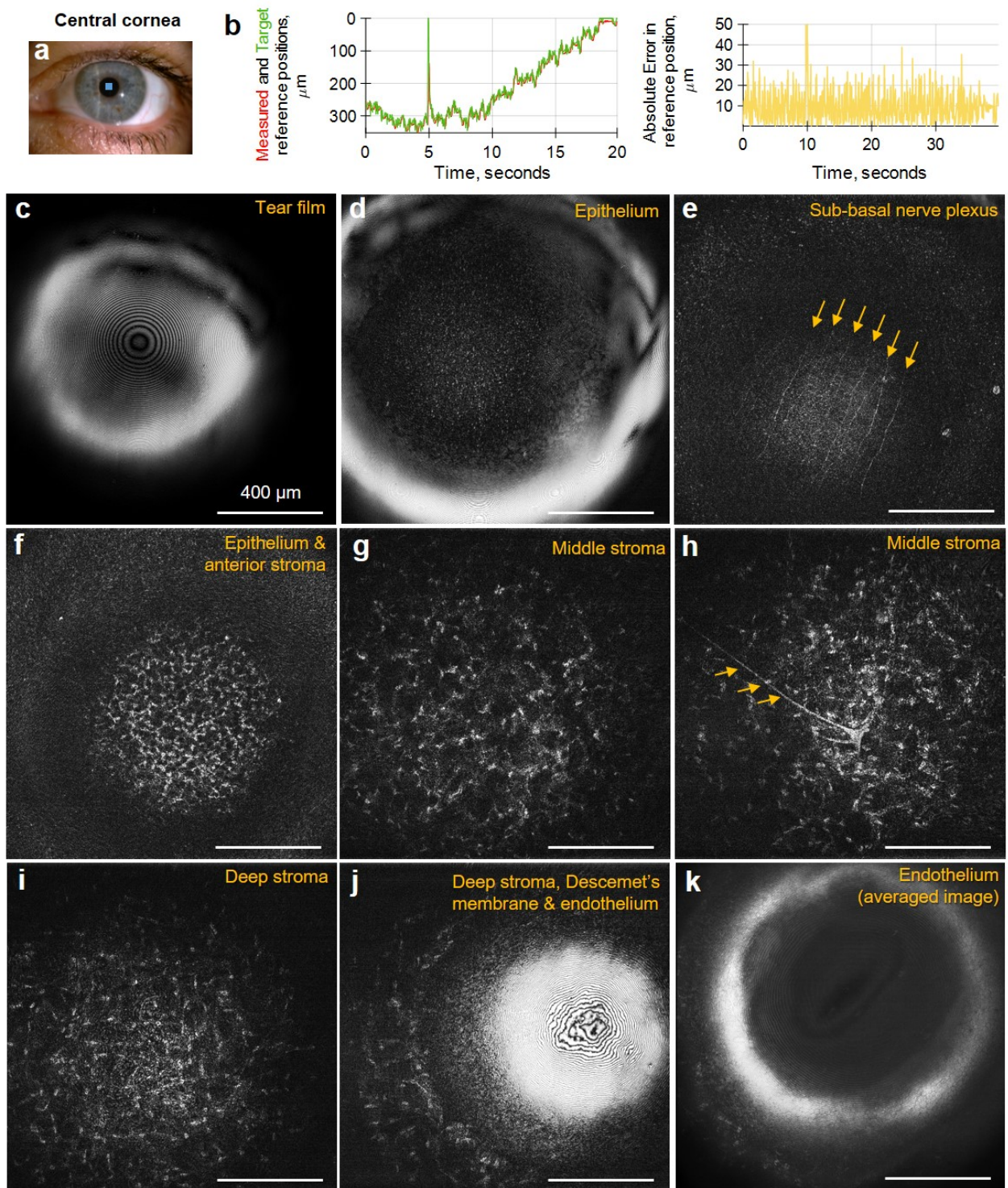


Figure 4.7 – Common-path FF/SD OCT imaging of central human cornea *in vivo*. (a) Slit lamp macro photo obtained from one of the subjects. Blue square depicts FFOCT field of view. (b) Performance of real-time defocusing correction, when imaging central part of *in vivo* human cornea. Measured reference mirror position (red), required reference location for ideal defocusing correction (green) and error between the two (yellow). Peak at 10 seconds corresponds to the blink of the eye. (c-k) Single frame FFOCT images through the entire thickness of the central cornea extracted from the real-time videos. Epithelial cells, sub-basal and stromal nerves (yellow arrows), keratocyte cells with nuclei and endothelial cells were visible. All unlabelled scale bars 400 μm .

The frame rate of real-time acquisition and display was ~ 10 frames/s, with each image captured in 3.5 ms. The operator of the instrument could simultaneously view FFOCT videos of *en face* images, OCT videos with cross-sectional images of the main corneal reflex, which is an indicator of the current imaging depth, and plots illustrating the performance of the defocusing correction. The instrument was able to acquire videos from central, peripheral and limbal parts of the *in vivo* cornea, simultaneously correcting optical mismatch with $9.4 \pm 6.2 \mu\text{m}$, $11.3 \pm 7.2 \mu\text{m}$ and $7.2 \pm 6.6 \mu\text{m}$ (mean \pm s.d.) errors, respectively.

Non-averaged single FFOCT frames, extracted from the videos, had sufficiently high signal in all corneal layers (figure B.14). In the central cornea we observed tear film. It appears with a fringe pattern, as FFOCT is an interferometric technique, meaning that interference fringes are visible on flat surfaces such as tear film. Right below, we could see superficial epithelial cells 40 - 50 μm in diameter with dark 8 - 13 μm nuclei. These cells were revealed by image filtering in the Fourier domain (by masking the bright spots, corresponding to fringes, in the Fourier domain and making an inverse Fourier transform). We could also see structures from other epithelial layers (wing, basal), however were unable to reliably resolve individual cells, due to low reflection contrast between them. Below the epithelium, we saw the sub-basal nerve plexus (SNP) with 2 - 4 μm thick nerves in a vertical orientation, which is characteristic of the central corneal area, located superior to the whorl-like nerve pattern [101]. Due to the curvature of the cornea and small thickness of the SNP, only part of the layer was visible. Nevertheless, the area of the visible nerve section was 0.317 mm^2 - 3 times larger compared to what is possible with the state-of-the-art IVCM. As a result, a large-scale view of SNP can potentially be obtained with a smaller number of “stitched” images [63], leading to significantly faster screening and processing times. Underneath the SNP, we enter the anterior part of the stroma with numerous bright oval-shaped nuclei of keratocyte cells, measured about 15 μm in diameter. In the mid stroma, the density of keratocytes decreases and, in addition to the nuclei, we can resolve the cell bodies and branching 10 μm thick stromal nerves. With increasing depth, nuclei become more elongated and their density decreases. Descemet’s membrane was also visible as a dark band separating stromal keratocytes from the endothelial cells. Endothelium viewed in a single FFOCT image was hindered by a strong specular reflection; nevertheless, on an averaged image we could resolve the hexagonal mosaic of 20 μm diameter cells and sometimes a 5 μm nucleus.

All of the above images were acquired without any physical contact with the eye, with a distance of about 2 cm between the cornea and the microscope objective. We also benefited from the insensitivity of FFOCT to aberrations [83], which will be discussed in more detail in the upcoming chapter about the FFOCT retinal imaging. In brief, the FFOCT resolution remained unchanged through the entire cornea, despite the presence of spherical and astigmatic aberrations.

4.3.3 Imaging of *in vivo* human cornea (peripheral)

We also looked at the appearance of stroma in the central and peripheral cornea, and sclera (figure B.15). Initially the dark background of central corneal stroma, becomes bright at the periphery, which is explained by increased light scattering from the stromal fibrils, irregular in diameter and arrangement, known from electron and confocal microscopy studies [23,28]. Keratocyte cell nuclei, easily visible in central cornea, are more difficult to resolve in the periphery.

Blood vessels, visible with their shadows, were perforating the upper sections of the sclera.

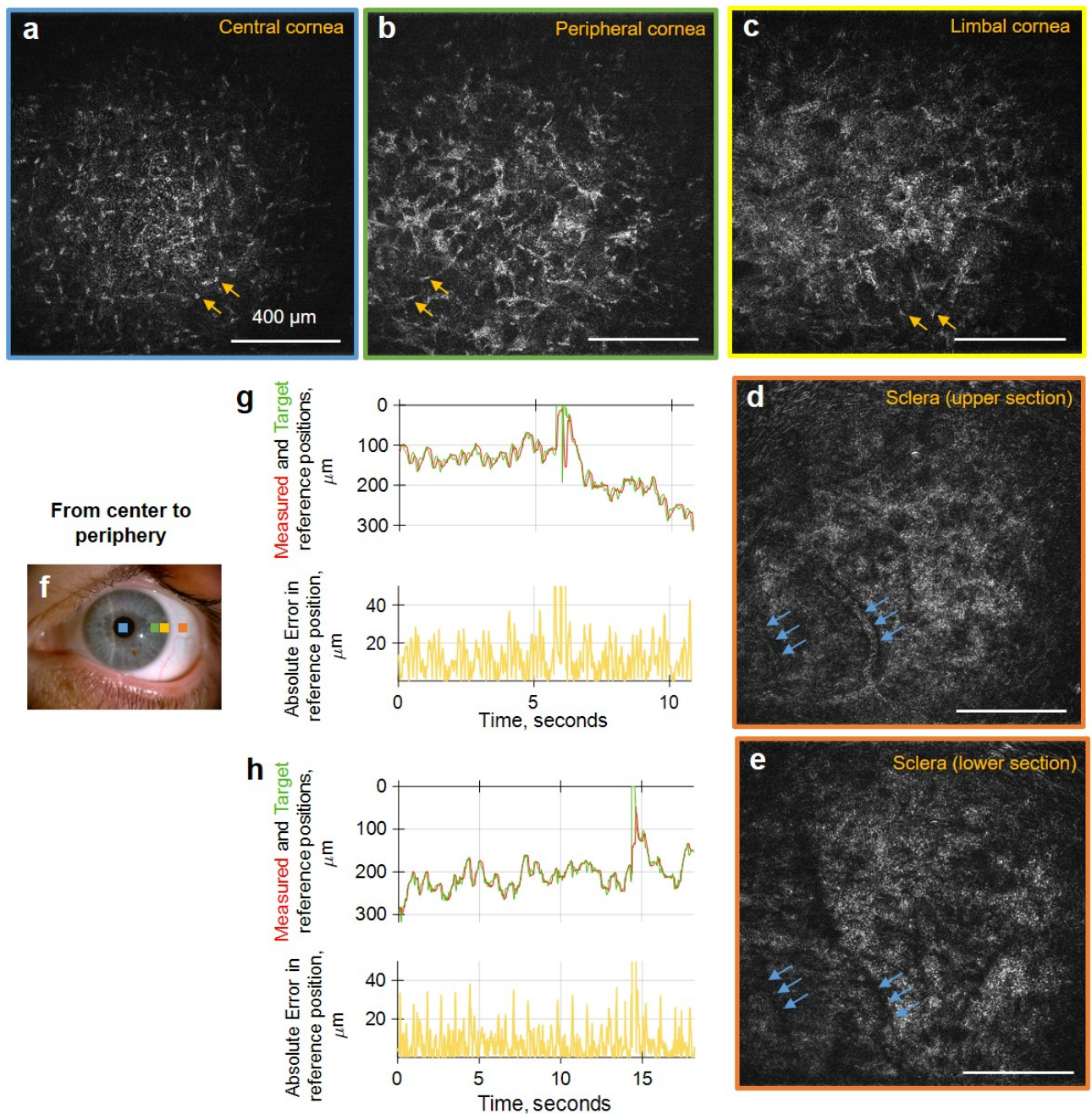


Figure 4.8 – Common-path FF/SD OCT imaging of peripheral, limbal human cornea and sclera *in vivo*. (a-e) Single frame FFOCT images from central cornea to periphery, extracted from real-time videos. Resolving individual keratocyte nuclei (yellow arrows) was increasingly more difficult, when imaging further from the center. Blue arrows show vessels and their shadows in the sclera. (f) Slit lamp macro photo, with squares indicating the peripheral locations, where FFOCT images were acquired. (g,h) Performance of real-time defocusing correction, when imaging the peripheral part of *in vivo* human cornea. Peaks at 6 and 14 seconds correspond to the blinks of the eye. All unlabelled scale bars 400 μm .

4.3.4 Cell and nerve quantification

We also show that clinically valuable [102] measurement of nerve and cell densities can be performed with FFOCT (figure 4.9). Nerves were segmented using semi-automatic NeuronJ [103] plugin for ImageJ [96]. Their density measured 15 mm/mm^2 , within the healthy margins [20]. Nerve density correlates with keratoconus, dry eye, several types of keratitis and diabetes [104]. Endothelial cells were manually counted using Multi-point tool of ImageJ. Their density measured 3096 cells/mm^2 , in agreement with the literature [105]. Endothelial cell density correlates with dystrophies, uveitis and acute ischemic stroke [106].

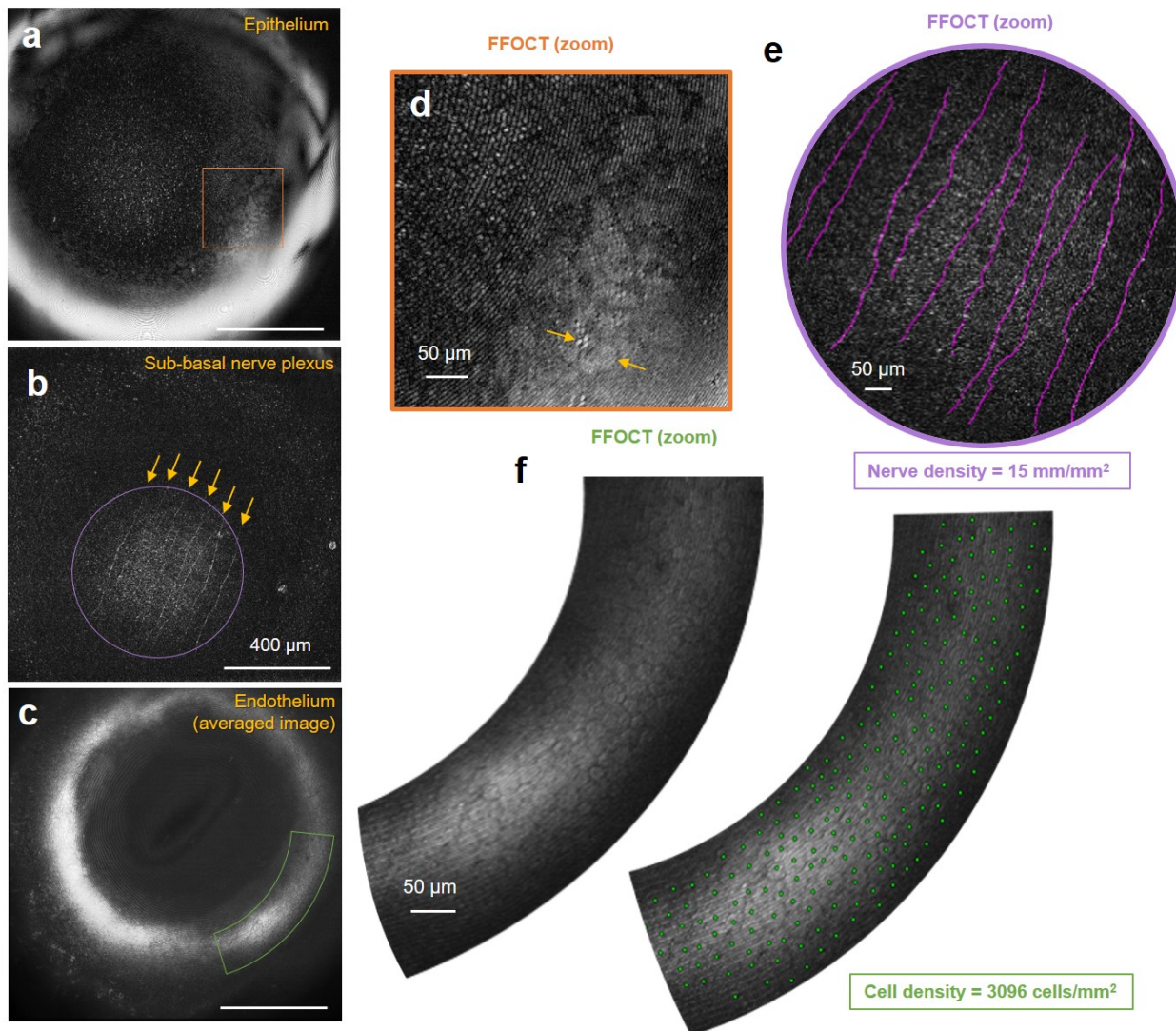


Figure 4.9 – Cellular quantification can be performed with FF/SD OCT. (a-c) Single frame FFOCT images of the central cornea with indicated cellular mosaics. (d) Zoomed and bandpass filtered FFOCT image of superficial epithelial cells with dark nuclei. (e) Zoomed FFOCT image of sub-basal nerves. Semi-automated nerve segmentation and density analysis were performed with NeuronJ [103]. (f) Zoomed FFOCT image of endothelial cell mosaic. ImageJ [96] Multi-point tool was used for cell counting. All unlabelled scale bars 400 μm.

4.3.5 Imaging of *in vivo* human limbus

In the inferior limbal region, 30 μm wide radial palisades of Vogt (POV) were visible (figure B.16). The distance between the palisades measured 30 – 200 μm . Marginal corneal vascular arcades (MCA) with thin 3 - 7 μm vessels and their dark shadows appeared to protrude from inside of the palisades, in agreement with the literature [33, 107, 108]. These vessels, parallel to the ocular surface, appeared to be connected with a perpendicular oriented vessel network, visible as dark round shadows. Closer to the cornea, vessels were curling into the loops, while continuing to spread in the radial direction. Beneath, we could see thicker 40 μm branching vessels.

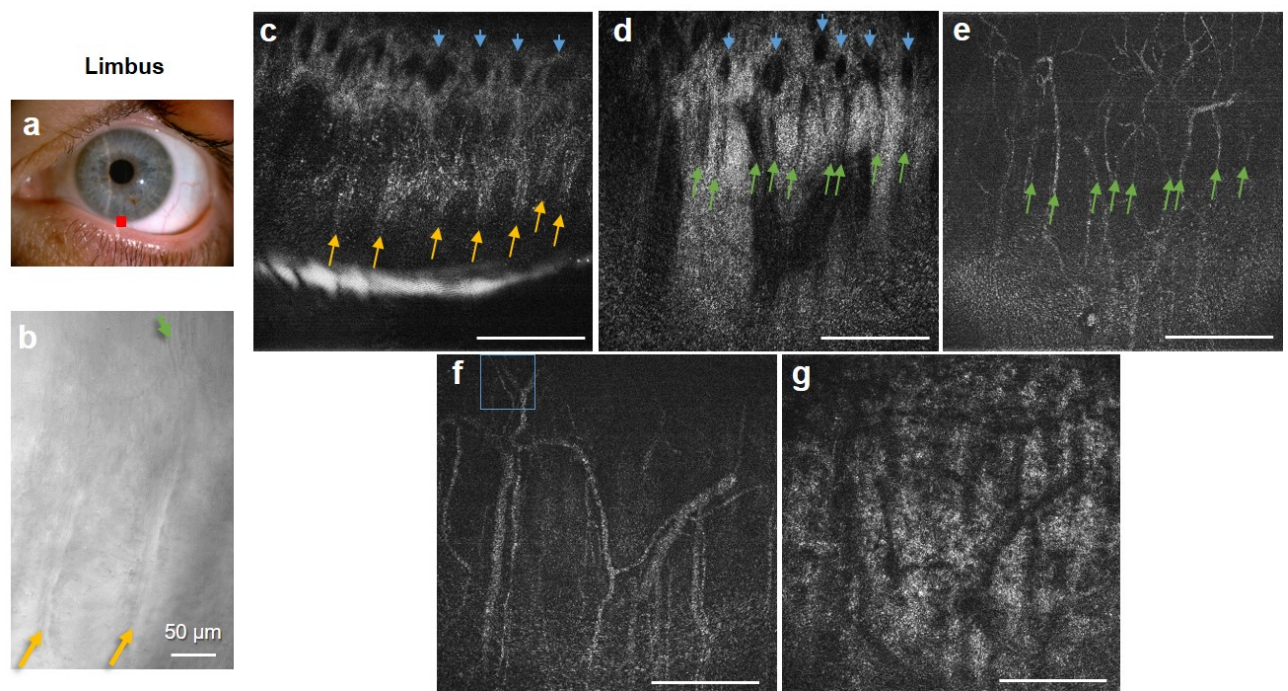


Figure 4.10 – Common-path FF/SD OCT imaging of *in vivo* human limbus. (a) Slit lamp macro photo obtained from one of the subjects. Square depicts locations, where FFOCT images were acquired. (b) Single frame direct reflection image of palisades of Vogt (yellow arrows) and vessels (green arrow) in limbus. (c-g) Single frame FFOCT images of consecutively lower depths in limbus. Yellow arrows – palisades, green arrows – thin vessels hosted within palisades, blue arrows – perpendicular vessel network thought to be connected with horizontal vessels. Underneath, thicker vessels and scattering stroma-sclera medium with vessel shadows were seen. Unlabelled scale bars 400 μm .

4.3.6 Intermediate conclusion

In this chapter we transformed the first *in vivo* FFOCT prototype into a reliable instrument, which can consistently acquire real-time videos from the entire human cornea, limbus and sclera. This became possible by combining FFOCT with an SDOCT into a common path FF/SD OCT device. Thanks to the real-time defocusing correction, even the single frame FFOCT images had a high signal, which removed the need for time-consuming image averaging (and aligning). The above opened opportunity for implementation of FFOCT in clinical research. In the next chapter we will further explore the capabilities of this device. Particularly, in application to visualizing dynamic processes in the eye, such as blood and tear flow.

Monitoring dynamic processes in the eye with FFOCT

Table of contents

5.1	Dynamic processes in the eye - potential for FFOCT	82
	Blood flow	82
	Tear film	83
5.2	FFOCT <i>in vivo</i> angiography	84
5.3	FFOCT for tear film imaging	87

5.1 Dynamic processes in the eye - potential for FFOCT

Clinical diagnosis benefits from every piece of information, which can shed the light on the cause of the ocular disorder and reveal the disease. Changes in the static tissue morphology are good indicators, but they are just part of all the information that is available. Another source are all kinds of dynamic processes in the eye.

Blood flow

Dynamic methods for blood quantification had a long history and today range from the well-established fluorescein angiography (for example, Indocyanine green angiography (ICGA)) and slit lamp biomicroscopy to a flourishing OCT-angiography (or OCT-A). These methods are most popular for characterization of retinal vasculature, nevertheless there is also an on-going research in their application to the anterior eye.

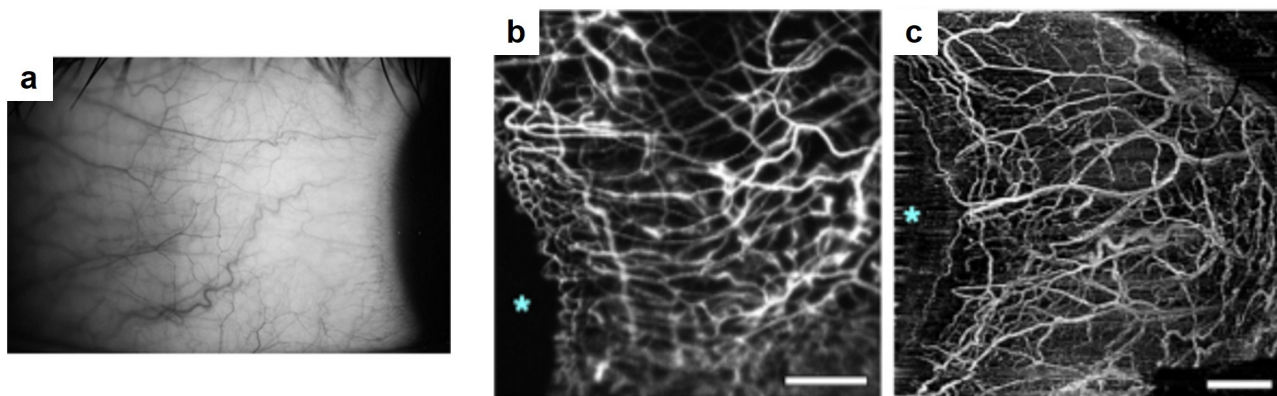


Figure 5.1 – Normal vasculature of the anterior eye. (a) Slit lamp image from [109]. (b) Fluorescein angiography. (c) OCT-A. Asterisks indicate location of the cornea. Scale bar = 1 mm. Adapted from [110].

Fluorescein angiography, slit lamp biomicroscopy and OCT-A provide images, which reveal the anterior eye vasculature (figure 5.1). Each of these methods have their benefits and drawbacks. Fluorescein angiography can directly show the propagation of the blood (with contrast agent) through the vessel layers. It acquires images with a 2D camera without motion artifacts. However, this is an invasive method, requiring prior injection of fluorescein agent. Moreover, following the injection, angiography map can be captured during a limited period of only several minutes. Slit lamp biomicroscopy, on the contrary, is a non-invasive non-contact method, however it provides a relatively low contrast in the blood flow images, reducing its diagnostic capacity. In addition, the slit lamp can not tell, which vessels are located at which depth (no

sectioning ability). OCT-A is non-invasive, non-contact and has a sectioning ability, enabling reconstruction of the volumetric limbal vessel images [111]. It creates angiography maps by highlighting the signal fluctuations in the conventional OCT images through time. Unfortunately, similarly to the previously discussed conventional OCT, *en face* plane is not the main orientation for the OCTA. This leads to the appearance of motion-induced artifacts and limited resolution. Because of the same speed limitation, OCT-A is unable to directly view the propagation of the blood flow. Similar is applicable to confocal microscopy. It has a sufficient resolution to resolve individual blood cells, but is unable to track them or estimate the velocity.

The above limitations are not pertinent to FFOCT, which makes its application to blood flow monitoring interesting. FFOCT is non-invasive, non-contact like OCT, but, in addition, prioritizes the *en face* view, immune to motion artifacts, provides very high speed and resolution.

Tear film

Dynamics of tear film is important to diagnose and quantify the well-spread dry eye condition. One of the established clinical methods is called tear break-up time (TBUT) (figure 5.2). TBUT measures the time between the blink and appearance of the first dry spot (where the tear film is lacking). To enhance the contrast the fluorescein is used. The disadvantages of the method include invasiveness (fluorescent injection) and large variability of the results.

Another family of the tear film monitoring instruments, which we mentioned before (figure 1.12), is based on the original tearscope design [39]. It utilizes the white light interference from the lipid layer to increase the contrast of tear film images. This type of device does not require contact with an eye, can directly view the dynamics of the tear film and perform the quantitative analysis. Unfortunately, it is a single-purpose instrument, which can not be applied for other applications.

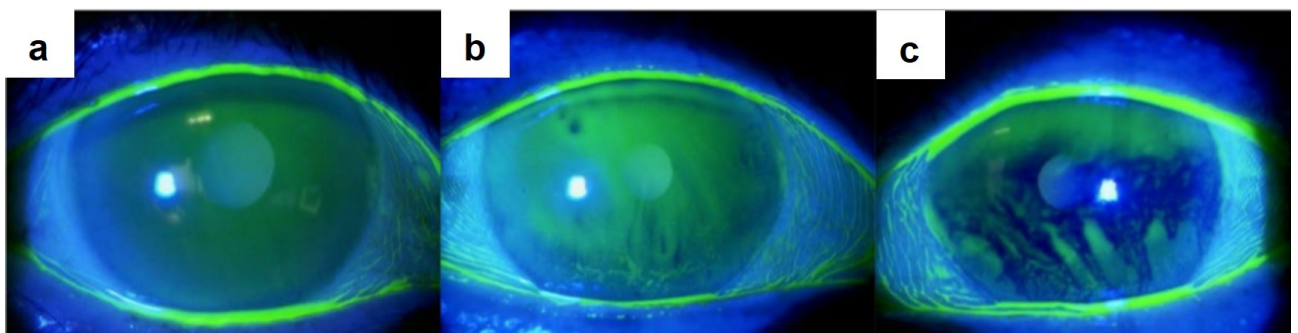


Figure 5.2 – Measurement of tear break-up time. Fluorescein is introduced into the eye (a-b) With time the dark spots, corresponding to breaks in tear film, appear. Adapted from [112].

Interestingly, in the early 2000's one more way of monitoring tear film dynamics has been researched: using a microscope and a high-speed camera [113]. The method demonstrated reproducible measurements of the tear flow velocity and tear stabilization time following the blink and proposed these two factors for quantitative characterization of dry eye condition. Unfortunately, given the immaturity of CCD camera technology at that time, the quality of tear images was very low and only the contrasting particle secretions from Meibomian glands on top of the tear film could be visualized.

Up to this moment, we know FFOCT as an optical coherence tomography method for optical sectioning the sample. Interestingly, by shutting the reference arm of interferometer, we come up with a conventional microscope design. In this configuration FFOCT can provide high dynamic range, high speed imaging of tear film. Switching between the tomography and microscopy configurations is very easy and can be done during the on-going examination.

5.2 FFOCT *in vivo* angiography

It is interesting to compare FFOCT with the scanning OCT and confocal systems in terms of the *en face* acquisition speed. FFOCT system acquires 550 conventional camera frames/s or 275 tomographic images (2-phase scheme). Each image is composed of 1440×1440 pixels, which leads to the *en face* acquisition speed of:

$$1440 \times 1440 \times 275 \approx 0.6 \text{ billion } \frac{\text{pixels}}{\text{s}} \quad (5.1)$$

This speed is well beyond the current capabilities of the beam scanning SDOCT-SSOCT and confocal microscopy (in terms of *en face* acquisition speed). For example, one of the fastest scanning OCT systems applied to the eye demonstrated 80 times smaller acquisition velocities, about 7 MHz [114].

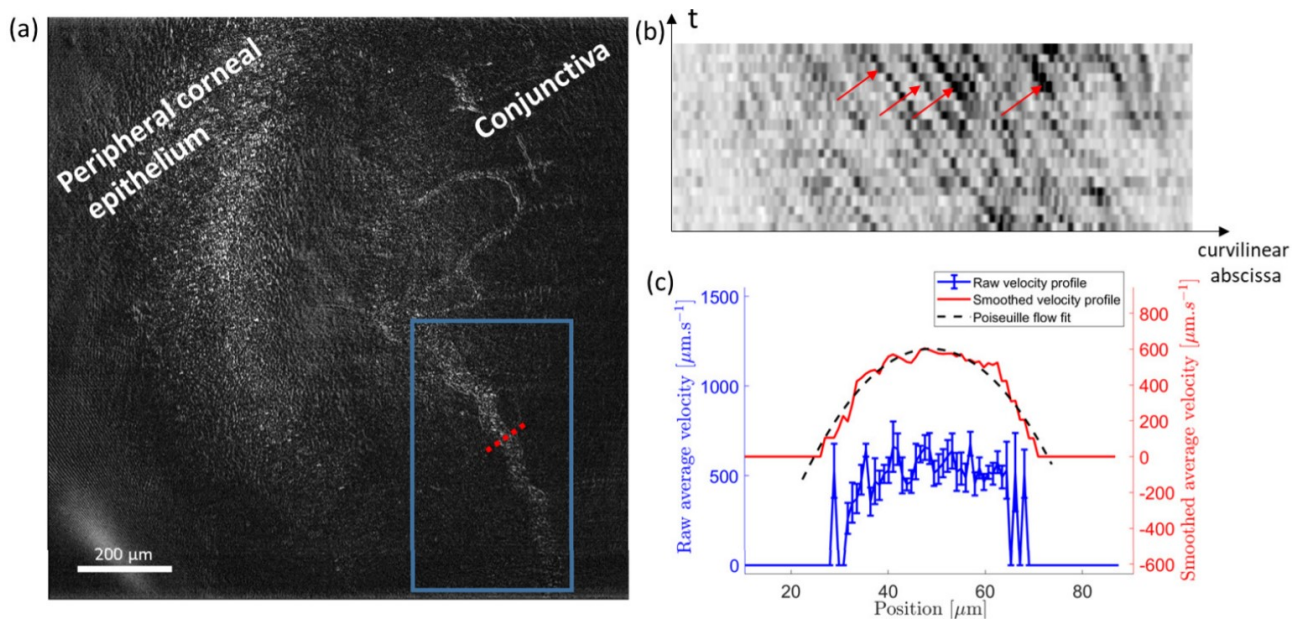


Figure 5.3 – Conjunctival blood flow near the temporal limbal region of the *in vivo* anterior human eye [93]. (a) Single-frame FFOCT image. (b) Example of a kymograph plot (space-time domain) inside the blood vessel. Grayscale is inverted, so that the black particles indicated by the red arrows are red blood cells flowing through the vessel. The slope corresponds to the particle speed. (c) Raw velocity profile inside the blood vessel (blue) computed along the dotted line in (a). The smoothed profile (red) with the fit to a Poiseuille flow profile (black dashed line) are superimposed and voluntarily shifted up for increased visibility.

In the first FFOCT study we explored the surface vessels in the temporal limbus (figure 5.3) [93]. The propagation of the blood flow inside the vessel was directly visible. In order to quantify the flow velocity, at first we removed the lateral misalignment between images by

using the template-matching plugin in ImageJ [97]. Then we plotted a kymograph - a graph, where one axis is a curvilinear abscissa of the vessel (in simple words, a line along the vessel), and the second axis is time. Blood cells, moving within a vessel, produce lines on a kymograph. The derivative (slope of the lines) gives the cell propagation speed. This speed corresponds only to one location in the vessel. By making the same calculations for the different curvilinear abscissas between the vessel walls, we constructed a plot of blood velocities in one vessel cross-section. To reduce the effect of noise, each speed was calculated as an average of 4 to 18 derivatives taken from the different cell lines within one kymograph plot. Different speeds were calculated with different errors, depending on the exact number of the averaged derivatives. The resulting smoothed velocity profile fitted to a Poiseuille flow, typically observed in the capillaries [115], given by the equation:

$$v(r) = v_{\max} \left(1 - \frac{r^2}{R_{\max}^2} \right), \quad (5.2)$$

where r is the distance from the center of the vessel, R_{\max} - vessel radius, v_{\max} - the maximal velocity in the vessel center and $v(r)$ - velocity at distance r from the vessel center.

Maximum blood flow velocity was measured about $600 \mu\text{m/s}$. Both the speed and vessel diameters were in agreement with the previous experimental findings in the literature [116,117]. Moreover, our measurements demonstrate 1 order of magnitude higher accuracy [116,118,119].

We also performed another experiment, where we used a combined FF/SD OCT. With real-time defocusing correction, we could look in depth of the inferior limbal region, below the palisades of Vogt (figure B.17). In order to get the quantitative blood flow information, we used a different improved approach. As we have seen, previously the flow velocities were retrieved using a kymograph plot. Given that each plot provides only a single local velocity value, obtaining a full-field map, would require a vast amount of manual efforts. As alternative, we used a method based on a block-matching algorithm. This algorithm tracks the features inside vessels, allowing rapid semi-automatic mapping of blood flow velocities and orientations in full-field. To be more precise, we cross-correlated 16×16 pixels sub-image windows and retrieved the cross-correlation maximum for each pixel in the vicinity corresponding to a maximal speed of 2 mm/s . Low cross-correlation peaks were discarded in order to remove artifacts and outliers. A velocity array was then created based on 8 frames, so that the velocity computed for each pixel is the average of the 7 velocities computed by the block-matching algorithm. Then the velocities and orientations were mapped on the HUE channel, the FFOCT image was mapped on the value channel and the saturation was arbitrarily set to 0.8 for each pixel. This resulted in semi-automatic obtaining of micrometer-level resolution blood flow velocity and blood flow direction maps. Average velocity was measured to be $0.446 \pm 0.270 \text{ mm/s}$ (mean \pm standard deviation), with the lowest speeds close to the vessel walls and highest speeds in the middle of the vessels, at junctions and also in locations where vessels were overlaying each other. Blood flow was mostly radial going towards or backwards from the cornea.

We were also able to resolve the individual $7 \mu\text{m}$ erythrocytes. This became possible by subtracting two consecutive conventional images from the camera without taking their absolute value. In the resulting image, we lost half of the useful signal (pixels with negative values), however the contrast was more intuitive to directly view the cells.

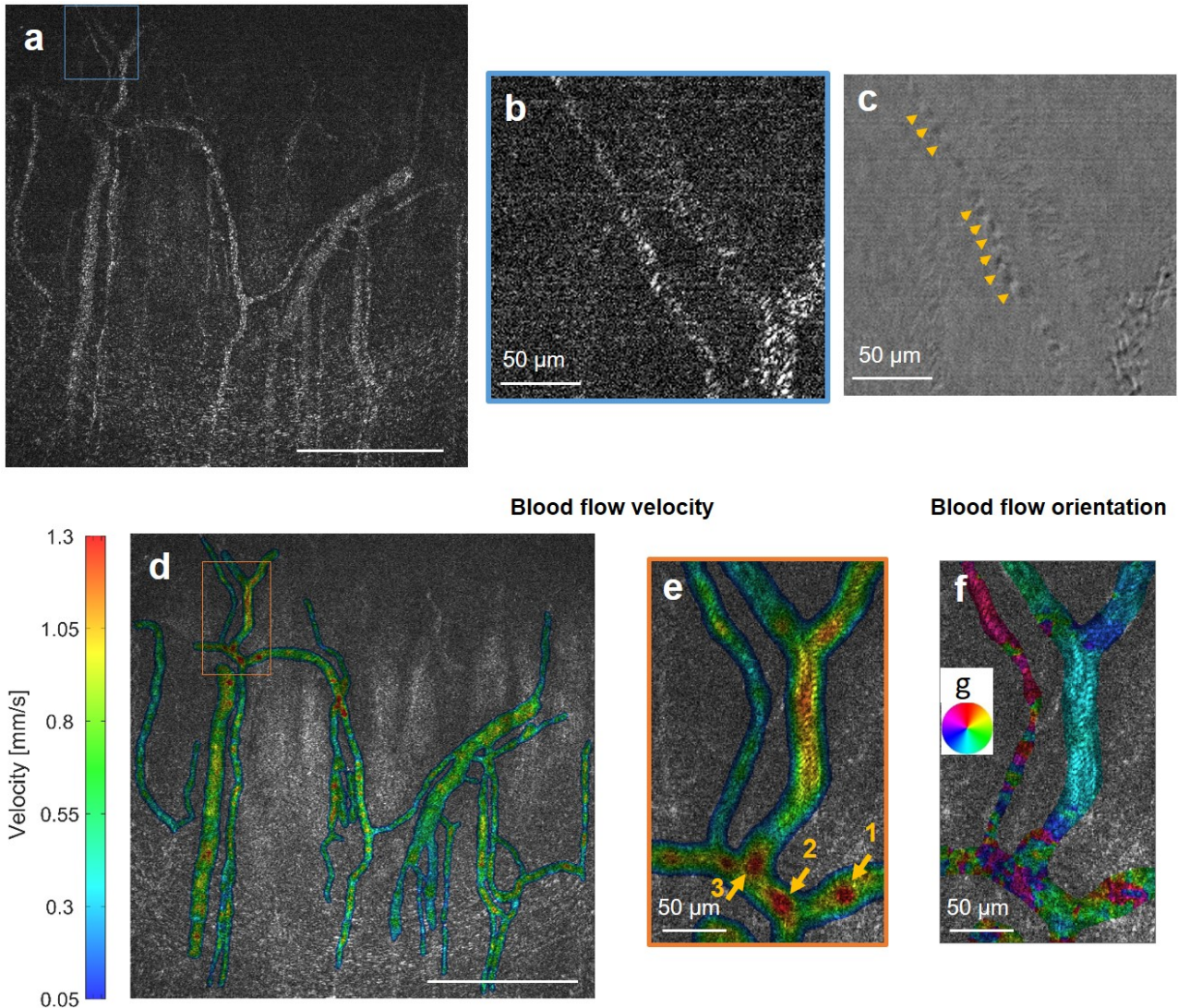


Figure 5.4 – Blood flow in the inferior limbal region below the palisades of Vogt. (a-b) Single FFOCT-frame of blood flow with a zoomed image. (c) The same zoomed image, but obtained as simple difference between the two direct reflection images (two conventional camera shots subtracted). Contrast is reduced, but is more intuitive for resolving individual erythrocytes (yellow arrows). (d,e) Blood flow velocity map, retrieved from the rapidly acquired video at 275 images/s, together with a zoomed image. The lowest speeds were measured close to vessel walls and the highest speeds in the middle of the vessels, in junction points (point 2 and point 1 (with merging vessel coming to point 1 visible only in the video)) and also, as artifacts, if vessels were overlaying on top of each other (point 3). (f) Blood flow orientation map retrieved from the video. Each color corresponds to a certain direction of blood flow, according to the colormap (g). Unlabelled scale bars 400 μm .

Previously, general information about the blood flow velocity and vessel dimensions from the fluorescein angiography proved to be useful for distinguishing between the various forms of scleral inflammation, in particular between the severe episcleritis and diffuse anterior scleritis; or between the peripheral corneal opacification and corneal thinning [120]. With FF/SD OCT, we can have access to the same information and can view the blood flow with a high contrast, but without the fluorescein injection and with the examination taking a fraction of a second. Furthermore, the ability of the instrument to capture high-resolution maps of blood flow velocities and orientations can potentially be useful for opening up new “localized” diag-

nostic methodologies and new ways to monitor effects of therapies locally. This could bring new insights about the anatomy and physiology of the vascular system in the anterior eye and, in particular about the limbal vessels and MCA supplying the cornea. Moreover, we suggest that the intravascular mapping of the blood flow with our device may be a promising platform for testing *in vivo* microfluidic theories [121].

5.3 FFOCT for tear film imaging

FFOCT can be converted to a conventional microscope by simply blocking the reference arm of the interferometer. This is useful to directly view the surface of the tear film with the high contrast and speed. Both are feasible thanks to the fast acquisition rate of the camera (550 conventional camera images/s) and high-full well capacity, providing high dynamic range in a condition of strong illumination from the surface specular reflection. In order to further increase contrast, an image of stray light from the beam splitter, acquired without the sample, was each time subtracted from the tear film image.

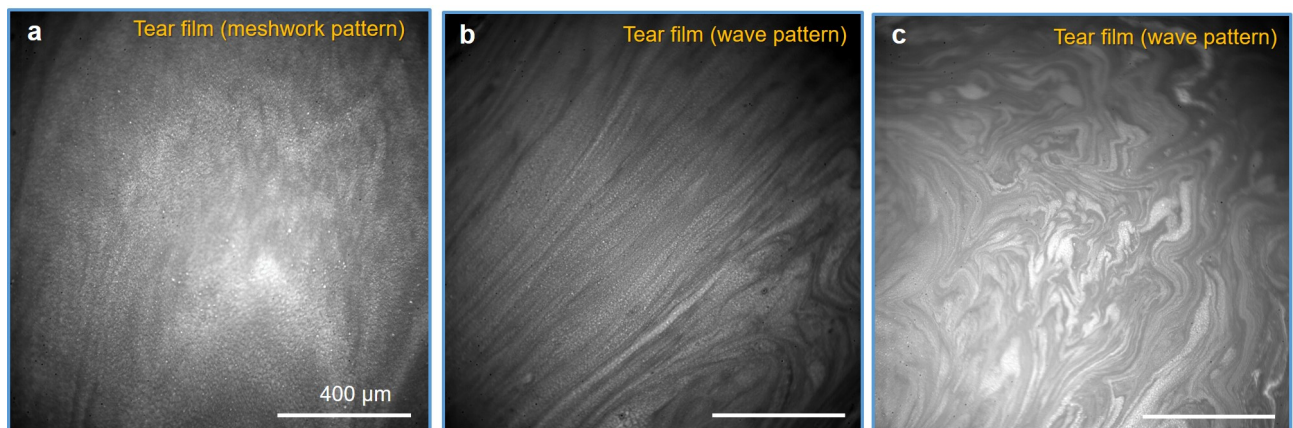


Figure 5.5 – Imaging human tear film *in vivo* with conventional microscope configuration of FF/SD OCT. (a-d) Single frame direct reflection images from the tear film. Interference patterns on the surface can be used to evaluate thickness of the lipid tear layer.

Before each examination, subjects were asked to keep their eyes closed for 2 minutes to replenish the tear film reservoir. Right after the eyes opened, a wave pattern was typically observed (figure 5.5). In the condition of opened eyes with blinks present, we often saw the meshwork patterns. We acquired videos of tear flow after the blink and after the half-blink, when the eye was not completely closed, but the tear film shifted. With the blink, the upper lid rapidly moved upward and the layer of tears followed with a slight delay. At 150 milliseconds after the blink, the flow velocity was 4.2 mm/s and rapidly decreased to 0.8 mm/s after 1 second, completely stabilizing to zero in 9 seconds, in agreement with the literature [15, 122] (figure B.18). Isolated particular matter in the lipid and aqueous layers about 1 - 40 μm , thought to be accumulations of newly secreted lipid from the Meibomian glands [15], were found in all subjects. Particles were static, changing locations only from blink to blink together with the movement of the tear film. We also noticed that small particles were frequently surrounded by the liquid drops, which were evaporating over time.

The instrument opens a door to a quantitative diagnosis of dry eye condition by providing information about tear film velocity and stabilization time following a blink, the evaporation

time of the liquid micro-droplets on the surface of the eye, and potentially the thickness of the tear film by grading the lipid interference patterns.

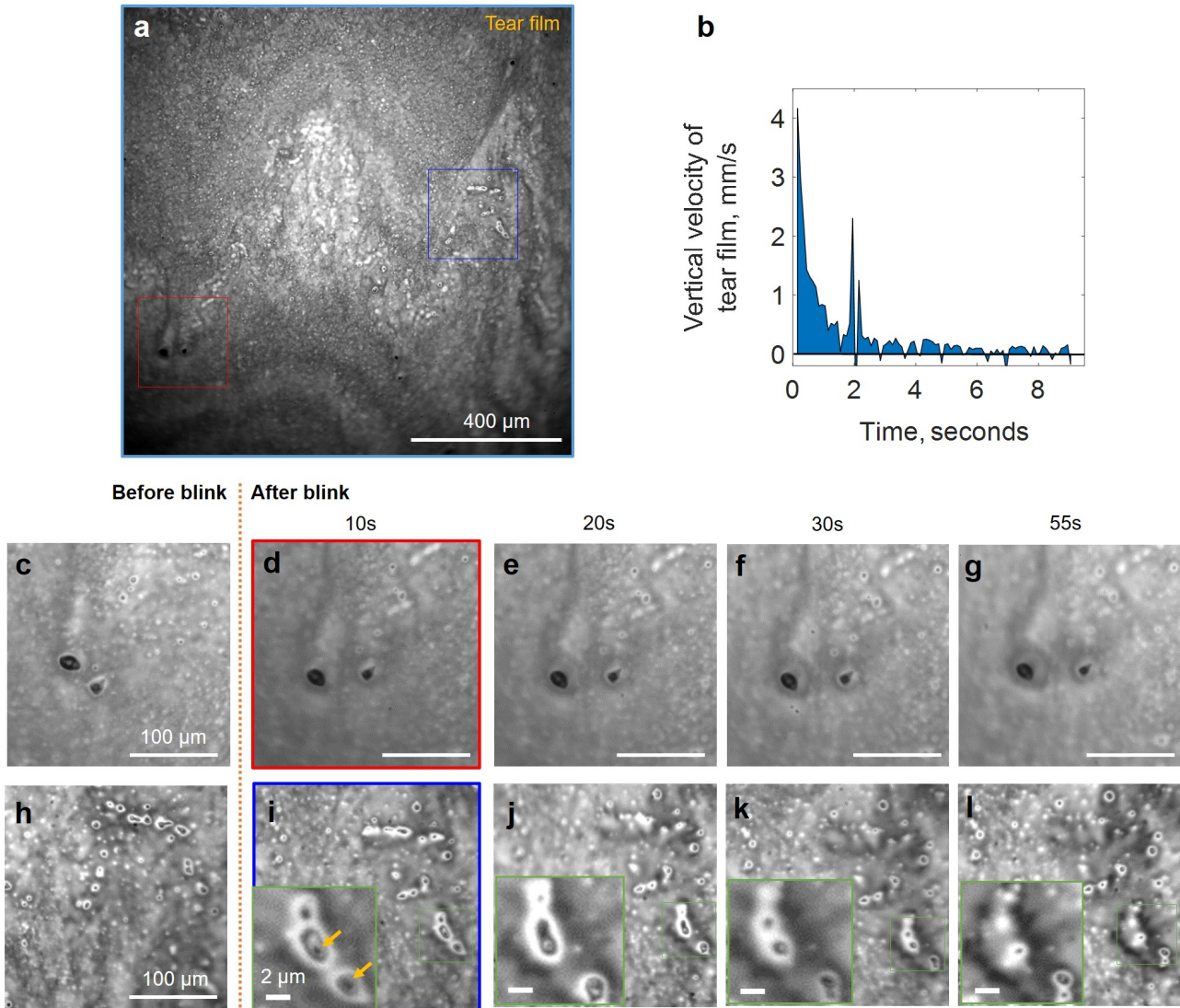


Figure 5.6 – Imaging human tear film *in vivo* with conventional microscope configuration of FF/SD OCT. (a) Single frame direct reflection image from the tear film. (b) Vertical velocity of the tear film, measured by manually tracking movements of particles in the video. Tear film stabilized after 9 seconds following the blink. Peak at 2 seconds corresponds to saccadic eye motion. (c-g, h-l) Zoomed images from the real-time blink video. Isolated particular matter, thought to be accumulations of newly secreted lipid from the Meibomian glands, were found in all the subjects. Particles were static, changing locations only from blink to blink together with the movement of the tear film. Green: zoomed images show liquid drops surrounding small particles. Liquid was evaporating over time.

CHAPTER 6

Remark on extending field of view in FFOCT

Table of contents

6.1	Extending field of view in FFOCT	90
-----	--	----

6.1 Extending field of view in FFOCT

Field of view (FOV) is important in diagnostic imaging. With a small FOV there is always a risk that a disease spot can be missed. To avoid that, a long examination time is required, which is not always available in a busy clinical setting. Nowadays, this factor is among the biggest barriers on the way to a broad clinical adoption of confocal microscopy.

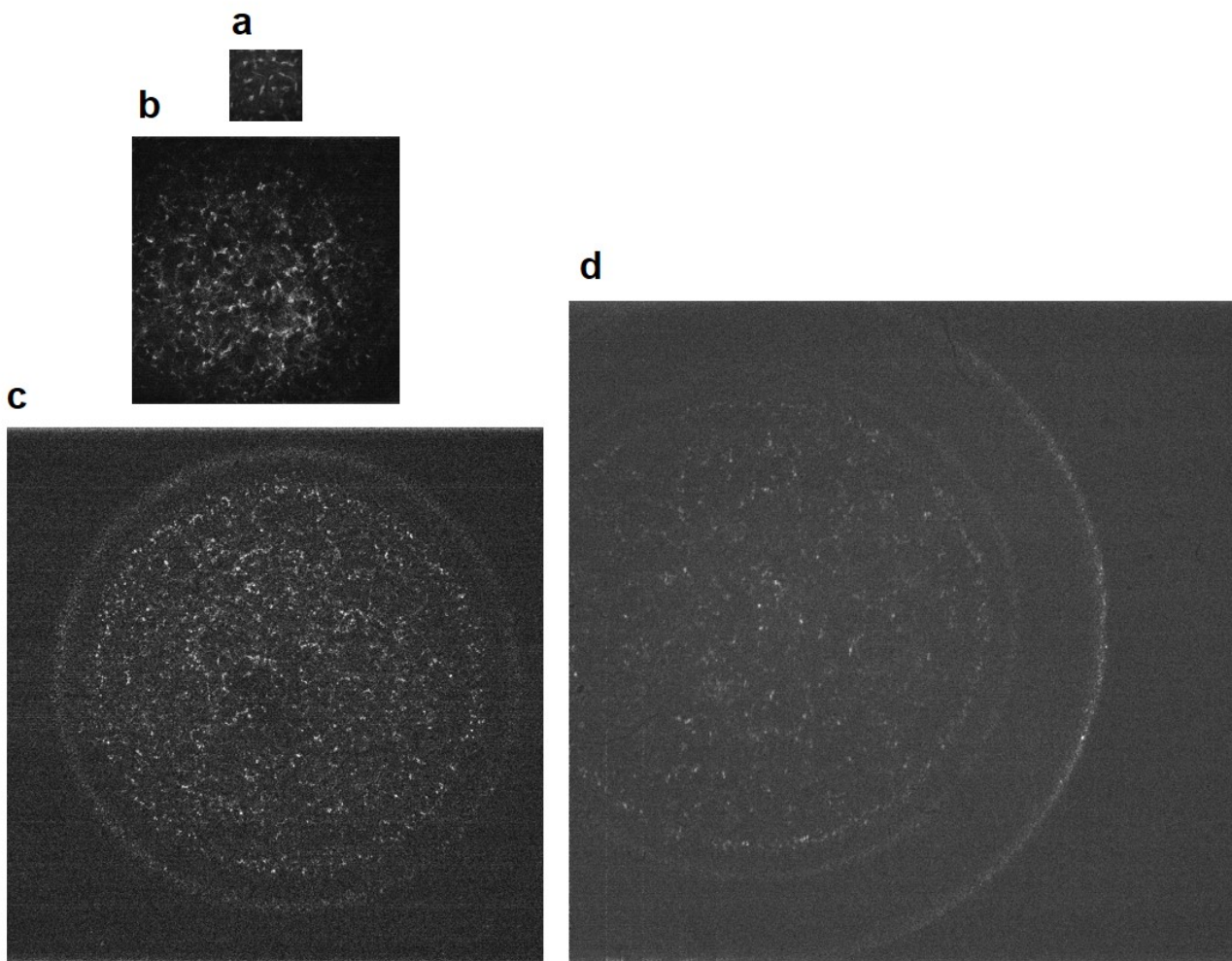


Figure 6.1 – *In vivo* human cornea, imaged with different fields of view. (a) Confocal microscopy image ($0.3 \text{ mm} \times 0.3 \text{ mm}$). (b) FFOCT ($1.25 \text{ mm} \times 1.25 \text{ mm}$). (c) FFOCT ($2.5 \text{ mm} \times 2.5 \text{ mm}$). (d) FFOCT ($3.1 \text{ mm} \times 3.1 \text{ mm}$). Image has a reduced SNR, due to the use of the visible light and not NIR microscope objective.

Previously, we have shown that FFOCT can provide a FOV of about $1.25 \text{ mm} \times 1.25 \text{ mm}$. Despite the fact that it is about an order of magnitude larger than FOV of the confocal microscope, it is still relatively limited. Therefore, we created the two additional configurations

of FFOCT device with a slightly reduced lateral resolution, but significantly higher FOV. We substituted the $10\times$, 0.3 NA microscope objectives by $5\times$, 0.14 NA in the first configuration and by $4\times$, 0.1 NA in the second. This reduced a total magnification of microscope to $7\times$ and $5\times$, increased the FOV to $2.5\text{ mm} \times 2.5\text{ mm}$ and even $3.1\text{ mm} \times 3.1\text{ mm}$, at the same time reducing the lateral resolution to $3.5\text{ }\mu\text{m}$ and $4.3\text{ }\mu\text{m}$, respectively. The reduction in lateral resolution is caused by the decrease in the numerical aperture of the optics. Alternatively, the field of view could be increased by changing the tube lens (therefore, changing magnification), while keeping the NA. In this case, however the resolution would be still reduced, because of the limited number of pixels on the camera (not sufficient spatial pixel quantization to get the full benefit of the NA resolution). Interestingly, given the recent progress in dense-pixel fabrication of CMOS sensors, it is not an overestimation to expect the development of high-full well capacity multi-million pixels sensors in the near future, opening a way to large FOV FFOCT imaging with a μm resolution.

The results are presented in the figure B.19. Bright stromal keratocytes can be resolved with every FOV. Interestingly, due to the corneal curvature, images typically show several corneal layers. For example, with the largest FOV FFOCT captures corneal epithelium, Bowman's layer, anterior and part of middle stroma in a single image. In this way FFOCT can be used, like OCT, for precise measurement of layers' thicknesses. As one example, FFOCT can potentially detect the thinning and deformation of Bowman's layer - one of the symptoms of keratoconus.

One more interesting point to notice: by using 0.1 NA objective instead of 0.3 NA, we increase the depth of focus by 9 times 3.1. Therefore, defocusing correction is no longer a requirement for imaging the anterior cornea, and the device can be considerably simplified by removing the SDOCT. Nevertheless, a drawback of lateral resolution loss should be always kept in mind.

CHAPTER 7

A glance at retinal imaging with FFOCT

Table of contents

7.1	Application of FFOCT to retinal imaging	94
-----	---	----

7.1 Application of FFOCT to retinal imaging

Together with Peng Xiao and colleagues we also worked on applying, for the first time, the time-domain FFOCT for imaging the human retina *in vivo*. Retinal imaging differs from corneal imaging in many aspects. In one way retinal imaging is easier: our ocular optics (cornea and lens) always focus the light on the retina, therefore a complicated real-time defocusing correction is not needed. However, our optics is not perfect, but affected by aberrations, which prevent the ideal point-like focusing and efficient collection of light from the retina - both factors being important for imaging. Interestingly, recently, Xiao et al. [123] discovered that resolution in FFOCT is unaffected by aberrations, but only the signal is reduced. This unique property of FFOCT is achieved thanks to interference of spatially incoherent light. In brief, if we have used a spatially coherent light source, then the aberrated broadened point-spread function (PSF) from the retina would interfere with an undisturbed reference PSF, and the retrieved OCT image would be aberrated and blurred. However, we use a spatially incoherent light source, thus the undisturbed reference PSF will interfere effectively only with the "undisturbed" part of the sample PSF, which is located in a zone within the spatial coherence of the light source. As a result, the detected interference pattern and the final image are not distorted by the aberrations. The above makes incoherent light FFOCT attractive for high-resolution retinal imaging. However, before we look through the FFOCT retinal images, it is important to also mention the drawback of FFOCT - the signal level is reduced in comparison to the adaptive optics systems, due to: 1) low proportion of undisturbed light among the total light reflected from the retina, 2) not-effective broadened retinal illumination due to aberrations.

FFOCT was adapted to retinal imaging by removing the microscope objective from the sample arm. The objective left in the reference arm was $10\times$, 0.25 NA. Light source was a 850 nm LED with a 30 nm bandwidth, providing $7.7\ \mu\text{m}$ axial resolution. Field of view was $700\ \mu\text{m}$. SDOCT was combined with FFOCT without synchronization to locate the eye position. A silicon mirror with increased reflectivity of 30% was used to saturate the camera in condition of low amount of reflected light from the retina. Camera acquired FFOCT images at 200 Hz. FFOCT device was not working in real-time, but in a single exposure pulses, acquiring 80 conventional (or 40 FFOCT) images. Images were processed with ImageJ to remove the lateral motion and averaged to increase the SNR.

The subject was sitting in front of the FFOCT device with a head positioned on a chin rest. By minimizing the light level in the room, the subject's pupil was increased to about 4.5 mm without application of the dilatation drugs. This gave the expected diffraction-limited lateral resolution of $4\ \mu\text{m}$, sufficient to resolve the photoreceptor mosaic at 6° eccentricity from the fovea center. The Fourier transform image of the photoreceptor layer, shows the ring, which corresponds to the spatial spacing of cones about $9.5\ \mu\text{m}$, as expected at 6° - 7° from the fovea.

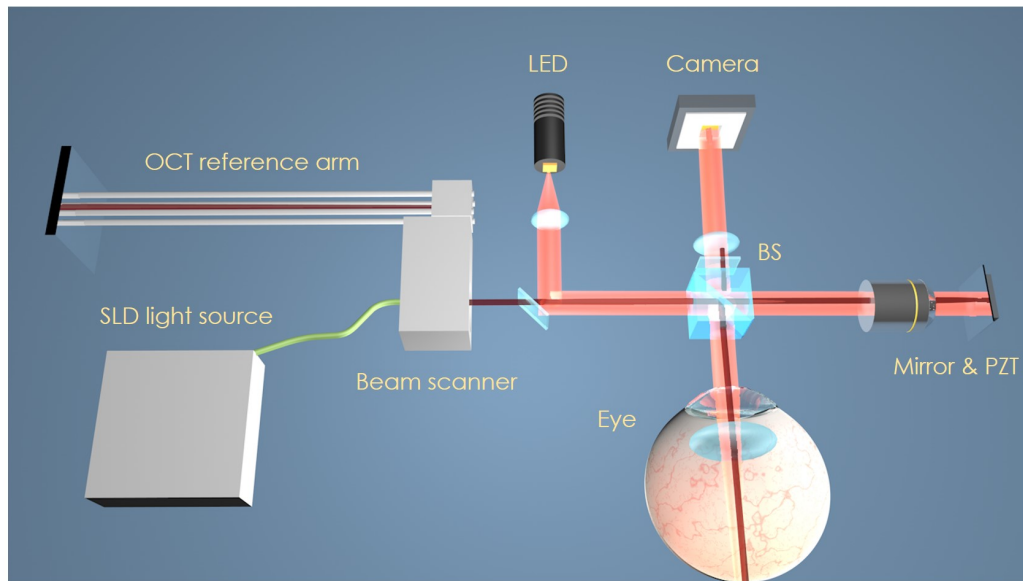


Figure 7.1 – FFOCT device for retinal imaging. FFOCT and OCT independently display the *en face* and *cross-sectional* images of the retina.

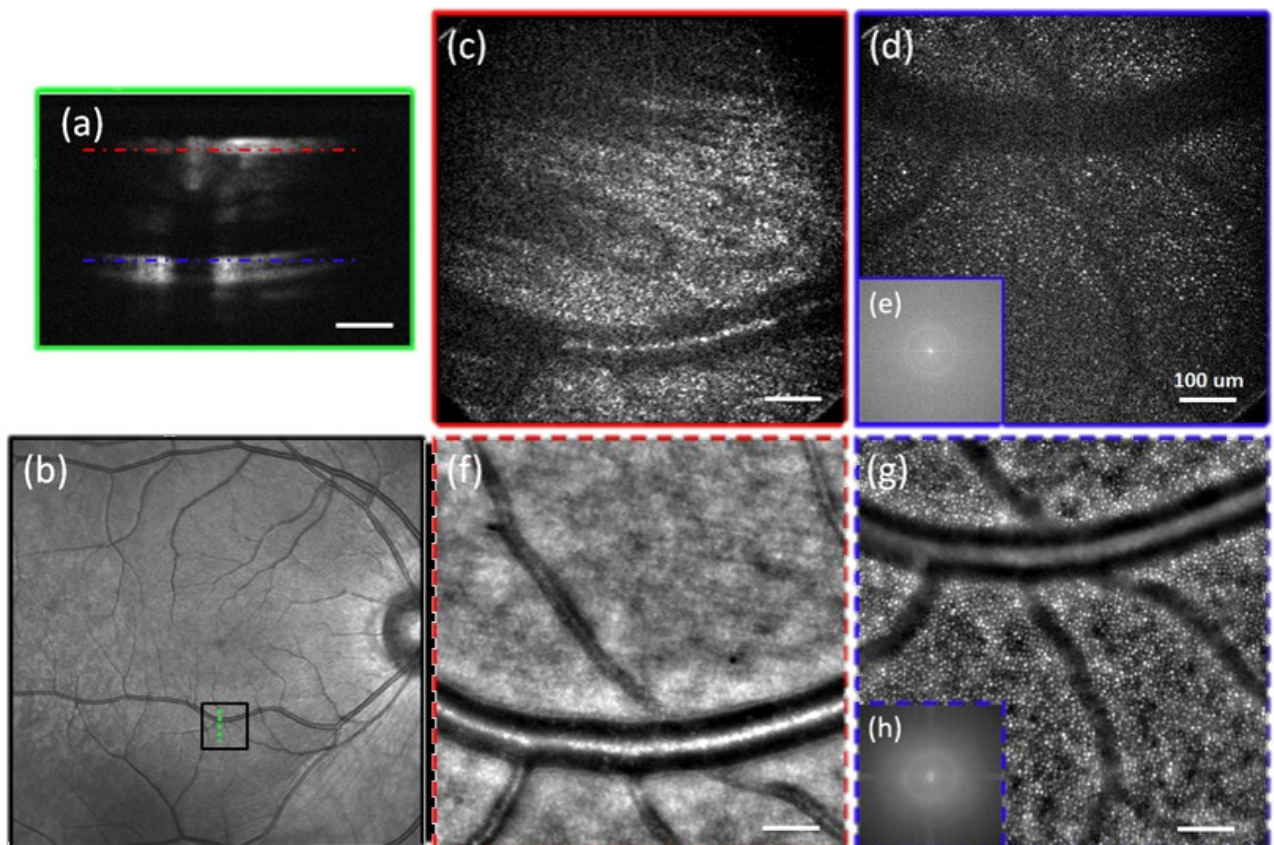


Figure 7.2 – FFOCT images of *in vivo* human retina at 6° eccentricity inferior to the fovea center [83]. (a) SDOCT image. (b) Fundus image with the black box indicating the FFOCT imaging area and the green dashed line showing the SDOCT scanning position. (c) FFOCT images of RNFL. (d) FFOCT image of the photoreceptor layer. (e) Fourier image with a ring, indicating regular spacing of the cones. (f) AO retinal camera image of RNFL. (g) AO image of photoreceptor layer. (h) Fourier image with a ring, indicating cone spacing. All scale bars = 100 μm .

We also obtained images from the above retinal nerve fiber layer (RNFL) with visible fiber orientation as well as the branching blood vessels

We compared the FFOCT images with that of a commercial AO retinal camera (RTX1, Imagine Eyes, France). AO showed the same structures, but with a higher signal. Beyond the above mentioned reasons, it is also explained by a much higher sectioning ability of FFOCT. The higher axial sectioning of FFOCT over AO is evident by comparing images (c) and (f) in figure B.20. FFOCT captures light from a fine $7.7\ \mu\text{m}$ section and does not see the blood vessel underlying the RNFL, while AO captures nerves and underlying vessels in a single image.

We also looked at the center of the fovea, however neither FFOCT nor AO device were able to reliably resolve the photoreceptor mosaic. We also conducted experiment with a dilated pupil using mydriatic drugs. In brief, we measured the decrease in cone size with increased pupil diameter, in agreement with the expected improvement in lateral resolution. However, more work is required to enable the reliable high-signal imaging of the foveal mosaic. Another important goal for the future is achieving a consistent real-time imaging and display.

CHAPTER 8

Simplifying FFOCT

Table of contents

8.1	Back to technology fundamentals: a new solution for simple FFOCT	98
8.2	Phase modulation with natural movements of <i>in vivo</i> eye	98
8.3	Intermediate conclusion	104

8.1 Back to technology fundamentals: a new solution for simple FFOCT

In the previous chapters we have seen, how FFOCT was transformed from the *ex vivo* to *in vivo* and to real-time device. In a course of this evolution it was becoming more and more complex: camera and piezo-element became very rapidly modulating in a synchronized way, moreover the entire FFOCT was morphed with the SDOCT, which together were doing the synchronized shifting of the reference motor. This type of instrumentational complexity is an important factor, which blocks many exciting imaging technologies from transferring to bedside. In this chapter we will explore, how one of the synchronization chains can be avoided, decreasing the device complexity, while keeping the comparable performance.

8.2 Phase modulation with natural movements of *in vivo* eye

In the conventional FFOCT design, the reference mirror modulates axially without stop, enabling phase-shifting and optical sectioning. Interestingly, similar thing is happening in the sample arm of the interferometer. As we know from the chapter 4, the *in vivo* human eye is constantly modulating axially, due to the heartbeat and breathing. Now, we can explore, how this movements influence on the amplitude retrieval process in FFOCT.

First, we measured the axial movements of *in vivo* human eye in time and frequency (figure 8.1). Measurements were performed with SDOCT, which acquired a new eye position every 5.5 ms. Unfortunately, this period is more sparse than the 2 frame exposure time of 3.5 ms, which prohibits analysis of the phase shift between the consecutive camera frames. Luckily, we are allowed to add more data points by making a linear approximation, because eye movements appear smooth on a short timescale, due to the lack of high frequency components. The entire approximated dataset was divided into the imaginary time windows, corresponding to 2 camera exposures (2 images). The selection of the camera acquisition start is arbitrary, thus by delaying this moment, we can add more exposure windows for our analysis.

With the first analysis we measured the phase difference between the consecutive camera frames (figure 8.2). Large proportion of the phase shifts are above π and even 2π , which leads to a conclusion that the eye movements give the leading contribution in the phase shifting. The phase shift can be either ideal, quadrature - π or absent - 0, 2π , or something in between. Another important quantity is the corneal shift between the frames. The fact that it is below the axial resolution ($7.7 \mu\text{m}$) means that we are staying within the same coherence volume during the 2 camera frames, and therefore are able to reconstruct a FFOCT image.

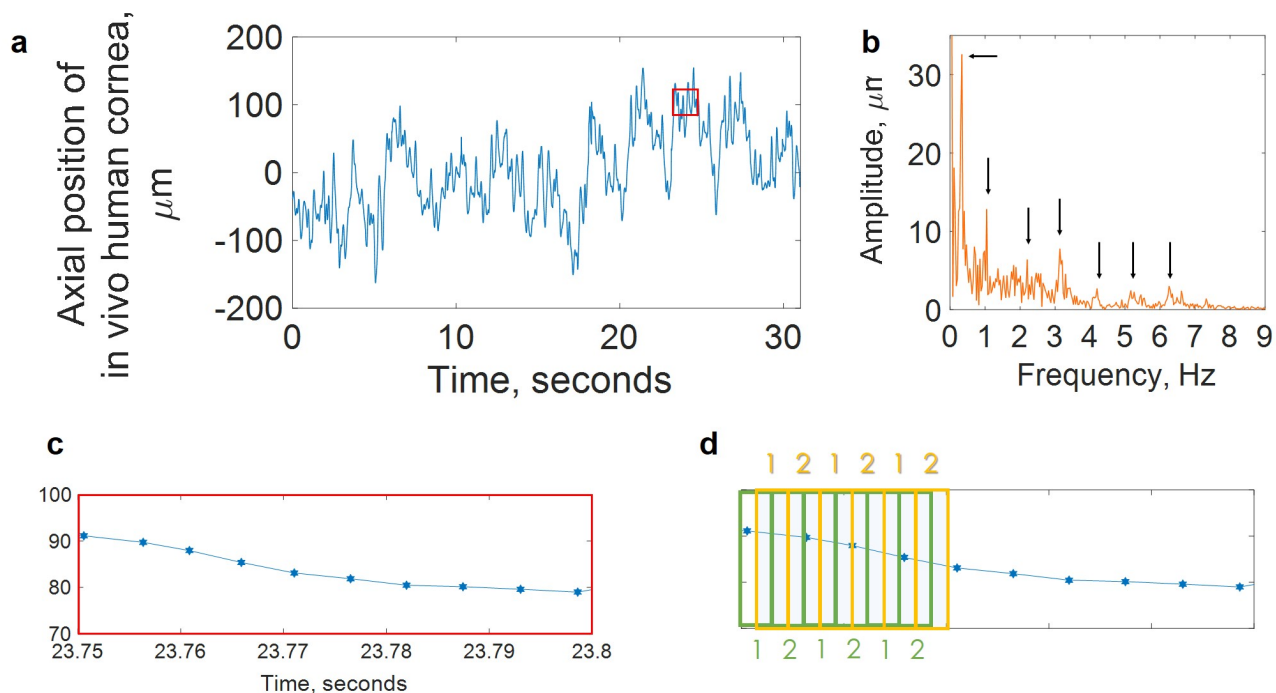


Figure 8.1 – Analysis of eye movements. (a) Axial movements of the *in vivo* human eye, measured with SDOCT. (b) Eye movement frequencies derived from the Fourier transform of (a). (c) Zoomed view on 50 ms section in the image (a). On that scale eye position slowly changes, due to absence of high frequencies in the eye motion. (d) Explanation on selecting camera exposure windows. Both yellow and green windows can be used.

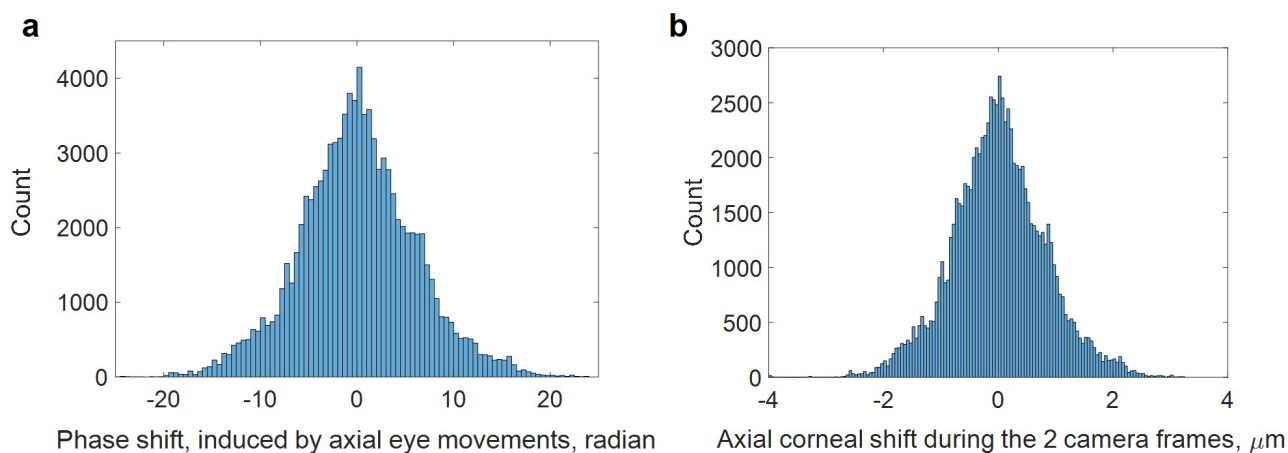


Figure 8.2 – Shifts of corneal position and phase between the 2 consecutive camera frames. (a) Histogram of phase shift between the consecutive camera frames, induced by the *in vivo* axial movements of the eye. Plot is scaled in radians ($\pi = 3.14$). (b) Histogram of axial corneal position shift between the consecutive camera frames. All the shifts are smaller than the 7.7 axial resolution of FFOCT device, thus we are always able to reconstruct the FFOCT image.

Next we looked at the FFOCT images, retrieved with a phase-shifting by the movements of the eye. As we have seen before 3.1, intensity on the camera (at one pixel) can be written as:

$$I = \frac{I_0}{4} \cdot \left\{ R_{inc} + R_{coh-sample} + R_{ref} + 2 \cdot \sqrt{R_{coh-sample} \cdot R_{ref}} \cdot \cos[\psi] \right\} \quad (8.1)$$

Before, we considered that the phase ψ is precisely determined by the piezo and is constant during one image acquisition. Now, we will consider that the eye movements also contribute to the phase shift. Thus, phase is always changing: $\psi = \psi(t)$.

For each acquisition frame, camera integrates the light during the exposure time $T_0 - T_1$:

$$I = \frac{I_0}{4} \cdot \left\{ R_{inc} + R_{coh-sample} + R_{ref} + 2 \cdot \sqrt{R_{coh-sample} \cdot R_{ref}} \cdot \int_{T_0}^{T_1} \cos[\psi_1(t)] dt \right\} \quad (8.2)$$

If we subtract two frames and square them, like in the two phase-shifting scheme:

$$(I_1 - I_2)^2 = const \cdot R_{coh-sample} \cdot \left\{ \int_{T_0}^{T_1} \cos[\psi_1(t)] dt - \int_{T_1}^{T_2} \cos[\psi_2(t)] dt \right\}^2, \quad (8.3)$$

where $T_1 - T_2$ is the exposure time of the second frame. This is different, in comparison with the equation, obtained 3.4 using only piezo modulation:

$$(I_1 - I_2)^2 = const \cdot R_{coh-sample} \quad (8.4)$$

Now, a new term:

$$\left\{ \int_{T_0}^{T_1} \cos[\psi_1(t)] dt - \int_{T_1}^{T_2} \cos[\psi_2(t)] dt \right\}^2 \quad (8.5)$$

8.5 stands out, which determines the strength of the FFOCT signal. If the 8.5 is high - the FFOCT signal is high. We calculated this term over the above *in vivo* data to determine the values, that it can have. For convenience, the term was normalized, by dividing by the two frame exposure time $T_2 - T_0$, to have the maximum absolute value limited to 1.

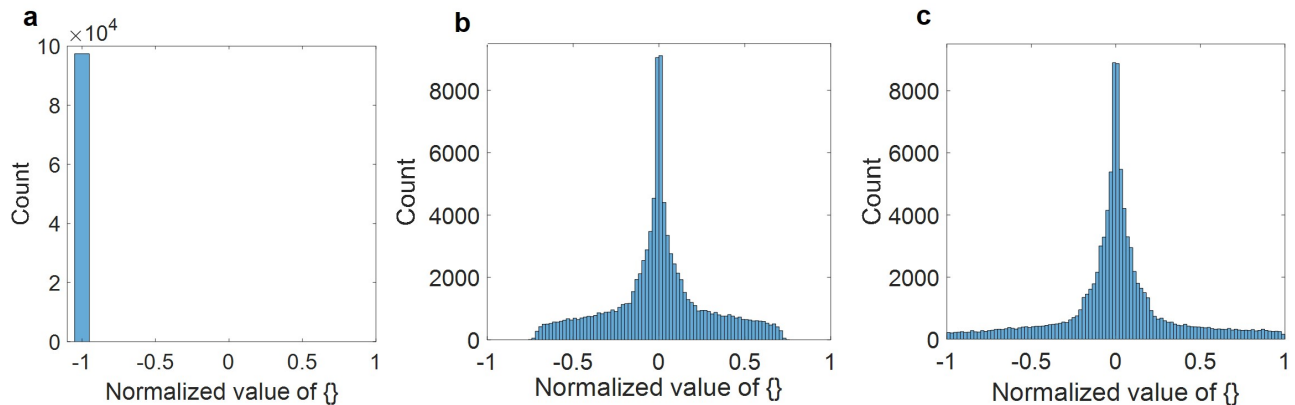


Figure 8.3 – Calculations of 8.5 for different phase-shifting schemes. (a) Phase-shifting only with π piezo modulation between the consecutive images (eye movements are ignored). In this case the FFOCT signal is maximized. (b) Phase-shifting only with *in vivo* movements of the eye (piezo is static). Interestingly, in this case maximum achievable FFOCT is limited to about 70% (comparing to the signal FFOCT signal level, achieved with a simple π phase-shifting without eye movements). Explanation is given below. (c) Phase-shifting with piezo and *in vivo* movements of the eye. In this case FFOCT signal can reach 100%.

As expected, the ideal phase shifting with an absolute value 1 is achieved, if we consider π

piezo modulation between the consecutive images, while ignoring the eye movements. Rather unusual values are obtained, if we consider only modulation by *in vivo* movements of the eye and a static piezo. More precisely, if we rely only on the phase-shifting by eye movements, we cannot have FFOCT signal higher than 70%. Interestingly, this cannot be explained by the too small movements of the eye, because, as we have seen above, they frequently give the π , 2π and higher phase-shifts between the consecutive frames. Finally, if we add a π piezo modulation to the *in vivo* movements, then FFOCT signal can reach 100%.

The explanation for this behaviour will be provided below. As we will see, in case of modulation by the eye movements, the phase is a continuous function of time, while, in case of piezo modulation, it is not. The discontinuous step-like modulation leads to the higher values of the FFOCT signal.

We start with equation 8.5. For simplicity, we can assume that on the scale of camera exposure time the phase is a linear function:

$$\int_{T_0}^{T_1} \cos[\psi(t)] dt - \int_{T_1}^{T_2} \cos[\psi(t)] dt = \{\psi(t) = a \cdot t\} = \int_{T_0}^{T_1} \cos[a \cdot t] dt - \int_{T_1}^{T_2} \cos[a \cdot t] dt \quad (8.6)$$

The integrals can be directly computed:

$$\frac{1}{a} [\sin(a \cdot T_1) - \sin(a \cdot T_0) - \sin(a \cdot T_2) + \sin(a \cdot T_1)], \quad (8.7)$$

Where a is the linear coefficient. Then, by taking $T_0 = 0$ and dividing by the 2 frame exposure time $T_2 - T_0 = T_2 - 0$ for normalization, we end up with:

$$\frac{\sin \tau \cdot [1 - \cos \tau]}{\tau}, \quad (8.8)$$

where $\tau = a \cdot T_1$.

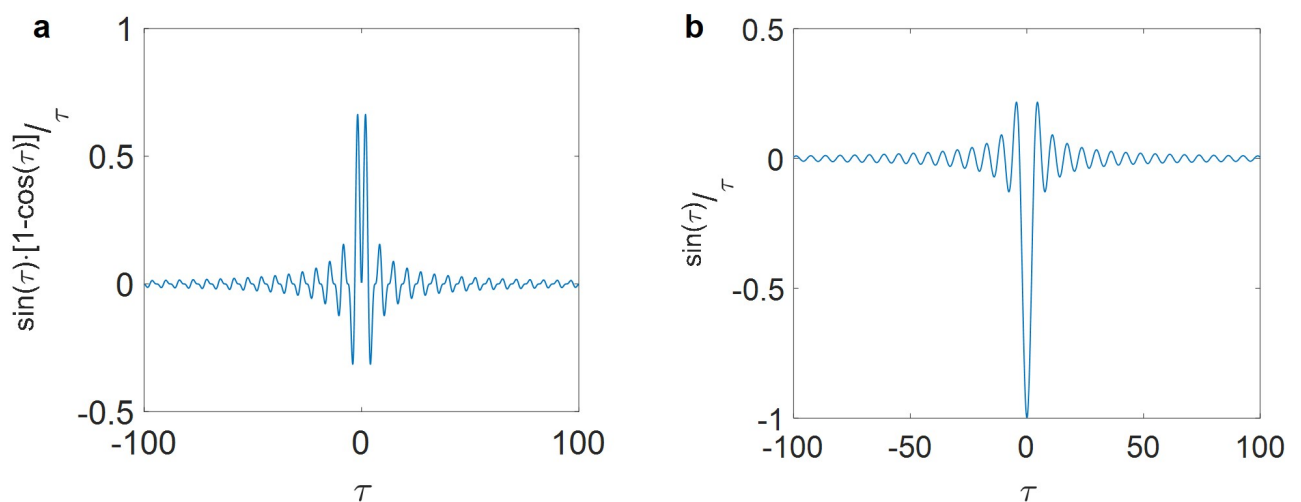


Figure 8.4 – Computing function 8.5. (a) Only linear eye modulation, no piezo. The maximum value of 0.66 can be achieved. (b) Linear eye modulation, assisted with piezo step movement. The maximum value of 1 can be achieved.

As well as the a and τ , this function can take various values with the maximum being 0.66

(figure 8.4). This is also a limit for FFOCT signal, retrieved using only eye movement phase-shifting. On the contrary, if, in addition to the *in vivo* phase-shifting, we turn on the π piezo modulation:

$$\int_{T_0}^{T_1} \cos [a \cdot t + \pi] dt - \int_{T_1}^{T_2} \cos [a \cdot t] dt = - \int_{T_0}^{T_2} \cos [a \cdot t] dt \tag{8.9}$$

Again normalizing equation by dividing with 2 frame exposure time, we end up with:

$$- \frac{\sin \tau}{\tau} \tag{8.10}$$

This function can have all the values up to the maximum of 1 (figure 8.4). Therefore, with piezo and eye modulation together, 100% FFOCT signal can be achieved.

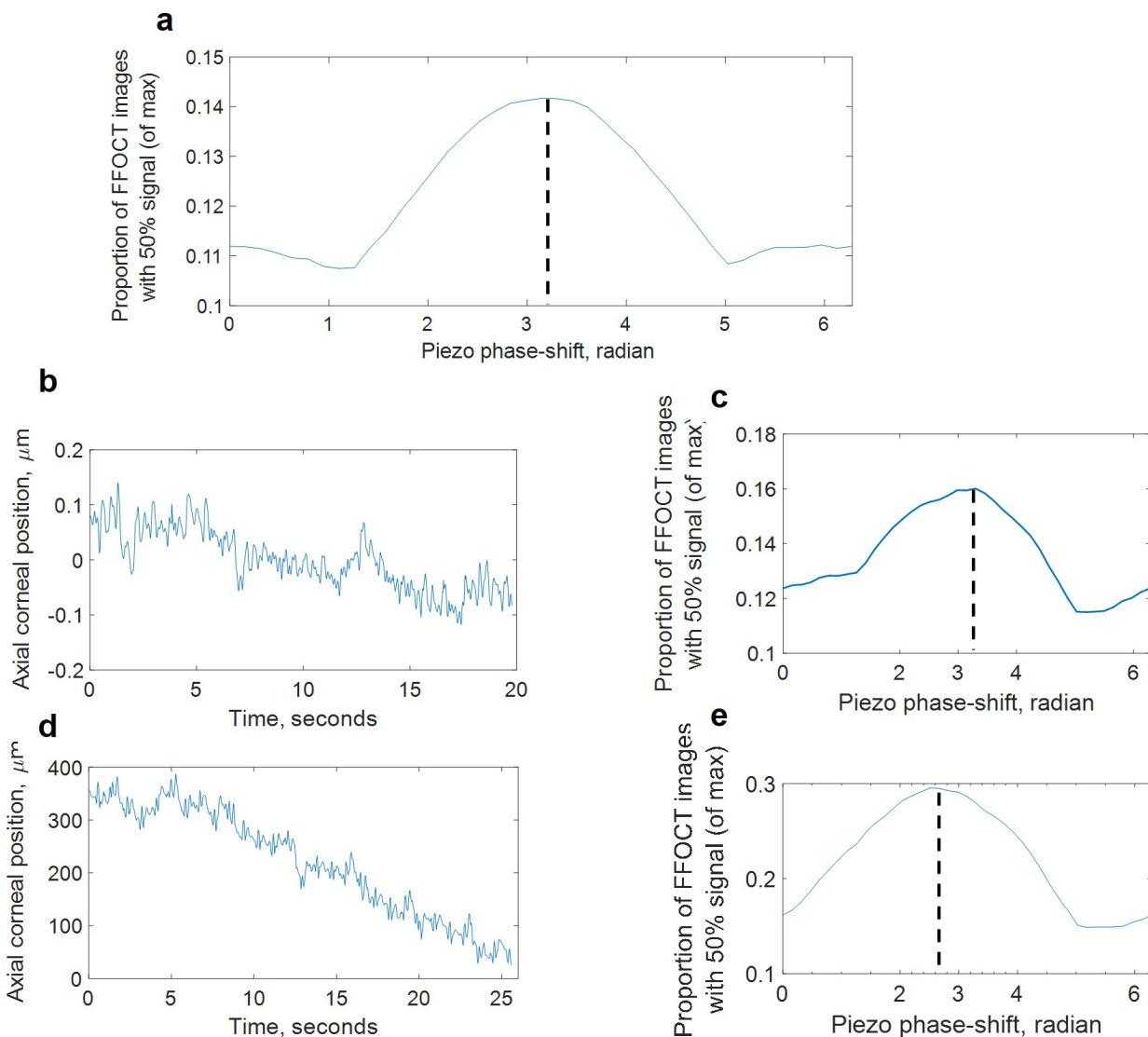


Figure 8.5 – Plots of probability to have FFOCT images with a high signal (>50%) depending on the additional phase-shift, induced by the piezo. Measurements from 3 normal subjects. (a,c,e) Dependency of percentage of high Only linear eye modulation, no piezo. The maximum value of 0.66 can be achieved. (b,d) Axial eye movement plots, corresponding to the (c,e) graphs, respectively.

Next, it is interesting to check, how FFOCT signal changes with a changing amplitude of

piezo modulation (here we are considering that the *in vivo* movements are present and piezo provides an additional phase-shift). FFOCT achieves the maximum signal at π piezo shifting (figure 8.5), which is explained by the large proportion of 0, 2π , etc. phase shifts in the ocular motions. With a π piezo modulation, about 14% of the FFOCT images will have more than 50% of maximum achievable signal. Interestingly, with piezo modulation disabled, about 11% of all FFOCT images will have the same 50% of the highest signal. Therefore, by keeping piezo modulation, we are by 1.3 times more likely to get high (50%) FFOCT signal in the images, moreover among these 50% many signals can be above 70%, which is not possible without piezo modulation

We repeated the same measurements for 3 subjects and have seen the similar behaviour (figure 8.5). At the peak, the percentage of FFOCT images with the highest (50%) signal was reaching 30%. Typically, axial eye position fluctuates around the same mean value, due to the periodic motions of heartbeat and breathing. Sometimes, however, subject's head maybe be unintentionally steadily shifting in the axial direction. Clearly, in this case we measure the different optimal piezo shift, which is smaller or larger depending on the direction of the eye movements.

We also looked at the changes happening with reducing and increasing the exposure time of the camera (figure 8.6).

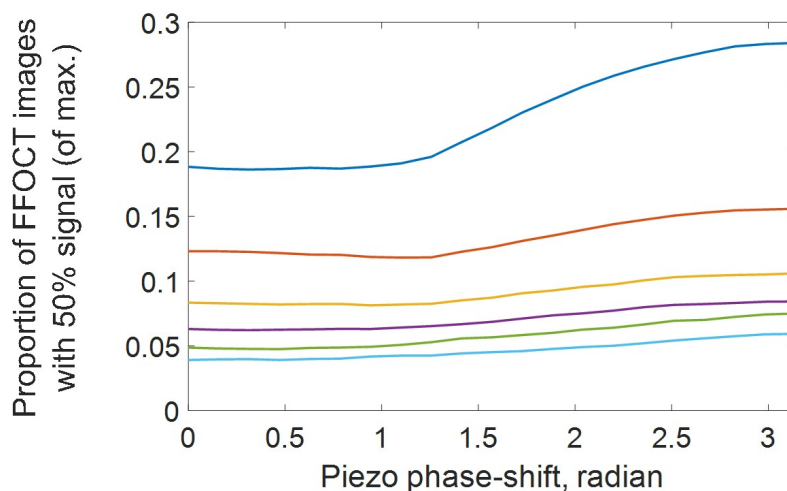


Figure 8.6 – Different curves correspond to different 2 camera frame exposure times. Plots show the percentage of high signal (>50%) FFOCT images depending on the additional phase-shift, induced by the piezo. The shortest exposure time in the graph is 1.75 ms (high blue), the longest is 10.5 ms (low cyan). The lower the curve the larger is the exposure time. Step between the curves - 1.75 ms.

The exposure time for the two images was varying from 1.75 ms to 10.5 ms. With increasing time, the effect of piezo-modulation was becoming less pronounced, because during the longer exposure time the axial motions are larger and play the decisive role. Now, if we ignore the piezo modulation, we notice that the shorter is the exposure time, the higher is the percentage of high signal FFOCT images. This can be explained from the figure 8.4. By decreasing the exposure time, we decrease the time τ , therefore coming closer to the 0 position (maximum) for the same linear coefficient a .

We also successfully obtained FFOCT images using just the axial eye motion (figure 8.7). Although the high-signal images were slightly less frequent, the instrument became considerably simplified without the camera-piezo synchronization.

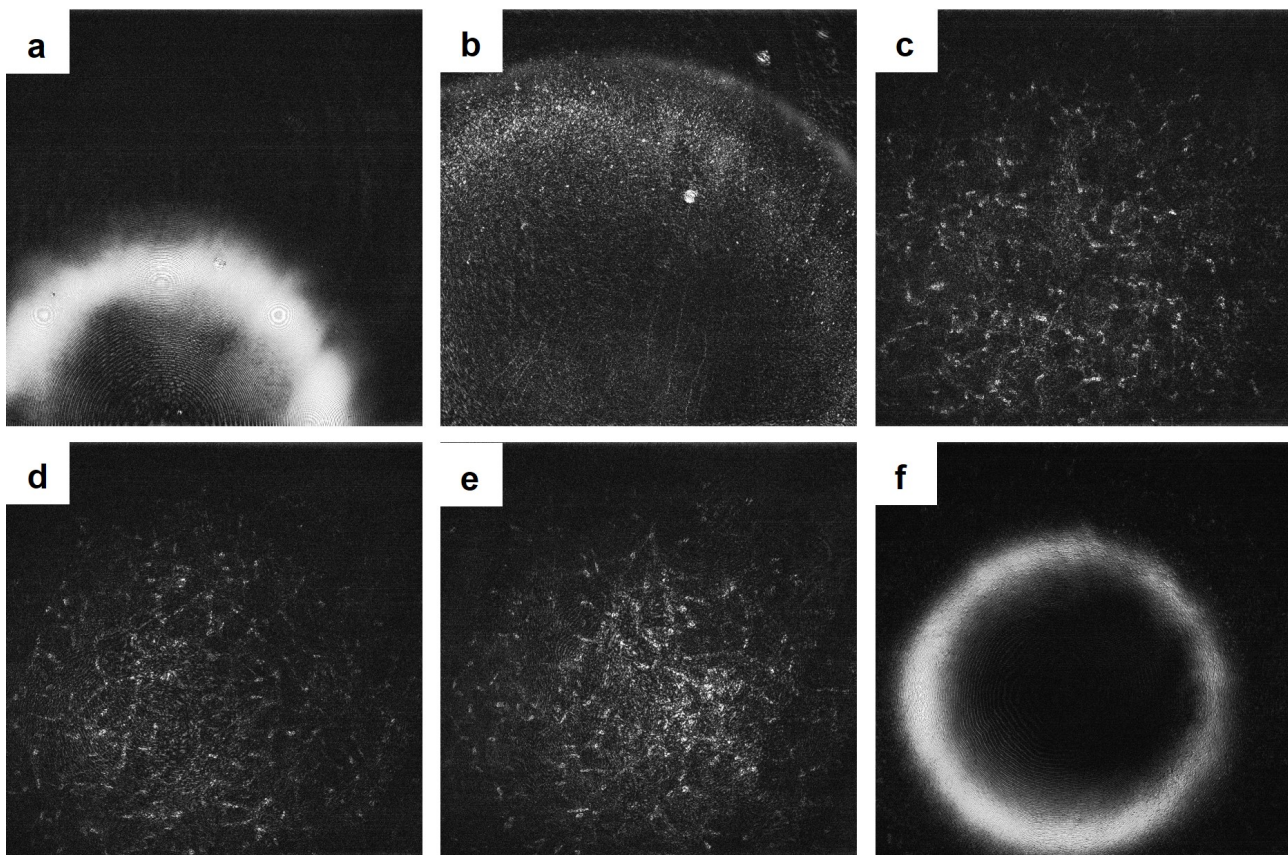


Figure 8.7 – FFOCT images, obtained by phase-shifting with the axial eye motion (no piezo). (a) Reflection from the epithelium and tear film. (b) Epithelium and sub-basal nerves. (c-e) Anterior, middle, posterior stroma. (f) Endothelium.

8.3 Intermediate conclusion

Here we have shown that, on the scale of several milliseconds, axial eye movements of the human eye play essential role in optical phase-shifting and image retrieval in FFOCT. Therefore, instead of talking about the reliable FFOCT image retrieval, we have to talk about the probability of having a FFOCT image with a high signal. We saw that this probability is slightly higher, when the π piezo shifting is used. Piezo shifting also increases the signal level. Nevertheless, if the main concern is the simplicity of the device, piezo can be made static and the camera-piezo synchronization can be removed, while the FFOCT images with a sufficient signal can be still retrieved.

Conclusions and perspectives

Through this manuscript, we have seen the evolution of time-domain full-field optical coherence tomography (FFOCT) from the purely *ex vivo* device for tissues screening into an *in vivo* tool for diagnostics in the human eye. Manuscript has highlighted our development of the two original optical microscopes that can capture corneal images from *in vivo* human eye with a μm -level 3D resolution.

The initial FFOCT microscope [3] became the first system to view *in vivo* human cornea with a high lateral resolution together with a relatively large $1.26 \mu\text{m} \times 1.26 \mu\text{m}$ field of view at the same time. Large field of view makes it easier to locate the clinical area of interest and follow the healing progress of the same location over time. Moreover, this device became a pioneer in non-contact imaging of the entire human cornea, visualizing the sub-basal nerves, endothelium cells and anterior, middle, posterior stromal keratocytes. Comparing to the contact confocal microscopy method, currently used in clinics, the non-contact approach improves patient comfort, removes risk of corneal damage and risk of infection, and opens up the possibility for high-resolution imaging in a risk-sensitive population (e.g. young children, candidates for corneal transplant surgery with fragile corneas).

The second developed device was a combined common-path full-field OCT / spectral-domain OCT (FF/SD OCT). It could perform real-time axial eye tracking together with a simultaneous defocusing correction, enabling real-time *in vivo* FFOCT imaging for the first time. Unlike the first device, FF/SD OCT was not limited to the central cornea and could explore the entire ocular surface, including the corneal periphery, limbus and sclera. Moreover, images from the real time videos, which it provided, had a sufficiently high signal to perform the quantitative analysis of the corneal health. Cells and nerves could be precisely counted according to the existing medical protocols for clinical confocal microscopy, assisting in diagnosis of acute ischemic stroke, diabetes, corneal dystrophies, keratitis etc. The above opens a path for FFOCT implementation in clinical research and translation into practice.

We also emphasized the first application of FFOCT to dynamic processes in the eye. The fast image acquisition design (0.6 billion camera pixels/second) allowed direct monitoring of the blood flow dynamics with a high contrast, without fluorescein injection (unlike, the clinical ICGA today) and with examination taking a fraction of a second. Resolution was high enough to see the propagation of individual cells inside the thin vessels. Furthermore, this technology

enabled the creation of a full-field high-resolution blood flow velocity map of the human limbus for the first time. This could be potentially useful for opening new "localized" diagnostic methodologies of scleral inflammation and new ways to monitor the effects of therapies locally. Interestingly, FFOCT can be easily (during the on-going examination) converted into the conventional microscope, useful to follow the tear film evolution. The instrument opens a door to quantitative diagnosis of dry eye condition by providing information about the tear film velocity and stabilization time following a blink, the evaporation time of the liquid micro-droplets on the surface of the eye, and potentially the thickness of the tear film by grading the visible lipid interference patterns.

This thesis also presents an application of the conventional FFOCT to *in vivo* human retinal imaging [83]. A FFOCT design, close to that of FFOCT corneal instrument, allowed μm -level resolution imaging, resolving the cone photoreceptor mosaic and orientation of the retinal nerve fibers.

Lastly, we proposed several potentially useful improvements to the *in vivo* FFOCT. The first one demonstrated the increased field of view up to $3.1 \text{ mm} \times 3.1 \text{ mm}$, which is suited for measuring the thicknesses of corneal layers and for showing OCT-like corneal cross-section. The second improvement simplified the FFOCT design by substituting the phase modulation, induced with the piezo via the phase modulation, induced with the natural axial movements of *in vivo* human eye.

The manuscript was committed to provide a global state-of-the-art picture on corneal diagnostics, synthesizing together the fundamental research, practical technology and medical applications.

It is highly likely that FFOCT and other *en face* full-field imaging modalities will have a significant impact on the healthcare in the future. The main argument supporting this prediction is that the layers in the human tissues are typically oriented laterally (this is also applicable for cornea and retina). Therefore, instrument with a lateral view can be used to count cells and nerves within the same layer and come up with a quantitative diagnosis, based on this counting. These types of applications motivate the broad research devoted to increasing the speed of a classical scanning OCT, which needs to acquire 3D images to retrieve the *en face* view. As we have seen in the manuscript, it is unlikely that even the fastest scanning OCT systems will soon be able to reach the *en face* imaging speed of the *en face* full-field systems (there is currently a margin of order of 100). Therefore, in *en face* view, full-field methods will continue to have less movement artifacts and higher time accuracy for monitoring the dynamic processes, comparing to the scanning OCT.

In this manuscript we have demonstrated the very first application of conventional FFOCT to *in vivo* human eye imaging, and there is still a large room for potential improvements. These improvements, like in every OCT technique, largely depend on the developments in the underlying component supplying industry. While the classical OCT has already formed its market and is supported by the manufacturers of the light sources and detectors, the FFOCT is still in its infancy with only a single company producing application-focused camera sensors. In this way it is remarkable that FFOCT without the industry support can produce *in vivo* images comparable and even advantageous (in some aspects) to OCT. There is a possibility that with a coming introduction of FFOCT to clinics the new target clinical applications will

be found, potentially creating a market opportunity and a consequent interest of a component supplying industry. Below, we will explore, which future improvements are expected in FFOCT, given the current state of the optical equipment technology.

Recent years have shown great developments in the CMOS camera sensor technology. One of the development directions was focused on the dense pixel manufacturing. Today we can see the output of this work in the 64 megapixel compact cell-phone cameras and 102 megapixel consumer cameras. Therefore, we can expect the increase in the number of pixels of FFOCT sensors, which currently provide just around 2 megapixels. With more pixels, FFOCT can have a high resolution and a very large field of view at the same time. Fundamentally, the field of view is limited by the microscope objective, nevertheless from the current state it can be increased by several times before the aberrations will start to have a noticeable effect. Even if more pixels are not used to increase the field of view, they can be applied to average the signals and vastly improve the image quality. The image averaging is one of the biggest benefits of the flourishing clinical swept-source OCT systems. These systems do not provide improvement in lateral resolution, nevertheless the rapid, dense A-line acquisition makes the signal-to-noise ratio considerably better.

With more pixels we increase the amount of information that camera acquires and sends to the computer, which may prohibit real-time imaging. However, the upcoming communication technologies are likely to solve the communication speed problems, with even casual consumer USB 4.0 permitting 5 Gbyte/second transfer rate.

Another important improvement for FFOCT is the increase in the pixel capacity and bit depth. The higher is the pixel capacity, the more sensitive is the camera to the small variations of signal intensity under the strong illumination conditions, and, therefore, more sensitive to FFOCT interference signals. Unfortunately, the higher full-well capacity camera requires more light to get it saturated. At the same time, the ocular safety standards set the upper limit for the maximal corneal and retinal illuminations. Thus, with the higher pixel capacity and higher illumination, we will be required to increase the pause between the exposures, thus considerably reducing the real-time frame rate. Interestingly, a solution to this bottleneck problem may come within several years. Currently, a new project ISO 15004-2 standard is under consideration as a substitution for the up-to-date ISO 15004-2:2007 ocular safety standard, dating back to 2007. The proposed ISO in many ways matches with the recently accepted ANSI Z80.36-2016. For cornea it removes the bounding 60 mW/cm^2 (100 mW/cm^2 for Group 2) limit for wavelength below 915 nm, therefore allowing us to have considerably larger corneal exposure levels and, thus the higher pixel capacity and SNR. The last question on the way to the higher SNR that was not discussed before: can light emitting diodes (LED) provide the sufficient power? Many powerful LED's are present on the market with some being used even for the illumination on highways. However, they typically operate in the visible range, moreover, due to a large chip size, it is challenging to focus them into the small illumination spot on the cornea without having a lot of stray light coming from the other locations of the eye. Luckily, a new generation of powerful and very compact LED's is coming now, driven by the application of face recognition on the smartphones. These LED's operate in the near infrared (NIR) range and have various spectral bandwidths. By choosing the broadband LED we can increase the axial resolution in FFOCT, at the same time compensating for signal loss from the thinner section by increasing the illumination power.

Lateral resolution in FFOCT can be improved by increasing the numerical aperture (NA). In the recent years a large number of high-NA long working distance objectives became available. By using $NA = 0.45$, we can have $1.1 \mu\text{m}$ resolution and 9 mm working distance, while $NA = 0.65$ allows the $0.8 \mu\text{m}$ resolution and 5 mm working distance.

As one could notice, the list above was limited only to the technology-level improvements. However, undoubtedly, the interesting innovations coming from research, which created an OCT itself, should not be disregarded.

Papers

Viacheslav Mazlin, Peng Xiao, Jules Scholler, Kristina Irsch, Kate Grieve, Mathias Fink and A. Claude Boccara, "Real-time, non-contact, cellular imaging and angiography of human cornea and limbus with common-path Full-field/SD OCT," **Nature Communications (Under review)**.

Jules Scholler, **Viacheslav Mazlin**, Olivier Thouvenin, Kassandra Groux, Peng Xiao, José-Alain Sahel, Mathias Fink, Claude Boccara, and Kate Grieve, "Probing dynamic processes in the eye at multiple spatial and temporal scales with multimodal full field OCT," **Biomed. Opt. Express** 10, 731-746 (2019).

Peng Xiao, **Viacheslav Mazlin**, Kate Grieve, Jose-Alain Sahel, Mathias Fink, and A. Claude Boccara, "In vivo high-resolution human retinal imaging with wavefront-correctionless full-field OCT," **Optica** 5, 409-412 (2018).

Viacheslav Mazlin, Peng Xiao, Eugénie Dalimier, Kate Grieve, Kristina Irsch, José-Alain Sahel, Mathias Fink, and A. Claude Boccara, "In vivo high resolution human corneal imaging using full-field optical coherence tomography," **Biomed. Opt. Express** 9, 557-568 (2018).

Oral presentations and conference proceedings

Viacheslav Mazlin, Eugénie Dalimier, Kate Grieve, Kristina Irsch, José-Alain Sahel, Mathias Fink and A. Claude Boccara, "Non-contact full-field optical coherence tomography: a novel tool for in vivo imaging of the human cornea," Proceedings Volume 10045, Ophthalmic Technologies XXVII; 1004519, **SPIE Photonics West 2017**.

Viacheslav Mazlin, Peng Xiao, Eugénie Dalimier, Kate Grieve, Kristina Irsch, José Sahel, Mathias Fink and A. Claude Boccara, "In vivo imaging through the entire thickness of human cornea by full-field optical coherence tomography," Proceedings Volume 10474, Ophthalmic Technologies XXVIII; 104740S, **SPIE Photonics West 2018**.

Viacheslav Mazlin, Peng Xiao, Kate Grieve, Kristina Irsch, Mathias Fink and A. Claude Boccara, "A novel non-contact instrument for en face cellular resolution imaging of *in vivo* human cornea based on full-field OCT", **ARVO 2018**, Abstract 3437.

Viacheslav Mazlin, Peng Xiao, Kate Grieve, Kristina Irsch, José Sahel, Mathias Fink and A. Claude Boccara, "Volumetric Imaging of In Vivo Human Eye by Full-Field OCT," Ophthalmic Technologies XXVIII, **SPIE Photonics West 2019**.

Viacheslav Mazlin, Peng Xiao, Kate Grieve, Kristina Irsch, José Sahel, Mathias Fink and A. Claude Boccara, "Real-Time Defocus-Corrected Full-Field OCT with Axial Eye Tracking for Consistent High-SNR Imaging of In Vivo Anterior Human Eye," Optical Coherence Tomography and Coherence Domain Optical Methods in Biomedicine XXIII, **SPIE Photonics West 2019**.

Viacheslav Mazlin, Jules Scholler, Peng Xiao, Kate Grieve, Kristina Irsch, Mathias Fink and A. Claude Boccara, "Non-contact, cell-detail, real-time full-field OCT: capabilities and potential clinical applications of the novel anterior eye imaging tool", **ARVO Imaging in the Eye 2019**.

A.1 General remarks

Safety requirements for the ophthalmic instruments in European Union are defined by the up-to-date standards of the International Organization for Standardization (ISO) (15004-2:2007 and 15004-1:2007 standards [124, 125]). Scope of these standards is broad and encompasses all the ocular diagnostic instruments, ocular monitoring instruments, microscopes, and therefore the FFOCT device. Safety of FFOCT device will be evaluated based on the permitted light exposure levels according to ISO 15004-2:2007.

The ISO 15004-2:2007 standard sets safe light exposure limits for ophthalmic instruments. It classifies them, based on their exposure type, into continuous or pulsed and, based on the accuracy of exposure measurements, into group 1 or group 2. Instrument is set into group 2 and can be evaluated based on the group 2 limits, if the uncertainty in the optical radiation measurements is less than $\pm 30\%$ [126], otherwise it is set into group 1; instrument should emit optical radiation in pulses shorter than 20 seconds to be classified as pulsed, otherwise it is classified as continuous. Given that the uncertainty in FFOCT optical radiation measurements is substantially less than $\pm 30\%$ (accuracy of measurement instruments is provided below) and that every pulse duration is shorter than 1 second (measured pulse patterns are provided below), FFOCT was evaluated as group 2 pulsed device.

In normal practice FFOCT can be used in two configurations: configuration for anterior segment imaging and configuration for retinal imaging. Both are shown in figure A.1. Below, we will evaluate the safety of these configuration in the several example exposure scenarios.

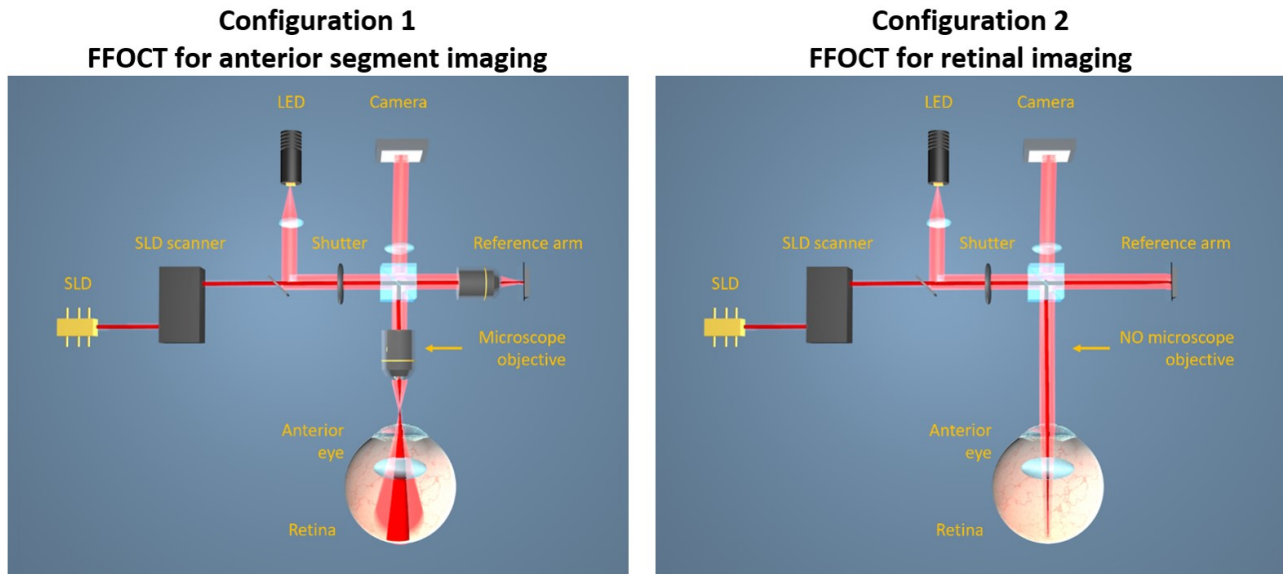


Figure A.1 – illustration of two device configurations. Configuration 1 is used for anterior segment imaging. Configuration 2 is used for retinal imaging. Illumination in both configurations is given by near-infrared (NIR) 850 nm light emitting diode (LED) and infrared (IR) 930 nm superluminescent diode (SLD), comfortable for viewing due to low sensitivity of the retina to NIR and IR light.

A.2 Light safety analysis for the FFOCT device according to the ISO 15004-2:2007 standard

A.2.1 Security analysis considerations

The potential hazards of the FFOCT device are related only to the exposure of the eye (to the illumination from LED and SLD beams). LED emits NIR light at 850 nm, while SLD emits IR light with central wavelength of 935 nm. Both light sources are comfortable for viewing, due to low sensitivity of the retina to NIR and IR light. Figure A.2 shows the measured spectrums of light sources.

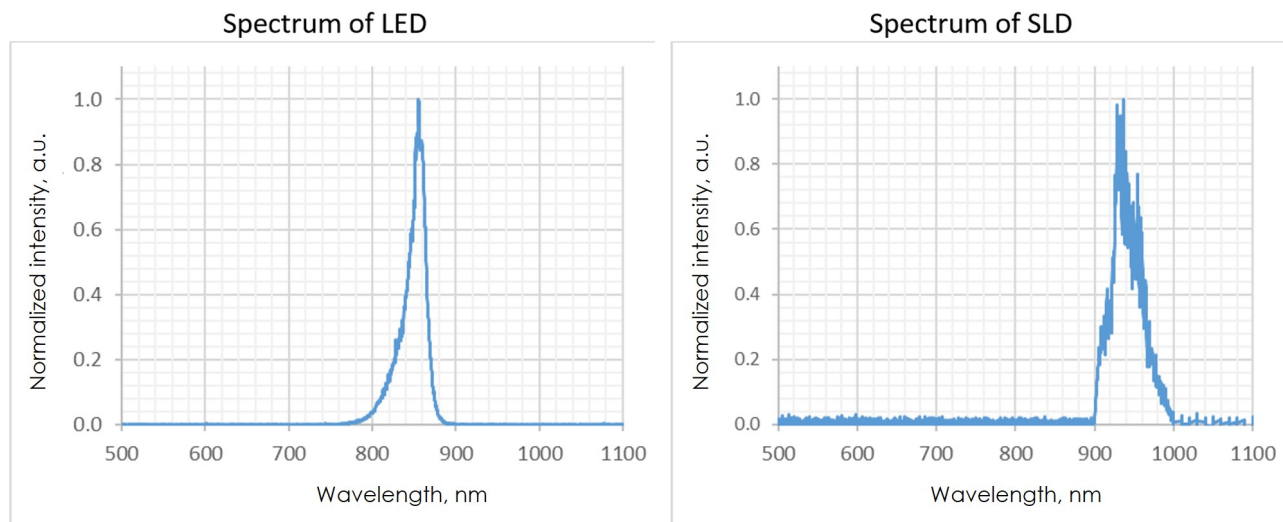


Figure A.2 – Measured spectrums of the LED and SLD light sources.

Measurements were performed using a precise spectrometer (CCS175/M, Thorlabs, USA), providing 0.6 nm spectral accuracy (equivalent to less than 0.1 % measurement uncertainty at 850 nm). Both sources emit light only with the wavelengths above 700 nm, therefore exposure poses no danger associated with the photochemical aphakic damage and only potential hazard of thermal damage has to be considered.

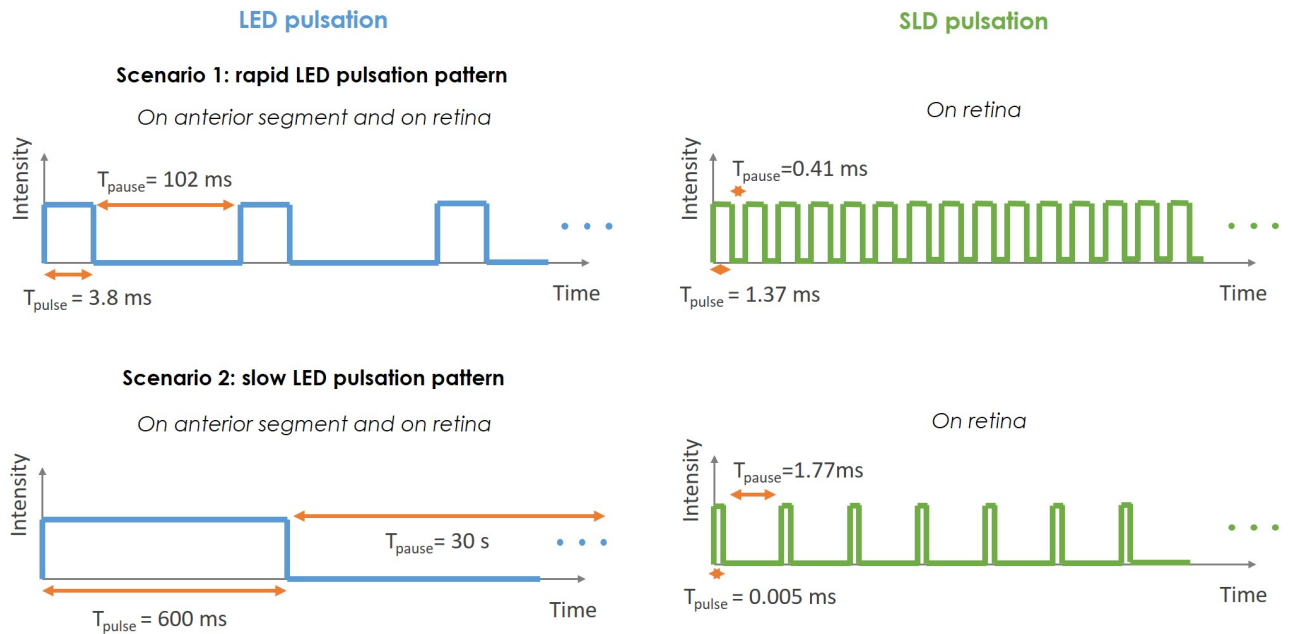


Figure A.3 – Pulsation patterns for LED and SLD in configuration 1.

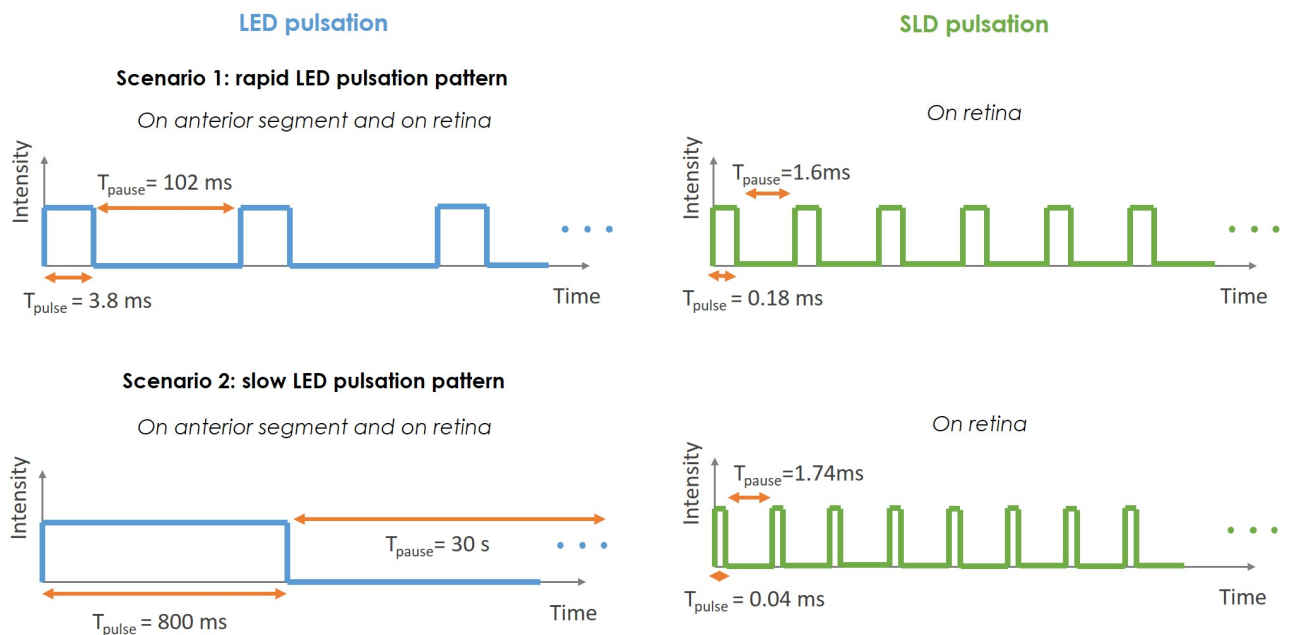


Figure A.4 – Pulsating exposure patterns for LED and SLD in configuration 2.

To ensure safety, LED was used in a uniformly pulsed mode and the SLD was used in a uniformly scanning mode. To address different applications, LED can be used in two pulsating modes: rapid and slow. In agreement with ISO, scanning SLD will be evaluated using the pulsed

instrument criteria. In this case, pulse duration is the time, during which the scanning beam is located within the diameter of the measurement aperture, specified by the ISO standard. Pause duration is the time, during which the scanning beam is located outside of the diameter of the measurement aperture, specified by the ISO standard. Given that the pulse pattern depends on the scanning range and the diameter of the measurement aperture, the pattern will be different for configurations 1 and 2, and, for each configuration, different on the anterior eye and retina. Figure A.3 illustrates pulsation patterns for LED and SLD for configuration 1, while figure A.4 illustrates pulsation patterns for LED and SLD for configuration 2. In normal mode user has an option to use LED in rapid pulsation mode (scenario 1) or in slow pulsation mode (scenario 2).

For LED the durations of pulses and pauses in the pulse pattern were determined by measuring the change in time of the LED current using the precise oscilloscope (model TDS2014B, Tektronix, USA). For SLD the pulse and pause durations were computed from the set parameters of the beam scanner (from Thorlabs, USA). Beam scanner is manufactured in conformity with EN ISO 12100 and EN 61326-1 standards. One configuration of set parameters is: scanning speed = 36000 A-scans/s, Number of scanning points in scanning range = 64. The scanning range was verified experimentally by viewing the spread of the beam with the camera.

Example of pulse pattern calculation for SLD in configuration 1 on anterior segment (measurement aperture diameter = 1 mm):

$$\begin{aligned} t_{CL}^{pulse-930nm} &= \frac{\text{Aperture size}}{\text{Scanning range}} \cdot \frac{\text{Number of scanning points within range}}{\text{Scanning speed}} = \\ &= \frac{1 \text{ mm}}{1.3 \text{ mm}} \cdot \frac{64 \text{ points}}{36000 \text{ scanning points/sec.}} = 1.37 \text{ ms} \end{aligned} \quad (\text{A.1})$$

$$\begin{aligned} t_{CL}^{pause-930nm} &= \frac{\text{Scanning range} - \text{Aperture size}}{\text{Scanning range}} \cdot \frac{\text{Number of scanning points within range}}{\text{Scanning speed}} = \\ &= \frac{1.3 \text{ mm} - 1 \text{ mm}}{1.3 \text{ mm}} \times \frac{64 \text{ points}}{36000 \text{ scanning points/sec.}} = 0.41 \text{ ms} \end{aligned} \quad (\text{A.2})$$

Example of pulse pattern calculation for SLD in configuration 1 on retina (measurement aperture diameter = 30 μm):

$$\begin{aligned} t_R^{pulse-930nm} &= \frac{\text{Aperture size}}{\text{Scanning range}} \cdot \frac{\text{Number of scanning points within range}}{\text{Scanning speed}} = \\ &= \frac{30 \mu\text{m}}{11 \text{ mm}} \cdot \frac{64 \text{ points}}{36000 \text{ scanning points/sec.}} = 0.005 \text{ ms} \end{aligned} \quad (\text{A.3})$$

$$\begin{aligned} t_R^{pause-930nm} &= \frac{\text{Scanning range} - \text{Aperture size}}{\text{Scanning range}} \cdot \frac{\text{Number of scanning points within range}}{\text{Scanning speed}} = \\ &= \frac{11 \text{ mm} - 30 \mu\text{m}}{11 \text{ mm}} \times \frac{64 \text{ points}}{36000 \text{ scanning points/sec.}} = 1.77 \text{ ms} \end{aligned} \quad (\text{A.4})$$

Example of pulse pattern calculation for SLD in configuration 2 on anterior segment (measurement aperture diameter = 1 mm):

$$t_{CL}^{pulse-930nm} = \frac{\text{Aperture size}}{\text{Scanning range}} \cdot \frac{\text{Number of scanning points within range}}{\text{Scanning speed}} =$$

$$= \frac{1 \text{ mm}}{10 \text{ mm}} \cdot \frac{64 \text{ points}}{36000 \text{ scanning points/sec.}} = 0.18 \text{ ms} \quad (\text{A.5})$$

$$\begin{aligned} t_{CL}^{\text{pause-930nm}} &= \frac{\text{Scanning range} - \text{Aperture size}}{\text{Scanning range}} \cdot \frac{\text{Number of scanning points within range}}{\text{Scanning speed}} = \\ &= \frac{10 \text{ mm} - 1 \text{ mm}}{10 \text{ mm}} \times \frac{64 \text{ points}}{36000 \text{ scanning points/sec.}} = 1.6 \text{ ms} \end{aligned} \quad (\text{A.6})$$

Example of pulse pattern calculation for SLD in configuration 2 (measurement aperture diameter = 30 μm):

$$\begin{aligned} t_R^{\text{pulse-930nm}} &= \frac{\text{Aperture size}}{\text{Scanning range}} \cdot \frac{\text{Number of scanning points within range}}{\text{Scanning speed}} = \\ &= \frac{30 \cdot 10^{-3} \text{ mm}}{1.3 \text{ mm}} \cdot \frac{64 \text{ points}}{36000 \text{ scanning points/sec.}} = 0.04 \text{ ms} \end{aligned} \quad (\text{A.7})$$

$$\begin{aligned} t_R^{\text{pause-930nm}} &= \frac{\text{Scanning range} - \text{Aperture size}}{\text{Scanning range}} \cdot \frac{\text{Number of scanning points within range}}{\text{Scanning speed}} = \\ &= \frac{1.3 \text{ mm} - 30 \cdot 10^{-3} \text{ mm}}{1.3 \text{ mm}} \times \frac{64 \text{ points}}{36000 \text{ scanning points/sec.}} = 1.74 \text{ ms} \end{aligned} \quad (\text{A.8})$$

Instrument was evaluated, considering 2 hour examination time per person per day, in agreement with ISO rationale. This is greatly longer comparing to the examination time of 20 minutes, typical for the FFOCT instrument. Following ISO rationale, safety of a pulses was verified using the pulsed instruments criteria (ISO 15004-2:2007, Tables 3 and 6). Table 5 is not applicable for FFOCT instrument, because it emits light with wavelengths longer than 700 nm. According to ISO 15004-2:2007, if the instrument exposes eye with light from the two light sources simultaneously, limit is given by the expression:

$$\frac{E_1}{Limit_1} + \frac{E_2}{Limit_2} \leq 1, \quad (\text{A.9})$$

where E is measured irradiance, $Limit$ is maximum safe irradiance and 1,2 are the indexes of the light sources.

Irradiance measurements were performed according to the ISO rules. Measuring powermeter was located in the positions (laterally and axially) of the highest irradiances. In order to measure the irradiance at the anterior segment of the eye (configuration 1), we used 1 mm measurement aperture. For measuring irradiance in the retina (configuration 2), we were considering 30 μm measurement aperture, used in the strict case of the immobilized eye. Apertures were moved around the illumination field to search for hot spots. The maximal measured irradiances were used for safety evaluation.

In order to verify the anterior segment safety we used criteria 5.5.1.3, 5.5.2.2 and not the 5.5.1.4, 5.5.2.3 because the first ones are more limiting in the wavelengths range of LED, SLD light sources.

The safety was evaluated at the highest exposure condition with the LED and SLD output powers set to their maximum values. According to the recommendations of ISO (ISO 15004-2:2007, table 6, Note 1) pulsed exposure was checked to be below the safety limit for every moment within the 20 seconds time window. Due to the fact that the duration of every

individual pulse exposure in FFOCT is below 20 seconds, and that FFOCT does not make exposure in ultraviolet light, there is no requirement to verify safety according to the continuous wave limit.

A.2.2 Light safety analysis

Light safety in normal use

We evaluated the safety of anterior segment and retina in configuration 1 and in configuration 2. For each configuration we made calculations for the two scenarios: rapid or slow LED pulsating pattern. Pulsed exposure of each scenario and each configuration was checked to be below the limit for each moment in time within 20 seconds. Safety evaluation criteria of group 2 instruments according to ISO (ISO 15004-2: 2007, table 6), taking into account the simultaneous exposure to multiple light sources, is shown below.

$$\frac{H_{IR-CL}^{850\text{ nm}}}{1.8 \cdot t^{1/4} \frac{J}{\text{cm}^2}} + \frac{H_{IR-CL}^{930\text{ nm}}}{1.8 \cdot t^{1/4} \frac{J}{\text{cm}^2}} < 1 \quad (\text{A.10})$$

$$\frac{H_{VIR-R}^{850\text{ nm}}}{\left(\frac{10}{d_r^{850\text{ nm}}} \cdot t^{3/4}\right) \frac{J}{\text{cm}^2}} + \frac{H_{VIR-R}^{930\text{ nm}}}{N^{-1/4} \cdot \left(\frac{10}{d_r^{930\text{ nm}}} \cdot t^{3/4}\right) \frac{J}{\text{cm}^2}} < 1 \quad (\text{A.11})$$

Formula in the first row evaluates safety of the anterior segment, while formula in the second row evaluates safety of the retina. Only $t < 20\text{sec.}$ should be used. H_{IR-CL} is the unweighted radiant exposure $\left(\frac{J}{\text{cm}^2}\right)$ at the anterior segment. It is calculated as accumulated irradiance over time t , based on measured irradiance and the pulsation patterns in figures A.3,A.4, as $H_{IR-CL} = E_{IR-CL} \cdot \Delta t_{CL}$, where Δt_{CL} is total duration of pulses on anterior segment within time t . E_{IR-CL} is the unweighted irradiance $\left(\frac{W}{\text{cm}^2}\right)$ measured at the anterior segment, according to the measurement methods, specified in ISO 15004-2:2007. H_{VIR-R} is the weighted radiant exposure $\left(\frac{J}{\text{cm}^2}\right)$ at the retina. It is calculated as accumulated irradiance over time t , based on measured irradiance and the pulsation patterns in figures A.3,A.4, as $H_{VIR-R} = E_{VIR-R} \cdot \Delta t_R$, where Δt_R is the total duration of pulses on retina within time t . E_{VIR-R} is the weighted irradiance $\left(\frac{W}{\text{cm}^2}\right)$ at the retina. It is calculated as $E_{VIR-R} = \sum_{380}^{1400} E_\lambda \cdot R(\lambda) \cdot \Delta\lambda$, based on the power value, measured according to the ISO 15004-2: 2007 measurement methods, light source spectrum (figure A.2) and spectral weighting function $R(\lambda)$, specified in Annex A of ISO standard. d_r is the diameter (mm) of the exposure spot on the retina. Following rules of ISO 15004-2:2007, we used d_r value of 1.7 mm, when it was above 1.7 mm and value of 0.03 mm, when it was below 0.03 mm. For the repetitive laser (in our case SLD) exposure of retina ISO 15004-2:2007 requires introduction of the correction factor $N^{-1/4}$, where N is the number of pulses. All the times are measured in seconds.

Configuration 1

Below we provide safety evaluation of anterior segment and retina in the two scenarios of different LED pulsating patterns, when FFOCT device is used in anterior segment imaging configuration 1. We checked that the pulsed exposure from FFOCT is below the safety limits

for every moment in time within 20 seconds, according to the recommendations of ISO standard. These graphs (figure A.5) were calculated from formulas A.10,A.11 using experimentally measured irradiances (Table 1), pulse and pause durations (A.3, Table 1). Power measurements were performed using the precise powermeter (S130C, PM100D, Thorlabs, USA) with the measurement uncertainty of $\pm 3\%$. Additionally, for power measurements we used the precise pinhole apertures (P()D, Thorlabs, USA) with diameter tolerance of 1%.

Table 1. Configuration 1. Measured parameters.										
Scenario	LED					SLD				
	E_{IR-CL}^{850}	E_{VIR-R}^{850}	$t_{CL}^{pulse-850}$	$t_R^{pulse-850}$	d_r^{850}	E_{IR-CL}^{930}	E_{VIR-R}^{930}	$t_{CL}^{pulse-930}$	$t_R^{pulse-930}$	d_r^{930}
1	2	0.11	0.0038	0.0038	1.7	0.035	0.036	$1.37 \cdot 10^{-3}$	$0.005 \cdot 10^{-3}$	0.03
			0.102	0.102				$0.41 \cdot 10^{-3}$	$1.77 \cdot 10^{-3}$	
2	2	0.11	0.6	0.6	1.7	0.035	0.036	$1.37 \cdot 10^{-3}$	$0.005 \cdot 10^{-3}$	0.03
			30	30				$0.41 \cdot 10^{-3}$	$1.77 \cdot 10^{-3}$	

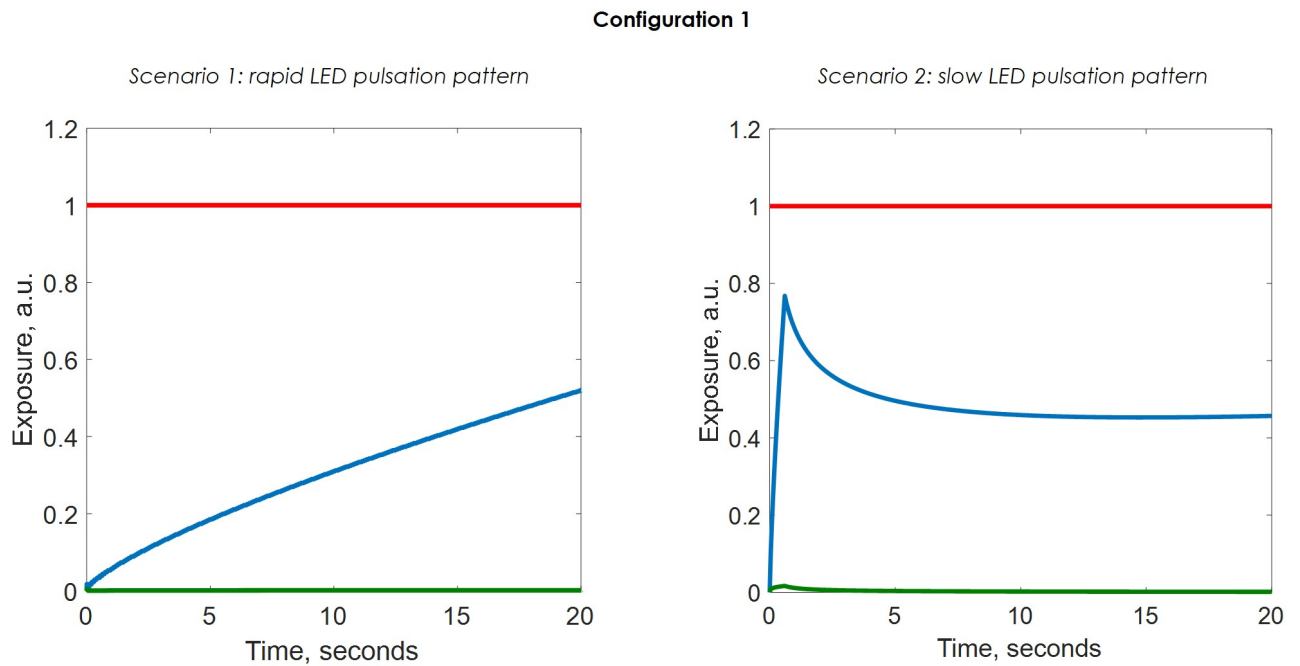


Figure A.5 – Exposures of cornea (blue) and retina (green) through time. Safety limit is shown in red.

Table 2 shows the values of the highest FFOCT exposure in comparison with the limit.

Table 2. Configuration 1. Pulsed safety evaluation at the highest exposure moments.			
Scenario	FFOCT exposure (arbitrary units)		Limit
	$\left\{ \begin{array}{l} \frac{H_{IR-CL}^{850nm}}{1.8 \cdot t^{1/4}} \frac{J}{cm^2} + \frac{H_{IR-CL}^{930nm}}{1.8 \cdot t^{1/4}} \frac{J}{cm^2} < 1 \\ \frac{H_{VIR-R}^{850nm}}{\left(\frac{10}{d_r^{850nm}} \cdot t^{3/4}\right) \frac{J}{cm^2}} + \frac{H_{VIR-R}^{930nm}}{N^{-1/4} \cdot \left(\frac{10}{d_r^{930nm}} \cdot t^{3/4}\right) \frac{J}{cm^2}} < 1 \end{array} \right.$		
1	$\left\{ \begin{array}{l} 0.52 \\ 0.005 \end{array} \right.$		$\left\{ \begin{array}{l} 1 \\ 1 \end{array} \right.$
2	$\left\{ \begin{array}{l} 0.77 \\ 0.016 \end{array} \right.$		$\left\{ \begin{array}{l} 1 \\ 1 \end{array} \right.$

Light exposure from the FFOCT instrument in configuration 1 is below the retinal and anterior segment limits for both use scenarios. In the most limiting case (scenario 2) FFOCT makes exposure, which is 77% of the anterior segment limit and 1.6% of the retinal limit, recommended by the ISO 15004-2:2007. Safety was evaluated under condition of LED and SLD light sources set to their maximum output power, together with the condition of 2 hour exposure. The typical use practice of FFOCT instrument implies smaller and much shorter exposures (about 20 minutes), which results in a comfortable safety margin. All the measurements were conducted with accuracy, greatly exceeding the required accuracy for group 2 instruments of 30%.

Configuration 2

Below we provide safety evaluation of anterior segment and retina in two scenarios of different LED pulsating patterns, when FFOCT device is used in retinal imaging configuration 2.

Table 3. Configuration 2. Measured parameters.										
Scenario	LED					SLD				
	E_{IR-CL}^{850}	E_{VIR-R}^{850}	$t_{CL}^{pulse-850}$	$t_R^{pulse-850}$	d_r^{850}	E_{IR-CL}^{930}	E_{VIR-R}^{930}	$t_{CL}^{pulse-930}$	$t_R^{pulse-930}$	d_r^{930}
1	0.12	0.98	0.0038	0.0038	1.25	0.011	49	$0.18 \cdot 10^{-3}$	$0.04 \cdot 10^{-3}$	0.03
			0.102	0.102				$1.6 \cdot 10^{-3}$	$1.74 \cdot 10^{-3}$	
2	0.12	0.98	0.6	0.6	1.25	0.011	49	$0.18 \cdot 10^{-3}$	$0.04 \cdot 10^{-3}$	0.03
			30	30				$1.6 \cdot 10^{-3}$	$1.74 \cdot 10^{-3}$	

Configuration 2

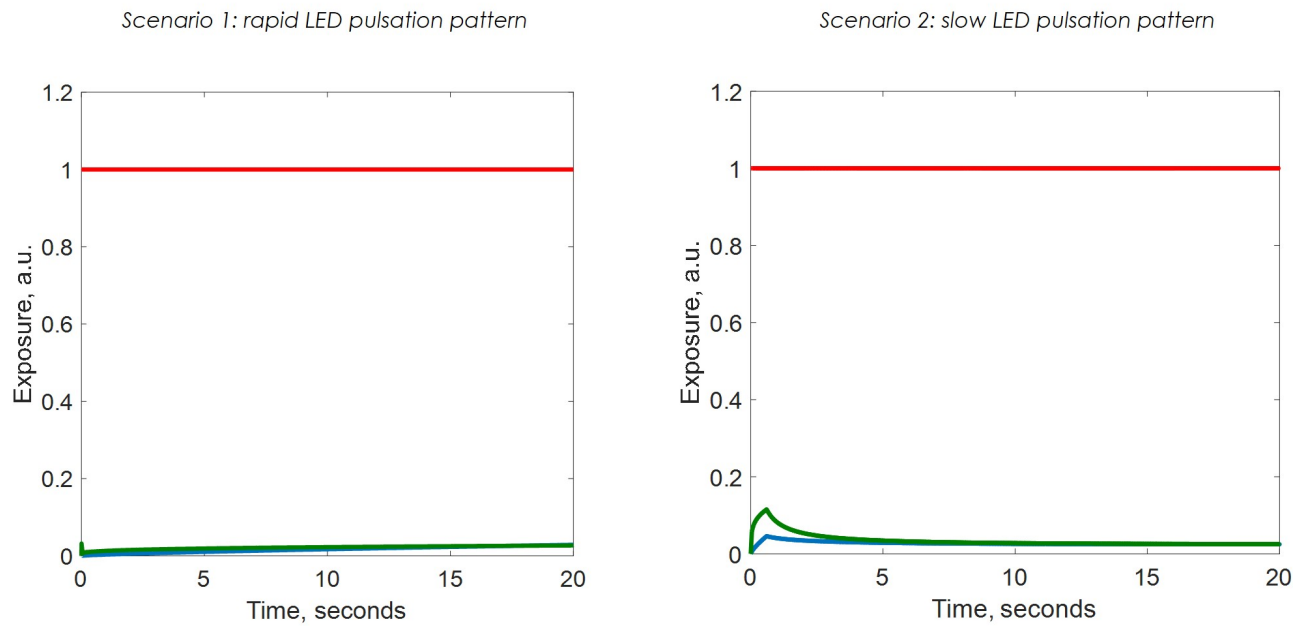


Figure A.6 – Exposures of cornea (blue) and retina (green) through time. Safety limit is shown in red.

We checked that the pulsed exposure from FFOCT is below the safety limits for every moment in time within 20 seconds, according to the recommendations of ISO standard. These graphs (figure A.6) were calculated from formulas A.10,A.11 using experimentally measured irradiances (Table 3), pulse and pause durations (Table 3, A.4). Power measurements were performed using the precise powermeter (S130C, PM100D, Thorlabs, USA) with measurement uncertainty of $\pm 3\%$. Additionally, for power measurements we used precise pinhole apertures (P()D, Thorlabs, USA) with diameter tolerance of 1%.

Table 4. Configuration 2. Pulsed safety evaluation at the highest exposure moments.		
Scenario	FFOCT exposure (arbitrary units)	Limit
	$\left\{ \begin{array}{l} \frac{H_{IR-CL}^{850nm}}{1.8 \cdot t^{1/4} \frac{J}{cm^2}} + \frac{H_{IR-CL}^{930nm}}{1.8 \cdot t^{1/4} \frac{J}{cm^2}} < 1 \\ \frac{H_{VIR-R}^{850nm}}{\left(\frac{10}{d_r^{850nm}} \cdot t^{3/4}\right) \frac{J}{cm^2}} + \frac{H_{VIR-R}^{930nm}}{N^{-1/4} \cdot \left(\frac{10}{d_r^{930nm}} \cdot t^{3/4}\right) \frac{J}{cm^2}} < 1 \end{array} \right.$	
1	$\left\{ \begin{array}{l} 0.029 \\ 0.081 \end{array} \right.$	$\left\{ \begin{array}{l} 1 \\ 1 \end{array} \right.$
2	$\left\{ \begin{array}{l} 0.046 \\ 0.120 \end{array} \right.$	$\left\{ \begin{array}{l} 1 \\ 1 \end{array} \right.$

Table 4 shows the values of the highest FFOCT exposure in comparison with the limit.

Light exposure from the FFOCT instrument in configuration 2 is below the retinal and anterior segment limits for both use scenarios. In the most limiting case (scenario 2) FFOCT makes exposure, which is 4.6% of the anterior segment limit and 12% of the retinal limit, recommended by the ISO 15004-2:2007. Safety was evaluated under condition of LED and SLD light sources set to their maximum output power, together with the condition of 2 hour exposure. The typical use practice of FFOCT instrument implies smaller and much shorter exposures (about 20 minutes), which results in even larger safety margin. All the measurements were conducted with accuracy, greatly exceeding the required accuracy for group 2 instruments of 30%.

Light safety in case of failure

Additionally to the condition of normal use, safety of the FFOCT instrument was verified in case of a single instrumentation (hardware or software) failure. Normal use condition was satisfied in the assumption of the maximal output power from the light sources, therefore hardware or software error can not lead to an increased power impinging the eye. However, we identified two reasons that potentially can result in the increased eye exposure over time: hardware or software failure in the SLD scanner and failure of the software, controlling the LED pulsation. Failure of the SLD scanner is highly unlikely, given the quality of the scanners (from Thorlabs, USA) and its conformity with EN ISO 12100 and EN 61326-1 standards. Failure of software controlling LED pulsation is highly improbable either, given the quality of the controller (Thorlabs, USA). Nevertheless, we checked that the safety of FFOCT device is satisfied in case of these unlikely failures. Each of these failures may lead to continuous (instead of pulsed) exposures. In order to prevent potential overexposure, FFOCT is equipped with a fast mechanical shutter (SH1/M, Thorlabs, USA), which rapidly shuts down the light in case of a SLD scanner failure, and shuts the light in case of lack of LED pulsation. The shutting time is 0.014 s, according to the specification. Below, we estimate the maximal durations of the safe continuous LED and SLD light exposures, which are within the limits of ISO 15004-2:2007. We confirm that these durations are longer than the closing time of the optical shutter, which verifies the safety of FFOCT device in case of the instrumentation failure. We provide safety evaluation of the anterior segment and retina in the two configurations of FFOCT device in accordance with ISO 15004-2:2007 methodology.

- *Failure of LED pulsation (continuous LED exposure)*

Configuration 1, Configuration 2

We provide safety evaluation of anterior segment and retina in case of continuous LED and pulsed SLD exposures. Figure A.7 below was calculated from formulas A.10,A.11 using experimentally measured irradiances (Table 1 for configuration 1 and Table 3 for configuration 2), pulse and pause durations for SLD (Figure A.3, Table 1 for configuration 1 and Table 3 for configuration 2).

Safe exposure duration is limited primarily by the anterior segment criteria. In configuration 1 the permitted continuous exposure of 0.854 seconds (A.7, Table 7) is more than 60 times

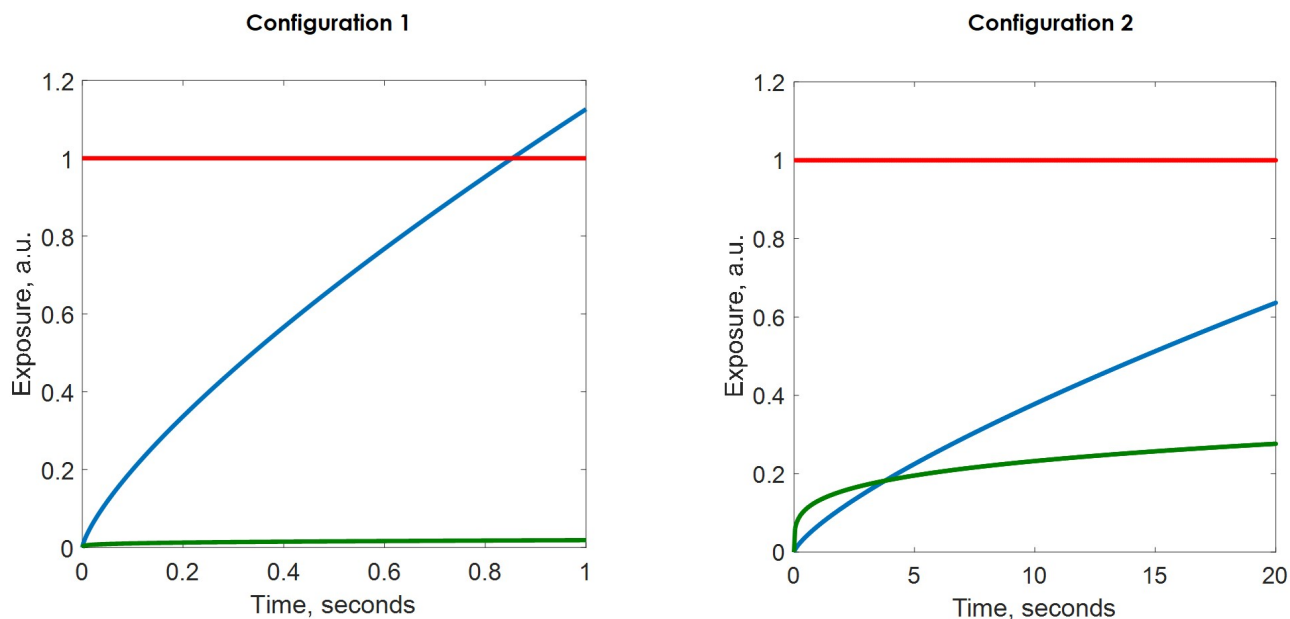


Figure A.7 – Exposures of cornea (blue) and retina (green) through time in case of failure of LED pulsation. Safety limit is shown in red. In configuration 1 exposure is safe during first 0.854 seconds. In configuration 2 exposure is safe during more than 20 seconds.

Table 5. Failure of LED pulsation (continuous LED exposure).			
Configuration	Scenario	Parameters taken from	Maximal safe duration:
1	NA	Table 1	$\begin{cases} (\Delta t_{CL}^{850nm})_{Max} = 0.854 s \\ (\Delta t_{VTR-R}^{850nm})_{Max} > 20 s \end{cases}$
2	NA	Table 3	$\begin{cases} (\Delta t_{CL}^{850nm})_{Max} > 20 s \\ (\Delta t_{VTR-R}^{850nm})_{Max} > 20 s \end{cases}$

longer than the closing time of the shutter, while in configuration 2 the permitted continuous exposure is longer than 20 seconds, which is more than 1400 times longer than the closing time of the shutter, which confirms the safety of both configurations in case of LED pulsation failure.

- *Failure of SLD scanning (continuous SLD exposure)*

Configuration 1, Configuration 2

We provide safety evaluation of anterior segment and retina in case of continuous LED and pulsed SLD exposures. Figure A.8 below was calculated from formulas A.10,A.11 using experimentally measured irradiances (Table 1 for configuration 1 and Table 3 for configuration 2), pulse and pause durations for SLD (Figure A.4, Table 1 for configuration 1 and Table 3 for configuration 2).

The permitted continuous exposure is longer than 20 seconds (A.8, Table 6) for all configurations and all pulsation scenarios, which is more than 1400 times longer than the closing time of the shutter. Not only this means that the SLD scanner failure does not present any dangers,

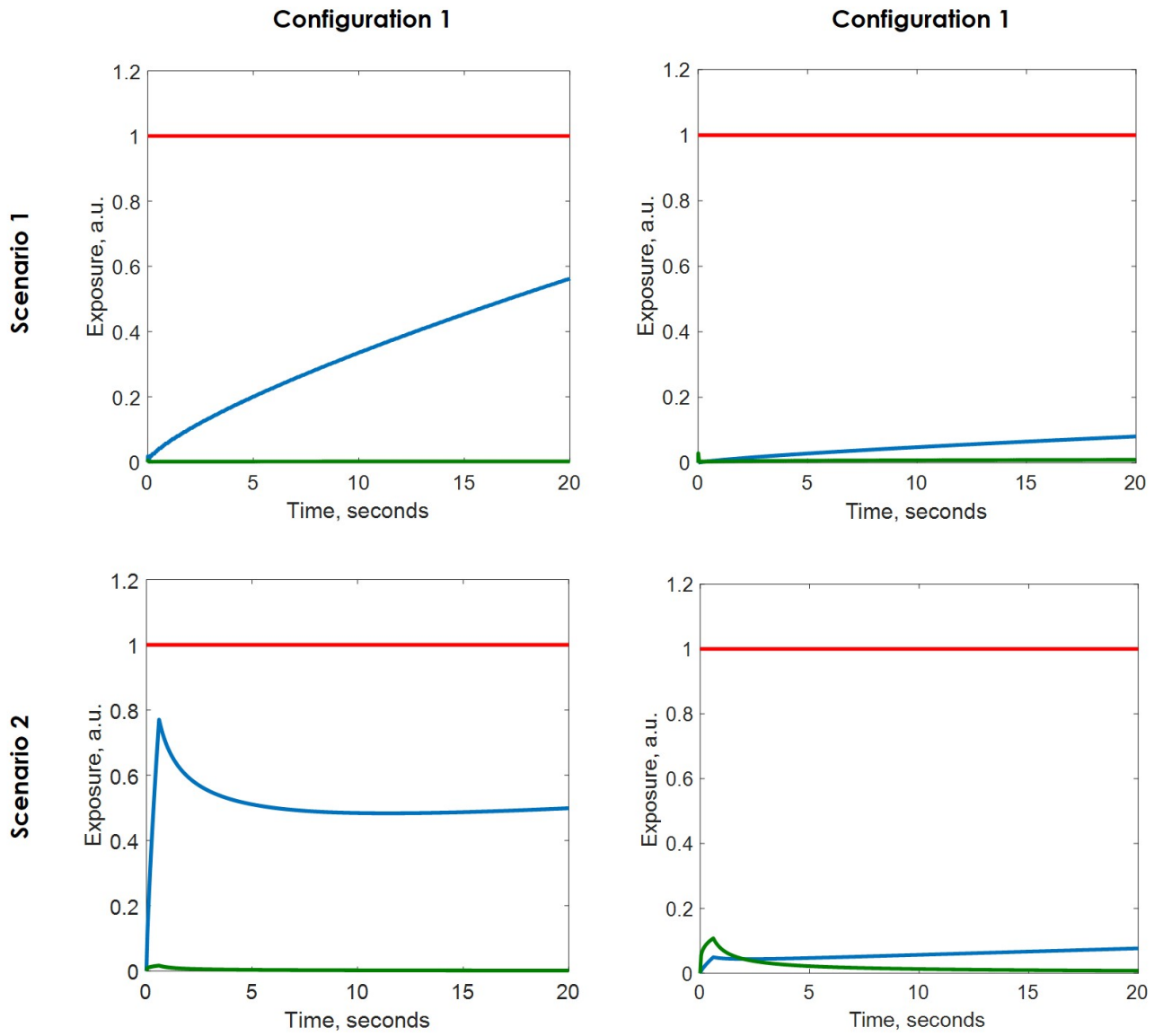


Figure A.8 – Exposures of cornea (blue) and retina (green) through time in case of failure of SLD pulsation. Safety limit is shown in red. Configurations 1 and 2 are safe during more than 20 seconds.

Table 6. Failure of SLD pulsation (continuous SLD exposure).			
Configuration	Scenario	Parameters taken from	Maximal safe duration:
1	1,2	Table 1	$\begin{cases} (\Delta t_{CL}^{850nm})_{Max} > 20 s \\ (\Delta t_{VIR-R}^{850nm})_{Max} > 20 s \end{cases}$
2	1,2	Table 3	$\begin{cases} (\Delta t_{CL}^{850nm})_{Max} > 20 s \\ (\Delta t_{VIR-R}^{850nm})_{Max} > 20 s \end{cases}$

but also it means that the shutter is not compulsory, because 20 seconds time is sufficient for operator to determine the SLD scanner failure (by listening to the change or lack of sound from the scanning mirrors) and to shut the illumination down.

- *Additional case: failure of LED pulsation following the normal exposure in configuration 1, scenario 2*

Even that strongly improbable, the largest total exposure can potentially happen, if the highest normal exposure (configuration 1, LED pulsation scenario 2) is right away followed by the instrumentation failure with the highest exposure (configuration 1). In this case the maximal safe duration, during which the light should be shut down is given by $0.854 - 0.6 = 0.254$. This is more than 17 times longer comparing to the closing time of the shutter, which confirms the safety of FFOCT device.

In order to ensure the mechanical, electrical safety and avoid unwanted light reflections from reaching the eye, FFOCT instrument was enclosed into a blunt light absorbing black hardboard cover (figure A.9).

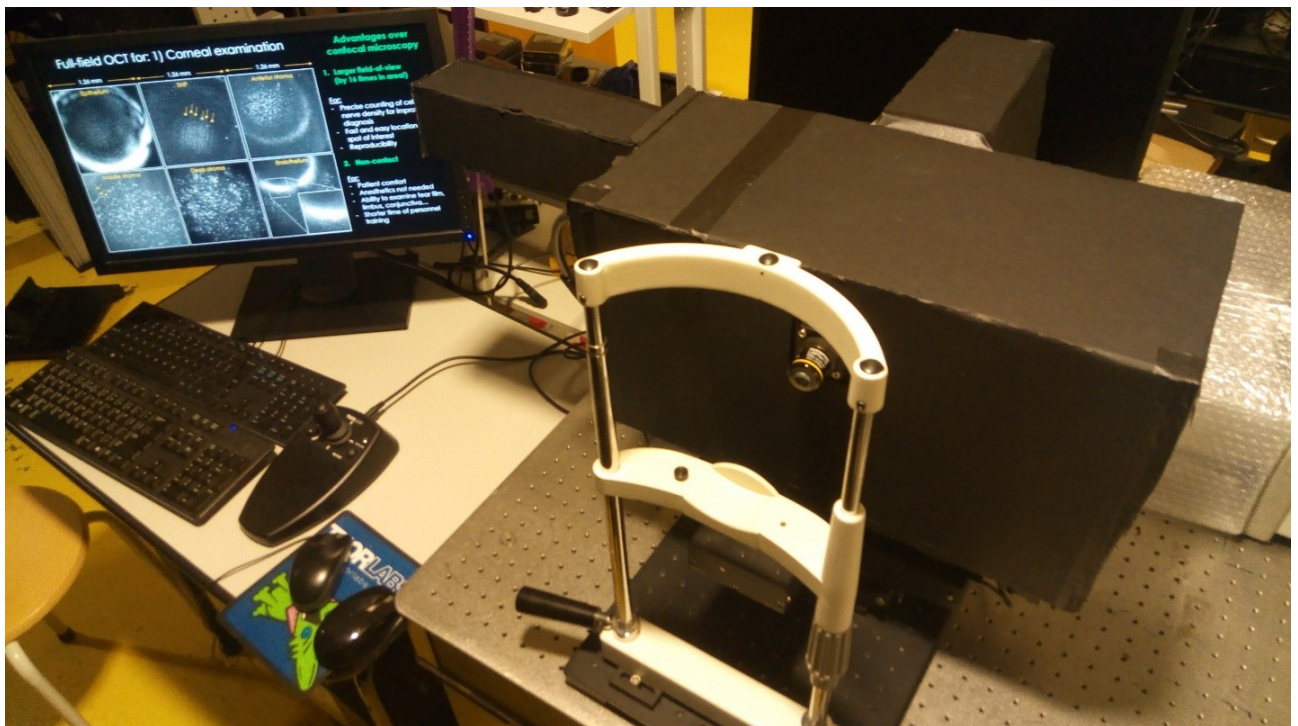


Figure A.9 – FF/SD OCT device, covered in a blackout material.

Cette annexe est destinée à fournir un résumé substantiel de la thèse en français. Ci-dessous, je décrirai de manière générale les objectifs du travail. Ensuite, je guiderai le lecteur chapitre par chapitre, en se concentrant sur les informations et les résultats les plus importants. Cette thèse concernant la mise au point d'une approche nouvelle pour l'imagerie de l'œil j'illustrerai par des images les résultats obtenus ainsi que la comparaison avec des méthodes concurrentes.

B.1 Introduction

Cette thèse appartient au domaine de la tomographie par cohérence optique (OCT). Aujourd'hui, l'OCT est un mode d'imagerie indispensable pour le diagnostic oculaire des chambres antérieure et postérieure en ophtalmologie clinique. Pour l'imagerie rétinienne l'OCT présente des images bien supérieures en qualité comparées à d'autres méthodes dans tous les domaines: champ de vision, résolution axiale et latérale (grâce à l'utilisation de l'optique adaptative en particulier). Pour ce qui est de la partie antérieure de l'œil, ou plus précisément de l'imagerie cornéenne, l'OCT était sans concurrence en termes de champ de vue et de résolution axiale, cependant, une haute résolution en imagerie « en face » restait à obtenir.

Au cours de la première année du projet, nous avons obtenu les premières images cornéennes haute résolution en vue de face [3]. Au cours des années suivantes, nous avons encore amélioré la technologie pour permettre une imagerie en temps réel, ce qui ouvre le champ de la recherche clinique et l'espoir de la faire adopter comme pratique hospitalière. Cette recherche a été réalisée avec un type spécial d'OCT appelé FFOCT (time-domain full-field OCT). La FFOCT a été développée dans notre laboratoire il y a 20 ans en 1998 [4]. En la comparant à l'OCT conventionnelle, la FFOCT utilise une optique à ouverture numérique (NA) élevée, pour obtenir une résolution latérale au niveau du micromètre, ainsi qu'une caméra 2D pour obtenir des images en face sans balayage. La FFOCT a démontré son efficacité pour de nombreuses applications dont la plus réussie est l'analyse de biopsies instantanée au cours d'opérations chirurgicales.

Le projet de thèse en cours avait (et atteint) un objectif de transformation de la FFOCT *ex vivo* en un instrument capable d'être utilisé dans le domaine de l'ophtalmologie *in vivo*.

La thèse est divisée en plusieurs chapitres:

- Le chapitre 1 décrit la structure et les fonctions des tissus de la partie antérieure de l'œil (comprenant : toute la cornée, le limbe, la sclère et le film lacrymal).
- Le chapitre 2 montrera l'évolution des instruments de diagnostic de l'œil, de la lampe à fente qui est le « standard » des instruments d'analyse du fond d'œil jusqu'aux appareils de recherche qui ont émergé depuis.
- Au chapitre 3, nous suivrons la transformation de la FFOCT à partir du dispositif à contact *ex vivo* en un outil de diagnostic *in vivo* sans contact. Les premières images FFOCT *in vivo* de cornée humaine seront présentées.
- Au chapitre 4, le premier prototype de FFOCT sera combiné et synchronisé avec un système d'OCT spectrale (SDOCT) afin d'aboutir à un système unique FF / SD OCT, permettant d'effectuer un contrôle oculaire axial en temps réel ainsi que le suivi et la correction de défocalisation à la volée. Ceci permet une FFOCT capable de fournir, en temps réel, une imagerie de la cornée entière, du limbe et de la sclérotique, ouvrant la technologie pour une utilisation en clinique tant au niveau de la recherche que de la pratique médicale.
- Le chapitre 5 présentera les premières données d'angiographie par FFOCT. Les images, extraites de des vidéos de la circulation sanguine dans la conjonctive seront montrées.
- Au chapitre 6, nous présenterons une configuration de la FFOCT avec un champ de vision étendu (jusqu'à 3.1 mm × 3.1 mm), potentiellement utile pour mesurer l'épaisseur des couches cornéennes avec une présentation de type OCT classique.
- Le chapitre 7 donnera un aperçu des travaux réalisés afin d'aboutir à la première imagerie rétinienne humaine *in vivo* avec une FFOCT conventionnelle, recherche à laquelle j'ai eu le plaisir de participer avec mon collègue Peng Xiao.
- Le chapitre 8 montrera comment les mouvements axiaux naturels de l'œil peuvent être utilisés pour la modulation de phase et la récupération d'images FFOCT, ouvrant un chemin pour une FFOCT simplifiée, sans synchronisation caméra-actuateur piézoélectrique.
- L'annexe fournit une analyse rigoureuse des normes de sécurité oculaire pour plusieurs configurations d'imagerie FFOCT.

B.2 Chapitre 1: Structures superficielles oculaires, maladies et diagnostics cliniques.

La surface oculaire, composée de toutes les épaisseurs de cornée, du limbe et de la sclérotique, de la conjonctive bulbaire et du film lacrymal, a trois fonctions principales : 1) maintenir la clarté optique, 2) créer une surface réfractive pour la focalisation de la lumière sur la rétine, et 3) assurer la protection des les structures de l'oeil. Afin de remplir ces fonctions, chaque partie de la surface oculaire possède une micromorphologie complexe et hautement spécialisée,

qui comprend des fibres, des cellules, une phase aqueuse contenant les nutriments ainsi que des nerfs et des vaisseaux sanguins.

B.2.1 Brève introduction aux structures de la surface oculaire

La **cornée** est la partie la plus externe de l'œil, composée de plusieurs couches : 1) l'épithélium qui possède une structure cellulaire, 2) la couche de Bowman à base de collagène, 3) le stroma, avec un feuillet multicouches de collagène et de cellules, 4) l'endothélium avec une seule nappe de cellules hexagonales, 5) la membrane basale et la membrane de Descemet formées de collagène, 6) le plexus nerveux sous-basal et 7) le film lacrymal aqueux (figure B.1).

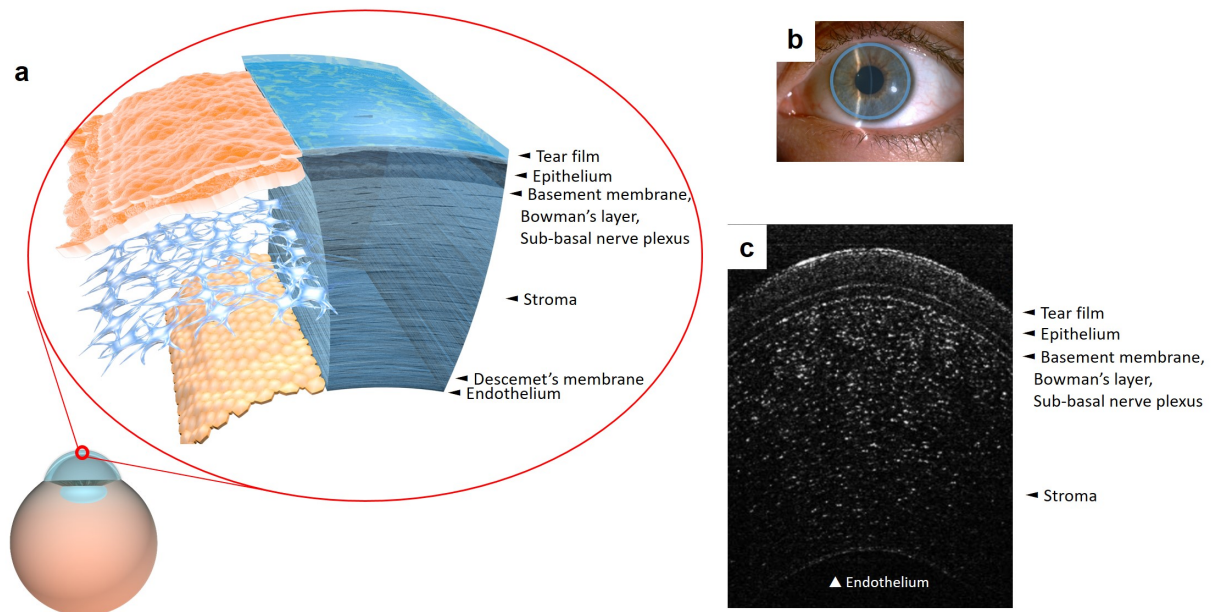


Figure B.1 – Cornée. (a) Dessin schématique de la structure de l'œil. L'insert est un dessin en 3D de la cornée avec une vue de face des mosaïques cellulaires des couches sélectionnées. (b) Image macro avec la lampe à fente d'un œil humain. Un cercle bleu rempli montre la cornée. (c) cornée humaine normale *in vivo*, imagée par tomographie par cohérence optique (OCT) à haute résolution axiale [7].

Le **Limbe** est une zone de transition de 1 à 1.5 mm entre la périphérie de la cornée et la sclérotique. C'est une zone spécifique et unique, hébergeant une population de cellules souches dans les palissades de Vogt (POV).

La **sclérotique** est la partie périphérique de la partie antérieure l'œil qui, comme la cornée, est presque entièrement composée de fibrilles de collagène.

Le **bulbe conjonctif** est une fine membrane semi-transparente qui recouvre la surface de l'œil, allant de la sclérotique jusqu'au bord de la cornée.

B.2.2 Troubles de la surface oculaire et diagnostics cliniques

B.2.3 Vision globale des troubles de la surface oculaire

Un petit dysfonctionnement dans une partie du système sophistiqué de la surface oculaire peut entraîner une gamme de troubles cornéens pouvant potentiellement rendre aveugle. Quelques

exemples choisis de défis pour la médecine sont actuellement: la sécheresse oculaire, la dystrophie endothéliale de Fuch (FECD), la Kératite et le Kératocône. Les figures ci-dessous illustrent les caractéristiques de la maladie de Fuch révélées par des outils issus de technologies récentes de diagnostic. Utilisés ensemble, ces instruments sont capables de diagnostiquer presque tous les troubles cornéens; l'utilisation de certains instruments est toutefois à éviter en raison de l'inconfort de la procédure, soit en raison d'un contact physique direct avec les yeux (microscope confocal *in vivo* (IVCM)), ou à cause d'une injection de fluorescéine.

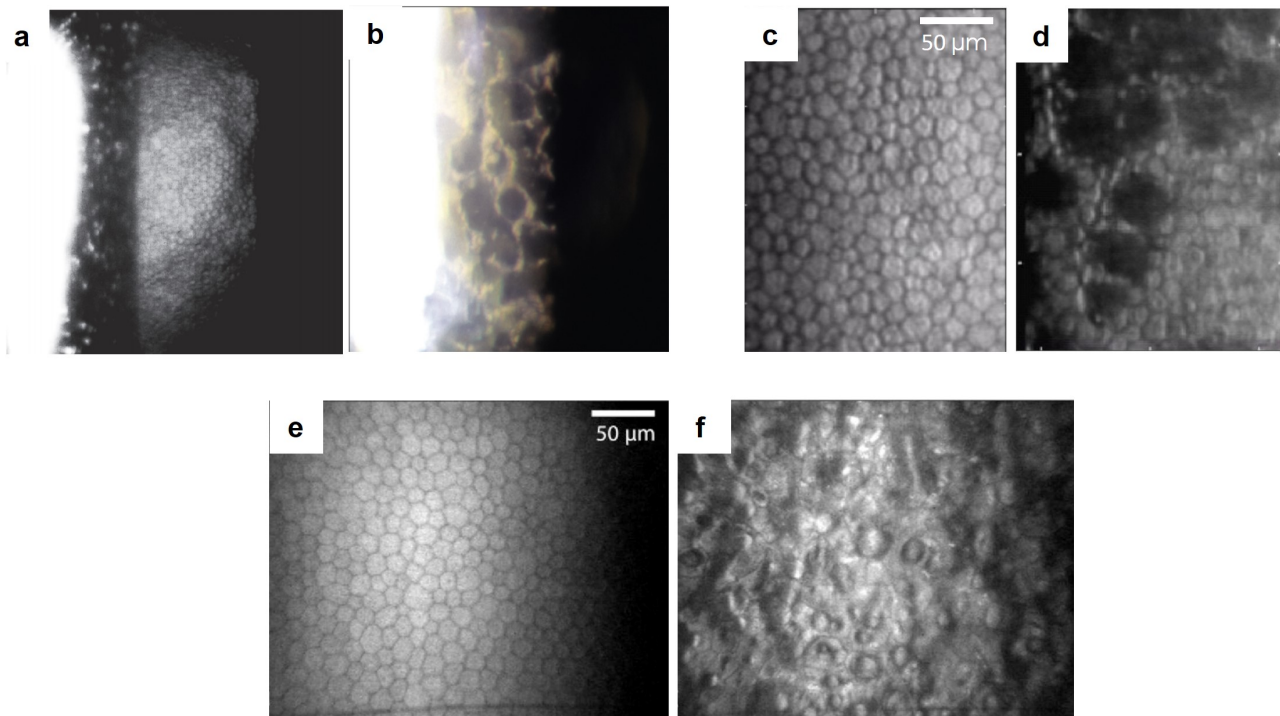


Figure B.2 – Méthodes de diagnostic de la dystrophie endothéliale de Fuch. (a,b) Le biomicroscope à lampe à fente peut être utilisé pour visualiser la mosaïque cellulaire chez des sujets normaux (a) et des patients atteints de dystrophie de Fuch (b), figure adaptée de [10]. Grossissement: $\times 40$. (c,d) Images de microscopie spéculaire de endothélium de l'oeil normal (c) et malade (d) [40]. (e,f) Données de microscopie confocale *in vivo* du sujet normal (e) et d'un patient atteint de la maladie (f) [41].

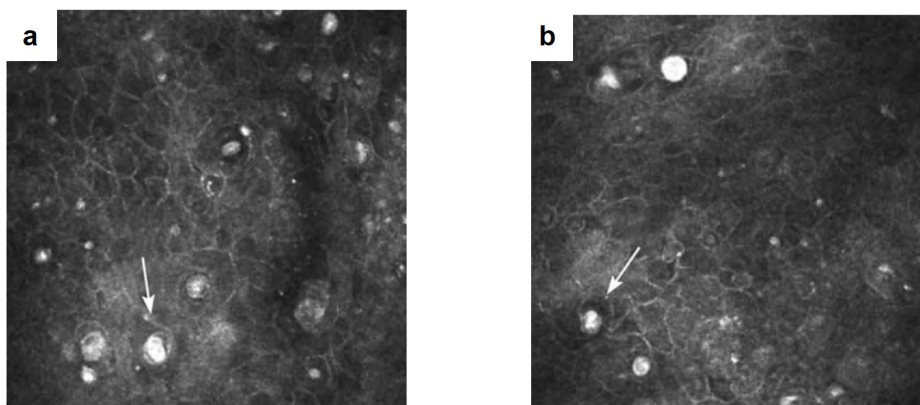


Figure B.3 – Microscopie confocale dans le diagnostic de la kératite Acanthamoeba. Les kystes, ronds de taille caractéristique 20 microns qui sont localisés dans l'épithélium, sont clairement visibles.

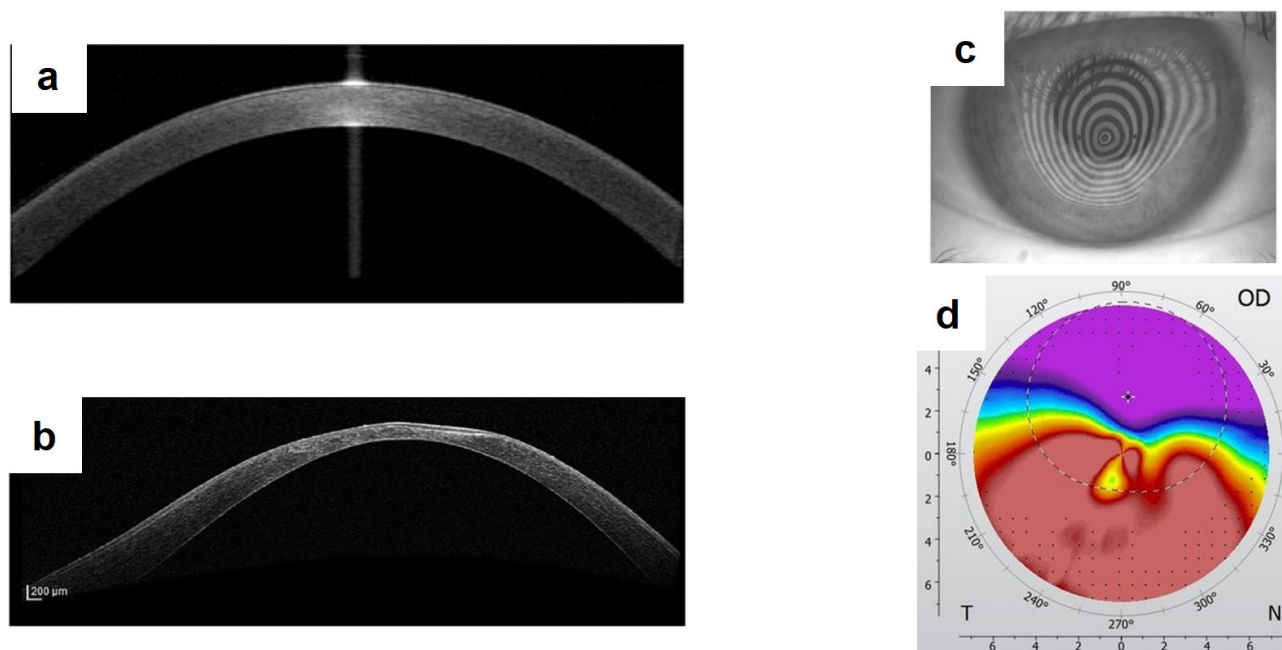


Figure B.4 – Diagnostic du kératocône. (a-b) Oeil normal (haut) et kératoconique (bas) examiné par OCT, adapté de [45,46]. L'amincissement de la cornée centrale est apparent. (c-d) Mesures au kératographe dans l'œil kératoconique de [47].

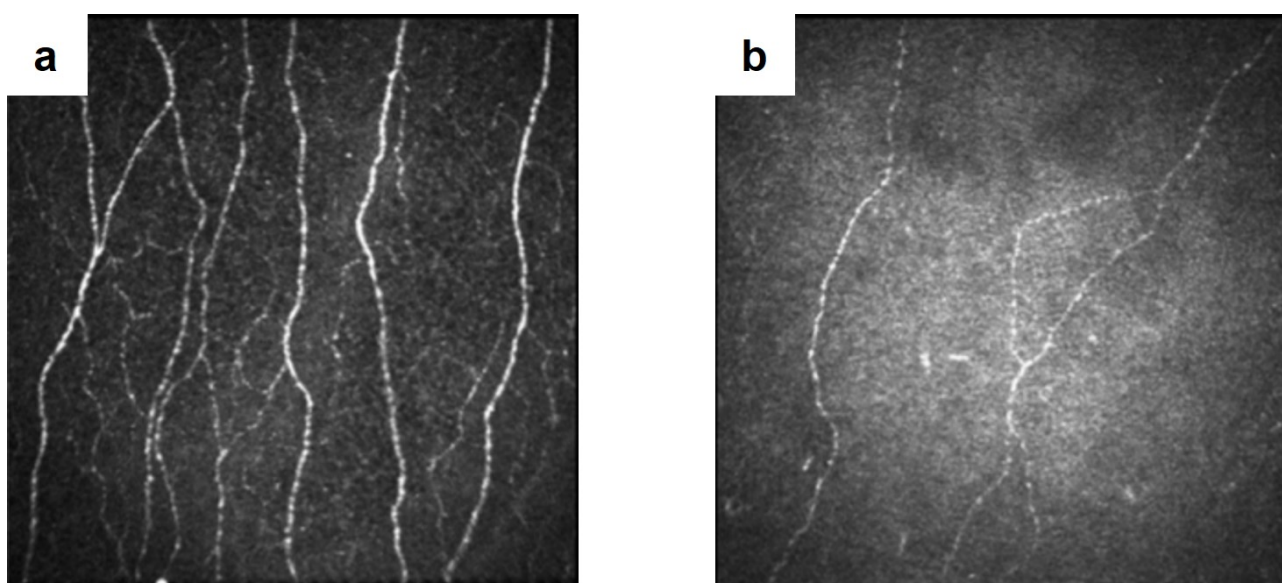


Figure B.5 – La microscopie confocale permet de reconnaître la différence de densité nerveuse cornéenne chez les patients normaux et diabétiques. (a) Sujet en bonne santé. (b) Patient atteint de neuropathie diabétique sévère. Adapté à partir de [50].

B.3 Chapitre 2 : Etat de l'art et méthodes émergentes pour l'imagerie de la surface oculaire

Les installations de diagnostic oculaire actuelles rassemblent les instruments bien établis respectant les normes (lampe à fente, microscopes spéculaires et confocaux) et de nouveaux dispositifs

en évolution rapide (Spectral-domain OCT, à balayage). Les figures ci-dessous illustrent leurs capacités. Parmi tous les appareils, l'IVCM est le seul instrument fournissant une résolution cellulaire et des images en face sur toute l'épaisseur de la cornée. Cependant, il est rarement utilisé dans les cliniques en raison de la nécessité d'avoir un contact direct avec l'œil du patient, procédure précédée d'une anesthésie oculaire ; de plus l'IVCM fournit un champ de vision réduit, inférieur à 0.5 mm.

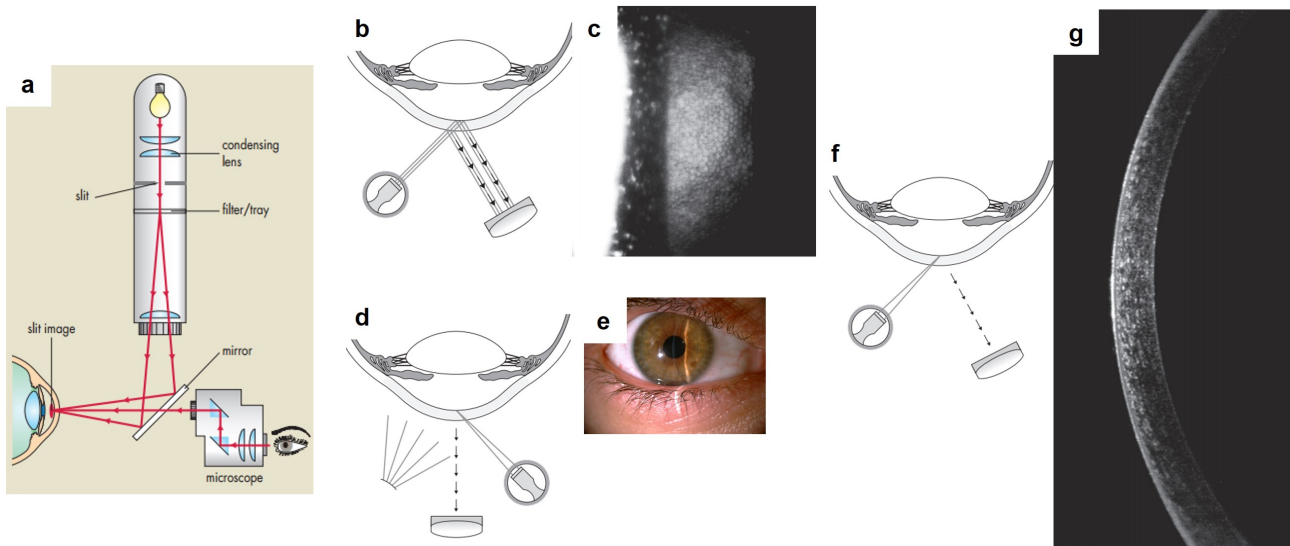


Figure B.6 – Diagnostics avec la lampe à fente. (a) Schéma du microscope et exemple de photo du dispositif à partir de [56]. (b-f) Différentes configurations d'imagerie à partir de [10]. (c,e,g) De la mosaïque de l'endothélium, de la vue macro et de la coupe transversale de la cornée. Les images sont adaptées de [57], [10].

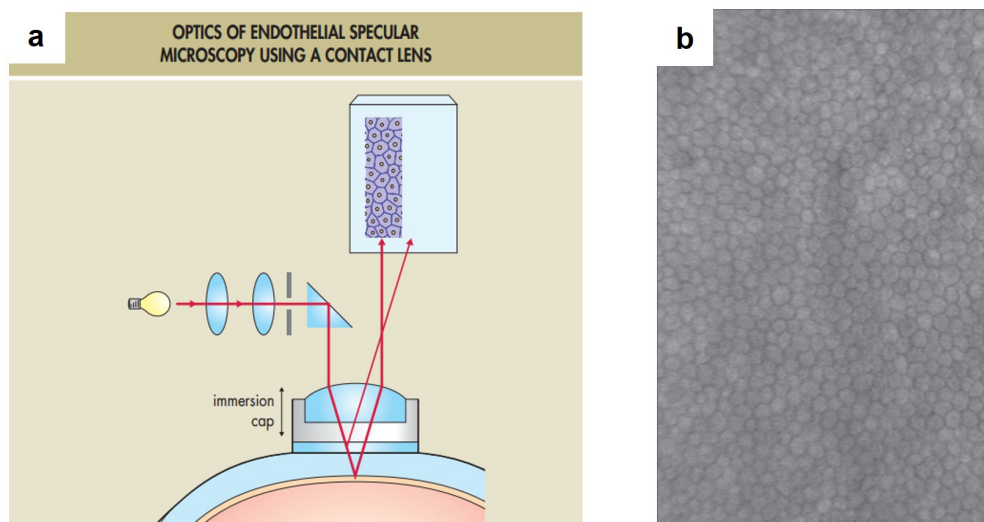


Figure B.7 – Microscopie spéculaire pour le diagnostic endothélial. (a) Schéma de la configuration avec contact à partir de [56]. (b) Mosaïque de cellules endothéliales [10]. Champ $490 \mu\text{m} \times 690 \mu\text{m}$.

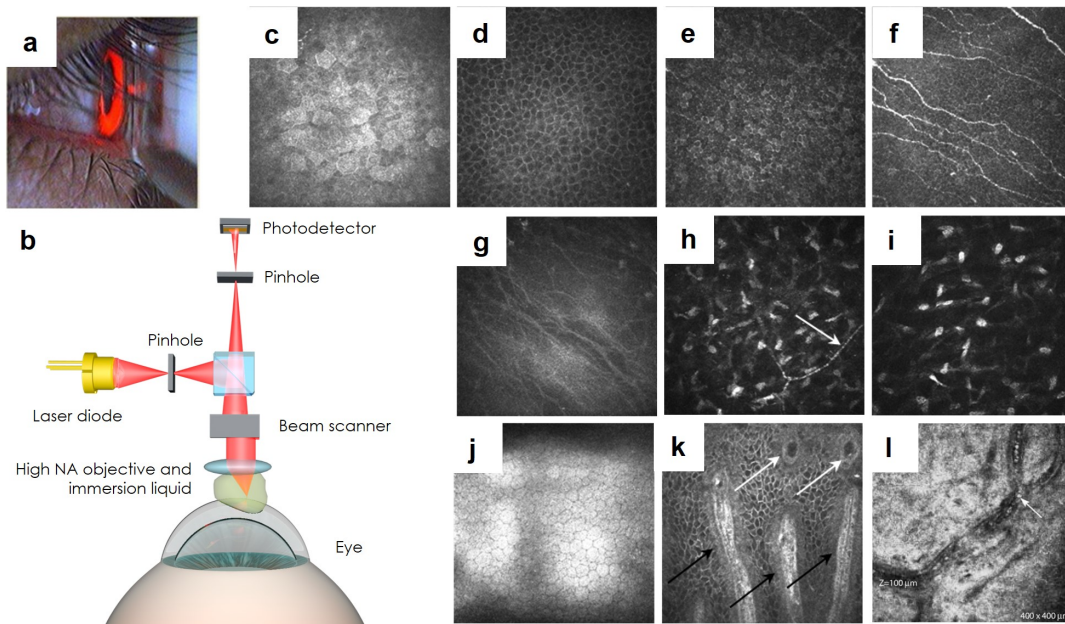


Figure B.8 – Microscopie confocale clinique avec contact oculaire. (a) Vue de la caméra d'alignement sur l'œil du patient et contact avec la frontale de l'objectif. (b) Schéma du microscope confocal. (c-l) Images de différentes couches cornéennes, adaptées de [11, 18]. Champ 400 μm.

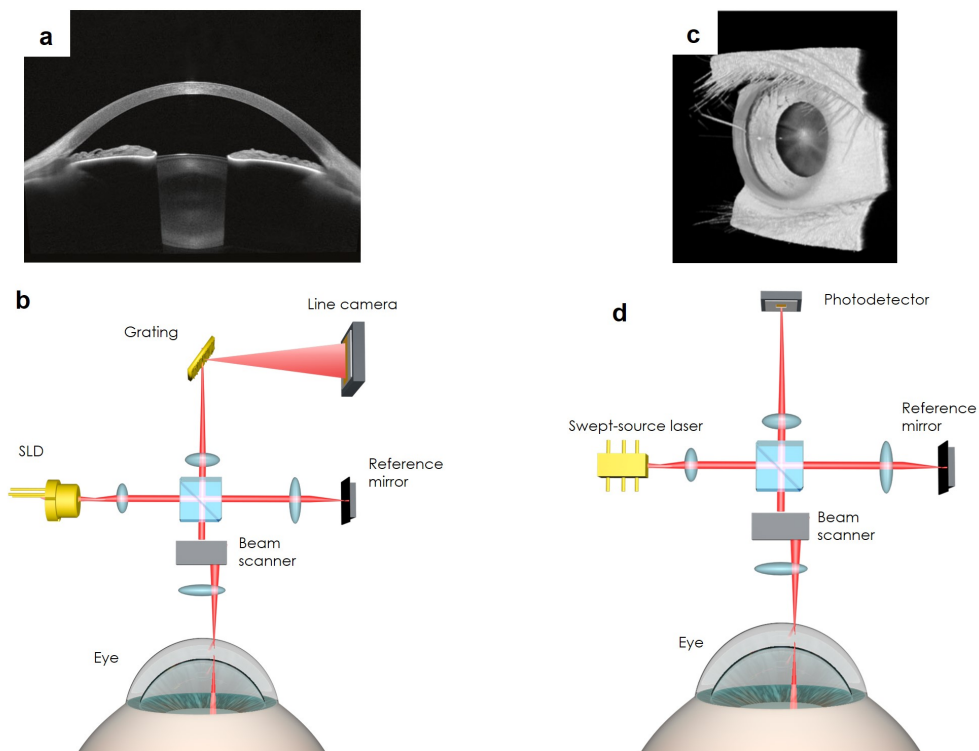


Figure B.9 – Spectral-Domain OCT (SDOCT) et OCT à source laser balayée spectralement (SSOCT). (a) Coupe transversale par SDOCT et vue sur l'ensemble de la partie antérieure de l'œil avec une grande profondeur de champ [84]. (b) Schéma de l'instrument pour la SDOCT. (c) Images volumétriques la partie antérieure de l'œil [79, 87]. (d) Schéma de l'instrument pour la SSOCT.

B.4 Chapitre 3: Imagerie Tomographique par Cohérence optique plein champ (FFOCT) appliquée à l'oeil humain *in vivo*

La tomographie par cohérence optique plein champ dans le domaine temporel (FFOCT), une extension parallélisée de l'OCT du domaine temporel classique, a été développée dans notre laboratoire en 1998 [4]. Contrairement à SDOCT, FFOCT ne fournit pas d'images en coupe axiale, mais en face. En outre, aucun balayage n'est nécessaire car tous les points dans un plan de face sont capturés simultanément à l'aide d'une caméra 2D. Etant donné que la FFOCT donne la priorité au plan « en-face », elle ne nécessite pas de grande profondeur de champ et peut utiliser des objectifs avec un nombre d'ouverture (NA) élevé pour obtenir une résolution latérale au niveau du μm . Avant le début de cette thèse, la FFOCT était limitée aux applications *ex vivo*, principalement axées sur la détection à haute résolution latérale de cellules cancéreuses dans le sein, la prostate, le cerveau et d'autres tissus *ex vivo* [90]. Dans cette thèse, j'avais pour objectif d'étendre les applications de la FFOCT à l'imagerie de la cornée humaine *in vivo*. Ce but était assez ambitieux pour être le seul objectif de mon travail, mais après les premiers succès, beaucoup d'autres d'objectifs ont été atteints dont nous discuterons plus loin.

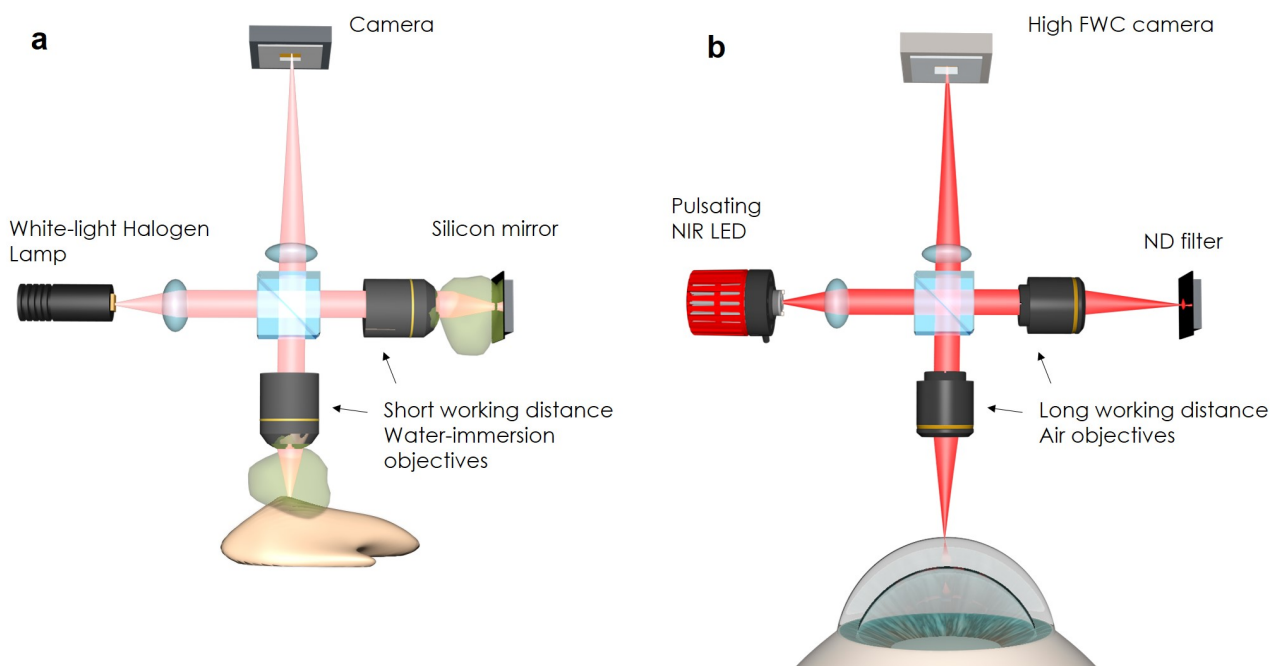


Figure B.10 – Transformation du montage de FFOCT *ex vivo* en *in vivo* (a) Dispositif *Ex vivo*. (b) Dispositif *In vivo*.

La transformation du dispositif FFOCT avec contact *ex vivo* en non contact *in vivo*, est devenue possible grâce à un choix très minutieux de chaque composant de la FFOCT; avec un fort accent sur la sensibilité et en respectant scrupuleusement les normes de sécurité oculaire. La figure (B.10) souligne les changements entre les dispositifs *ex vivo* et *in vivo*. Une autre amélioration concerne la vitesse d'acquisition, ce qui est très important pour l'imagerie de tissus *in vivo* en mouvement. En améliorant le traitement, nous avons atteint la vitesse de 550 images/s avec un temps d'exposition 1.7 ms de temps d'exposition. Nous avons également

utilisé le schéma le plus rapide actuellement à deux phases, conduisant à un temps de 3.4 ms pour acquérir une image complète FFOCT.

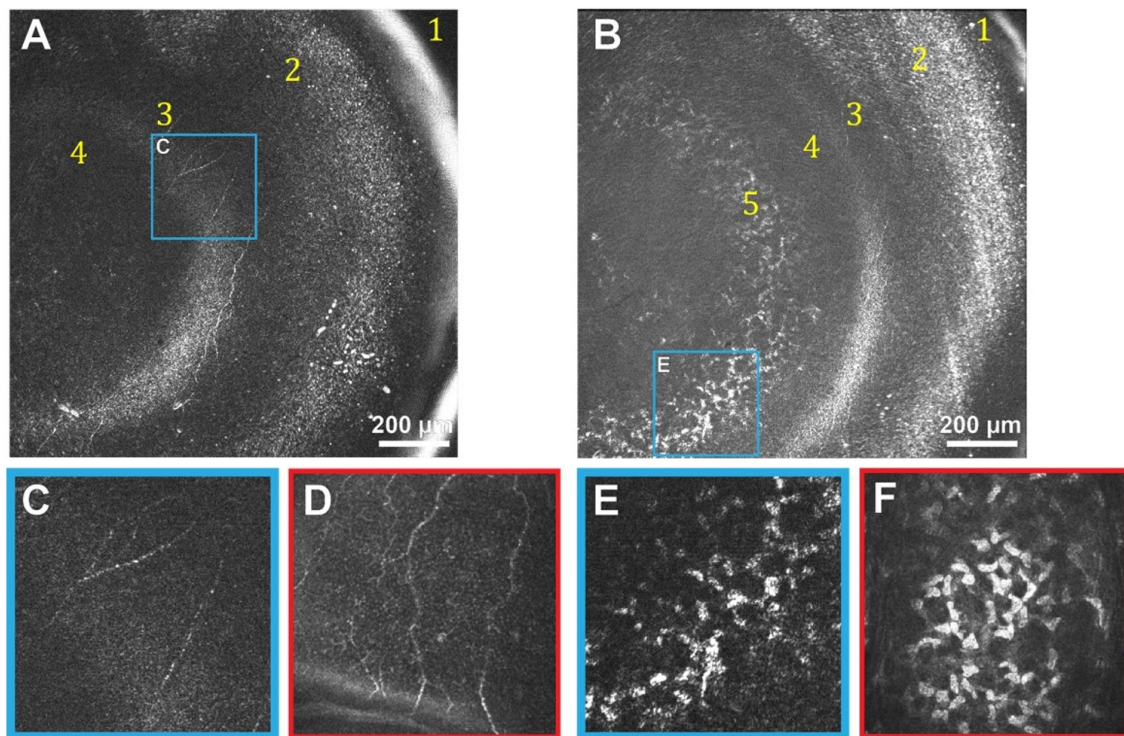


Figure B.11 – Images de la partie antérieure de la cornée humaine *in vivo*, obtenues par FFOCT et IVCM [3].

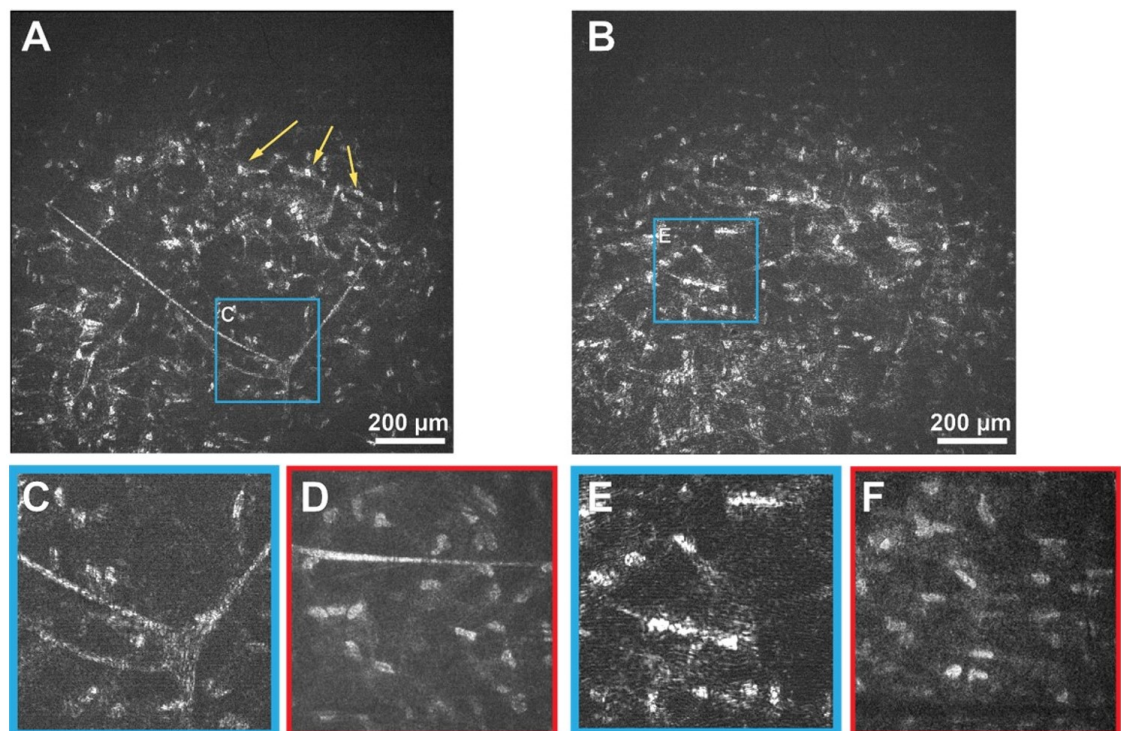


Figure B.12 – Images cornéennes *in vivo* du stroma moyen et postérieur, obtenues par FFOCT et IVCM [3].

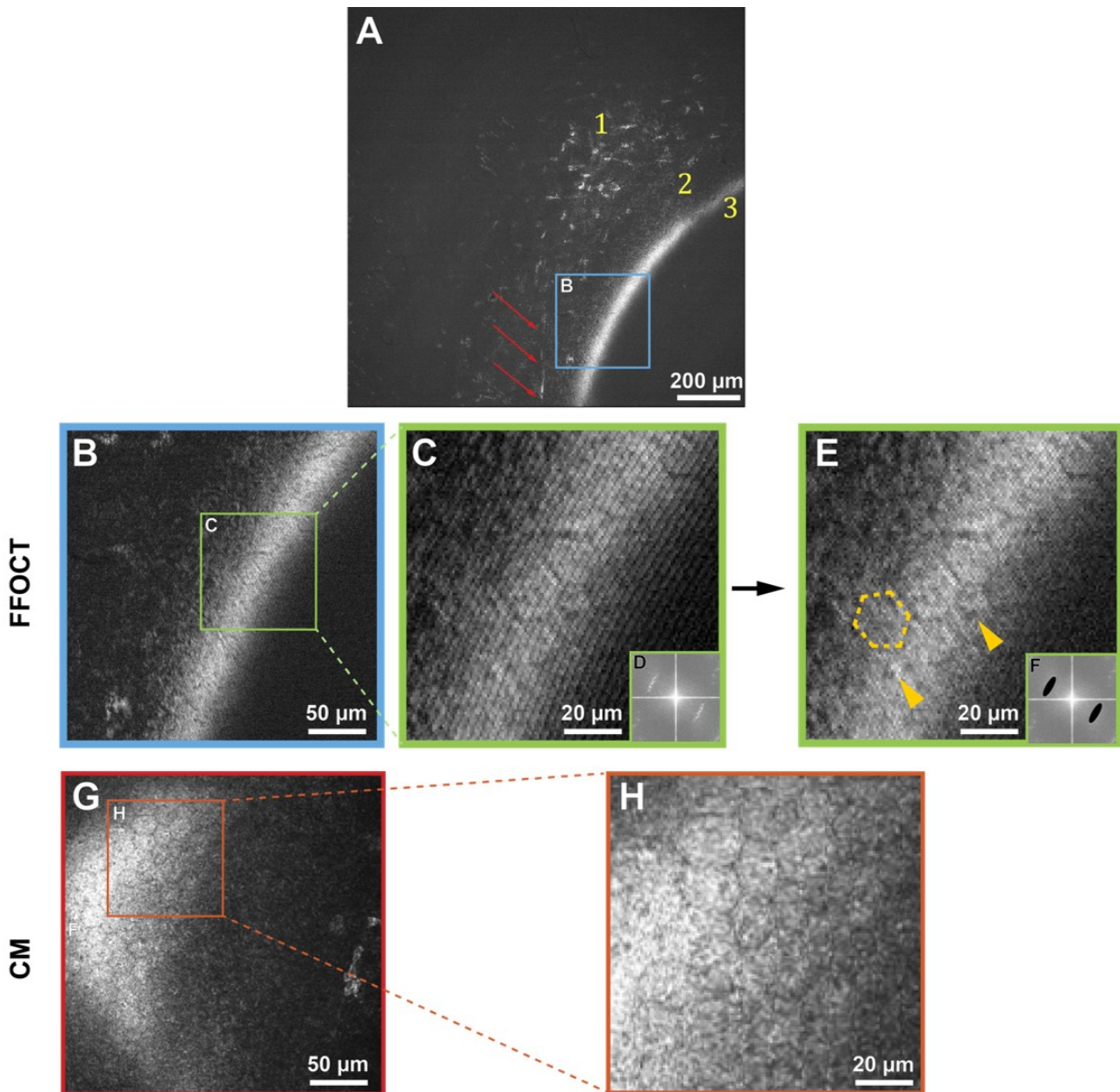


Figure B.13 – Images cornéennes humaines *in vivo* du stroma et de l'endothélium postérieurs, obtenues avec par FFOCT et IVCM [3].

B.5 Chapitre 4 : Vers la FFOCT *in vivo* en temps réel

La première conception *in vivo* de la FFOCT a permis de capturer des images prometteuses, mais seulement lorsque les longueurs de chemin optique des deux bras d'interféromètre étaient parfaitement adaptées, ce qui ne se produit que rarement en raison du problème lié à la défocalisation. La défocalisation est le décalage entre la position de la mise au point de l'objectif (là où la lumière est focalisée dans l'échantillon) et la position du plan de cohérence (plan à l'intérieur de l'échantillon, qui correspond à la différence de marche nulle avec le miroir de référence). Cette défocalisation conduit à une perte rapide du signal avec la profondeur d'imagée. Nous avons combiné FFOCT et SDOCT dans un instrument FF/SD OCT à trajet commun, qui

pourrait en temps réel suivre la position de l'œil et corriger la défocalisation à la volée, donc permettre la prise d'images FFOCT en temps réel.

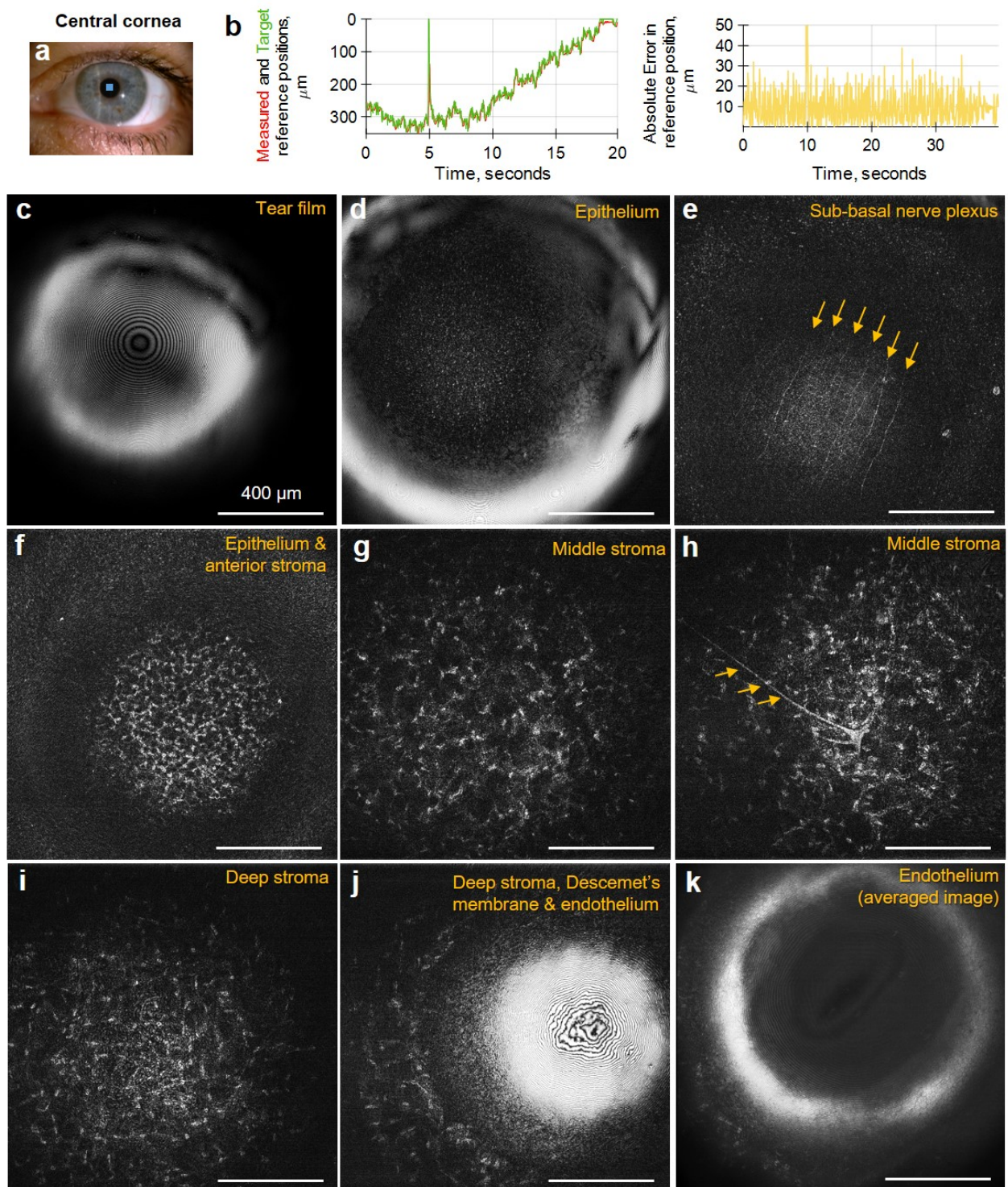


Figure B.14 – Imagerie FF/SD OCT à trajet commun de la cornée centrale humaine *in vivo*.

Nous avons appliqué une OCT FF/SD à trajet commun pour visualiser la cornée humaine *in vivo* en temps réel. L'étude a été réalisée sur trois sujets sains. Nous avons capturé des images en temps réel à partir de : cornée centrale et limbe, cornée et limbes périphériques, révélant des détails cellulaires avec un rapport signal-sur-bruit élevé et des images FFOCT sans moyenne. Nous avons également calculé la valeur de la densité nerveuse et cellulaire [102] dont on sait

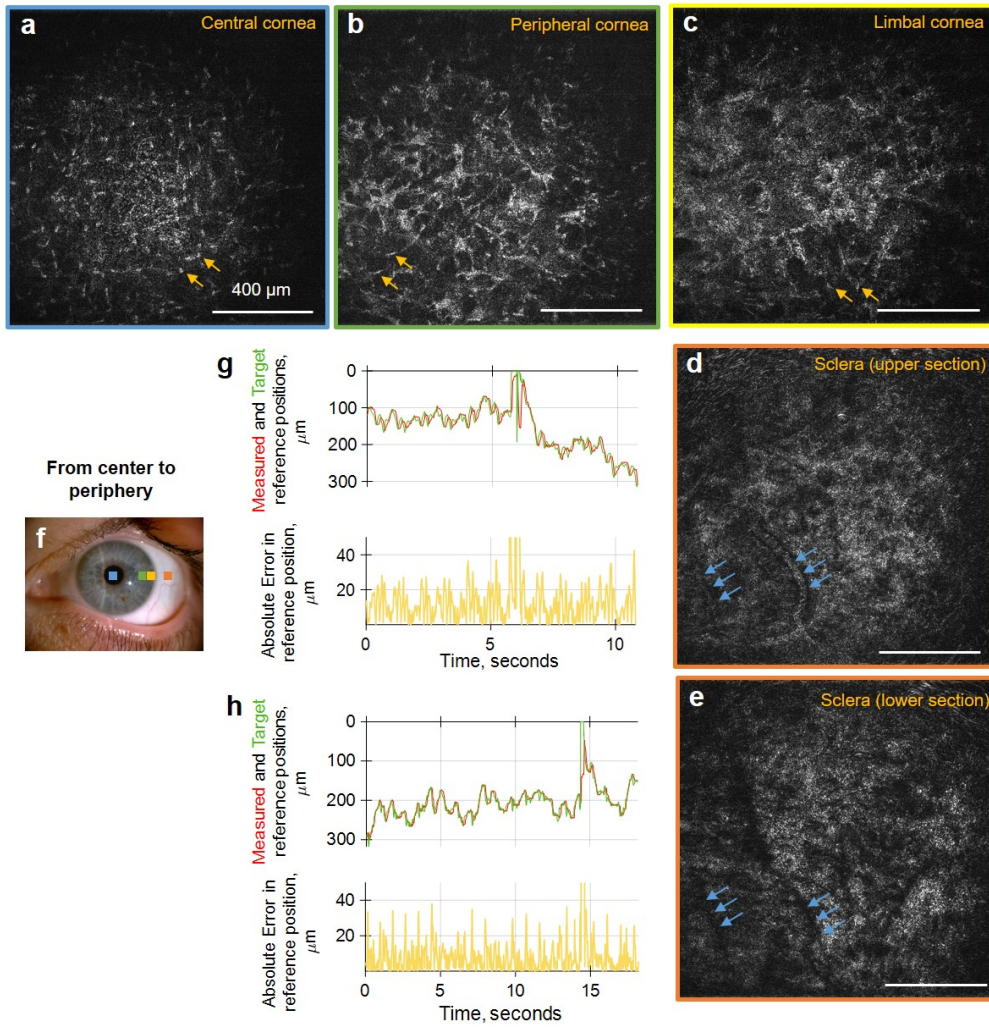


Figure B.15 – Imagerie FF/SD OCT à trajet commun de cornée et sclérotique humaines périphériques et limbales *in vivo*.

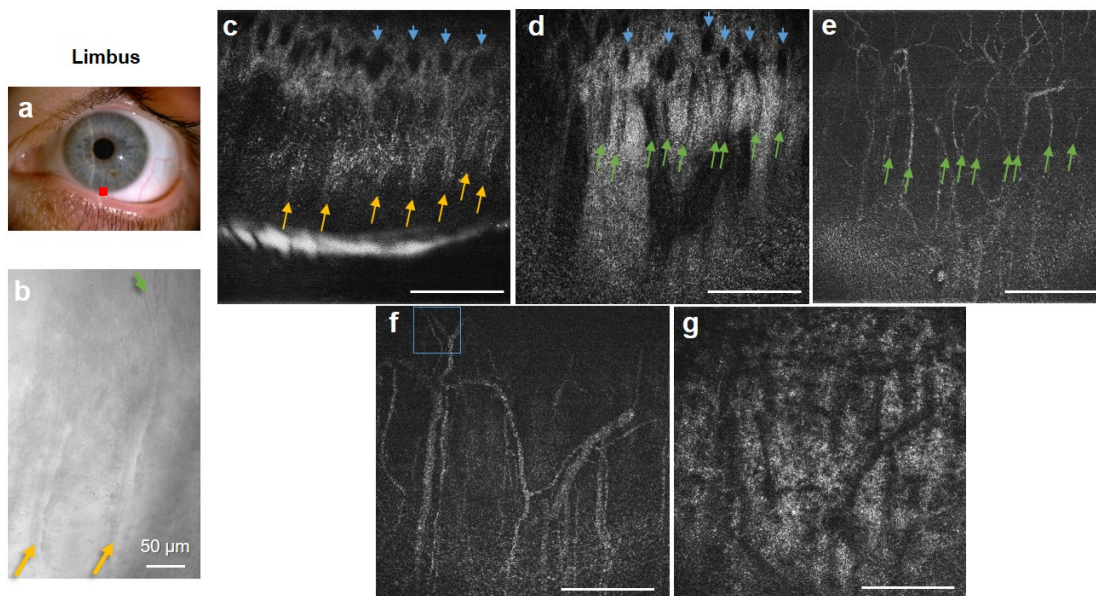


Figure B.16 – Imagerie FF/SD OCT à trajet commun du limbe humain *in vivo*.

qu'elle est cliniquement utile, ces densités peuvent être donc mesurées par FFOCT.

B.6 Chapitre 5 : Suivi des processus dynamiques dans l'oeil par FFOCT

Grâce à la vitesse d'acquisition élevée de 275 images en face /s, la FFOCT peut directement suivre la circulation sanguine dans les vaisseaux ainsi que l'évolution du film lacrymal.

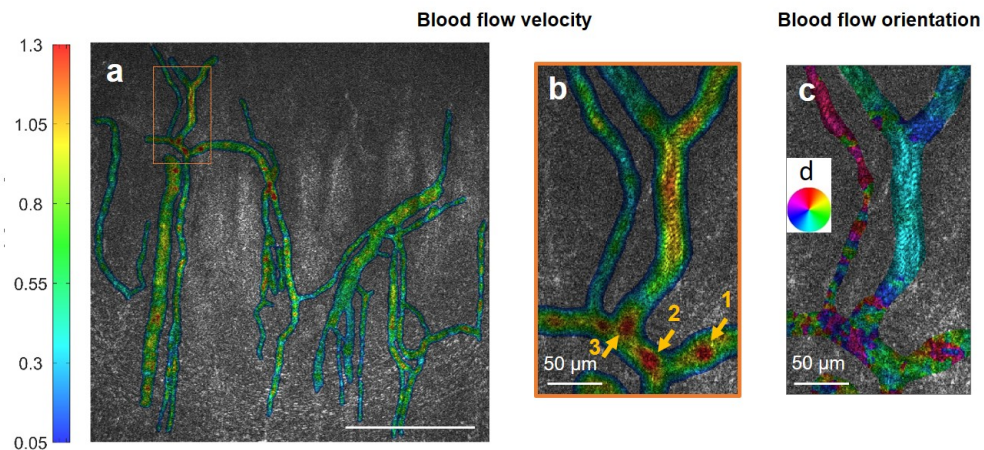


Figure B.17 – Débit sanguin dans la région limbale inférieure sous les palissades de Vogt.

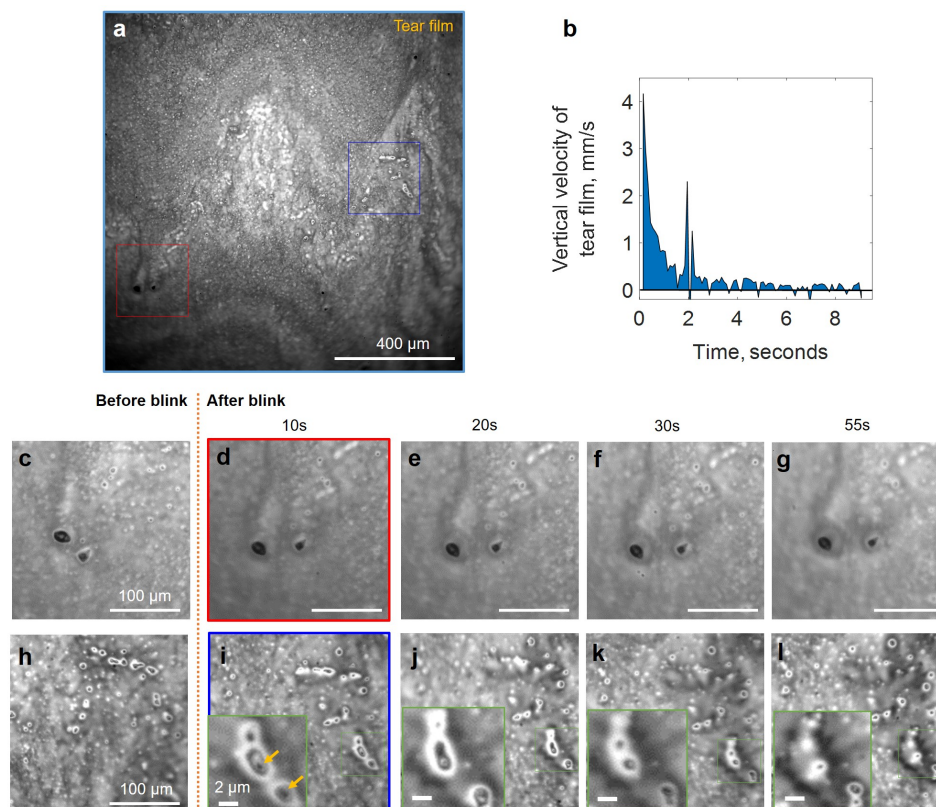


Figure B.18 – Imagerie dynamique d'un film lacrymal humain *in vivo* après le clignement des yeux avec l'OCT FF/SD en configuration microscope.

B.7 Chapitre 6 : Remarque sur l'extension du champ de vision en FFOCT

Etant donné que la FFOCT est une méthode sans balayage, qui utilise les objectifs de microscope de NA modérée, il est facile d'augmenter le champ de vision en changeant la focale de la lentille de tube. Un champ de vision plus large réduit le risque qu'une tache spécifique de la maladie puisse être manquée.

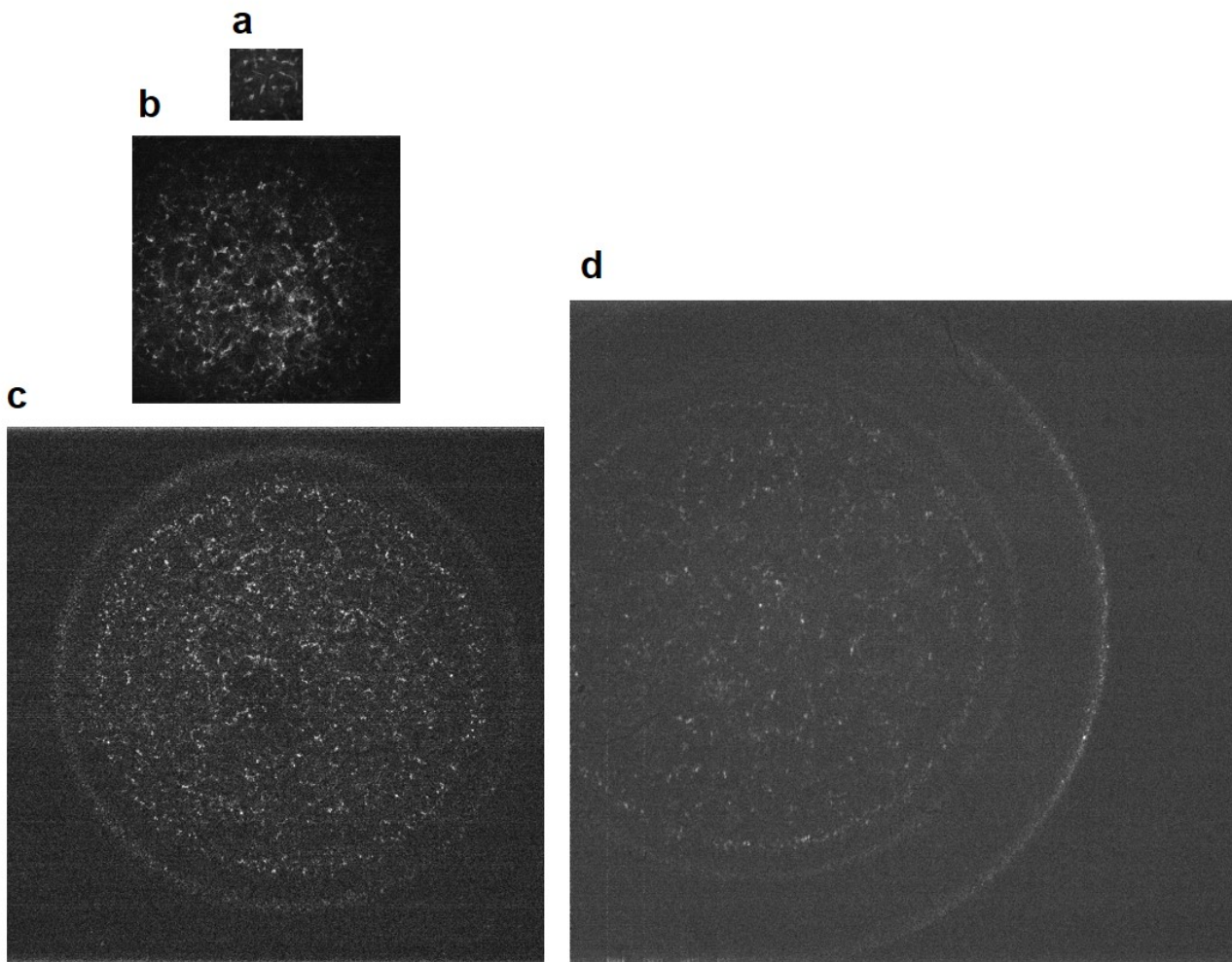


Figure B.19 – Cornée humaine *in vivo*, imagée avec différents champs de vision. (a) Microscopie confocale, image de $0.3 \text{ mm} \times 0.3 \text{ mm}$. (b) FFOCT ($1.25 \text{ mm} \times 1.25 \text{ mm}$). (c) FFOCT ($2.5 \text{ mm} \times 2.5 \text{ mm}$). (d) FFOCT ($3.1 \text{ mm} \times 3.1 \text{ mm}$). L'image a un SNR réduit, en raison de l'utilisation de l'objectif non traité pour la lumière proche infrarouge.

B.8 Chapitre 7 : Un coup d'œil sur l'imagerie de la rétine avec FFOCT

Avec Peng Xiao et ses collègues, nous avons également travaillé pour appliquer, pour la première fois, la FFOCT dans le domaine temporel pour l'imagerie de la rétine humaine *in vivo*. Les

premières images sont présentées ci-dessous.

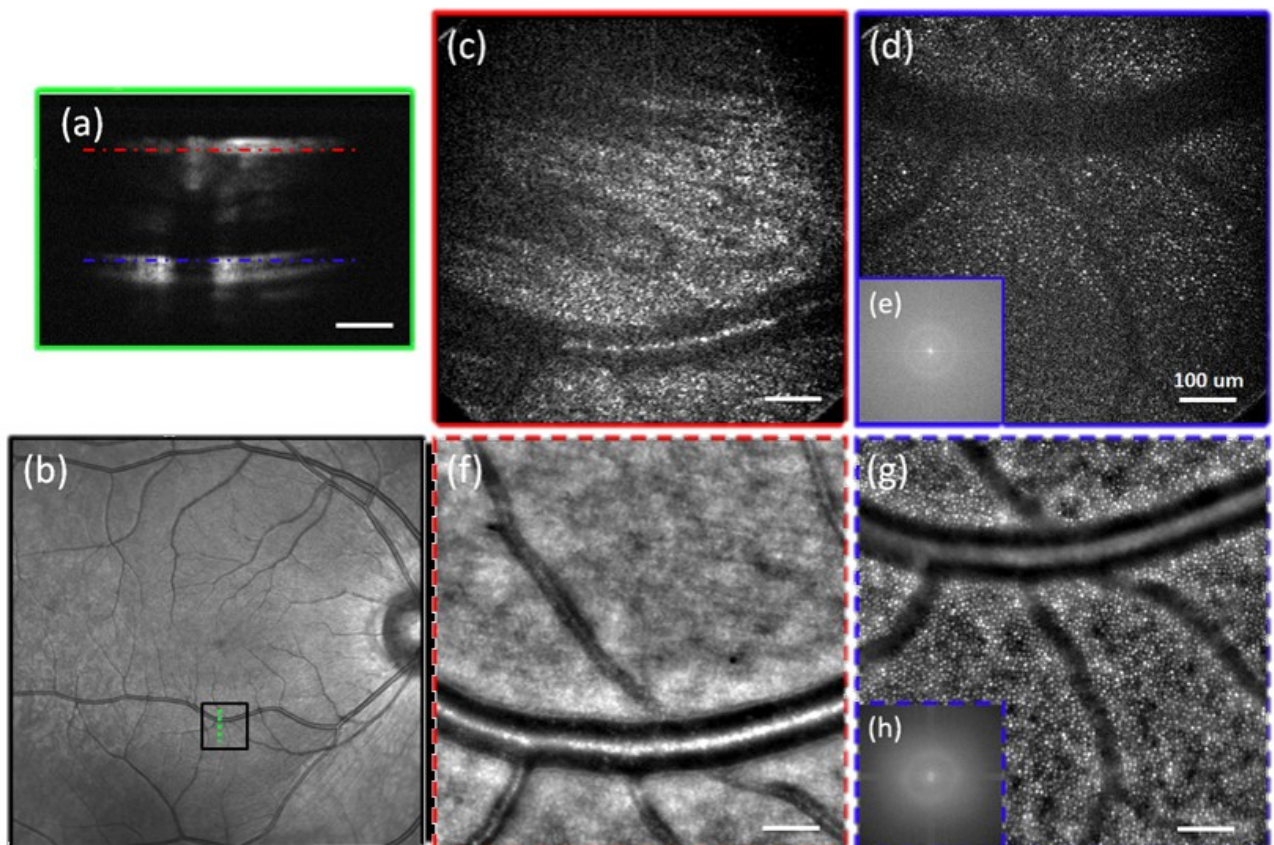


Figure B.20 – Images FFOCT de la rétine humaine *in vivo* à 6° d'excentricité sous le centre de la fovéa [83]. (a) Image SDOCT. (b) Image du fond d'œil avec la zone noire indiquant la zone d'imagerie FFOCT et la ligne pointillée verte indiquant la position de numérisation de la SDOCT. (c) Images FFOCT de RNFL (fibres nerveuses). (d) Image FFOCT de la couche de photorécepteur. (e) Transformée de Fourier de l'image avec un anneau, indiquant l'espacement régulier des cônes. (f) Image par Optique Adaptative (AO) rétinienne de RNFL. (g) Image par AO de la couche de photorécepteurs. (h) Image de Fourier avec un anneau indiquant l'espacement des cônes. Toutes les barres d'échelle = 100 μm .

B.9 Chapitre 8 : Simplification de la FFOCT

Enfin, nous avons également démontré que les mouvements oculaires axiaux jouent un rôle déterminant dans la modulation de phase. Nous avons confirmé que l'image de FFOCT peut être obtenue uniquement à l'aide de mouvements oculaires axiaux sans modulation de la différence de marche.

References

- [1] D Huang, E. Swanson, C. Lin, J. Schuman, W. Stinson, W Chang, M. Hee, T Flotte, K Gregory, C. Puliafito, and al. et. Optical coherence tomography. *Science*, 254(5035):1178–1181, November 1991.
- [2] James Fujimoto and David Huang. Foreword: 25 Years of Optical Coherence Tomography. *Investigative Ophthalmology & Visual Science*, 57(9):OCTi, July 2016.
- [3] Viacheslav Mazlin, Peng Xiao, Eugénie Dalimier, Kate Grieve, Kristina Irsch, José-Alain Sahel, Mathias Fink, and A. Claude Boccara. In vivo high resolution human corneal imaging using full-field optical coherence tomography. *Biomedical Optics Express*, 9(2):557, February 2018.
- [4] E. Beaupaire, A. C. Boccara, M. Lebec, L. Blanchot, and H. Saint-Jalmes. Full-field optical coherence microscopy. *Optics Letters*, 23(4):244, February 1998.
- [5] Ocular surface visible through slit-lamp. <https://www.slideshare.net/tbf413/understanding-the-slit-lamp/>.
- [6] Edward A. Boettner and J. Reimer Wolter. Transmission of the ocular media. *Investigative Ophthalmology & Visual Science*, 1(6):776–783, 12 1962.
- [7] Rahul Yadav, Kye-Sung Lee, Jannick P. Rolland, James M. Zavislan, James V. Aquavella, and Geunyoung Yoon. Micrometer axial resolution OCT for corneal imaging. *Biomedical Optics Express*, 2(11):3037, November 2011.
- [8] M. J. Hogan, J. A. Alvarado, and J. E. Weddell. *Histology of the Human Eye: An Atlas and Textbook*. Saunders, 1971.
- [9] RA Thoft and G Smolin. *Smolin and Thoft's The Cornea: Scientific Foundations and Clinical Practice*. Lippincott Williams & Wilkins (LWW), 2004.
- [10] Mark J. Mannis and Edward J. Holland. *Cornea: Fundamentals diagnosis and management*. Elsevier, 2017.
- [11] N Lagali, BB Peebo, J Germundsson, U Edén, R Danyali, M Rinaldo, and P Fagerholm. Laser-scanning in vivo confocal microscopy of the cornea: Imaging and analysis methods for preclinical and clinical applications, confocal laser microscopy - principles and applications in medicine, biology, and the food sciences. *IntechOpen*, 2013.

- [12] William D. Mathers and Thomas E. Daley. In vivo observation of the human tear film by tandem scanning confocal microscopy. *Scanning*, 16(5):316–319, April 2008.
- [13] B. A. Nichols, M. L. Chiappino, and C. R. Dawson. Demonstration of the mucous layer of the tear film by electron microscopy. *Investigative Ophthalmology & Visual Science*, 26(4):464–473, April 1985.
- [14] P. Ewen King-Smith, Jason J. Nichols, Richard J. Braun, and Kelly K. Nichols. High Resolution Microscopy of the Lipid Layer of the Tear Film. *The Ocular Surface*, 9(4):197–211, October 2011.
- [15] H Owens and J Phillips. Spreading of the tears after a blink: Velocity and stabilization time in healthy eyes. *Cornea*, 20(5):484–487, July 2001.
- [16] E Holland, M Mannis, and W Barry Lee. *Ocular Surface Disease: Cornea, Conjunctiva and Tear Film*. Elsevier, 2013.
- [17] Hai-Bo Chen, Shigeki Yamabayashi, Bo Ou, Yuko Tanaka, Shinichi Ohno, and Shigeo Tsukahara. Structure and composition of rat precorneal tear film. *Investigative Ophthalmology Visual Science*, 38(2):381–387, 1997.
- [18] R.F. Guthoff, C. Baudouin, and J. Stave. *Atlas of Confocal Laser Scanning In-vivo Microscopy in Ophthalmology*. Springer, 2006.
- [19] D. A. Dartt, D. P. Bex, P. D. Reza, Mcloon D.L., and Niederkorn J. *Ocular Periphery and Disorders*. Elsevier, 2011.
- [20] RA Copeland and N Afshari. *Copeland and Afshari's Principles and Practice of Cornea*. JP Medical Ltd, 2013.
- [21] P D Yurchenco and J C Schittny. Molecular architecture of basement membranes. *The FASEB Journal*, 4(6):1577–1590, April 1990.
- [22] Tsugiaki Utsunomiya, Taiji Nagaoka, Kazuomi Hanada, Tsuneaki Omae, Harumasa Yokota, Atsuko Abiko, Masakazu Haneda, and Akitoshi Yoshida. Imaging of the Corneal Subbasal Whorl-like Nerve Plexus: More Accurate Depiction of the Extent of Corneal Nerve Damage in Patients With Diabetes. *Investigative Ophthalmology & Visual Science*, 56(9):5417, August 2015.
- [23] Yoshiko Komai and Tatsuo Ushiki. The three-dimensional organization of collagen fibrils in the human cornea and sclera. *Investigative Ophthalmology Visual Science*, 32(8):2244–2258, 1991.
- [24] D. M. Maurice. The structure and transparency of the cornea. *The Journal of Physiology*, 136(2):263–286, April 1957.
- [25] James V. Jester. Corneal crystallins and the development of cellular transparency. *Seminars in Cell & Developmental Biology*, 19(2):82–93, April 2008.
- [26] Holt WS and Kinoshita JH. The soluble proteins of the bovine cornea. *Invest Ophthalmol.*, 12(2):114–26, 1973.
- [27] Toichiro Kuwabara. CIL_10944, Homo sapiens, corneal endothelial cell: <http://www.cellimagelibrary.org/images/10944>, 2011. type: dataset.

- [28] Tianyu Zheng, Qihua Le, Jiayu Hong, and Jianjiang Xu. Comparison of human corneal cell density by age and corneal location: an in vivo confocal microscopy study. *BMC Ophthalmology*, 16(1), December 2016.
- [29] Josef Amann, Glenn P Holley, Sang-BuMm Lee, and Henry F Edelhauser. Increased endothelial cell density in the paracentral and peripheral regions of the human cornea. *American Journal of Ophthalmology*, 135(5):584–590, May 2003.
- [30] <https://wasatchphotonics.com/oct-image-gallery/>.
- [31] Ilene K Gipson. The epithelial basement membrane zone of the limbus. *Eye*, 3(2):132–140, March 1989.
- [32] Morton Goldberg and Anthony Bron. Limbal palisades of vogt. *Transactions of the American Ophthalmological Society*, 80:155–71, 02 1982.
- [33] Kostadinka Bizheva, Bingyao Tan, Benjamin MacLellan, Zohreh Hosseinaee, Erik Mason, Denise Hileeto, and Luigina Sorbara. In-vivo imaging of the palisades of Vogt and the limbal crypts with sub-micrometer axial resolution optical coherence tomography. *Biomedical Optics Express*, 8(9):4141, September 2017.
- [34] Dipika V. Patel, Trevor Sherwin, and Charles N. J. McGhee. Laser Scanning In Vivo Confocal Microscopy of the Normal Human Corneoscleral Limbus. *Investigative Ophthalmology & Visual Science*, 47(7):2823, July 2006.
- [35] Donatella Pascolini and Silvio Paolo Mariotti. Global estimates of visual impairment: 2010. *British Journal of Ophthalmology*, 96(5):614–618, May 2012.
- [36] J. P. Whitcher and M. P. Upadhyay. Corneal blindness: a global perspective. *Bulletin of the World Health Organization : the International Journal of Public Health*, 79(3):214–221, 2001.
- [37] WHO. *Universal eye health: a global action plan 2014–2019*. WHO, 2013.
- [38] <https://www.easytearviewplus.com/en/gallery/>.
- [39] J. P. Guillon. Non-invasive Tearscope Plus routine for contact lens fitting. *Contact Lens & Anterior Eye: The Journal of the British Contact Lens Association*, 21 Suppl 1:S31–40, 1998.
- [40] <https://konanmedical.com/cellchek/specular-fundamentals/>.
- [41] Jie Zhang and Dipika V. Patel. The pathophysiology of Fuchs’ endothelial dystrophy – A review of molecular and cellular insights. *Experimental Eye Research*, 130:97–105, January 2015.
- [42] David Schlossberg, editor. *Clinical Infectious Disease*. Cambridge University Press, Cambridge, 2 edition, 2015.
- [43] Nicholas J. R. Maycock and Rakesh Jayaswal. Update on Acanthamoeba Keratitis: Diagnosis, Treatment, and Outcomes. *Cornea*, 35(5):713–720, May 2016.
- [44] Karen Winchester, William Mathers, John Sutphin, and Thomas Daley. Diagnosis of Acanthamoeba Keratitis In Vivo with Confocal Microscopy. *Cornea.*, 14(1):10–17, January 1995.

- [45] Marcus Ang, Mani Baskaran, René M. Werkmeister, Jacqueline Chua, Doreen Schmidl, Valentin Aranha dos Santos, Gerhard Garhöfer, Jodhbir S. Mehta, and Leopold Schmetterer. Anterior segment optical coherence tomography. *Progress in Retinal and Eye Research*, 66:132–156, September 2018.
- [46] Harry Yip and Elsie Chan. Optical coherence tomography imaging in keratoconus. *Clinical and Experimental Optometry*, 102(3):218–223, May 2019.
- [47] Keratoconus. <http://lonestareyecenter.com/keratoconus-treatments-in-austin-tx-lone-star-eye-center>.
- [48] IDF diabetes atlas - 2017 Atlas: <https://diabetesatlas.org/resources/2017-atlas.html>.
- [49] Nikolaos Papanas and Dan Ziegler. Corneal confocal microscopy: Recent progress in the evaluation of diabetic neuropathy. *Journal of Diabetes Investigation*, 6(4):381–389, July 2015.
- [50] Roni M. Shtein and Brian C. Callaghan. Corneal Confocal Microscopy as a Measure of Diabetic Neuropathy. *Diabetes*, 62(1):25–26, January 2013.
- [51] Mario Nubile, Manuela Lanzini, Ammar Miri, Augusto Pocobelli, Roberta Calienno, Claudia Curcio, Rodolfo Mastropasqua, Harminder S. Dua, and Leonardo Mastropasqua. In Vivo Confocal Microscopy in Diagnosis of Limbal Stem Cell Deficiency. *American Journal of Ophthalmology*, 155(2):220–232, February 2013.
- [52] Milton Lionel Berliner. *Biomicroscopy of the Eye: Slit Lamp Microscopy of the Living Eye*, volume 1. Hoeber, 1943.
- [53] Wolfgang Drexler and James G. Fujimoto. *Optical Coherence Tomography Technology and Applications*. 2. Springer International Publishing, 2015.
- [54] Keith M. Meek and Carlo Knupp. Corneal structure and transparency. *Progress in Retinal and Eye Research*, 49:1–16, November 2015.
- [55] Yifei Huang and Keith M. Meek. Swelling Studies on the Cornea and Sclera: The Effects of pH and Ionic Strength. *Biophysical Journal*, 77(3):1655–1665, September 1999.
- [56] Myron Yanoff and Jay S. Duker. *Ophthalmology*. Elsevier, 5 edition, 2018.
- [57] Csaba L. Martonyi, Charles F. Bahn, and Roger F. Meyer. *Slit Lamp: Examination and Photography*. Time One Ink, 2007.
- [58] Deane B. Judd and Günther Wyszecki. *Color in Business, Science, and Industry*. Wiley-Interscience, 1973.
- [59] Confocal Microscopy - Resolution and Contrast in Confocal Microscopy | Olympus Life Science: <https://www.olympus-lifescience.com/en/microscope-resource/primer/techniques/confocal/resolutionintro/>.
- [60] W. Matthew Petroll, Matthew Weaver, Saurabh Vaidya, James P. McCulley, and H. Dwight Cavanagh. Quantitative 3-Dimensional Corneal Imaging In Vivo Using a Modified HRT-RCM Confocal Microscope. *Cornea*, 32(4):e36–e43, April 2013.
- [61] Nicola Pritchard, Katie Edwards, and Nathan Efron. Non-contact laser-scanning confocal microscopy of the human cornea in vivo. *Contact Lens and Anterior Eye*, 37(1):44–48, February 2014.

- [62] Stephan Allgeier, Susanne Maier, Ralf Mikut, Sabine Peschel, Klaus-Martin Reichert, Oliver Stachs, and Bernd Köhler. Mosaicking the Subbasal Nerve Plexus by Guided Eye Movements. *Investigative Ophthalmology & Visual Science*, 55(9):6082, September 2014.
- [63] Stephan Allgeier, Andreas Bartschat, Sebastian Bohn, Sabine Peschel, Klaus-Martin Reichert, Karsten Sperlich, Marcus Walckling, Veit Hagenmeyer, Ralf Mikut, Oliver Stachs, and Bernd Köhler. 3d confocal laser-scanning microscopy for large-area imaging of the corneal subbasal nerve plexus. *Scientific Reports*, 8(1), December 2018.
- [64] Sebastian Bohn, Karsten Sperlich, Stephan Allgeier, Andreas Bartschat, Ruby Prakasam, Klaus-Martin Reichert, Heinrich Stolz, Rudolf Guthoff, Ralf Mikut, Bernd Köhler, and Oliver Stachs. Cellular in vivo 3d imaging of the cornea by confocal laser scanning microscopy. *Biomedical Optics Express*, 9(6):2511, June 2018.
- [65] Sebastian Bohn, Karsten Sperlich, Heinrich Stolz, Rudolf F. Guthoff, and Oliver Stachs. In vivo corneal confocal microscopy aided by optical coherence tomography. *Biomedical Optics Express*, 10(5):2580, May 2019.
- [66] Wolfgang Drexler and James G Fujimoto. *Optical coherence tomography: Technology and applications*, 2015.
- [67] Joseph A. Izatt. Micrometer-Scale Resolution Imaging of the Anterior Eye In Vivo With Optical Coherence Tomography. *Archives of Ophthalmology*, 112(12):1584, December 1994.
- [68] Roger F. Steinert and David Huang. *Anterior Segment Optical Coherence Tomography*. Slack Incorporated, 2008.
- [69] Robert C. Youngquist, Sally Carr, and D. E. N. Davies. Optical coherence-domain reflectometry: a new optical evaluation technique. *Optics Letters*, 12(3):158, March 1987.
- [70] Kazumasa Takada, Itaru Yokohama, Kazumori Chida, and Juichi Noda. New measurement system for fault location in optical waveguide devices based on an interferometric technique. *Applied Optics*, 26(9):1603, May 1987.
- [71] A. F. Fercher, K. Mengedoht, and W. Werner. Eye-length measurement by interferometry with partially coherent light. *Optics Letters*, 13(3):186, March 1988.
- [72] Maciej Wojtkowski, Rainer Leitgeb, Andrzej Kowalczyk, Tomasz Bajraszewski, and Adolf F. Fercher. In vivo human retinal imaging by Fourier domain optical coherence tomography. *Journal of Biomedical Optics*, 7(3):457, 2002.
- [73] Johannes F. de Boer, Barry Cense, B. Hyle Park, Mark C. Pierce, Guillermo J. Tearney, and Brett E. Bouma. Improved signal-to-noise ratio in spectral-domain compared with time-domain optical coherence tomography. *Optics Letters*, 28(21):2067, November 2003.
- [74] Michael Choma, Marinko Sarunic, Changhuei Yang, and Joseph Izatt. Sensitivity advantage of swept source and Fourier domain optical coherence tomography. *Optics Express*, 11(18):2183, September 2003.
- [75] S. R. Chinn, E. A. Swanson, and J. G. Fujimoto. Optical coherence tomography using a frequency-tunable optical source. *Optics Letters*, 22(5):340, March 1997.

- [76] René M. Werkmeister, Sabina Sapeta, Doreen Schmidl, Gerhard Garhöfer, Gerald Schmidinger, Valentin Aranha dos Santos, Gerold C. Aschinger, Isabella Baumgartner, Niklas Pircher, Florian Schwarzhans, Anca Pantalon, Harminder Dua, and Leopold Schmetterer. Ultrahigh-resolution OCT imaging of the human cornea. *Biomedical Optics Express*, 8(2):1221, February 2017.
- [77] Bingyao Tan, Zohreh Hosseinaee, Le Han, Olivera Kralj, Luigina Sorbara, and Kostadinka Bizheva. 250 kHz, 1,5 μm resolution SD-OCT for in-vivo cellular imaging of the human cornea. *Biomedical Optics Express*, 9(12):6569, December 2018.
- [78] Ireneusz Grulkowski, Michalina Gora, Maciej Szkulmowski, Iwona Gorczynska, Daniel Szlag, Susana Marcos, Andrzej Kowalczyk, and Maciej Wojtkowski. Anterior segment imaging with Spectral OCT system using a high-speed CMOS camera. *Optics Express*, 17(6):4842, March 2009.
- [79] Ireneusz Grulkowski, Jonathan J. Liu, Benjamin Potsaid, Vijaysekhar Jayaraman, Chen D. Lu, James Jiang, Alex E. Cable, Jay S. Duker, and James G. Fujimoto. Retinal, anterior segment and full eye imaging using ultrahigh speed swept source OCT with vertical-cavity surface emitting lasers. *Biomedical Optics Express*, 3(11):2733, November 2012.
- [80] Laurin Ginner, Tilman Schmoll, Abhishek Kumar, Matthias Salas, Nastassia Pricoupenko, Lara M. Wurster, and Rainer A. Leitgeb. Holographic line field en-face OCT with digital adaptive optics in the retina in vivo. *Biomedical Optics Express*, 9(2):472, February 2018.
- [81] Dierck Hillmann, Hendrik Spahr, Helge Sudkamp, Carola Hain, Laura Hinkel, Gesa Franke, and Gereon Hüttmann. Off-axis reference beam for full-field swept-source OCT and holoscopy. *Optics Express*, 25(22):27770, October 2017.
- [82] Helge Sudkamp, Peter Koch, Hendrik Spahr, Dierck Hillmann, Gesa Franke, Michael Müntz, Fred Reinholz, Reginald Birngruber, and Gereon Hüttmann. In-vivo retinal imaging with off-axis full-field time-domain optical coherence tomography. *Optics Letters*, 41(21):4987, November 2016.
- [83] Peng Xiao, Viacheslav Mazlin, Kate Grieve, Jose-Alain Sahel, Mathias Fink, and A. Claude Boccara. In vivo high-resolution human retinal imaging with wavefront-correctionless full-field OCT. *Optica*, 5(4):409, April 2018.
- [84] ANTERION - Multimodal Imaging Platform Optimized for the Anterior Segment | Heidelberg Engineering: <https://business-lounge.heidelbergengineering.com/gf/en/products/anterion/anterion/>.
- [85] René M. Werkmeister, Aneesh Alex, Semira Kaya, Angelika Unterhuber, Bernd Hofer, Jasmin Riedl, Michael Bronhagl, Martin Vietauer, Doreen Schmidl, Tilman Schmoll, Gerhard Garhöfer, Wolfgang Drexler, Rainer A. Leitgeb, Martin Groeschl, and Leopold Schmetterer. Measurement of Tear Film Thickness Using Ultrahigh-Resolution Optical Coherence Tomography. *Investigative Ophthalmology & Visual Science*, 54(8):5578, August 2013.
- [86] Kostadinka Bizheva, Bingyao Tan, Benjamin MacLellan, Olivera Kralj, Mojtaba Hajialamdari, Denise Hileeto, and Luigina Sorbara. Sub-micrometer axial resolution OCT

- for in-vivo imaging of the cellular structure of healthy and keratoconic human corneas. *Biomedical Optics Express*, 8(2):800, February 2017.
- [87] Michalina Gora, Karol Karnowski, Maciej Szkulmowski, Bartłomiej J. Kaluzny, Robert Huber, Andrzej Kowalczyk, and Maciej Wojtkowski. Ultra high-speed swept source OCT imaging of the anterior segment of human eye at 200 kHz with adjustable imaging range. *Optics Express*, 17(17):14880, August 2009.
- [88] Egidijus Auksorius and A Claude Boccara. Dark-field full-field optical coherence tomography. *Optics letters*, 40(14):3272–3275, 2015.
- [89] Amaury Badon, Dayan Li, Geoffroy Lerosey, A. Claude Boccara, Mathias Fink, and Alexandre Aubry. Smart optical coherence tomography for ultra-deep imaging through highly scattering media. *Science Advances*, 2(11):e1600370, November 2016.
- [90] Arnaud Dubois. *Handbook of full-field optical coherence microscopy: technology and applications*. Pan Stanford Publishing, 2016.
- [91] LLTech Imaging: <http://www.lltechimaging.com/>.
- [92] Wajdene Ghouali, Kate Grieve, Salima Bellefqih, Otman Sandali, Fabrice Harms, Laurent Laroche, Michel Paques, and Vincent Borderie. Full-Field Optical Coherence Tomography of Human Donor and Pathological Corneas. *Current Eye Research*, 40(5):526–534, May 2015.
- [93] Jules Scholler, Viacheslav Mazlin, Olivier Thouvenin, Kassandra Groux, Peng Xiao, José-Alain Sahel, Mathias Fink, Claude Boccara, and Kate Grieve. Probing dynamic processes in the eye at multiple spatial and temporal scales with multimodal full field OCT. *Biomedical Optics Express*, 10(2):731, February 2019.
- [94] Jules Scholler. Dynamic Full Field OCT: <https://www.jscholler.com/2019-01-28-dffoct/>.
- [95] Kate Grieve, Arnaud Dubois, Manuel Simonutti, Michel Paques, José Sahel, Jean-François Le Gargasson, and Claude Boccara. In vivo anterior segment imaging in the rat eye with high speed white light full-field optical coherence tomography. *Optics Express*, 13(16):6286, 2005.
- [96] Johannes Schindelin, Curtis T. Rueden, Mark C. Hiner, and Kevin W. Eliceiri. The ImageJ ecosystem: An open platform for biomedical image analysis. *Molecular Reproduction and Development*, 82(7-8):518–529, July 2015.
- [97] Q. Tseng, E. Duchemin-Pelletier, A. Deshiere, M. Balland, H. Guillou, O. Filhol, and M. Thery. Spatial organization of the extracellular matrix regulates cell-cell junction positioning. *Proceedings of the National Academy of Sciences*, 109(5):1506–1511, January 2012.
- [98] S. Labiau, G. David, S. Gigan, and A. C. Boccara. Defocus test and defocus correction in full-field optical coherence tomography. *Optics Letters*, 34(10):1576, May 2009.
- [99] Kate Grieve, Djida Ghoubay, Cristina Georgeon, Gael Latour, Amir Nahas, Karsten Plamann, Caroline Crotti, Romain Bocheux, Marie Borderie, Thu-Mai Nguyen, Felipe Andreiuolo, Marie-Claire Schanne-Klein, and Vincent Borderie. Stromal striae: a new insight into corneal physiology and mechanics. *Scientific Reports*, 7(1), December 2017.

- [100] Roy de Kinkelder, Jeroen Kalkman, Dirk J. Faber, Olaf Schraa, Pauline H. B. Kok, Frank D. Verbraak, and Ton G. van Leeuwen. Heartbeat-Induced Axial Motion Artifacts in Optical Coherence Tomography Measurements of the Retina. *Investigative Ophthalmology & Visual Science*, 52(6):3908, May 2011.
- [101] Dipika V. Patel and Charles N. J. McGhee. Mapping of the Normal Human Corneal Sub-Basal Nerve Plexus by In Vivo Laser Scanning Confocal Microscopy. *Investigative Ophthalmology & Visual Science*, 46(12):4485, December 2005.
- [102] Brittany Simmons Shaheen, May Bakir, and Sandeep Jain. Corneal nerves in health and disease. *Survey of Ophthalmology*, 59(3):263–285, May 2014.
- [103] E. Meijering, M. Jacob, J.-C.F. Sarria, P. Steiner, H. Hirling, and M. Unser. Design and validation of a tool for neurite tracing and analysis in fluorescence microscopy images. *Cytometry*, 58A(2):167–176, April 2004.
- [104] Andrea Cruzat, Deborah Pavan-Langston, and Pedram Hamrah. In Vivo Confocal Microscopy of Corneal Nerves: Analysis and Clinical Correlation. *Seminars in Ophthalmology*, 25(5-6):171–177, November 2010.
- [105] Bernard E McCarey, Henry F Edelhauser, and Michael J Lynn. Review of Corneal Endothelial Specular Microscopy for FDA Clinical Trials of Refractive Procedures, Surgical Devices, and New Intraocular Drugs and Solutions:. *Cornea*, 27(1):1–16, January 2008.
- [106] Adnan Khan, Saadat Kamran, Naveed Akhtar, Georgios Ponirakis, Hamad Al-Muhannadi, Ioannis N. Petropoulos, Shumoos Al-Fahdawi, Rami Qahwaji, Faheem Sartaj, Blessy Babu, Muhammad Faisal Wadiwala, Ashfaq Shuaib, and Rayaz A. Malik. Corneal Confocal Microscopy detects a Reduction in Corneal Endothelial Cells and Nerve Fibres in Patients with Acute Ischemic Stroke. *Scientific Reports*, 8(1), December 2018.
- [107] Alfred Vogt and Robert von der Heydt. *Atlas of the Slitlamp-Microscopy of the Living Eye*. Springer-Verlag Berlin Heidelberg, 1921.
- [108] K. Grieve, D. Ghoubay, C. Georgeon, O. Thouvenin, N. Bouheraoua, M. Paques, and V.M. Borderie. Three-dimensional structure of the mammalian limbal stem cell niche. *Experimental Eye Research*, 140:75–84, November 2015.
- [109] Xupeng Shu, Jianhua Wang, and Liang Hu. A review of functional slit lamp biomicroscopy. *Eye and Vision*, 6(1):15, 2019.
- [110] Tadamichi Akagi, Akihito Uji, Alex S. Huang, Robert N. Weinreb, Tatsuya Yamada, Manabu Miyata, Takanori Kameda, Hanako Ohashi Ikeda, and Akitaka Tsujikawa. Conjunctival and Intrasceral Vasculatures Assessed Using Anterior Segment Optical Coherence Tomography Angiography in Normal Eyes. *American Journal of Ophthalmology*, 196:1–9, December 2018.
- [111] Raju Poddar, Robert J Zawadzki, Dennis E Cortés, Mark J Mannis, and John S Werner. *In vivo* volumetric depth-resolved vasculature imaging of human limbus and sclera with 1 μ m swept source phase-variance optical coherence angiography. *Journal of Optics*, 17(6):065301, June 2015.

- [112] Takenori Inomata, Masao Iwagami, Yoshimune Hiratsuka, Keiichi Fujimoto, Yuichi Okumura, Tina Shiang, and Akira Murakami. Maximum blink interval is associated with tear film breakup time: A new simple, screening test for dry eye disease. *Scientific Reports*, 8(1), December 2018.
- [113] Owens, H and Phillips, J. Spreading of the tears after a blink: velocity and stabilization time in healthy eyes. *Cornea*, 20:484–487, 2001.
- [114] Thomas Klein, Wolfgang Wieser, Lukas Reznicek, Aljoscha Neubauer, Anselm Kampik, and Robert Huber. Multi-MHz retinal OCT. *Biomedical Optics Express*, 4(10):1890, October 2013.
- [115] Roy Munson and Donald F. Young. *Fundamentals of fluid mechanics*. Wiley, 1990.
- [116] M. Shahidi, J. Wanek, B. Gaynes, and T. Wu. Quantitative assessment of conjunctival microvascular circulation of the human eye. *Microvascular Research*, 79(2):109–113, March 2010.
- [117] Liang Wang, Jin Yuan, Hong Jiang, Wentao Yan, Hector R. Cintrón-Colón, Victor L. Perez, Delia C. DeBuc, William J. Feuer, and Jianhua Wang. Vessel Sampling and Blood Flow Velocity Distribution With Vessel Diameter for Characterizing the Human Bulbar Conjunctival Microvasculature:. *Eye & Contact Lens: Science & Clinical Practice*, 42(2):135–140, March 2016.
- [118] Andreas Wartak, Richard Haindl, Wolfgang Trasischker, Bernhard Baumann, Michael Pircher, and Christoph K. Hitzenberger. Active-passive path-length encoded (APPLE) Doppler OCT. *Biomedical Optics Express*, 7(12):5233, December 2016.
- [119] Cameron J. Pedersen, David Huang, Mark A. Shure, and Andrew M. Rollins. Measurement of absolute flow velocity vector using dual-angle, delay-encoded Doppler optical coherence tomography. *Optics Letters*, 32(5):506, March 2007.
- [120] Pinar Aydin, Yonca A Akova, and Sibel Kadayifçılar. Anterior segment indocyanine green angiography in scleral inflammation. *Eye*, 14(2):211–215, March 2000.
- [121] Bernhard Sebastian and Petra S. Dittrich. Microfluidics to Mimic Blood Flow in Health and Disease. *Annual Review of Fluid Mechanics*, 50(1):483–504, January 2018.
- [122] Németh J. High-speed videotopographic measurement of tear film build-up time. *Invest Ophthalmol Vis Sci.*, (43):1783–1790, 2002.
- [123] Peng Xiao, Mathias Fink, and A Claude Boccara. Full-field spatially incoherent illumination interferometry: a spatial resolution almost insensitive to aberrations. *Optics letters*, 41(17):3920–3923, 2016.
- [124] ISO 15004-2:2007 - Ophthalmic instruments – Fundamental requirements and test methods – Part 2: Light hazard protection.
- [125] ISO 15004-1:2006 - Ophthalmic instruments – Fundamental requirements and test methods – Part 1: General requirements applicable to all ophthalmic instruments.
- [126] ISO/TR 20824:2007 - Ophthalmic instruments – Background for light hazard specification in ophthalmic instrument standards.

RÉSUMÉ

Ce projet de thèse vise à créer un système optique pour l'imagerie à haute résolution sans contact de la cornée humaine *in vivo*. Pour y parvenir, le système de tomographie par cohérence optique plein champ travaillant dans le domaine temporel *ex vivo* par contact (FFOCT) a été transformé en un dispositif d'imagerie *in vivo* sans contact et a été appliqué pour la première fois à l'œil humain. La FFOCT a permis d'acquérir des images de la cornée, du limbe, de la sclère et du film lacrymal sur des yeux humains, révélant des cellules et des nerfs, pouvant être quantifiés sur un champ de vision millimétrique, bien au-delà des capacités de la microscopie confocale et de la tomographie par cohérence optique (OCT) conventionnelle. Le flux sanguin et la dynamique du film lacrymal ont pu être suivis directement et quantifiés. De plus, la FFOCT a été combinée à un OCT spectral pour effectuer un suivi des mouvements axiaux de l'œil en temps réel et une correction de la défocalisation. Ce dernier ajout a permis l'imagerie et l'affichage FFOCT en temps réel, ce qui ouvre la voie à la mise en œuvre future de dispositifs dans pour la recherche que pour la pratique clinique. Le transfert de FFOCT du laboratoire à l'hôpital est en outre stimulé par plusieurs solutions qui sont proposées dans le manuscrit, dans le but de réduire la complexité instrumentale. Enfin, un dispositif FFOCT apparenté a été appliqué à l'imagerie rétinienne humaine *in vivo*, révélant des photorécepteurs.

MOTS CLÉS

Tomographie, Microscopie, Coherence, Cornee Diagnostic

ABSTRACT

This PhD project aimed to create an optical system for non-contact cellular resolution imaging of the human cornea *in vivo*. To achieve that, the contact *ex vivo* time-domain full-field optical coherence tomography (FFOCT) system was transformed into a non-contact *in vivo* imaging device and was for the first time applied to the human eye. FFOCT acquired images from the entire human cornea, limbus, sclera and tear film, revealing cells and nerves, which could be quantified over a millimetric field-of-view, beyond the capability of confocal microscopy and conventional optical coherence tomography (OCT). Blood flow and tear film dynamics could be directly followed and quantified. Furthermore, FFOCT was combined with a conventional OCT to perform real-time axial eye tracking and defocusing correction. The latter enabled real-time FFOCT imaging and display, which opens a path for future device implementation in clinical research and practice. Bench to bedside transfer of FFOCT is further stimulated by several solutions proposed in the manuscript, aiming to reduce the instrumentational complexity. Finally, a related FFOCT device was applied to imaging *in vivo* human retina, revealing the photoreceptors.

KEYWORDS

Tomography, Microscopy, Coherence, Cornea diagnostics